

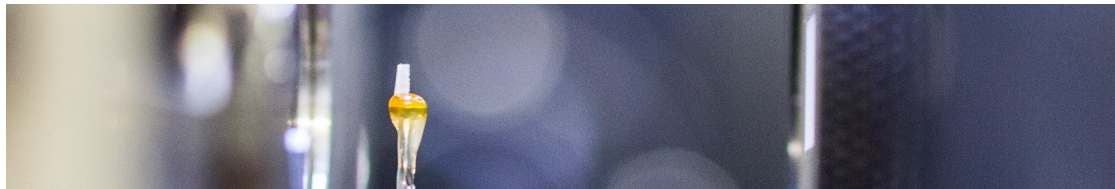


TECHNISCHE UNIVERSITÄT
BERGAKADEMIE FREIBERG

The University of Resources. Since 1765.



A Contribution to the Multidimensional and Correlative Tomographic Characterization of Micron–Sized Particle Systems



Von der Fakultät für Maschinenbau, Verfahrens- und Energietechnik
der Technischen Universität Bergakademie Freiberg

genehmigte

DISSERTATION

zur Erlangung des akademischen Grades

Doktor–Ingenieur (Dr.–Ing.)

vorgelegt von

Dipl.–Ing. (FH) Ralf Ditscherlein

geboren am 5. Januar 1983 in Rodewisch im Vogtland

Gutachter:

Prof. Dr.-Ing. Urs A. Peuker, TU Bergakademie Freiberg

Prof. Dr. rer. nat. habil. Erdmann Spiecker, FAU Erlangen-Nürnberg

Tag der Verleihung: 5. Juli 2022

Declaration

I hereby declare that I completed this work without any improper help from a third party and without using any aids other than those cited. All ideas derived directly or indirectly from other sources are identified as such. In the selection and use of materials and in the writing of the manuscript I received support from the following persons:

- Dr.-Ing. Thomas Leißner (supervisor)
- Dr.-Ing. Thomas Buchwald (proofreading)

Persons other than those above did not contribute to the writing of this thesis. I did not seek the help of a professional doctorate–consultant. No other persons have received any monetary benefits from me for work that has not been identified as such.

This thesis has not previously been published in the same or a similar form in Germany or abroad.

Ralf Ditscherlein
Freiberg, 27. Juli 2022



für Lotte

Danksagung (Acknowledgement)

Nun ist es soweit, und wer mich kennt, weiß dass so ein Absatz gefährlich ist, da ich sehr gerne und oft ins Philosophieren komme... ich versuche es kurz zu machen.

Als erstes möchte ich meinem Doktorvater Herrn Prof. Urs Peuker danken, dass er mir Ende 2017 die Möglichkeit gegeben hat, nach einigen Jahren empirischer Friemelei in der Industrie wieder in die wissenschaftliche Arbeit einzusteigen. Lisa bezeichnet es oft als überholte Denkweise, aber an dieser Stelle sei erwähnt, dass ich die Einstellung gegenüber ehemaligen FH-Studenten durchaus schon anders erlebt habe (Grüße an Holli-Bolli). Als Salamtaktiker hat er mich immer wieder in neue Aufgabenstellungen hineingeschoben. Obwohl wir uns in der Interpretation von Deadlines grundsätzlich unterscheiden, durfte ich so sehr viele neue Dinge dazulernen. Danke für viele interessante Diskussionen und vor allem für die Einwerbung der Geldmittel für so ein tolles Messgerät wie den Tomographen!

Ebenso möchte ich Herrn Prof. Erdmann Spiecker vom Institut für Mikro- und Nanostrukturforschung an der FAU Erlangen-Nürnberg danken, der sich zwischen zahlreichen Forschungsprojekten die Zeit genommen hat, das Zweitgutachten für die vorliegende Arbeit anzufertigen. Als wir am 10. November 2017 den Lehrstuhl zur Einweihung des neuen Nano-Computertomographen besucht hatten, war der Überblicksvortrag durch P. J. Withers (vergleichbar mit einem Treffen mit Simon Rattle, wenn man klassische Musik mag) und die anschließende Führung durch die Labore definitiv ein Motivationsschub zu Beginn meiner Arbeit.

Ich möchte den beiden T's danken: Thomas "TL" Leißner, der mich nach dem Vorstellungsgespräch beruhigte und meinte, das mit der Promotion als Bedingung für die Stelle sei wirklich kein Scherz (hier schon mal vielen Dank an meine Frau Lisa, dass Sie mich da im Ungewissen gelassen hat), ich solle mich dadurch aber nicht weiter beunruhigen lassen. Danke für die fruchtbaren Diskussionen und Ratschläge. Außerdem Thomas "Bukki" Buchwald, der mit unglaublicher Hingabe diese Arbeit gnadenlos aber konstruktiv gegengelesen hat. Der mit einer mir kaum bekannten Selbstsicherheit erschreckend selten irrt. Danke für viele Denkanstöße, Geduld und vor allem für Deine Freundschaft. Danke an meinen Freund Erik "la Créma" Löwer der mich jeden Tag ertragen musste. Danke für die tollen letzten Jahre in unserer Bassbox KKB 0038.

Dank an alle anderen lieben MVT Kollegen, allen voran Schüni, Katja und Susan. Danke an meine Hiwiline Trang und Diplomandin Judith für viele interessante Diskussionen und die gemeinsame Freude am Messen, schön, dass ihr jetzt auch meine Kollegen seid. Danke dem externen technischen Support von Holger Blank und Ingmar

Befeld. Ebenso ein großer Dank an die Deutsche Forschungsgemeinschaft (DFG) und an meine Kooperationspartner des SPP 2045, vor allem Orkun (dessen Vorlesungen ich sicherlich bald besuchen werde), der mich in den vergangenen Jahren immer positiv und konstruktiv begleitet hat und ein unglaublich gutes Gespür für die Schnittstelle von trockener Mathematik und der ingenieurmäßigen Anwendung an den Tag legt. Außerdem danke ich Prof. Volker Schmidt, der sich nicht zu schade war, auch das zehnte Mal einen guten Ratschlag zu geben. Johanna, Martin, Ruben und Silvan danke ich für viele interessante Aufgabenstellungen und Diskussionen.



Dank an Uli und Werner vom IG. Ein großer Dank an Jörg für die unglaublich schöne Zeit, vor allem auf See und auf dem Messmast! Dank an "Onkel" Axel für die musikalische Unterstützung. Euch beiden ein besonderer Dank für Hilfe in allen Lebenslagen und Inspiration für mein ganzes Leben. Danke an John und vor allem an Carsten für schöne Jahre an der WHZ in Zwickau und für unheimlich viel Spaß außerhalb der Vorlesungen. Vielen Dank an die Professoren Zahn, Schnabel, Hartmann und Neidhardt für ein wahnsinnig interessantes Studium. Außerdem Hans-Peter und den Rest der SolarWorld-Bande, insbesondere Heiko, Raik, Simone, Ralle, Gerd und Claudi.

Danke liebe Familie, meine Ditschis, Jauchis, Holzmüllis. Danke Mama und Papa, dass ihr immer für mich da seid. Ich glaube zwar, dass ihr nie genau im Detail wusstet, was ich mache, mich aber einfach habt machen lassen. Danke für eure Liebe. Danke Matthias, dass Du seit Deiner Geburt immer für mich da bist. Es kann keinen besseren Bruder geben! DANKE Lisa für Deine Liebe und für jeden einzelnen Tag mit Dir! Danke, dass ich einiges an Studienleben mit Dir zusammen nachholen durfte! Danke Lotte, dass Du so eine wunderbare Tochter bist und unser Leben so unglaublich bereicherst!

Wenn man bedenkt, in welcher Zeit ich diese Zeilen schreibe, sei vor allem auch dem da oben gedankt, dass wir in einem freien Land leben dürfen, ohne um unser Leben und das unserer Lieben fürchten zu müssen.

Ralf Ditscherlein
Freiberg, 27. Juli 2022

This cumulative dissertation is a summary of the following publications.

Paper A

Materials & Methods

R. Ditscherlein, T. Leißner, and U. A. Peuker. Preparation techniques for micron-sized particulate samples in X-ray microtomography. *Powder Technology*, 360:989–997, jun 2019. doi: 10.1016/j.powtec.2019.06.001[1]

R.D. (90%) method development, sample preparation, measurement and result evaluation, T.L. and U.A.P. contributed to method development. All authors contributed to elaborating the manuscript.

Paper B

Materials & Methods

R. Ditscherlein, T. Leißner, and U. A. Peuker. Self-constructed automated syringe for preparation of micron-sized particulate samples in X-ray microtomography. *MethodsX*, jan 2020. doi: 10.1016/j.mex.2019.11.030[2]

R.D. (90%) method development, sample preparation, measurement and result evaluation, T.L. and U.A.P. contributed to method development. All authors contributed to elaborating the manuscript.

Paper C

Materials & Methods

R. Ditscherlein, T. Leißner, and U. A. Peuker. Preparation strategy for statistically significant micrometer-sized particle systems suitable for correlative 3D imaging workflows on the example of X-ray microtomography. *Powder Technology*, 395:235–242, jan 2022. doi: 10.1016/j.powtec.2021.09.038[3]

R.D. (90%) method development, sample preparation, measurement and result evaluation, T.L. and U.A.P. contributed to method development. All authors contributed to elaborating the manuscript.

Paper D

Case Study

R. Ditscherlein, O. Furat, M. de Langlard, J. Martins de Souza e Silva, J. Sygusch, M. Rudolph, T. Leißner, V. Schmidt, and U. A. Peuker. Multiscale tomographic analysis for micron-sized particulate samples. *Microscopy and Microanalysis*, 26(4):676–688, jul 2020. doi: 10.1017/S1431927620001737[4]

R.D. (35%) method development including sample preparation, low-resolution and medium-resolution measurements (micro-CT), T.L. and U.A.P. contributed to method development, J.M. performed high-resolution measurements (nano-CT). O.F., M.L., and V.S. performed data analysis including image segmentation and multidimensional modelling (copula approach). J.S. and M.R. provided process-relevant particle systems (including pre-characterization). All authors contributed to elaborating the manuscript.

Paper E

Data Handling

R. Ditscherlein, O. Furat, E. Löwer, R. Mehnert, R. Trunk, T. Leißner, M. J. Krause, V. Schmidt, and U. A. Peuker. PARROT: A pilot study on the open access provision of particle-discrete tomographic datasets. *Microscopy and Microanalysis*, page 1–11, 2022. doi: 10.1017/S143192762101391X[5]

R.D. (30%) idea, concept, GUI design, particle sample preparation and data curation, O.F. and V.S. additional ideas regarding application examples, stochastic modelling, additional particle parameters, E.L. concept, particle segmentation, filtration example, R.M. design and implementation of the relational database, programming of the GUI and the import routines, R.T. and M.J.K. application example particle simulation, T.L. and U.A.P. project realization. All authors contributed to elaborating the manuscript.

Additionally, there are **contributions** to the following studies not covered by this thesis:

R. Wagner, M. Seleznev, H. Fischer, R. Ditscherlein, H. Becker, B. G. Dietrich, A. Keßler, T. Leißner, G. Wolf, A. Leineweber, U. A. Peuker, H. Biermann, and A. Weidner. Impact of melt conditioning and filtration on iron-rich β phase in AlSi9Cu3 and its fatigue life studied by μ CT. *Materials Characterization*, 174:111039, apr 2021. doi: 10.1016/j.matchar.2021.111039 [6]

XRM measurements, basic image processing and analysis strategies

D. Hoppach, E. Werzner, C. Demuth, E. Löwer, H. Lehmann, L. Ditscherlein, R. Ditscherlein, U. A. Peuker, and S. Ray. Experimental investigations of the depth filtration inside open-cell foam filters supported by high-resolution computed tomography scanning and pore-scale numerical simulations. *Advanced Engineering Materials*, page 1900761, oct 2019. doi: 10.1002/adem.201900761 [7]

Sample preparation strategy

T. Leißner, A. Diener, E. Löwer, R. Ditscherlein, K. Krüger, A. Kwade, and U. A. Peuker. 3D ex-situ and in-situ X-ray CT process studies in particle technology—A perspective. *Advanced Powder Technology*, oct 2019. doi: 10.1016/j.appt.2019.09.038 [8]

Section 2.3 Monitoring concentration differences

O. Furat, T. Leißner, R. Ditscherlein, O. Šedivý, M. Weber, K. Bachmann, J. Gutzmer, U. A. Peuker, and V. Schmidt. Description of ore particles from X-ray microtomography (XMT) images, supported by scanning electron microscope (SEM)-based image analysis. *Microscopy and Microanalysis*, 24(5):461–470, oct 2018. doi: 10.1017/s1431927618015076 [9]

Literature review regarding correlation absorption contrast and material

C. Voigt, J. Hubálková, L. Ditscherlein, R. Ditscherlein, U. A. Peuker, H. Giesche, and C. G. Aneziris. Characterization of reticulated ceramic foams with mercury intrusion porosimetry and mercury probe atomic force microscopy. *Ceramics International*, 44(18): 22963 – 22975, 2018. doi: 10.1016/j.ceramint.2018.09.094 [10]

Section 2.2 Sample characterization, sample preparation strategy, XRM measurement, qualitative image analysis

Results were also presented at the following conferences and workshops:

R. Ditscherlein, S. Englisch, O. Furat, L. Hansen, A. Weber, T. Leißner, V. Schmidt, E. Spiecker, and U. A. Peuker. Correlative measurement and multidimensional characterization of fine particle systems. In *ECCE/ECAB 2021 – 13th European Congress of Chemical Engineering and 6th European Congress of Applied Biotechnology*, September 2021 [11]

S. Englisch, R. Ditscherlein, O. Furat, L. Hansen, D. Drobek, J. Wirth, S. Carl, T. Leissner, B. A. Zubiri, A. Weber, V. Schmidt, U. A. Peuker, and E. Spiecker. Comprehensive, multidimensional and correlative particle characterization of a saxolite and talcum compound to support the understanding of complex separation processes. In *Microscopy & Microanalysis*, August 2021 [12]

J. Schreier, R. Ditscherlein, T. Leißner, U. A. Peuker, and U. Bröckel. Mikroröntgentomographie zur Charakterisierung des Trennerfolgs bei der mehrdimensionalen formselektiven Umbenetzungsagglomeration. In *Online Jahrestreffen der ProcessNet–Fachgruppen Mechanische Flüssigkeitsabtrennung, Zerkleinern und Klassieren sowie Agglomerations- und Schüttguttechnik*, March 2021 [13]

R. Wagner, A. Weidner, M. Seleznev, H. Fischer, H. Biermann, R. Ditscherlein, T. Leissner, U. A. Peuker, B. Dietrich, A. Kessler, and G. Wolf. μ CT–Untersuchungen zum Einfluss einer Schmelzekonditionierung und -filtration auf die eisenreiche β -Phase in AlSi9Cu3 und deren Ermüdungsverhalten. In *38. Vortrags- und Diskussionstagung Werkstoffprüfung*, December 2020 [14]

R. Ditscherlein, O. Furat, M. de Langlard, J. Martins de Souza e Silva, J. Sygusch, M. Rudolph, T. Leißner, V. Schmidt, and U. A. Peuker. Multi–Skalen Ansatz für die röntgentomographische Analyse partikulärer Proben im Bereich kleiner 10 μ m. In *Hybrides Jahrestreffen der ProcessNet–Fachgruppe Partikelmesstechnik und des Arbeitsausschusses Feinstäube*, March 2020 [15]

R. Ditscherlein, T. Leissner, O. Furat, J. Martins de Souza e Silva, J. Sygusch, M. Rudolph, V. Schmidt, and U. A. Peuker. Multi–scale particle analysis. In *ZEISS XEN 7th X–ray microscopy european network user workshop*, January 2019 [16]

R. Ditscherlein, T. Leissner, O. Furat, V. Schmidt, and U. A. Peuker. Segmentation–optimized preparation method for particulate samples in micro–CT analysis. In *International Congress on Particle Technology–PARTEC*, April 2019 [17]

Contents

1	Outline	1
2	Description of Particle Properties	4
2.1	Integral or Class-Based Description	4
2.2	Particle-Discrete Description	5
2.2.1	2D Description	5
2.2.2	Full 3D Description	6
2.3	Multidimensional Characterization on Basis of Particle-Discrete 3D Data	7
2.3.1	Motivation	7
2.3.2	Kernel Density Approach	9
2.3.3	Copula Approach	9
3	X-ray Tomography	11
3.1	Historical Context	11
3.2	X-ray Physics	12
3.2.1	X-ray Generation	12
3.2.2	Polychromatic Spectrum	13
3.2.3	Interaction with Matter	14
3.3	Tomographic Imaging	15
3.3.1	Motivation	16
3.3.2	Basic Idea	16
3.3.3	X-ray Microscopy Measurement Setup and Workflow	16
3.3.4	Tomographic Reconstruction via Filtered Back Projection	18
3.3.5	Region of Interest Tomography	20
3.4	Relevant Artefacts Related to Particle Measurement	22
3.4.1	Temperature Drift	22
3.4.2	Penumbral Blurring and Shadow	23
3.4.3	Cone Beam	23
3.4.4	Out-of-Field	24
3.4.5	Center Shift	24
3.4.6	Sample Drift	24
3.4.7	Beam Hardening	25
3.4.8	Rings	27
3.4.9	Noise	27
3.4.10	Partial Volume	27
3.4.11	Summary	28

4	Practical Implementation	30
4.1	Particle Sample Requirements	30
4.1.1	Geometry	30
4.1.2	Dispersity and Homogeneity	31
4.2	Statistics	32
4.2.1	Single Particle Properties	32
4.2.2	Properties of a Limited Number of Particles (10 to several 100)	32
4.2.3	Particle Populations with Distributed Properties	33
4.3	2D Validation	34
4.4	Measurement	34
4.4.1	X-ray Microscope	34
4.4.2	Source Filter	35
4.4.3	Detector Binning	36
4.4.4	Cone Beam Artefact Compensation	37
4.4.5	Center Shift Correction	38
4.4.6	Dynamic Ring Removal	39
5	Image Analysis	41
5.1	Image Quality	41
5.1.1	Grey Value Histogram	41
5.1.2	Resolution	43
5.1.3	Signal-to-Noise Ratio	45
5.1.4	Contrast and Dynamic Range	46
5.1.5	Sharpness	47
5.1.6	Summary	47
5.2	Basic Image Processing Strategies	48
5.2.1	Threshold-Based Segmentation	48
5.2.2	Machine Learning Assisted Segmentation	49
6	Correlative Tomography	51
6.1	Scouting Approach	52
6.2	Multiscale Approach	53
6.3	Multidisciplinary Approach	54
7	Data Management	55
7.1	Data Quality	56
7.2	Data Availability	56
7.2.1	Tomographic Datasets	56
7.2.2	Particle Database	57
8	Outlook on Further Research Activities	58
9	Publications	67
9.1	Copyright Declaration	67

9.2	Overview	68
9.3	List of Publications	68
	Paper A , Preparation techniques for micron-sized particulate samples in X-ray microtomography	69
	Paper B , Self-constructed automated syringe for preparation of micron-sized particulate samples in X-ray microtomography	79
	Paper C , Preparation strategy for statistically significant micrometer-sized particle systems suitable for correlative 3D imaging workflows on the example of X-ray microtomography	87
	Paper D , Multi-scale tomographic analysis for micron-sized particulate samples	104
	Paper E , PARROT: A pilot study on the open access provision of particle discrete tomographic datasets	126
10	Appendix	161
10.1	Application Example 1: Fracture Analysis	161
10.2	Application Example 2: 3D Contact Angle Measurement	162
10.3	Influence of the Source Filter	164
10.4	Influence of the X-rays on the Sample	164
10.5	Appropriate Filter Settings	165
10.6	Log File Parser	165

List of Figures

1.1	Difference in the visualisation of tomographic data	1
1.2	Placing the papers in the overall context	2
2.1	Sectional images from three different soda–lime glass particles	5
2.2	Sectional images with related 3D particle data	6
2.3	Marginal distributions of two different 2D datasets.	8
2.4	Comparison of KDE and Copula approach	10
3.1	X–ray generation, tube design, and interaction mechanisms	13
3.2	Possibilities of influencing the X–ray spectrum	14
3.3	X–ray absorption mechanisms of photons	15
3.4	Difference between 2D projection and 3D tomographic sections	17
3.5	X–ray microscopy setup and tomographic workflow	18
3.6	Back projection workflow with/without filtering	19
3.7	Projection images under varying rotation angle	21
3.8	Temperature drift of the excitation bulb	22
3.9	Cone beam artefact and its manifestations	23
3.10	Motion artefact, visualised by statistical measures	25
3.11	Motion artefact and its manifestations in the reconstruction	26
3.12	Beam–hardening examples	26
4.1	Particle samples suitable for XRM measurements	30
4.2	Setup of the X–ray microscope Zeiss Xradia VERSA 510	35
4.3	X–ray source filtering	35
4.4	X–ray source settings and related projection images	36
4.5	Detector pixel binning	37
4.6	Visualisation of the cone beam artefact	37
4.7	Quantification of the cone beam artefact	38
4.8	Verification of the cone beam artefact	39
4.9	Center shift correction	39
4.10	Dynamic ring removal	40
5.1	Bit depth of a grey scale image.	42
5.2	Image objects and their relation to the grey value histogram	43
5.3	Different combinations of geometric and optical magnification	44
5.4	Influence of exposure time on SNR	45
5.5	Overexposure of a projection image	47

5.6	Summary of factors influencing quantitative image data evaluation . . .	48
5.7	Particle segmentation strategies	50
6.1	Exemplary tomographic workflow for FOV scouting	52
6.2	Examples for multiscale and multidisciplinary approach	53
7.2	Sections of three different dolomite particles	57
8.1	X-ray tomographic workflow for element-specific analysis	58
10.3	Influence of the source filter	164
10.4	Colour change of epoxy matrix after X-ray exposure	164

List of Tables

3.1	Dependencies of the attenuated X-ray intensity after Beer-Lambert . . .	15
3.2	Overview of relevant XRM artefacts related to particulate material	29
5.1	Calculated total magnification of the XRM measurement setup	44
10.1	Source filter selection for X-ray tomographic measurements	165

Acronyms

AMC	adaptive motion compensation	HDR	high dynamic range
BH	beam hardening	KDE	kernel density estimation
CT	computed tomography	MLA	mineral liberation analysis
DEM	discrete element method	PFIB	plasma focused ion beam
DIC	digital image correlation	PVE	partial volume effect
DOI	digital object identifier	ROI	region of interest
DRR	dynamic ring removal	SEM	scanning electron microscopy
DVC	digital volume correlation	SNR	signal-to-noise ratio
EBSD	electron backscatter diffraction	TEM	transmission electron microscopy
EDXS	energy-dispersive X-ray spectroscopy	USFT	ultra sonic fatigue test
FBP	filtered back projection	VIS	visible spectrum
FFT	fast Fourier transformation	WEKA	waikato environment for knowledge analysis
FIB	focused ion beam	XRM	X-ray microscope
FMD	finite mixture distribution	XRD	X-ray diffraction
FST	Fourier slice theorem	XRF	X-ray fluorescence
FOV	field of view		

Abstract

Die vorliegende Arbeit ist im Rahmen des Schwerpunktprogramms SPP 2045 entstanden. Technische Feinstpartikelsysteme ($< 10 \mu\text{m}$) aus hochspezifischen Trennprozessen sollen hier hinsichtlich mehrdimensionaler Eigenschaftsverteilungen untersucht werden. Tomographische Messverfahren erlauben dabei eine vollständige 3D Beschreibung partikeldiskreter Datensätze statistisch relevanter Größe. Der Schwerpunkt der Arbeit liegt auf der röntgentomographischen Analyse mittels Mikro-Computertomographie (mikro-CT), die im Bedarfsfall unter Einbeziehung weiterer Messmethoden (nano-CT) auf mehrere Größenskalen erweitert und durch geeignete Elementanalytik (FIB-SEM + EBSD, EDX) ergänzt wird. Methodisch werden zwei Präparationsverfahren (Wachs, Epoxidharz) für unterschiedliche Partikelpräparate beschrieben, welche in einer Fallstudie bereits veröffentlicht bzw. im Ausblick der Arbeit Gegenstand aktueller Studien ist. Schließlich wird eine vernetzte Mehrfachnutzung der erzeugten Daten innerhalb einer online-Partikeldatenbank gezeigt und deren Anwendung an drei konkreten Beispielen erläutert.

The present work was carried out within the framework of the priority programme SPP 2045. Technical ultra-fine particle systems ($< 10 \mu\text{m}$) from highly specific separation processes are to be investigated here with regard to multi-dimensional property distributions. Tomographic measurement methods allow a comprehensive 3D description of particle-discrete data sets of statistically relevant size. The focus of the work is on X-ray tomographic analysis by means of micro-computed tomography (micro-CT), which, if necessary, is extended to several size scales by including further measurement methods (nano-CT) and supplemented by suitable elemental analysis (FIB-SEM + EBSD, EDX). Two preparation methods (wax, epoxy resin) for different particle preparations are described methodically, which have already been published in a case study or are the subject of current studies in the outlook of the work. Finally, a networked multiple use of the generated data within an online particle database is shown and its application is explained using three concrete examples.

1 Outline

In the last three decades, X-ray tomography has become a standard tool in a lot of research areas, like material science [18, 19], biology [20], hydrology [21], geoscience [22], or industrial applications [23, 24]. In particle technology and mineral processing, Lin et al. [25] and Miller et al. [26] prepared the first reviews on the topic, which largely refer to their own pioneering work in this field. Coming from 2D sectional imaging of minerals [27], they try to use the technique of non-destructive X-ray tomography well-known from medical applications for their own research. Although they were aware of the limitations of the time, especially due to computing technology, their work laid the foundation for a multitude of applications in this field. Looking at Fig. 1.1 shows the potential of this technology and the enormous progress that has been made in recent decades, especially by comparing two reconstructed sections from different particle samples.

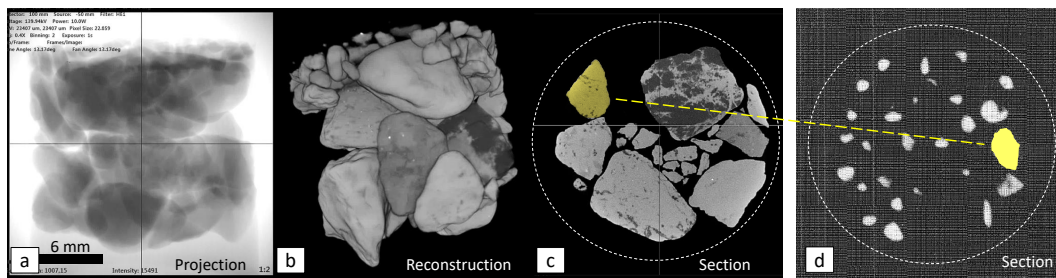


Figure 1.1: Difference between (a) an X-ray projection image from a 360°series, (b) the corresponding reconstructed 3D dataset with (c) an exemplary section in the XY-plane. Note, that the section can always be identified by its circular shape due to the reconstruction mechanism, see Sec. 3.3, and (d) the tremendous progress when comparing image quality with first measurements by Miller et al. [26]. The scale bar refers to (a) to (c), due to a missing scale bar in [26], comparable length scale is indicated in yellow on two comparable particles.

Although Fig. 1.1-d, which depicts as section acquired by Miller et al. [26], shows only single-phase particles, the image quality suggests that it was not at all possible to obtain detailed information of particle phases as can be seen in Fig. 1.1-c, which is acquired by a state-of-the-art lab-based system used in this thesis. Fig. 1.1-b shows the related 3D *tomogram*, which is reconstructed from a series of projection images, as can be seen in Fig. 1.1-a. The distinction of these kinds of image types will be essential for understanding the 3D particle analysis covered in the present thesis.

This thesis is a collection of five publications, each of which is self-contained, but all of which follow a common thread. **Paper A** [1] and **Paper B** [2] describe a detailed validation of an automated sample preparation method that utilizes a wax matrix with which it is possible to create dispersed particle systems without applying mechanical stress and which facilitates the segmentation process. **Paper C** [3] describes an analogues method, which uses a combination of epoxy resin with low X-ray absorbing nano spacer particles. Unlike the wax method, the resulting samples are mechanically very stable and suitable for processing with high-energy radiation,

photons in the case of laser milling and ions in the case of ion beam cutting. Contrary to the wax method, where the validation was done with a single-thresholding image processing workflow, the latter method was validated with the help of a machine learning algorithm. **Paper D** [4] describes an exemplary tomographic workflow for a multiscale characterization of micron-sized particle samples suitable for a mixture of single-phase particles, in this case fibres and spheres, where the wax preparation method from **Paper A** was used. Here, multidimensional correlation structures of both systems were captured using parametric copulas, a set of correlation functions described in detail in Sec. 2.3.1. An application example of the epoxy nano particle method from **Paper C**, which is particularly suitable for the analysis of multi-phase particles, is currently in the process of publication. First results are presented in Sec. 6. Fig. 1.2 is a summary that places the papers in perhaps the most important context of this topic—the increase in knowledge on particle properties as a function of structural resolution.

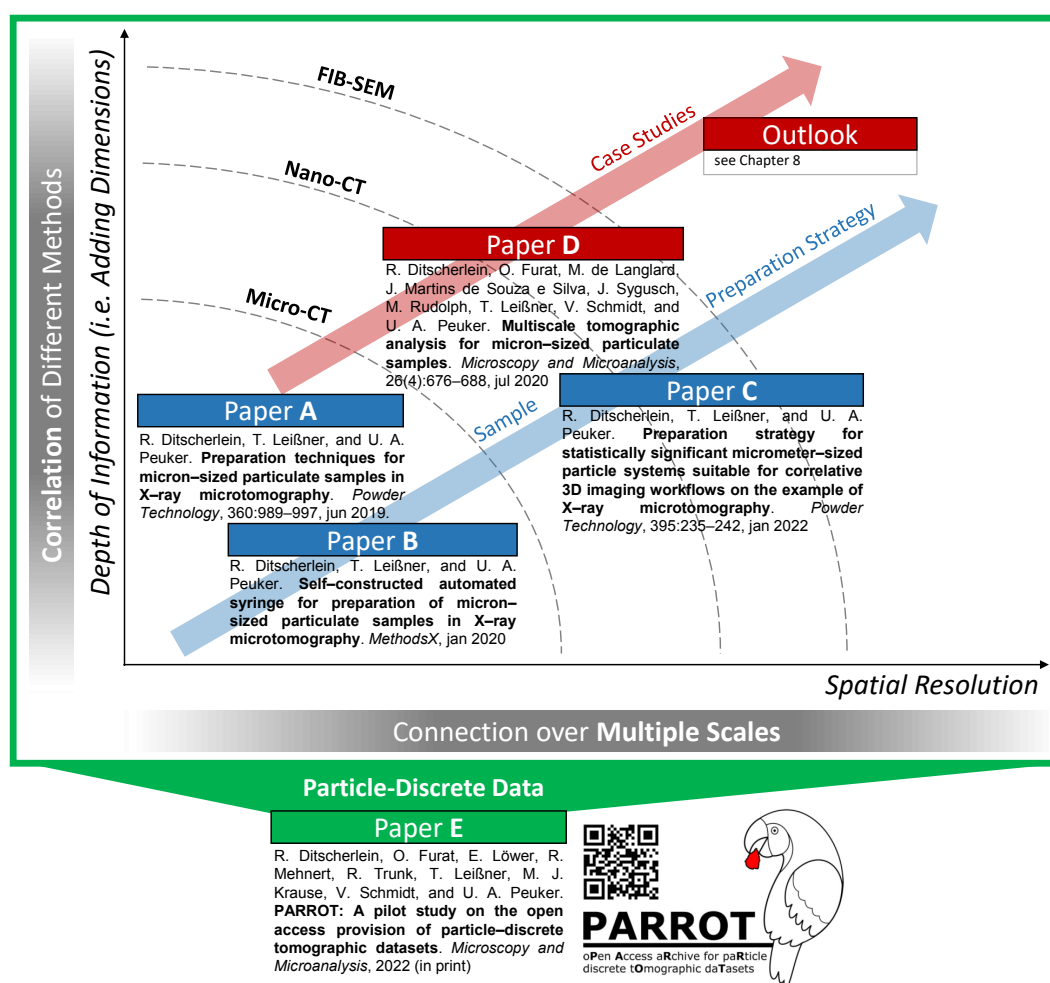


Figure 1.2: Placing the papers in the overall context.

Many challenges in this regard are referred to this: for example the possibility of correlating the information acquired by different three-dimensional measurement techniques, and doing this over multiple length scales; The design of suitable sample preparation strategies and implementation of practical workflows; And, as an ultimate goal, the connection of all this to gain multidimensional particle informa-

tion, which can be used to describe and guarantee highly specific multidimensional fractionation of technical fine particle systems to get very defined and highly pure starting products for a wide range of modern materials.

An interconnected scientific framework facing these challenges is the *Priority Programme SPP 2045* of the German Research Foundation. All publications covered by this thesis are part of the work within sub–project Z1 (313858373), which deals with multidimensional and correlative characterization of particle systems. At this point it is important to emphasise that without this collaborative work between the research teams, especially in the area of statistical image data analysis, and the methodological exchange within a large number of scientific meetings, the depth of the topic could not have been mapped in this detail. **Paper E** [5] gives a possible solution to provide the measurement results of the present work in a suitable form and thus lay the foundation for an ongoing common use in the form of a database comprised of the generated particle–discrete data.

Although each paper on its own has a motivation and a descriptive materials and methods section, they are linked by the following introducing part of this thesis, which also serves as enclosing bracket. In this regard, Sec. 2, *Description of Particle Properties*, works as a basic introduction into multidimensional particle analysis. In Sec. 3, *X–ray Tomography*, the main measurement principle used in all studies is described on an intermediate level that will allow to understand the principle in sufficient detail, but also the effects which can be seen in the results of the study. The last subsection of this Sec. 3 leads over to, Sec. 4, *Practical Implementation*, which is concerned with the sample, statistical considerations, validation methods, and finally the measurement. Sec. 5, *Image Analysis*, gives an overview of image quality measures, always discussed on examples from own measurements, followed by a short comparison of two different image segmentation strategies. In Sec. 6, *Correlative Tomography*, a short overview of the different goals of correlative measurement is given based on some examples. As visualized in Fig. 1.2, data handling is one of the major issues in data–driven analysis methods. A short overview of data quality assessment and the organization of tomographic datasets on a local file system, and of the particle–discrete datasets within a globally accessible online particle database is given in Sec. 7, *Data Management*. Sec. 8, *Outlook on Further Research Activities*, takes up Sec. 6 and gives an overview of the current state of research and a small outlook in this field.

In all sections, it was attempted to support all practice–relevant statements with examples from the literature and own observations in order to not only accept the relevant parameters and settings, as the basis of the publications, as best practice, but to specifically question them in order to generate additional added value in parallel to the publications, which can be used for further measurement tasks.

2 Description of Particle Properties

The main goal of the analysis of a particle system is to find suitable parameters for a reasonable description that can be used for quantification, and thus, for a comparison regarding different properties. Depending on the measurement method, this can be done either by aggregating the whole, or parts of the distribution, which is introduced in Sec. 2.1, or by direct image-based analysis in two or three dimensions, given in Sec. 2.2. It is less the question of whether a method is good or bad, but rather if it fits to the chosen particle system. In the present study, idealised particles were used in most cases, e.g. spheres or fibres, in order to be able to carry out a reasonable method development. To do this systematically within the context of this work, it was deliberately restricted to the parameter of particle size as one major geometrical property. However, all methods are designed in such a way that they can be applied to other particle systems as well as, in the case of multidimensional analysis, to other parameter distributions. This section will give a general motivation for the particle-discrete 3D analysis of particle systems. Simultaneously, the analysis of several distributed parameters of the particle system, a so-called multidimensional analysis, is discussed in detail in Sec. 2.3.

2.1 Integral or Class-Based Description

To aggregate information on particles in a reasonable manner, assumptions have to be made, depending on the used measurement principle. For example, under the assumption that all particles passing the beam path in laser diffraction are spherical, a mathematical model¹ can be applied to translate the diffraction pattern on the CCD into a particle size distribution. A back-calculation from the diffraction pattern to particle-discrete information is not possible [28]. The particles are only considered as a collective with collective properties.

Another approach is to divide the particle collective into discrete size fractions, also referred to as classes. For example, sieving divides a collective into particles that pass through and those that are too large and remain on the sieve. More classes require additional sieves differing in mesh size. Spherical particles smaller than the mesh size will pass the sieve with a certain probability. In case of non-spherical particles, the characteristic length is decisive here. The probability of passing is now not independent of the particle's shape. This method will by no means represent a fully comprehensive way of particle characterization. As will be shown in the next sections, this is only possible having particle-discrete data. When dealing with spherical particle systems, this description is a practical and reasonable approach and an established method for particle-size characterization. Moving away from these ideal systems, this may no longer be the case. In the following, an approach is introduced that does not focus on the particle collective but on the individual particle. Collective parameters can then be derived from a large number of these particles.

¹ *Fraunhofer* diffraction theory is applied for spherical particles above approx. 1 μm ; below this size, near the wavelength of the used laser light, the *Mie* scattering theory is applied.

2.2 Particle–Discrete Description

Particle–discrete in this case means that particles are considered individually. Although part of the particle collective, they each have their own property vector, which can be evaluated individually and used as filter criteria, see **Paper E**.

2.2.1 2D Description

In static image analysis like optical microscopy or scanning electron microscopy (SEM) particles are separated manually on a microscope slide² or embedded in a well machinable matrix. In some cases, serial sectioning by micro–milling [29] or focused ion beam (FIB) [30] are used to create quasi–3D datasets. Although it is also possible with this method to pick up a sufficiently large statistical relevant number of particles, there are large deviations when deducing a 3D volume from 2D sections, especially for irregularly shaped particles [31, 32, 33]. The low–dimensional view then results in an error between the measurement and reality, the so-called *stereological bias*. Ueda et al. [34] quantify this stereological bias by comparing 2D with 3D X–ray micro computed tomography (CT) data by imaging artificial minerals. They determined a stereological correction method which compensates this by up to 60% for the used artificial binary particles.

Another approach to deal with the stereological bias starts one step earlier in the preparation process. Because crushed materials with a wide particle size distribution segregate inside the matrix when using a standard embedding technique vertically, the observed particle size will strongly depend on the height at which the sample is cut. One possible way to compensate for this is given by Heinig et al. [35]. They cut the already prepared sample, rotate the individual parts by 90 degrees, such that the direction of segregation is not aligned horizontally, and again embed them.

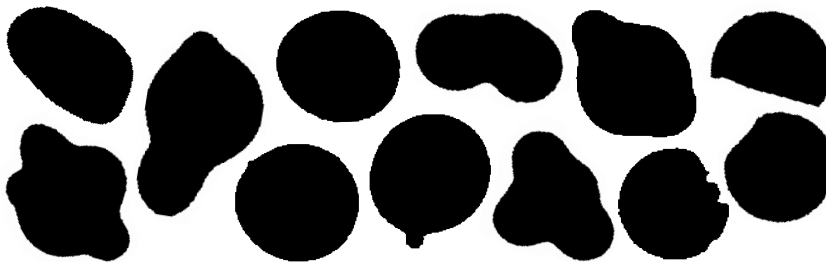
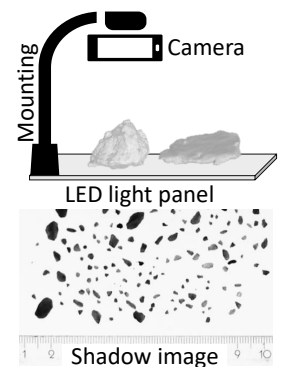


Figure 2.1: Exemplary sections originating from a 3D data set of three different soda–lime glass particles differing in shape; from an ideal sphere over little satellites on the particle surface towards a significant deviation from the spherical shape.

These methods were supplemented by dynamic approaches, which represent a significant development, especially with regard to the statistical representativeness of the samples [23]. Due to the particles passing by or falling past a static lens, a large number of particles enter the measurement field of view (FOV). However, the captured images are strongly dependent on the particles' current orientation [36]. Image tracking algorithms are used to compensate for that, but only down to particle sizes of around 100 μm [37]. A complete 3D description of a collective of particles smaller than 10 μm is not possible with these methods. Fig. 2.1 shows cross–sections

² One possible way to capture 2D particle information; Setup from a student practical training.



from 3D particle data. As can be seen, the shapes are diverse, but do not differ significantly from each other.

The cross-sections suggest that the particles are almost spherical and will not lead to a significant error in determining particle-related characteristics. But although the sample is homogeneous with a sufficiently large number of particles³, and a large number of cross-sections has been analysed, the effect of stereological bias will remain when dealing with particles that deviate strongly from the ideal spherical shape. This is discussed on the example of a mixture of fibres and spheres via a *multiscale approach*, see Sec. 6.2 and **Paper D**. The longest dimension, which is in this case the fibre length, cannot be captured sufficiently well in cross-sectional images. Without additional knowledge of the particle system's principal shape, significant errors can occur. Only a three-dimensional analysis method can capture individual particles.

³ Details regarding sampling and sample preparation theory are discussed in the methodological **Paper A** and **Paper C**

2.2.2 Full 3D Description

Taking the 2D sections from Fig. 2.1, a 3D tomographic measurement reveals four particles which, in some cases, show significant differences from the spherical shape, which are not apparent from the 2D sections, see Fig. 2.2.

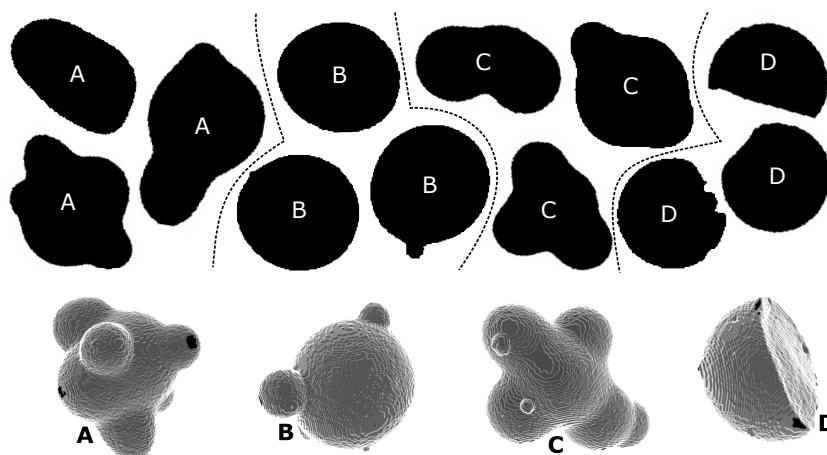


Figure 2.2: 2D sections shown in Fig. 2.1 grouped according to the affiliation to their 3D representatives A to D. Especially in case of particle C a significant deviation from the spherical shape can be observed which is not visible in the three chosen sections.

Before coming to a more detailed description of the applications of micro-CT in particle technology, see Sec. 4.2, the focus should now be on the nature of the 3D description. A possible categorization can be made as follows:

1. *intra-particle* or structural description, meaning a distinction of all particle sub-phases, for example natural mineral composition analysed by mineral liberation analysis (MLA)⁴ [32, 39, 40] or artificial composites and layer structures respectively [41], or microstructural particle features like pores or cracks [42, 43],
2. *particle-discrete* description, meaning a permanent particle characteristic, like size and shape [44, 45], which is only changed when the particle is mechanically, thermally, or chemically stressed, thereby deforming or breaking into individual parts, forming new particles with new inherent features, and
3. *inter-particle* description, meaning the relationship of individual particles to

⁴ One example for an MLA-analysis [38] result, which is a combination of an SEM-image, determining the actual particle image, and the results from an energy dispersive X-ray spectroscopy, determining the mineralogical composition of the particle's phases, coded by a distinct colour.



each other [46] within a solid particle composite or a loose particle bed [8], for example the porosity or coordination number within a filter cake structure [47].

In all presented studies, **Paper A to E**, the focus is on the particle–discrete description, as process–relevant parameters, like particle size and shape, cannot be treated separately from each other [48]. The more the particle deviates from the ideal spherical shape, which is assumed in many models, the more clearly various particle size definitions differ. Although there are other shape descriptors than sphericity, which include characteristics of such deviations, for example roundness, aspect ratio, or compactness [49, 50, 28, 44]⁵, but not as a *complete* description. Complete means that the calculated shape parameters can be traced back to the original particle geometry. Using calculated shape parameters, this can only be done approximately, since the basis for the calculations here are particle dimensions, like axis lengths or particle volume. An exact knowledge of the particle’s three–dimensional structure is essential to be able to evaluate the significance of the mentioned particle descriptors.

There are two methods to do this. The first is based on the voxel dataset gained after the reconstruction of tomographic data. Here, the particle shape is described by the volume that is enclosed by a surface boundary, called the *boundary method*, or all voxels of the particle’s surface are contributing, which is called the *assemblage method* [50]. Both strongly depend on the resolution of the measurement device [51] and have the problem of the fractal nature of the particle surface [52, 53]. The second method is the mathematical transformation of the voxel–based dataset into a functional representative of a particle. For example, one approach that can be interpreted as the equivalent of a 2D *Fourier*–analysis on the surface of a sphere in 3D, the so–called *spherical harmonics* [49, 54, 55]. Note again that this work focuses on the voxel–based description of particle–discrete size descriptors based on tomography data only.

2.3 Multidimensional Characterization on Basis of Particle–Discrete 3D Data

In contrast to integral or class–based distribution parameters, discrete particle data allow for the direct correlation of two or more distributed parameters, so–called *marginal distributions*, hereafter referred to as *multidimensional analysis*⁶.

2.3.1 Motivation

The following two examples serve to motivate the process of correlated multidimensional characterization of particle systems in further detail:

1. Marginal distributions that show *no discernible* patterns like local maxima or minima, as a special case of the uniform distribution, which, however, show different patterns in the two–dimensional overlay like the ones given in Fig. 2.3-a
2. Marginal distributions that show *discernible* patterns, suggesting a trivial connection in the two–dimensional plane, but which in reality can be derived from a wide variety of 2D patterns as can be seen in Fig. 2.3-b.

⁵ Note that this passage is only for motivation purposes and by no means a fully comprehensive introduction to this topic.

⁶ Note that the following examples are reduced in dimensionality for a simplified presentation. The histograms shown as sums of pixels in rows and columns of the 2D diagram is in reality a projection from a 3D space onto a 2D marginal distribution.

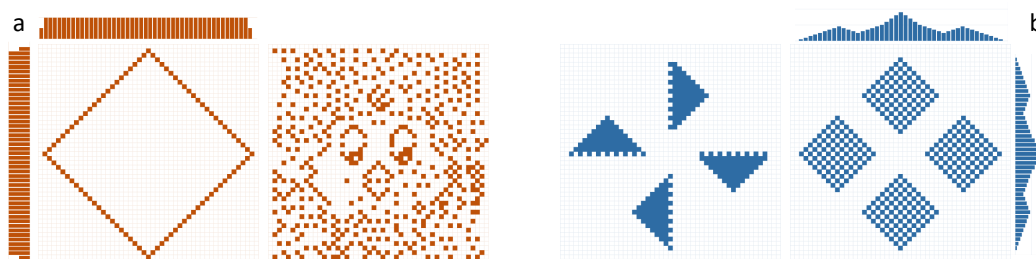


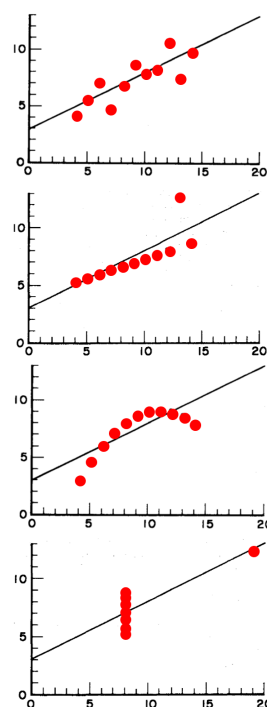
Figure 2.3: Connection between marginal 1D distributions and the original 2D counterpart. Both examples show two very different patterns in two dimensions giving the same 1D marginal distribution, (a) resulting in a uniform, (b) in marginal distributions with three local maxima.

Regarding 1D marginal distribution, Anscombe [56] showed on four data sets that although they have significantly different distributions, their basic statistical properties, such as average, standard deviation, correlation, and linear regression, are identical.⁷ Although Anscombe's intention was to emphasize the importance of graphical compared to statistical analysis, this example shows that the acquisition and processing of raw data is essential in order to work with datasets in a reasonable way. A conclusion from aggregated values to the true distribution without considering the underlying data points is not possible. This sounds trivial, but can be problematic in the case of integral and class-based methods. Rare "events", for example very sporadically occurring irregularly shaped particles as contaminations within an ideally spherical particle sample or mineralogical valuable material particles in very low concentrations, have no/hardly any influence on an aggregated value. However, a reliable estimate is the basis for many processes, even if for time or economic reasons an arbitrary enlargement of the sample size is not possible.

Mathematical models can help to solve this problem, either by doing some kind of interpolation on the basis of the data points, for example the kernel density estimation (KDE) approach [57, 58], or based on the functional relationship between the marginal distributions, for example the *Copula* approach. The latter is used in **Paper D** and is discussed in detail in the corresponding materials & methods sections. The aim in both cases is to generate a joint probability distribution.

In the following part, both approaches will be discussed only briefly, and not in all mathematical detail, to show the basic idea of these approaches. To summarize, methods are needed that give a complete description of the multidimensional parameter space. This can either be derived directly from the particle-discrete data sets or concluded from the associated parameter marginal distributions.

⁷ Anscombe's published example from 1973 with the goal of showing the influence of outliers on aggregated measures [56].



2.3.2 Kernel Density Approach

As stated by Schach et al. [59], the KDE is like an alternative for a histogram. The main difference is that the classes of a histogram have fixed borders, meaning a data point on the border of two classes falls within the left or the right one, determined by the classification rule. In KDE, each data point is considered as the maximum of a 2D density function, called the *kernel*⁸, whose decay behaviour is determined by a weighing parameter, the so-called *kernel bandwidth*, which has to be chosen reasonably [60]. To put it simply, the bandwidth describes how much the probability is scattered around the data point and thus to *interact* with its environment. If other data points are located there, the coinciding single particle probability distributions overlap, which ultimately results in a non-parametric joint probability distribution for the whole dataset. A possible analogy can be given by considering equally charged particles that superimpose their electric fields as they approach each other.

The KDE approach was used successfully to analyse data from mineral liberation analysis (MLA) [59, 61]. Here, a probability density function f of two correlated characteristics, C_A and C_B is defined as follows:

$$f_{C_A C_B}(x, y) = \sum_{i=1}^n \frac{1}{n} \cdot \kappa_x \left(\frac{x - x_i}{b_x} \right) \cdot \kappa_y \left(\frac{y - y_i}{b_y} \right) \quad (2.1)$$

where, n is defined as the number of value pairs (x, y) of a dataset $[(x_1, y_1), \dots, (x_n, y_n)]$ each assigned the same weighting $\frac{1}{n}$. The term $(x - x_i)$ and $(y - y_i)$ states that each value pair (x, y) is influenced more or less by the distance to value pairs (x_i, y_i) , which are part of the joint probability distribution, κ_x and κ_y are the kernel functions that determine the general shape of the curves used to generate the probability density function and b is the kernel bandwidth.

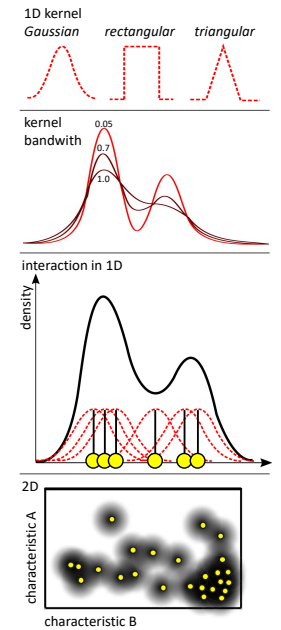
The advantage of this method is that there is no need to search for a suitable parametric family of distributions but it requires large sample sizes especially with increasing dimensionality, often referred to as the *curse of dimensionality*⁹ [62, 63]. Buchmann et al. [38] show the *bootstrap* [64] method as one possible way to deal with that by *resampling* a dataset of limited size. Resampling means to repeatedly draw a dataset with lay back to get an empirical distribution function.

Another way is by using a parametric approach, where not the value pairs but the corresponding parameter distributions—the marginal distributions—are coupled by a mathematical function, called a *Copula*. This approach is used in all the related multidimensional analyses performed in this study. A general introduction is given in the following section. A more detailed description is given in **Paper D**. One example from the previously mentioned publication [59] is given in Fig. 2.4-a.

2.3.3 Copula Approach

A *parametric* approach is not to start from the value pairs (x_i, y_i) , i.e. the data points, but from the associated distribution functions $f_{C_A}(x)$ and $f_{C_A}(y)$, the so-called *marginal distributions*. A *Copula* is one possibility to do this. It is defined as a function describing the relationship between the marginal distribution functions of different random variables thereby forming a joint probability distribution [65, 66, 67]. This approach was successfully implemented for MLA [68] and for the multidimensional correlation described in detail in **Paper D**, using a *multiscale* approach, which is described in more detail in Sec. 6. Another example is given by an application example

⁸ Different kernels, the expression of the related bandwidth, and the interaction between different kernels in 1D and 2D.



⁹ The *curse of dimensionality* was first introduced by Bellman and Page [62]. It states that the number of samples needed to estimate any function with a given accuracy grows exponentially with the number of input variables (i.e. dimensionality) of the function.

for the particle database in the Supplementary Material of **Paper E**.

A very general mathematical description is as follows. Starting from a cumulative distribution function $F_{C_A C_B}$ with marginal distribution functions F_{C_A} and F_{C_B} , one can show that there is a copula C such that

$$F_{C_A C_B}(x, y) = C(F_{C_A}(x), F_{C_B}(y)) \quad (2.2)$$

Thus, the *Copula* is a function which is able to couple marginal distribution functions to obtain their joint distribution¹⁰. The corresponding probability to Eq. 2.2 can be determined by calculating the derivative:

$$f_{C_A C_B}(x, y) = f_{C_A}(x) f_{C_B}(y) \cdot c(F_{C_A}(x), F_{C_B}(y)) \quad (2.3)$$

where f_{C_A} and f_{C_B} are the probability densities of F_{C_A} and F_{C_B} , and c is the two-fold derivative of C . This can be done in higher dimensions, meaning that the distribution of more parameters can be considered. Fig. 2.4 shows a graphical comparison of both methods leading to the typical diagrams used in the referred papers.

¹⁰ Copulas were initially used in financial credit risk analysis, in order to be able to make predictions about a clustered collapse of several debtors within a bond portfolio [69]

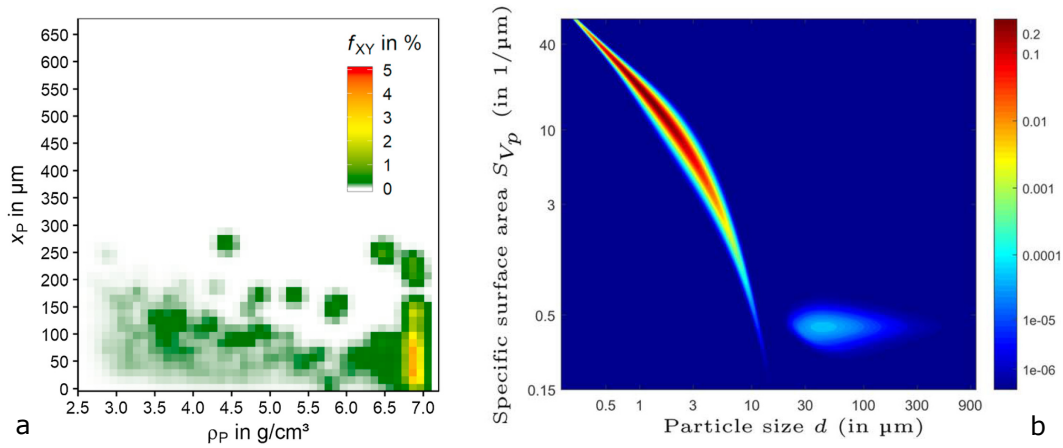


Figure 2.4: Comparison of the two approaches of multidimensional characterization with examples from the previously mentioned publications: (a) KDE by Schach et al. [59] and (b) Copula in **Paper D**. Note that the chosen colour scales are independent from each other showing two very different parameters.

The advantage of the Copula approach is, among other things, that it is not linked to mathematical conditions, such as the existence of a Gaussian distribution, but can be used for any type of marginal distribution. This is of great advantage if the method, which is presented here, is to be transferred to real (separation) processes.

Note that a non-destructive three-dimensional analysis of particulate samples by lab-based X-ray tomographic systems has enabled such analyses for micrometer-sized particle systems and thus lay the foundation for the following studies.

3 X-ray Tomography

This section starts with a short introduction into the beginning of X-ray tomography in Sec. 3.1 to understand the relevance of the method. The subsequent Sec. 3.2 provides basics in X-ray physics followed by methodological details of tomographic imaging in Sec. 3.3 with the related artefacts relevant for particle analysis described in Sec. 3.4.

3.1 Historical Context

Tomographic imaging is an inverse problem. That means that one can extrapolate from the effect, the two dimensional projection, to the cause, the radiated sample volume. In 1917, *Johann Radon* lay the theoretical basis for the mathematical solution of the problem [70], but with no practical application due to the missing possibility to calculate real-life data. In the middle of the 20th century, the needed computing power became available. After the Second World War, the former military radio technician *Godfrey Hounsfield* started his study of radio technology in London and subsequently started his career as technician at Electric and Musical Industries Ltd. (EMI), where he developed radar-guided weapons. As team leader of one research department, he was involved in designing the first English transistor-based computer.

While inventing an application for automated pattern recognition, the idea for a computer-based tomographic reconstruction was formed and got funding. For the rest of the financing Hounsfield tried to convince the renowned neuroradiologist *James Ambrose* from the Department of Health and Social Society of the additional benefit of this new technique. They started experiments with gamma rays on human brains [71]. The sensitivity was high enough to distinguish tumour from surrounding tissue¹¹. Ambrose and his team of radiological experts were deeply impressed by the capability of the new technology. By replacing the source with a more powerful X-ray source they were able to reduce scan time from 9 days to 9 hours. Changes in the senior management team of EMI compromised further development and Hounsfield had to fight to push the system to an industrial level. In 1979 Hounsfield received the nobel prize together with *Allan Cormack*, who had independently worked out the theoretical basis [72, 73].

At first, the CT-system was only established in medicine. CT-scanners were developed from needle- over fan- to cone-beam geometry. Also the detectors evolved from 1D line- to 2D flat-panel. These two inventions gave the opportunity to acquire all data in one scan without more than one rotation per scan. So, due to the reduced effect of mechanical movement, a much more precise measurement was possible. A detailed description of the evolutionary steps of the X-ray tomographic setup can be found in [74].

Beside technological aspects, the basics in X-ray physics are essential to understand signal formation on the detector and related artefacts. Both are strongly con-

¹¹ Hounsfield realized "that this technique may open up a new chapter in X-ray diagnosis." [71]

nected to the polychromatic nature of the X-ray spectrum and will be discussed in the following section. Based on this, in Sec. 3.3 the fundamentals of tomographic imaging are discussed by example of the most relevant reconstruction algorithm currently used in the field of X-ray microscope (XRM).

3.2 X-ray Physics

When X-rays pass from the source to the detector assembly, they interact with the matter in the sample volume non-destructively. The resulting radiation intensity I is given by the *Beer-Lambert* law:

$$I = \int_0^{E_{max}} I_0(E) \cdot e^{-\int_0^d \mu(E,x) dx} dE \quad (3.1)$$

with E the energy of the spectrum, integrated from zero to the highest energy E_{max} , which is determined by the acceleration voltage of the electron tube; μ the linear attenuation coefficient¹² and x the running length going from zero to the sample thickness d . The summed spectrum, which is in our case polychromatic, is changing significantly while passing the sample. The X-rays are attenuated and the initial radiation intensity I_0 is reduced to a measured intensity I on the detector. The following part should give an insight in the mechanisms of X-ray generation and their interaction with matter from an engineering point of view. A more detailed description of the physics is given by Pavlinsky [77], a deeper insight in the application is given by Buzug [74] and Russo [78].

3.2.1 X-ray Generation

Electromagnetic radiation between 100 eV and a few 100 keV is called X-rays. In nature, they occur wherever high-energy events take place. On our planet, for example, X-rays are generated in radioactive decay and in conjunction with lightning. The nearest major X-ray source in our solar system is the sun, in whose corona extremely hot gas emits high-energy radiation. Black holes are considered to be the strongest sources of X-rays.

In technical applications of X-ray sources, electrons are accelerated in electromagnetic fields, either in a circular or linear manner. When using circular accelerators, like used in synchrotron light sources, electrons at relativistic speed emit high-energetic electromagnetic radiation tangential to the direction of acceleration, called synchrotron radiation. This radiation comprises of electromagnetic waves from X-ray to Gamma range and can be decoupled from the accelerator in so-called beamlines. Here, high-precision filtering is carried out in the given energy range in order to subsequently guide almost monochromatic radiation of the desired frequency to the experiment. Due to the extremely narrow energy distribution of the radiation and its high intensity, experiments can be performed with very high accuracy and in a very short time—depending on sample geometry and material up to a factor of a thousand.

Furthermore, X-rays can occur as a product of the interaction of accelerated electrons with bulk material. In the case of an X-ray tube (see Fig. 3.1-a), electrons emerging from a hot cathode are accelerated in an electric field towards the anode, also called target¹³ where they interact with target material with high atomic num-

¹² The linear attenuation coefficient is a function of atomic number and atomic structure of the sample material. Tabulated values can be found in several sources [75, 76]. An illustrative measure is the penetration depth (PD) of X-rays as an intrinsic material parameter. X-ray penetration depth (PD) for examples used in this study: Epoxy [1], Al [6], Hg [10], all for a polychromatic X-ray source at 100 keV

	Epoxy	Al	Hg
Atomic number	6	13	80
Density in g cm ⁻³	2.3	2.7	13.6
PD in mm	2.9	2.2	0.1

¹³ In this study the X-ray source is equipped with a *transmission target*. Compared to a reflection target it is possible to generate minimum focal electron spot size but with less radiation power.

ber, for example tungsten. Fig. 3.1-b shows the enlarged interaction volume with X-rays and the target's bulk material, the so-called excitation bulb. As the penetration depth increases, various energy-dependent interactions occur. Depending on the material composition, very sharp peaks at exactly defined energies occur, which are called *characteristic X-rays*. All other mechanisms form a broad background that is called *bremsstrahlung*, see Fig. 3.1-b and Fig. 3.1-c. The integral over all resulting X-ray photon energies results in a sufficiently high intensity which enables to measure even at low acceleration voltages and reasonable exposure times on lab-scale.

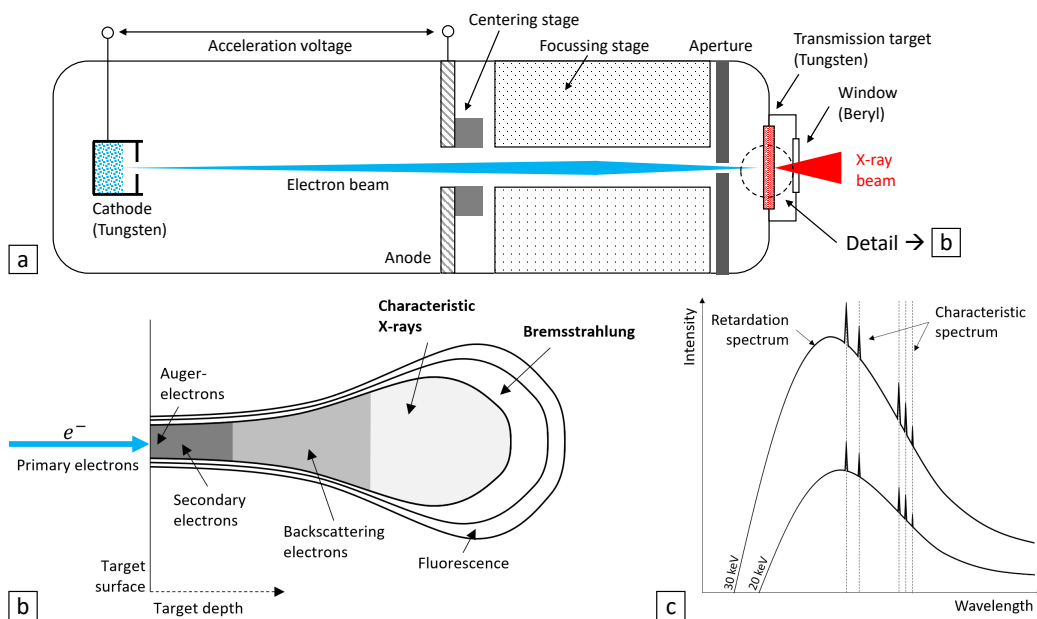


Figure 3.1: Details on the generation of polychromatic X-rays: (a) shows the construction of a polychromatic X-ray source with transmission target. The referred interaction volume is enlarged in (b) and given in relation to the penetration depth of X-rays in the bulk material. The illustrated excitation bulb has different parts, which are contributing more or less strongly to the resulting total spectrum, shown in (c) of the generated X-ray cone beam.

It should be stated that size, geometry and stability of the electron beam is essential for an accurate measurement signal over a scanning period. For example, the focal spot size on the target determines the resolution limit of the entire system. This focus size in turn depends on a repulsive space-charge zone generated within the interaction volume [79]. Another example is the stability of the focus spot (in position and size) on the target surface that significantly influences the geometry of the cone-beam and so location and size of the projection image on the scintillator and afterwards on the CCD. Modern systems are able to compensate for this before tomographic reconstruction.

3.2.2 Polychromatic Spectrum

Both continuous spectrum and characteristic spectral lines are used integrally in lab-based X-ray CT systems. Fig. 3.2 shows the possibilities of altering the overall spectrum by changing the acceleration voltage of the electrons in the electron tube. Here, the maximum photon energy and the integral intensity can be varied. Another option is to change the tube current¹⁴ that only shifts the integral intensity. The maximum photon energy is only related to the maximum possible kinetic energy

¹⁴ The tube current represents the photonic flux determining the number of photons of a certain energy range leaving the cathode.

of the electrons and is therefore fixed. Additionally, it is possible to apply a filter¹⁵ to the initial beam before it passes the sample. In most cases this is done with thin metal foils (alumina, copper). Further, air acts as a filter naturally.

For optimal measurement conditions it is necessary to generate a balanced spectrum adapted to the measurement situation. On the one hand, the process of filtering low-energy X-ray photons is essential to minimize beam hardening (BH) artefacts (details see Sec. 3.4). On the other hand, photons of too high-energy would penetrate the sample with less or no interaction with the sample's material. In this case the contrast of the projection image decreases. An image with good contrast in an acceptable scanning time is always a balance between acceleration voltage, power and adequate filtering.

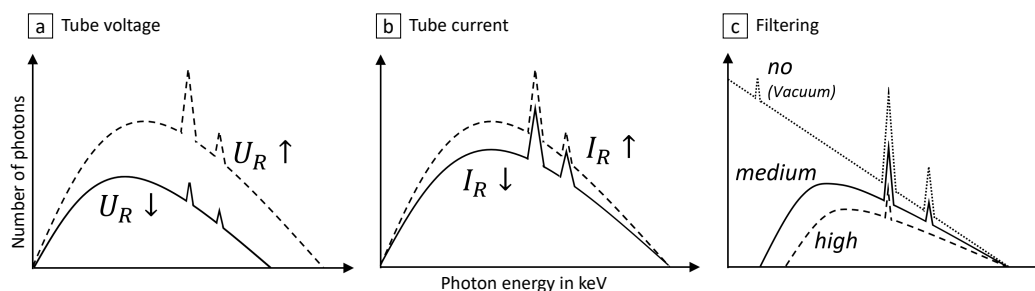


Figure 3.2: Possibilities of influencing the polychromatic X-ray spectrum. By (a) altering the tube voltage (electron acceleration voltage) to shift the maximum photon energy, (b) the tube current to increase the number of photons, and (c) filtering to decrease the number of low-energy photons that are causing artefacts in the final reconstruction volume.

The most important fact about polychromatic X-ray radiation is that every single interaction of an X-ray photon with matter changes its energy and so, the overall spectrum. So, even if the initial spectrum is known, it is not possible to directly use the detector signal as a quantitative measure [80]. Quantitative data based on X-ray microscope (XRM)-measurements can only be obtained by using energy-dispersive devices [81], by creating reference samples, which are often referred to as phantoms¹⁶ [82], or by correlating another measurement signal on the same or parts of the same measurement volume [9] (see also Sec. 6).

3.2.3 Interaction with Matter

In general, the X-ray absorption contrast is determined by the sample, its atomic number, material density and geometry, and the energy (or rather the wavelength: $E = h \cdot \nu$) of the polychromatic spectrum, see Tab. 3.1. Fig. 3.3 shows possible interaction mechanisms of the polychromatic X-ray spectrum with the sample. First, X-ray photons drive out electrons close to the nucleus, which is called *photoelectric effect* Fig. 3.3-a. In the borderline case, where one electron produces exactly one photon, there is maximum photon energy or minimum photon wavelength. The energetically determined state is filled up by an electron of a higher energy level. The energy difference between both states is emitted as a photon. In the spectrum of an X-ray source, the resulting sum signal appears as a peak, or a series of peaks, which is called *characteristic X-ray radiation*. This element-specific information can be used in radiographic measurement procedures, e.g. X-ray diffraction (XRD), as a means of element identification by comparing the determined spectra with known spectra that are stored in databases.

¹⁵ Note that the dramatic decrease in the number of low energy photons, see Fig. 3.2-c, is the result of the absorption by the atmosphere (no vacuum) in lab-based systems.

¹⁶ In this case the phantom must be comparable to the samples. This in atomic number, density and geometry. Coming initially from medical applications, the theory on phantom construction is very limited in the field of particle technology. In the case of particulate samples, there are significantly more degrees of freedom (by number and size of the particles), which are most likely to be difficult to adapt reasonable for different samples. Because designing one phantom for every single measurement situation is not an efficient approach, a correlative approach is favourable here (see Sec. 6).

Furthermore, X-ray photons can interact with quasi-free electrons¹⁷ leading to the emission of another X-ray quanta of less energy. This so-called *Compton effect*, shown in Fig. 3.3-b, can occur in several stages. Since the quasi-free electrons are not firmly bound in energetically defined nuclear shells, the energy of the generated X-ray photons is not in defined steps, but continuous. Finally, at energies higher than 1.022 MeV, X-ray quanta can produce matter in the form of electron-positron pairs, which then immediately dissipate, i.e. they cancel each other out as a matter-antimatter pair, emitting high-energy radiation as gamma quanta, an effect that is called *pair formation* Fig. 3.3-c. This effect is not relevant in the considered energy range, which in our case is 30 keV to 160 keV. Fig. 3.3-d shows the superposition of all three effects in the energy-dependent overall absorption curve.

¹⁷ When deriving the Compton effect theory, a free electron is assumed. If the electron is bound in an atom, the binding energy must be subtracted from the kinetic energy of the electron after the collision. The combination of the bound and free state of the electron is called quasi-free.

Table 3.1: Dependencies of the attenuated X-ray intensity given by the Beer-Lambert law for atomic number, X-ray wavelength, sample thickness, and material density. (*) Note that in case of a polychromatic beam this interaction is even more crucial, because every shift in wavelength of a single photon has an influence on the whole energy spectrum.

Parameter	Dependency	Comment
Atomic number	$\mu \sim Z^4$	When normalized to $\rho \rightarrow \frac{\mu}{\rho} \sim Z^3$
Wavelength	$\mu \sim \lambda^3$	Polychromatic spectrum (*)
Sample thickness	$\mu \sim d$	Best case: rotational symmetric
Density	$\mu \sim \rho$	Difference between background (matrix) and structure (particle, breakage) essential <i>Too low</i> : Not enough contrast for analysis <i>Too high</i> : Artefacts due to high attenuating phases

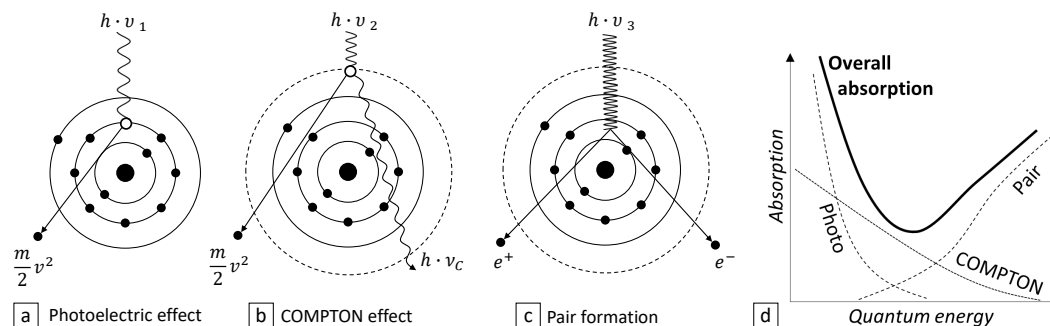


Figure 3.3: X-ray absorption mechanisms of photons in matter adapted from [74]: (a) shows the *photoelectric effect*, (b) the *Compton effect* and (c) the *pair formation*. Note that the initial quantum energy $h \cdot v$ is indicated by the wavelength of the incoming photon (short \rightarrow high, long \rightarrow low-energy). (d) shows the superposition of all effects to the overall absorption curve.

3.3 Tomographic Imaging

Tomography is a generic term for all imaging measurement methods that determine the internal structure of an object and visualize it as sectional images. The prefix “tomo” originates from the Greek word “tome”, meaning section or cut. Sectioning can be destructive in case of a microtome¹⁸ or a focused ion beam (FIB). Here, the cut sections can also be combined virtually afterwards to generate 3D volumes but mostly with non-uniform (non-isotropic¹⁹) voxels, especially with measurements of high lateral pixel resolution.

¹⁸ A *microtome* is a tool to cut very thin sections from an object to analyse internal structures with visible spectrum (VIS) or electron microscopy

¹⁹ If cutting depth cannot reach the same size as the high spatial resolution in the related cut section, such voxels are called non-isotropic.

A non-destructive technique is radiography. The following sections focus on X-ray microscope (XRM) only. FIB in combination with SEM (FIB-SEM) is discussed in Sec. 6 as one possible correlative method. It should also be stated that all investigations are performed in absorption contrast mode. The phase contrast mode [83] can be used if the difference in the linear attenuation coefficient between different phases is not sufficient for a significant contrast in absorption. This is often used when analysing organic material or phase boundaries, which in particular play a decisive role in mineralogical analyses. Details on other tomographic measurement methods are discussed by Buzug [74], but are not of concern here.

3.3.1 Motivation

As every preparation method alters the sample regarding the structural integrity, e.g. mechanical cutting/polishing of sub-volumes generating breakage of structures like pore networks, the functionality, e.g. in living structures, and sometimes the chemistry, e.g. oxidation of cut sample areas exposed to atmosphere, it has always been the goal to find a method of investigation which is non-invasive. This means that physical contact with the sample is not necessary, and in the best case non-intrusive, meaning that there is no influence on the process, in the case of in-situ experiments. As mentioned in Sec. 3.1, rapid advancements in computer technology enables scientists to apply known 2D non-destructive techniques to three dimensions. So, being able to solve the inverse problem of tomographic reconstruction in a reasonable time, XRM now has become the method of choice for numerous applications in engineering technologies like material science [19, 18]. Examples found in chemical engineering are given in **Paper A**. An overview of current ex- and in-situ studies in this field is given by Leißner et al. [8].

3.3.2 Basic Idea

In ordinary radiological 2D imaging, all attenuation coefficients along one line through the sample volume form a cumulated signal. This equals one specific grey value in the projection image. Thereby structures overlap, which are located in succession in the beam path and cannot be resolved individually. By scanning a specific field of view (FOV) of the sample under different angles the overlapping structures along the moving beam path change and a 3D reconstruction is possible. Extracted sections from this volume are no longer a sum signal but sections with grey values corresponding to the attenuation coefficients of the material.

Fig. 3.4-a shows a 2D X-ray projection image of a set of human teeth²⁰. The problem is that there is no possibility to separate distinct features like teeth and bones. Another example is an XRM projection image of a bumble bee given in Fig. 3.4-b and Fig. 3.4-c. Overall shape and body parts are visible but not distinct features like the attachment points of the flight musculature. Such details can only be captured in 3D.

²⁰ Note that the projection image is acquired with a scanner-detector setup rotating around the teeth, so that all structures appear in one plane. Parts of the spinal column can thus be seen on the sides of the image too.

3.3.3 X-ray Microscopy Measurement Setup and Workflow

A CT system with a second optical magnification step is called X-ray microscope (XRM). Depending on the community, the terms micro-CT and XRM are used interchangeably. Since this work focuses on the ability of the system to resolve very

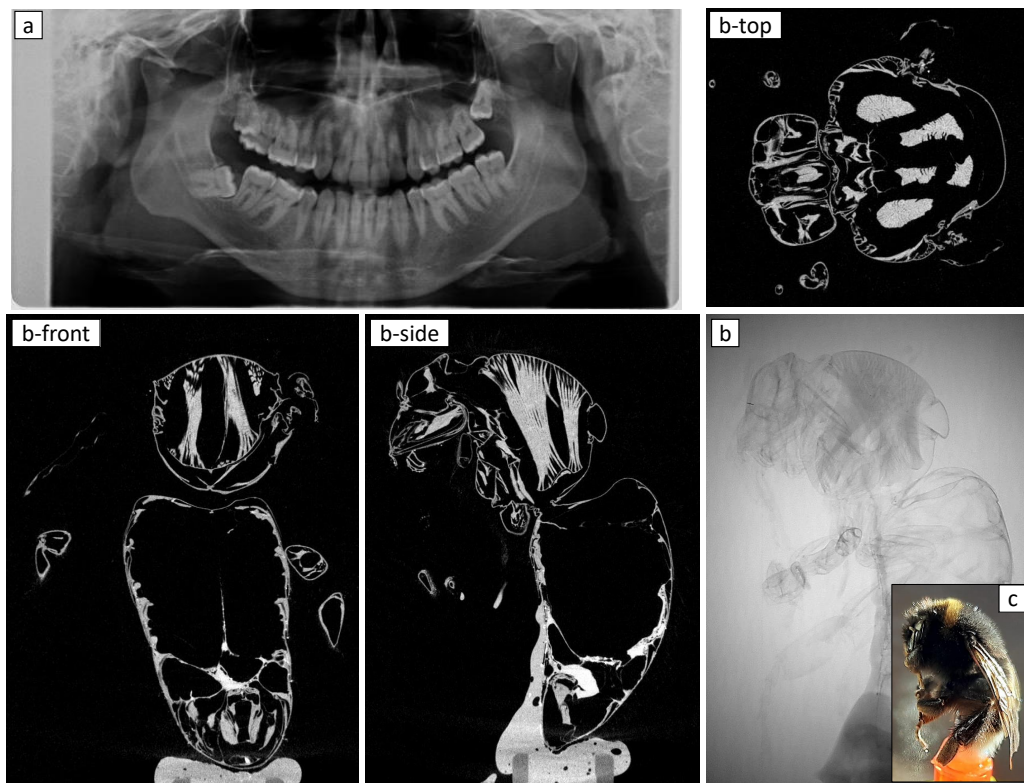


Figure 3.4: Comparison of two projection images from (a) a set of human teeth [84] and (b) of a humble bee. The latter allows the extraction of sectional images without overlapping in any desired direction (e.g. front, side, top). Note that (a) was captured with a moving source–detector system, which causes also the spinal column to appear on the sides of the image. Contrary to the sections from the 3D tomogram, the projection image always shows an overlapping of structures.

small structures, XRM will be used in the following to clearly distinguish the method from established micro–CT methods without additional magnification step. Fig. 3.5 shows a typical XRM–setup with the corresponding workflow. A *polychromatic* X–ray source (for details see Sec. 3.2) emits a conical–shaped beam which can be filtered after passing the aperture.

The high–energy X–ray radiation penetrates the sample that is mounted on a rotating stage and is geometrically magnified on a scintillator screen. Here, X–ray photons interact with the scintillator material²¹ to create VIS–photons. The resulting image on the scintillator is now captured and magnified by optical lenses with different possible magnifications (in case of the Zeiss Xradia 510 Versa, 0.4x, 4x, 20x, 40x) to a CCD flat panel detector resulting in a 2D projection image.

With state–of–the–art detectors with 2048² pixels and binning 2 (for details see Sec. 4.4.3) this results in approx. 1600 projection images²² per scan. The minimum number of projections is given by Crowther et al. [87], known as the *Crowther criterion*, stating that in case of the filtered back projection (FBP)–algorithm:

$$n_{\min} = \pi/2 \cdot n_{\text{DetectorPixels}} \quad (3.2)$$

Additional care must be taken when the FOV is smaller than the sample diameter, e.g. in case of high–resolution scans in **Paper D**. Kyrieleis et al. [88] emphasizes

²¹ In case of the Zeiss Xradia 510 Versa there is tellurium–doped caesium iodide deposited on needles which act as light guides to avoid unwanted scatter. A review of basic scintillator technologies is given by Nikl [85]. Note that the scintillator quality has a decisive influence on the system’s performance [86].

²² Note that there is always one projection image added when measuring over 360°. So, there is no real overlap of the first and second half of the entire rotation, real information is added and noise is reduced.

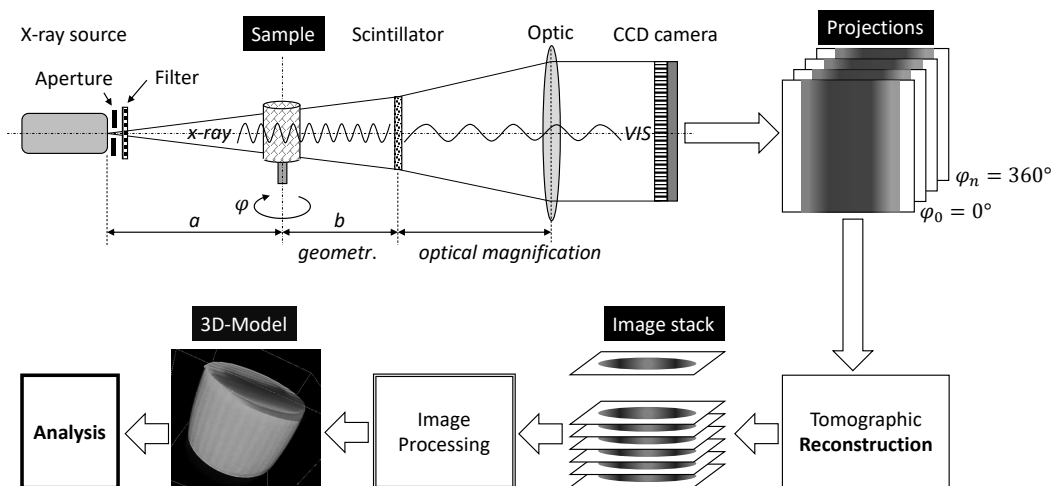


Figure 3.5: X-ray microscopic setup with two-step magnification for a typical tomographic workflow used in this study. The cone-beam left the X-ray source passing the aperture and an optional filter. After radiating the sample, the attenuated signal is projected on a scintillator screen and converted here into visual light that can be optically magnified and projected on a CCD camera. A series of projection images can now be reconstructed to a 3D volume, in most cases represented by a stack of TIFF images. This is the starting point for further image processing procedures to create a suitable 3D model, which can be used for a quantitative analysis.

that in this case $n_{\text{DetectorPixel}} = n_{\text{SamplePixel}}$, which means that an imaginary number of pixels is to be determined, which would correspond to a detector covering the total sample width. If the sample is much smaller than the FOV, e.g. in case of an overview scan to determine the homogeneity of a particle sample as done with sample cylinders from **Papers A to E** where $\frac{\text{height}_{\text{Sample}}}{\text{diameter}_{\text{Sample}}} \approx \frac{3}{1}$, the sample diameter is in the size range of $\frac{1}{3}$ of the FOV. So, in this case the effective number of covered pixels on the CCD detector is also $\frac{1}{3}$ that reduces the minimum number of projection images by $\frac{1}{3}$ too, meaning that in such a case a significant reduction of the number of projection images causes no loss of quality of the final reconstruction.

After capturing, the series of projection images is now transferred to a 3D volume by applying a mathematical algorithm, which is either *Fourier*-based, like the FBP algorithm just mentioned, *algebraic*, or *statistical* [74]²³. This process is called *tomographic reconstruction*. Depending on the sample, different reconstruction algorithms are suitable for the measurement situation. The following part focuses on the FBP-algorithm only.

²³ Note that with the last two it is possible to reduce the number of projections significantly.

3.3.4 Tomographic Reconstruction via Filtered Back Projection

Fig. 3.6 shows a simplified process chain of the FBP-algorithm, starting from an exemplary 2D structure in a 2D *object space* with coordinates x and y , see Fig. 3.6-a.

Note that in a real measurement, the illustrated process is in three dimensions, so, also the representation of a structure in the object space would be 3D, the projection image 2D and so on, all steps being one dimension higher. Displayed are two white rectangles on a black background. The overall goal is to have the same structure before and after the transformation process from Fig. 3.6-a to Fig. 3.6-d (-j). When

projecting these 2D rectangles on a 1D screen, illustrated by a line, the shadows, with coloured parts referring to the objects, differ depending on the projection angle—in some cases they even overlap. The horizontal alignment of the 1D projection of the object space representation, which can be seen in Fig. 3.6-b, indicated by numbers 1 to 5 and related colours, over the associated projection angle is called Radon transform, named after the Austrian mathematician *Johann Radon* (1887-1956). The visualization of this is called a *sinogram*, because of its wave-like structure, see Fig. 3.6-c. The sinogram is used sometimes for applying reconstruction filters, like the reduction of noise-induced streak artefacts by sinogram smoothing [89]. If the projection images from the sinogram are now smeared over the object space according to their related projection angles, both rectangles can now be *reconstructed* within the object space. This transformation is called *back projection*. But as can be seen in Fig. 3.6-d, the rectangles appear blurred, sharp edges have disappeared.

After performing a fast Fourier transformation (FFT), see Fig. 3.6-e, which gives a representation of the rectangles in the frequency domain, called the *Fourier space*²⁴, the reason can clearly be seen. A radial over-representation of low frequencies. Since low frequencies also mean long wavelengths, edge structures cannot be imaged clearly and sharply—the object gets blurred. This becomes even more clear when looking at one single projection in all three image domains, which are connected via the Fourier slice theorem (FST)²⁵, see Fig. 3.6-g.

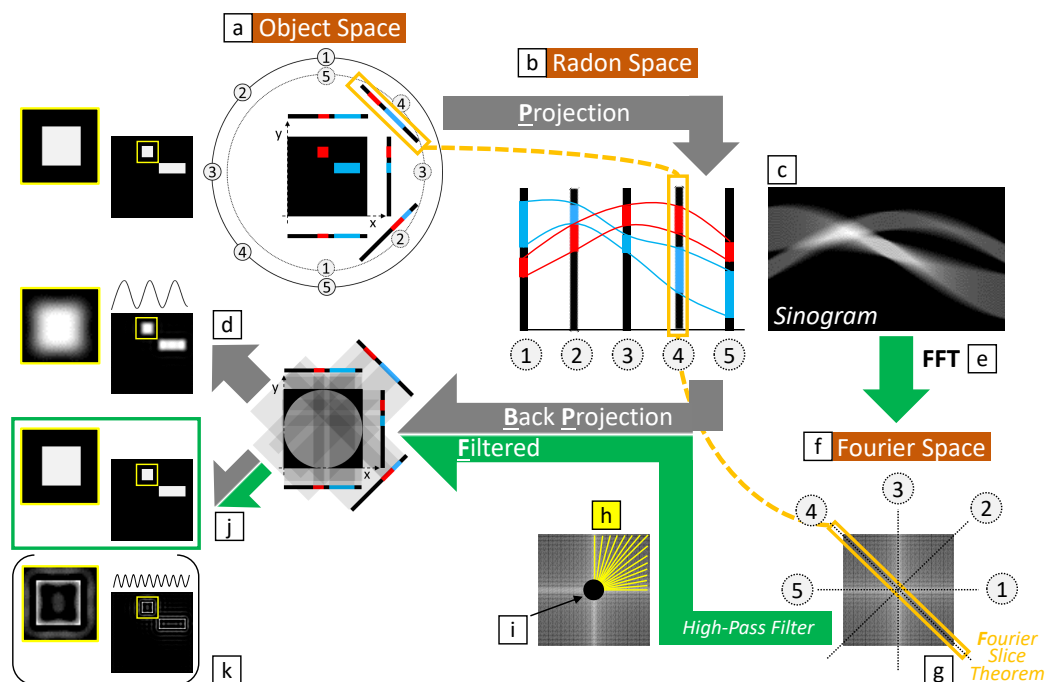
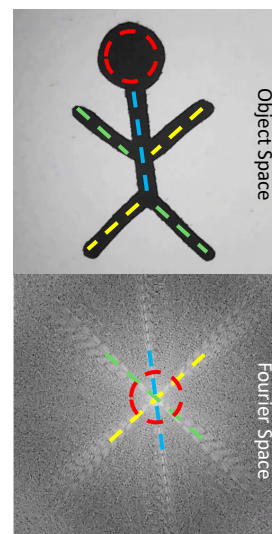


Figure 3.6: Illustration of the FBP algorithm beginning with (a) a 2D structure in the object space, and (b) its corresponding representation in the Radon space, (c) visualized in a so-called sinogram. After back projection, (d) the structure in the object space is reconstructed, but with blurred edges. After (e) performing a FFT, the (f) Fourier space representation of the structure shows the reason, a radial over-representation of low frequencies. This becomes even more clear when (g) looking at one single projection in all three image domains, which are connected via the FST. The (h) overemphasis of low frequencies can be (i) compensated by applying a high-pass filter. When back-projecting these filtered projections, (j) the structure is reconstructed correctly. An inverted filtering would lead to (k) a loss of image information.



²⁴ To illustrate the connection between the object space and the related Fourier space representation, a figure with legs, arms, and a head is shown above. Note that in the case of lines the angles are preserved but the location is lost, i.e. shifted into the origin of the Fourier space radial coordinate system. This visualisation was generated with a live Fourier transformation tool by Pauw [90].

²⁵ The Fourier slice theorem (FST) states that the 1D Fourier transformation of the detector signal, which represents the current projection image, exactly equals a line through the 2D Fourier space representation of the object.

The yellow lines in Fig. 3.6-h, converging in the middle of the Fourier space are showing this effect too. The overemphasis of low frequencies can be compensated by high-pass filtering, which works in the 2D Fourier space by turning low frequency parts, represented by a certain grey value, to black. As the coordinate system of the Fourier space is radial, this is done with a circle, as can be seen in Fig. 3.6-i. When back-projecting these filtered projections, the rectangles are reconstructed correctly, as can be seen in Fig. 3.6-j—this process is called *filtered back projection*.

The filtered back projection (FBP) algorithm which was used in all referred publications of this study is to-date the most widely used but certainly not necessarily the most ideal reconstruction approach. The rise of affordable GPU-based systems is increasingly leading to the use of significantly more computationally intensive reconstruction algorithms—most notably iterative algorithms. However, the reasons why FBP still plays such a big role for a long time are discussed in detail by Pan et al. [91]²⁶.

Fig. 3.6-k shows a loss of image information, by applying an inverted filter. In the given example, only the edges are remaining. In the real FBP reconstruction algorithm, filtering is not only done with a high-pass, but also with an additional low-pass, to suppress noise. This combination is known from signal theory and is called a *band-pass*. Note that the implementation of the algorithm can be realized in different ways, utilizing combinations of the here presented methodology. As the object space and the Fourier space are two representations of the same thing, filtering can be applied differently. Note also that the example given in Fig. 3.6 is with parallel beam geometry for illustrative purposes. Due to the cone beam geometry of the XRM, which is used in this study, the FBP algorithm must of course be adapted. Details are given by Buzug [93].

Although there is already a wide range of other algorithms, some of which offer significant advantages over FBP (fewer projections, better minimization of artefacts), the FBP algorithm is something like a standard, commonly used in lab-based tomographic systems. This is most likely due to the rapid development of lab-based systems. Software developments were often deprioritized and proven solutions were used [91]. Only when development speed of hardware slowed down, other reconstruction methods [74] became more and more important [94, 95]. Nonetheless, for a future implementation as a standard measurement tool, e.g. in a production environment, the sample throughput will be a major limiting factor, what must be achieved mainly by further optimization of the scanning parameters.

3.3.5 Region of Interest Tomography

region of interest (ROI) tomography is also called *truncated tomography*. As described in Appendix D of **Paper D**, the truncation happens when the sample is larger than the actual FOV. In every magnification step—from the whole sample to the region of interest—the penetrated length stays the same. But the angular range to cover sample features declines with increasing voxel resolution. So, more and more features intersect the X-ray beam path only at a limited number of projection angles. The smaller the ROI, the smaller this angular range will be. This causes problems in normal filtered back projection reconstruction and can lead to artefacts in the reconstructed ROI. Katsumata et al. [96] describes the effect with different combinations of FOV and the arrangement of defined structures in the sample volume. It could be shown that the more objects outside the FOV, the more artefacts appear in the ROI.

²⁶ Mainly because standard software of the laboratory instruments did not offer an interface for self-written code for a long time. This has changed in the last years and newer algorithms were implemented, one example is given by Pelt et al. [92]

Fig. 3.7-a shows an example of two samples embedded in epoxy glued on a needle pin, the standard sample preparation procedure for single particle analysis used in this thesis. One particular case presented here shows a particle consisting of low-attenuating touching another of high-attenuating phase (top).

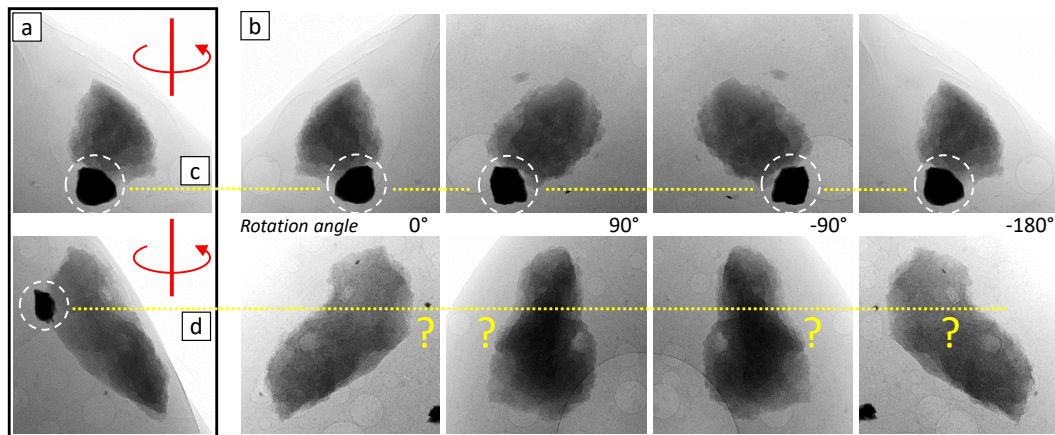
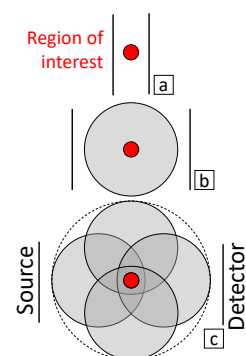


Figure 3.7: Comparison of structures in projection images under varying rotation angles: (a) showing an angle where a high attenuating particle (dark) is touching a lower attenuating one (light). The reason can be seen when (b) changing the rotation angle step by step. (c) in the top case, particles are actually touching, (d) in the bottom one, the highly absorbing particle is only briefly in the FOV. Only the projection in one single direction suggests, that both particles are close to each other. The truth can only be judged in 3D. Note that the axis of rotation is marked in red.

Also the second case (bottom) suggests the same. Thus, if only these two 2D projection images were available, one could not clearly predict which case actually exists and what could be a potential risk of out-of-field artefacts (see Sec. 3.4.4). A variation of the rotation angle, see Fig. 3.7-b, shows that only in the first case the two particles are really touching each other Fig. 3.7-c. The highly absorbing phase in the second case (bottom) is clearly outside the FOV and only apparently touches the particle, see Fig. 3.7-d. So, looking only at projection images can be misleading. Complete information is only available with the three dimensional tomogram.

Another approach is discussed by Xiao et al. [97]. They describe an error estimation for ROI tomography, here called *zoom-in tomography*. Starting with a high-resolution scan, the ROI is combined with a low-resolution scan of the whole sample. Here, the resulting error is determined to be lower than in classical truncated tomography. This method is not to be mistaken with neither scouting nor zooming. In contrast, here, the low-resolution scan of the total volume is used *directly* to improve the quality of the high-resolution ROI scan and to minimize artefacts. Alternatively, Parlanti et al. [98] propose a method with the rotation axis outside the FOV which is called *extended FOV acquisition*. Both methods will not be of further concern here.

When measuring larger sample sizes, a ROI, which is positioned far away of the sample's rotation axis, leads to a tumbling of the sample²⁷. That means, scanner and detector have to be placed sufficiently far away to prevent a collision with the sample.



²⁷ A potential source of collision of sample and detector is shown for a constant ROI and different FOV. Starting with the less critical case with an (a) adapted sample size fitting to the FOV, followed by (b) the same FOV in the center of a larger sample. The most critical case is when (c) the FOV is placed eccentrically in the same sample volume.

3.4 Relevant Artefacts Related to Particle Measurement

As already discussed in Sec. 3.3.4, all reconstructions were done with the FBP algorithm. Since the image details but also errors of the projection images are *smear*ed over the entire object space in the back projection process, this algorithm is prone to a large number of artefacts. In the following section, only the dominant effects are briefly described, which are related to particle measurement and are relevant for the particle embedding procedures presented in **Paper A** and **Paper C**. To provide a reasonable reference to the measuring system, the artefacts are ordered along an imaginary photon path from the X-ray source to the detector.

Referring to images, artefacts are defined as visible, unwanted displays that do not correspond to the original data, in our case the 3D object to be depicted. Artefacts can be related to the physical measurement principle, the measurement setup, the imaging method, and, in case of tomography, the subsequent reconstruction. Because they are not always clearly distinguishable, a basic understanding is essential for quantification of possible errors in image processing, especially in the case of high resolution measurements.

3.4.1 Temperature Drift

A large part of the kinetic energy of the electrons arriving at the target is converted into thermal energy, see Fig. 3.8-a. The interaction volume fluctuates laterally and in direction of the electron beam, see Fig. 3.8-b and also Fig. 3.1. Consequently, as the spot (source of the cone beam) is changing in size and position, the projection conditions change, which can be seen in Fig. 3.8-c.

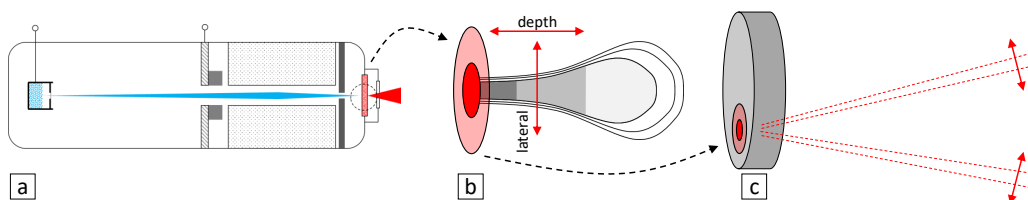


Figure 3.8: The (a) focused electron beam on the target is building up an interaction zone in the target volume, called excitation bulb (see also Fig. 3.1) that can (b) vary thermally induced lateral and in depth and can so (c) lead to a drift of the cone beam. Note that this divergence increases with increasing distance to the detector.

Additionally, secondary radiation induced by interaction of electrons with the tube housing can create extra-focal or off-focal drifts [99]. Particularly in high-resolution scans (voxel size $< 1 \mu\text{m}$ and very short source-sample distances), this can lead to significant differences between individual projection images and thus to blurring in the resulting tomogram [100]²⁸. Even if the overall system is kept thermally stable, thermal drifts cannot be easily corrected afterwards in reconstruction [101]. Therefore, a warm-up of the source is necessary to minimize the effect. As proposed by Wang et al. [102] and Limodin et al. [103], in this study a minimum warm-up time of 1 h is used for low- and 3 h for high-resolution scans. In addition there are three other possible drift correction methods: source drift, sample drift, and the tracking of features, like particles, during the rotation and apply an additional adaptive motion compensation (AMC) algorithm. AMC delivers good results for large particles but mostly temperature drift correction gives the best results.

²⁸ Note that there is an additional blurring in the static projection image solely caused by the non-negligible size of the focal spot. This effect is called *penumbral blurring*, see the following section.

3.4.2 Penumbra Blurring and Shadow

These effects, also referred to as geometrical blurring, are directly related to the X-ray source. Penumbra blurring is caused by a drift of the primary point source generated by the excitation bulb, see Sec. 3.2.1, which in reality has a finite dimension. Additional shadows on the projection image are generated by secondary radiation emitted and dependent on the tube design. Note that these two effects are practically a possible manifestation of the instabilities of the point source just described in Sec. 3.4.1.

Penumbra blurring can also be “deliberately” produced by the X-ray source itself. This can occur if the electron beam introduces too much energy into the target material due to a non-optimal operating point. To prevent too much stress on the target, the electron beam is slightly defocused and the area-specific energy input decreases. The associated significant lateral expansion of the excitation bulb enlarges the point source and the achievable structural resolution decreases. Especially for high-resolution measurements, see **Paper D**, careful adjustment of the X-ray source is therefore of greatest importance.

3.4.3 Cone Beam

As previously mentioned, the starting point of the X-ray radiation behaves like a point source that emits radiation over a certain angular range creating a beam of conical shape, as can be seen in Fig. 3.9-a.

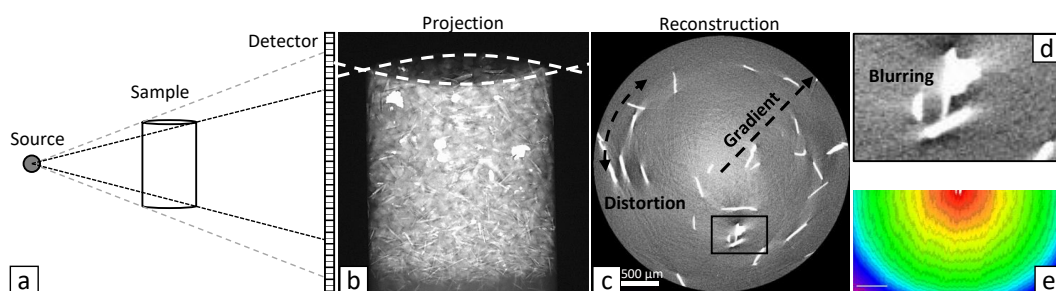


Figure 3.9: Cone beam measurement setup: Here, (a) the divergence of the beam leads to (b) significant differences in the beam paths at the lower and upper parts of the sample. This causes (c) radial grey value gradients, distortion, and (d) blurring. Note that the effect increases with greater distance to the beam center—illustrated as (e) a pseudocolour image with high intensity in red decreasing radially outwards to blue, representing the lowest energy value of the captured beam area.

In addition to the loss of intensity due to the conical beam widening with increasing distance, it also decreases significantly radially away from the beam axis²⁹. If the sample now extends out of the core cone, one can clearly see artefacts in the projection image, see Fig. 3.9-b. More obvious are the effects on the reconstruction, see Fig. 3.9-c, that appear as distortion, an artificial grey-value gradient, and blurring, see Fig. 3.9-d³⁰. Experience has shown that in the case of porous structures and particle samples, the first and last sections of an image stack (of approx. 50 images, see also the calculations in Sec. 4.4.4) must be removed for quantitative evaluations in order to prevent errors in the determination of distributed properties³¹. Fig. 3.9-e shows a 2D intensity profile of the cone beam with pseudocolours. Clearly visible is the high intensity area in the middle (red) with a rapid decrease to lower intensities

²⁹ Note that this effect is also called *multidetector row effect* because it is directly linked to the number of vertical pixel lines of the CCD array. The more lines the higher the artefact expression on the edges of the FOV.

³⁰ Note that also BH, see Sec. 3.4.7, is one main reason for blurring. In the given example it is most likely a superimposition of both effects.

³¹ A possible estimation of the influence on the measurements of the related studies can be found in Sec. 4.4.4

(yellow over green to blue) with the minima in the corner of the image (violet).

At this point it should be emphasized that the detector image is always the optical magnified image of the projection on the scintillation screen. Thus, X-ray aperture, VIS-optics and the properties of the scintillation material (homogeneity, sensitivity) also have a decisive influence on the measurable intensity distribution on the flat panel detector.

3.4.4 Out-of-Field

The out-of-field artefact is strongly connected to the ROI tomography, which has already been discussed in Sec. 3.3.5. Kyrieleis et al. [88] states that scanning with a small FOV inside a sample is like cutting a small region out of the sinogram (see Sec. 3.3). Cutting edges leads also to a grey value gradient to the edges in the final reconstruction (like with the cone beam artefact). More details can be found in the Supplementary Material, Appendix D of **Paper D**.

3.4.5 Center Shift

When capturing a projection series, the rotation center has to be determined manually while setting the acquisition parameters. This cannot be done with sufficient accuracy and so has to be corrected afterwards. This process, applied before final reconstruction, is called center shift correction. It has to be performed for every sample geometry, not only cylindrical shaped. One example can be found in Sec. 4.4.5.

3.4.6 Sample Drift

If there is additional sample motion apart from the rotation around its central axis, there will be a visible shift in the series of projection images as can be seen in Fig. 3.10. Clearly visible in high-resolution single particle analysis, this effect is even more critical with a large number of particles where the drift distance increases significantly in relation to the particle size and leads to a considerable change in the reconstructed sample volume compared to the sample. Thus, minimizing particle motion within the sample via a proper preparation method is essential for reliable measurements on this size scale.

In practice, multiple reasons for this phenomenon have been observed which are listed below in decreasing probability of occurrence:

1. The sample is not fixed properly on the sample holder³², either the adhesive attachment fails, or the glued contact area is too small compared to the sample size, which can cause the sample being tilted under gravitational force when warming up .
2. The structural integrity of the sample's material is not guaranteed over the whole measurement time, either the particle sample is not fixed within a matrix, or the sample itself or the matrix material is not cured but only highly viscous, which can cause particles to move or can create propagating bubbles. Another possibility is that the matrix material is getting viscous under the influence of the X-ray beam³³
3. The sample holder movement, which is static when either the sample gets in contact with the aperture of the X-ray source and changes its alignment in

³² Sometimes it is not possible to fix the sample, e.g. when investigating the contact area between a droplet on a substrate. In this case the stage movement has to be limited to a minimum, e.g. no dynamic ring removal (DRR), see Sec.4.4.6

³³ Measurements show that integrally there is no significant temperature increase, for the used sample size only up to 1K. Locally, it could be different, which is the only way to explain rarely observed drift effects when working with wax as matrix material.

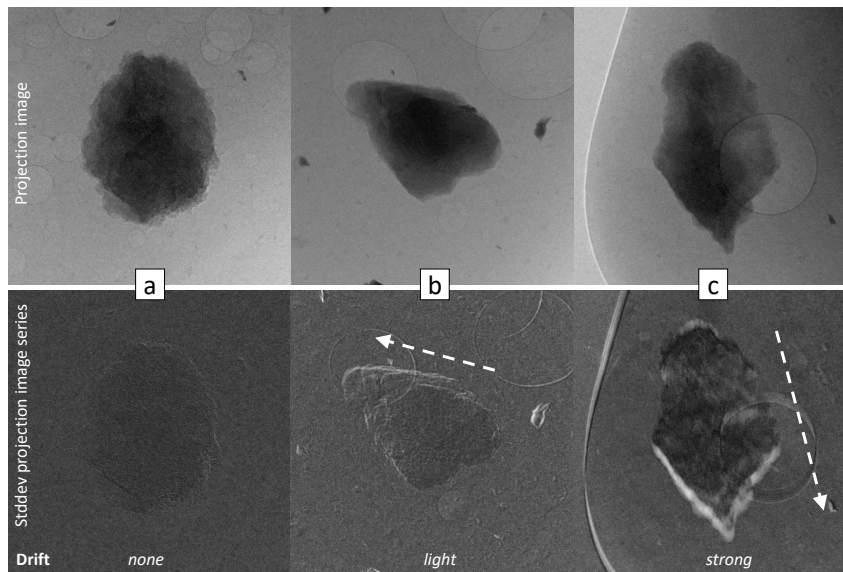


Figure 3.10: Example of a possible visualization method of the unwanted sample's motion, in addition to the rotation, using the standard deviation (stddev) translated into a grey scale image (bottom). Here, the stddev is calculated from a series of projection images (top) captured at a rotation angle of zero degrees, called drift series. Low stddev is indicated with black, high stddev with white. Examples are given for (a) no, (b) light, and (c) strong drift. Note that drift direction is indicated by the white arrow.

case of very small source–sample distances, especially when measuring inside the sample away from the rotation axis, or the sample holder is bent. The movement is dynamic, when the whole stage is tilted due to the excessive tensile stress of supply lines.

Even if efficient methods are available to correct the movement of the sample, it is better to suppress it as much as possible from the beginning. While capturing the projection series, the starting position is re-allocated in constant intervals. This image stack is called the drift-file. In the best-case scenario, all images show almost no variation, see Fig. 3.10-a. Light drifts, as in Fig. 3.10-b, can be corrected while reconstructing the volume data. If the drift is too strong, as can be seen in Fig. 3.10-c, volume reconstruction is possible, but with increasing image artefacts, which manifest as distorted air bubbles and ghost images behind real particle structures, shown in Fig. 3.11-a to Fig. 3.11-c.

3.4.7 Beam Hardening

As mentioned in Sec. 3.2, the polychromatic X-ray spectrum changes as it passes through matter. While high-energy X-rays can penetrate both large radiation lengths and highly attenuating phases, low-energy quanta are absorbed faster. The sum signal of the projection image on the detector is thus significantly higher on the edges areas of strongly absorbing regions than in the centre areas. Fig. 3.12-a shows an example of a mercury droplet on a less absorbing substrate. Here, beam hardening (BH) causes an increased centre-to-edge glowing that is represented by a convex curve of the cross-sectional intensity profile. If an increasing BH correction is now applied, the curve approaches a straight line, the ideal correction factor for reconstruction has been found. If this correction is exceeded, a concave curve indicates overcom-

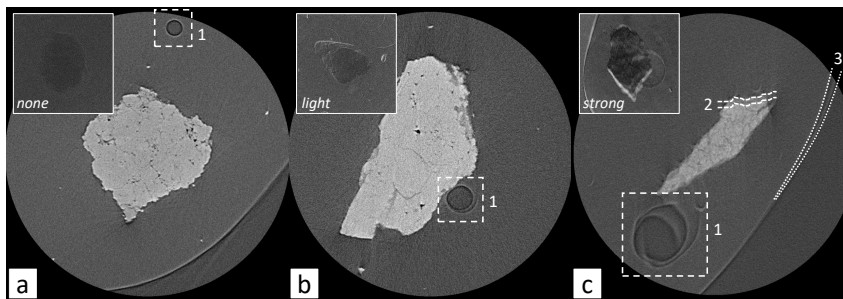


Figure 3.11: Manifestation of the motion artefact in the final reconstruction showed on exemplary sections. (a) shows no, (b) light, (c) and strong sample drift leading to a shadow image of the structure which in this case are single particle measurements. By a fortunate circumstance the drift strength is visible more clearly in air bubbles included within the epoxy matrix: a-1→b-1→c-1. In case of a strong drift there is also a significant shift of the particle (c-2) and the matrix border (c-3).

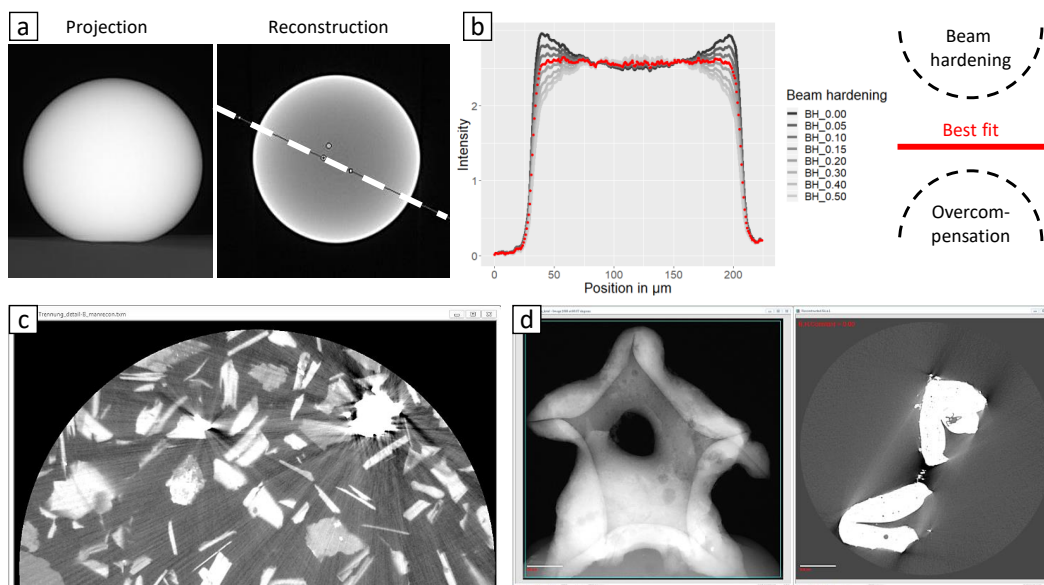


Figure 3.12: Examples visualizing the BH artefact: On a (a) highly X-ray attenuating phase, which in this case is a mercury droplet placed on a alumina substrate for 3D contact angle measurements. The effect can not be estimated by judging projection images but can clearly be seen in the referring reconstructed sections. The cross section marked in (a) gives (b) different lateral intensity profiles depending on the applied BH-correction factor. The correction optimum is reached, when the profile reaches a plateau. The same effect can be seen in (c) a second example consisting of mineralogical phases causing glowing and streaks, (d) a single aluminum oxide filter element appearing as streaks on edges.

pensation, see Fig. 3.12-b. Other manifestations of BH could look like starbursts and streaks³⁴ (see Fig. 3.12-c) or light–shadow effects (see Fig. 3.12-d). Best way to avoid BH is to apply sufficient filtering (see Sec. 3.3). The challenge always is to keep balance between filtering and reasonable exposure time. The most interesting question is how BH correction influences quantitative measures. Surely, strong BH has to be avoided, but correction algorithms also alter the image information and sometimes it is better to live with a light BH than to overcorrect the image [105]. Note that an assessment of beam hardening based on projection images only tends to lead to an underestimation of the effect in the final reconstruction. One strategy to avoid BH is by applying suitable source filters, which is presented in Sec. 4.4.2.

³⁴ Sometimes called metal artefact [104].

3.4.8 Rings

As already mentioned, the flat panel detector consists of a pixel array, each of which has a slightly different sensitivity. Under different rotation angles this variance is always pinned to the same location within the projection image, except for defective pixels not visible to the naked eye. After reconstruction, however, the appearing structure is clearly recognizable as rings, which are comparable to the structures produced by a dipping object on a fluid surface. To prevent the formation of such ring structures, the sample is shifted randomly in a plane with constant source–sample and sample–detector distance. This process is called dynamic ring removal (DRR) and discussed in detail in Sec. 4.4.6. The location of the detector (same for each pixel) is therefore different for every projection image. A subsequent software alignment guarantees a correct starting point for the final reconstruction. The only thing to note is that this form of correction reduces the possible FOV by a few pixels (about 10). In this study, DRR has always been applied. Because all particle samples are embedded in a matrix (also see Sec. 4.1), DRR–induced movement is not critical.

3.4.9 Noise

The signal–to–noise ratio (SNR) is a measure for the signal quality. The question is how much the measurement signal can stand out from the background noise. As discussed by Buzug [74], the SNR grows with the root of the mean value of the number of photons arriving at the detector. For a low photon number, the noise of the system³⁵ is the dominant effect and leads to a random pixel structure that is commonly referred to as “noise”. Buzug specifies 5 as the minimum SNR, meaning that the signal carrying the information must be at least 5 times stronger than a homogeneously noisy background. For the measuring device used in this study, this value is determined at 5,000 counts/exposure. So, at least 5,000 VIS photons per each single exposure must hit each detector pixel (or binned virtual pixel, see Sec. 4.4.3). As it is shown in Sec. 5.1.3, 5,000 counts is much above the minimum SNR proposed by Buzug. More details regarding SNR, in particular the role for the final image quality, is also discussed in this section.

³⁵ The total noise is composed of the quantum noise, which is the statistical fluctuation in scattering and absorption of the X-ray photons in the scintillation material, and the detector noise, which is the thermal noise of the electrons.

3.4.10 Partial Volume

Whether a structure can be identified metrologically by means of tomography depends on its relation to the size of the smallest finite tomographic element—the voxel. Every voxel is a discrete digital representation of the related object volume,

summarizing attenuation signals from all phases inside this region, resulting in a nonlinear average grey value. Thus, partial volumes are no longer distinguishable from each other. In case of particles, this could lead to blurry edges and segmentation errors of contacting particles, e.g. in a loose bulk. Details on the partial volume effect (PVE) can be found in Appendix B of the Supplementary Material of **Paper D**.

3.4.11 Summary

Additionally, there are numerous other artefacts that would exceed the scope of this work. A short overview of all relevant artefacts, how they manifest themselves and how to minimize them, especially when dealing with particle samples, is listed in order of their origin from X-ray generation to detection in Tab. 3.2³⁶. More details are given by Davis and Elliott [107] and Boas and Fleischmann [108].

Besides the focus on the actual scan there are interesting approaches to include additional information to realize a sufficient correction of motion-related artefacts. One example is given by Salmon et al. [100] who proposes a post-scan procedure on defined rotation angles to correct for very small geometry or position changes of the sample. A similar method is used in the Zeiss Xradia 510 Versa, which is used in this study, but here at fixed intervals during the measurement. In medical computed tomographic imaging the situation becomes even more complicated. Here, in most cases, the living “sample” cannot be assumed to be static. Organs such as the heart and the breathing lungs cause significant but unavoidable movements, which of course have a major effect on the quality of the tomogram. One example is given by Zhang et al. [109]. To capture high quality tomograms of a breathing lung, they apply a model which is adapted to the patient by using a respiration-correlated image set. Specifics regarding the causes of artefacts and the related reduction techniques in the field of medical imaging are summarized by Barrett and Keat [110].

After a sufficiently long warm-up (minimizing temperature drift) of a well-tuned X-ray source (min. penumbral blurring, shadow), a correct alignment (min. centre shift) and fixation (min. sample motion) of the particle sample, the selection of X-ray energies and X-ray filters suitable for the sample dimensions and the sampled material (min. beam hardening), the selection of a sufficiently long exposure time of a low-noise detector (min. noise), the partial volume artefact is to be considered most critical with regard to the analysis of particle systems. In other words, the best possible measurement results can only be achieved if errors are minimized in all the steps just listed, since a certain PVE is an inherent feature of the actual setup of the system.

In the following section, the considerations introduced here are explained in more detail using examples from particle analysis.

³⁶ Recap how many of these artefacts cause unsharpness in the final projection image. Maire and Withers stated correctly: “Images come without error bars”. Like in other measurement workflows, minimizing errors during image acquisition is essential *before* they propagate.

Table 3.2: Overview of relevant artefacts related to XRM of particulate material with artefact name, visual appearance within the image, causes and minimization techniques ordered along the way from X-ray source to detector.

Artefact	Looks like...	Caused by...	Minimized by...
X-ray source	<i>Temperature drift</i>	Fluctuation of X-ray interaction volume in target material	Warmup 1h (low-) 3h (high-resolution)
	<i>Penumbra blurring</i>	Unsharpness	Non-negligible electron beam spot size, see also Sec. 3.4.2
	<i>Shadow</i>	Duplicated structures	Secondary off-focal X-rays induced by target backscattering electrons [99]
	<i>Cone beam</i>	Top and bottom sections are affected by radial grey value gradient, distortion and blurring of structures	Non-uniform illumination due to the cone beam
Sample	<i>Center shift</i>	Ring type ghost images	Center of rotation is not determined with sufficient accuracy
	<i>Sample motion</i>	Unsharpness	Insufficient fixation (hardening process not finished, thermal expansion), sample's structural integrity, sample holder movement
	<i>Out-of-field</i>	Radial grey value gradient, streak artefacts in case of high attenuating phases outside the FOV	Sample size much larger than FOV → these parts are only partly visible within the projection image series
	<i>Beam hardening</i>	Glowing edges, brighter areas even though same phase (<i>pseudo enhancement</i>), stars and streaks (<i>metal artefact</i>)	Surrounding high attenuating phases
Detector	<i>Ring</i>	Concentric waves	Defect detector pixels
	<i>Noise</i>	Rushing TV picture	Too less intensity (quanta)
	<i>Partial volume</i>	Unsharpness	Limited spatial resolution causing mixed voxels not clearly assigned to single phases
			Moving of the sample with every new projection (DRR), see Sec. 4.4.6
			Exposure time determined by minimum detector intensity of each point in the projection image
			Voxel size minimum 3 to 5 times better than target spatial resolution

4 Practical Implementation

This section should serve as practical guide to particle analysis with the help of XRM. Starting with the specific requirements that are placed on the sample in Sec. 4.1. Followed by a statistical consideration of the sample size in X-ray tomographic measurements in Sec. 4.2 with a possible way for validation of the results in Sec. 4.3. Sec. 4.4 gives a short introduction into a reasonable measurement setup for particulate samples.

4.1 Particle Sample Requirements

In order to prepare a particle sample as good as possible with regard to subsequent image data evaluation, several requirements must be complied with. Starting from two-dimensional analysis methods, it was obvious to adopt existing methods from SEM [111, 112] and transmission electron microscopy (TEM) [113] and adapt them accordingly. However, three-dimensional tomographic characterisation poses particular challenges in terms of sample geometry, degree of dispersion and representativeness of the particle sample [114, 115]. In the following section, these points are only briefly discussed with focus on embedding techniques. Details regarding wax embedding can be found in the methodological **Papers A** and **B** and for epoxy embedding in **Paper C** respectively. Fig. 4.1 shows examples of particle samples, where Fig. 4.1-e and Fig. 4.1-f referring to low resolution and Fig. 4.1-g and Fig. 4.1-h referring to high resolution measurements for epoxy and wax samples.

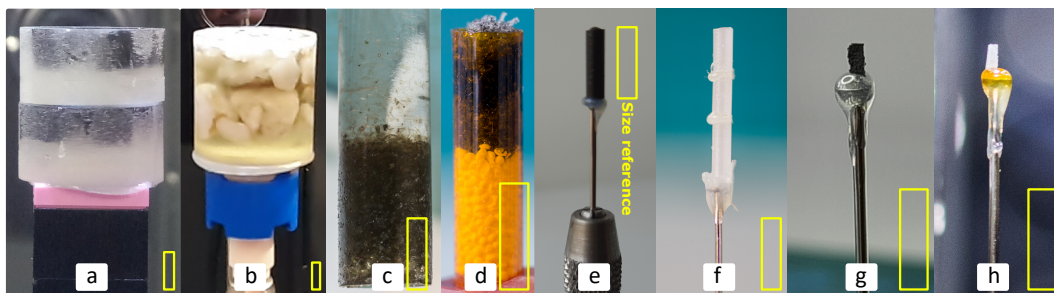


Figure 4.1: Particle samples: (a) Double layer mineralogical sample originating from MLA measurements, (b) mm- and (c) μm -sized particles embedded in epoxy resin, (d) compressed as loose bulk, particles in the size range below $10\ \mu\text{m}$ (e) with graphite nanoparticles as spacer embedded in epoxy resin and (f) as sample stack in wax, cut to small bars (g, h).

4.1.1 Geometry

As already discussed in Sec. 3.2, 3.3, and 3.4, the best case scenario would be a sample that is rotationally symmetric, resulting in equal radiated lengths, and fits into the FOV to avoid artefacts when performing ROI tomography. To achieve this, the particle samples were prepared using a polymeric tube with an internal diameter

of 2 mm that matches the target voxel size of 2 μm (as described in **Papers A, B** and **C**). For the medium resolution measurements, performed with the XRM, the sample cylinders are cut down manually to small angular bars with a diameter of approx. 400 μm fitting to the minimum voxel size of the XRM, in this case 400 nm. These scans are used as overview to identify appropriate sub-volumes for the high-resolution scans with the nano-CT, see in **Paper D** and Sec. 8. Since spherical and fibre particles were analysed in the multiscale analysis, the same sample bar could be used with a voxel size of 64 nm even if the FOV is much smaller than the actual sample size. Structures outside the FOV are not critical here because of the low absorbing phases. Details regarding this so-called ROI scans are given in Sec. 3.3.5. Contrary, in the correlative analysis, presented in Sec. 6.3, highly absorbing phases from the used mineralogical samples would have caused significant artefacts and increased exposure times significantly. Thus, the sample had to be reduced in size. The wax matrix used in **Papers A, B** and **D** cannot withstand high-energy processes, but the epoxy-nanoparticle matrix used in **Paper C** does. In the latter, so, it was possible to use a laser mill to cut a cylinder with a diameter of 60 μm from the bars, enabling to use this sample geometry for FIB-SEM analysis as well, see Sec. 8.

4.1.2 Dispersity and Homogeneity

As it is discussed in **Paper A**, the embedded particles should be well dispersed and homogeneously distributed over the whole sample volume. This implies a minimization of *agglomeration* and *segregation* effects. The two effects would result in an insufficient distance between single particles, and thus, lead to problems in the subsequent image processing, i.e., the particle segmentation. Examples of over-segmented or under-segmented particles for six different particle systems can be found in the Supplementary Material of **Paper E**.

Dispersity can be determined in different ways depending on what objects are to be characterized, e.g. polymers [116], metals [117, 118] or nanoparticle assemblies [119, 120]. For the particle systems used in this study, agglomerates were detected manually in a preview of the data set after the measurement. As stated in **Paper A**, there were only a small number of agglomerates, which could also be identified by the method given in the next paragraph. A possibility for an automated method is given by Wu et al. [121] and will be implemented for further studies. Here, a measure for the share of agglomerates is determined by using a combination of morphological image processing operators³⁷, a method first proposed in pore network analysis [122].

As also can be seen in **Paper A**, one possibility to quantify homogeneity is to plot the volumetric solids fraction per cross-section over the sample height. This visualization is used to decisively improve the sample extraction. Since the concentration is aggregated for each cross-sectional image, however, no statement can thus be made about local effects. This can be solved by a method proposed by Rudolph et al. [119]. Here, *Voronoi*³⁸ polygon meshes are used to divide cross-sectional images into sub-areas. The coefficient of variation of these individual areas can be used as a quantitative measure for the homogeneity of each cross-section. A good overview of further methods for particle systems is given by Crouter and Briens [124].

³⁷ A series connection of erode and dilate allows agglomerates to "merge" into large particles due to the very small inter-particle spacing.

³⁸ This method is also known as pre-step in image segmentation algorithms [123].

4.2 Statistics

In addition to the requirements already described, the particle sample must of course be representative of the population. Sampling of particulate material is a sequence of subsample extraction, e.g. from a mineral deposit, assembling a homogenous mixture, sample conditioning, and sample splitting in order to ultimately obtain a representative analytical sample. All these four steps are subject to errors. A detailed description of the possible individual errors will not be given here. The interested reader is referred to the work of Gy [125, 126].

A more detailed insight into the most critical part, the statistical representativeness, is given in **Paper A** and **D**. For the purpose of statistical representativeness, the contributions are grouped according to the number of examined particles. The present work is in the order of over 1,000, in the case of **Paper A** and **Paper C** over 20,000, particles per sample. However, this list is only intended to provide a rough overview and is not to be understood as a full review.

4.2.1 Single Particle Properties

In tomographic single particle analysis, either the spatial distribution of internal structures or phases as well as the structure and homogeneity of particle layers are of interest. Evans et al. [39] perform XRM measurements on mineral grains and compare them with MLA regarding grain size distributions. Lowe et al. [41] analyse the microstructure of *TRISO*-particles³⁹. Here, a standard SEM analysis of an embedded, cut and polished sample would alter the particle's structure by destroying the porous network which is of main interest. Bhuiyan et al. [127] also analyse pores regarding their size distribution within iron ore green pellets⁴⁰ to guarantee optimal heat transfer properties for the pelletizing processes. Garcia et al. [42] determine the interphase area of copper ore particles before and after comminution to quantify the degree of decomposition and so to optimize process characteristics. Sondej et al. [128] investigate coating layer morphology and porosity as a critical factor for dense layers of functional particles in pharmaceutical applications.

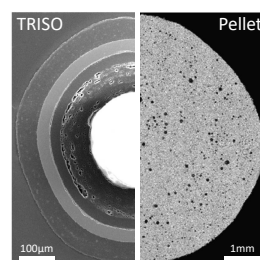
4.2.2 Properties of a Limited Number of Particles (10 to several 100)

If the composition of individual particles is known from previous investigations or is not of interest, the next step is to understand the relationships between different particles. This task requires a particle collective that has been preserved as far as possible in its original state. This is contrary to the requirement for a well-dispersed particle sample, which is beneficial for an optimal particle segmentation image processing workflow (see also Sec. 5.2) but problematic in terms of structural parameters, such as particle orientation and packing density of the bulk, which cannot be determined as the related structures would have been destroyed.

Videla et al. [129] determined the composition and spatial distribution of mineral phases. The data is also used for finite mixture distribution (FMD)⁴¹ modelling. Sittner et al. [130] extend this method by using an additional X-ray energy dispersive detector. Basically, this method is an extension of 2D MLA into the third dimension. As will be shown in the following chapters, the use of X-ray computed tomography is non-trivial for several reasons. Alizadeh et al. [131] analysed the shape driven segregation during heap formation. Here, XRM data is used to validate a *clumped*

³⁹ *TRISO* stands for *TRi*-structural *ISO*tropic particle fuel. These are particles for high energy reactors comprising of several layers with an uranium core.

⁴⁰ A hard porous sphere, typically 8mm to 18mm in diameter, containing various aggregates in addition to iron (approx. 70%) raw material for the production of raw iron in a blast furnace process.



⁴¹ FMD are probability distributions used for modelling data, assuming that they contain subsets of observations (clusters). This can be used to determine, for example, the number of component distributions in the mixture as well as the parameters of these distributions.

*spheres approach*⁴² used for discrete element method (DEM) simulation of particle bed behaviour during build-up. In this regard, Thompson et al. [132] proposed a method to create something like benchmark datasets for a latter error estimation by using artificially created packing structures, like cubic, rhombohedral, and random sphere packing. Babout et al. [133] investigate granular materials to find the most promising ones for numerical simulations. Here, particle shape as key parameter is captured with XRM on a limited number of particles giving a reasonable amount of voxels per particle in a certain FOV. Bagheri and Bonadonna [44] analysed approx. 300 regular and irregular shaped particles to predict drag coefficients. They also compared the results from XRM with results from 2D SEM and a 3D scanner, which shows that the size range is above the one in the presented papers. All these studies show the high value of 3D datasets, but with the limited number of particles, it is not possible to describe distributed properties in sufficient detail, especially when going to non-spherical particle systems.

4.2.3 Particle Populations with Distributed Properties

Some measuring devices already provide pre-aggregated values, either from discrete measurements or derived via mathematical models. But as already mentioned, only single particle information can be used to determine single property distributions on the one hand and correlate them in a multidimensional manner on the other. Distributed particle properties such as size and shape can only be determined by collecting enough distinct particle information. Note that the focus in **Papers A to E** is on particle size only, although the presented methods can also be used to determine other particle-discrete characteristics.

For example, Bhuiyan et al. [127] determine particle size distribution of iron ore green pellets. Cepuritis et al. [134] do the same for the specific surface area on the example of crushed concrete particles. Fu et al. [135] analyse particle packing in pharmaceutical powders using a model system of spherical particles validating a DEM model for particle bed simulations. Bernier et al. [136] characterize powder for additive manufacturing. Löwer et al. [47] performed filtration experiments to predict micro processes, filter cake formation and porous media flow characteristics on single particle/single pore level, which until now have mostly been described in terms of models with integral parameters. The precise knowledge of the related parameter distribution itself, but also in terms of the spatial distribution, enables a more accurate prediction and optimisation of the macroscopic process properties.

The question is how many particles are needed for a sufficiently accurate description of property distributions, e.g. particle size. As described in **Paper A**, some models are under the assumption that there is no initial information about the particle system of interest. In most cases, however, additional information is provided by other analysis methods, from supplier specifications, or from the production and comminution process. For example, Masuda and Iinoya [137] describe the theoretical basis for a log-normal distribution, and test the theoretical assumptions by comparing results from simulations [138] that confirm the theoretical results. Wedd [139] challenge the assumptions by comparing results from laser diffraction measurements with good agreement for a glass bead particle system. This example shows that, generally speaking, just as the average value approaches more and more the expected value with an increasing number of measurement points, the empirical distribution function, i.e. the distribution of the measurement values, converges

⁴² Here, an attempt is made to replace the non-spherical particle volume with a certain number of spheres of different sizes. Alizadeh et al. stated that “the effect of particle shape is not limited to the rolling mechanism of the particles, rather it affects the particles contacts in a more complex network”. This is precisely what builds the bridge to filtration [47].

towards the actual distribution. From this, a confidence band can be derived that is described differently for different distribution types [140, 141].

The required number of particles for a reliable measurement is therefore defined by the size of the error that is acceptable within a certain confidence interval, the prior knowledge of the process, which gives an indication of the expected distribution and its variance. It is also defined by the type of the particle system, which can be monodisperse or polydisperse, spherical or non-spherical, comprise of one or multiple orders of magnitude. As stated in **Paper A**, the number of particles used for low-resolution and medium-resolution measurements is clearly above the calculated minimum. The high-resolution measurements used for the characterization over multiple size scales in **Paper D** is combined virtually to reach the minimum particle number.

4.3 2D Validation

Image-based measurement methods should most reasonably be compared with other image-based methods. As shown exemplarily in **Paper A**, it has proven to be very beneficial to validate quantitative results from tomographic measurements with data acquired from 2D image analysis methods like optical microscopy or SEM. In particular, this “optical inspection” gives essential information on special features within the particle sample, e.g. satellite particles or hollow structures, that may cause problems in image processing. Certainly, results in this respect are to be critically questioned, especially with regard to non-spherical particles. Since integral methods, e.g. laser diffraction, strongly depend on assumptions made by mathematical models. The application of these models should be considered even more critical, since the possibility of visual control, even if only by random sampling, is missing.

SEM images were also used in this study to validate the results from tomographic measurements in terms of particle size. This effort pays off, as it provides a comparative value that does not allow calibration of the system due to the stereological bias, but can provide indications of possible errors in the workflow of tomographic image data evaluation. This method was used in **Paper C** and **Paper D**.

4.4 Measurement

4.4.1 X-ray Microscope

Fig. 4.2 shows the XRM, type Zeiss Xradia 510 Versa. The device is encapsulated inside a lead-plated casing on top of a vibration-damped stone plate. Fig. 4.2-a shows the source and detector assembly which can be moved on a slide to reach a certain geometrical magnification (first step of magnification). The sample on the sample holder can also be moved in all three spatial axes to find an appropriate FOV and to align the centre of rotation. Spectral filters (LE: low-energy, HE: high-energy) can be manually applied in front of the aperture, see Fig. 4.2-b,detail, to reduce BH, see Sec. 3.4.7. The optics (second step of magnification) are mounted on a lateral sliding table—0.4x objective on one side, 4x/20x/40x mounted on a rotating turret on the other side (see Fig. 4.2-c,detail). Pictures and details of the setup, can be found in the Appendix C of the Supplementary Material of **Paper D**.

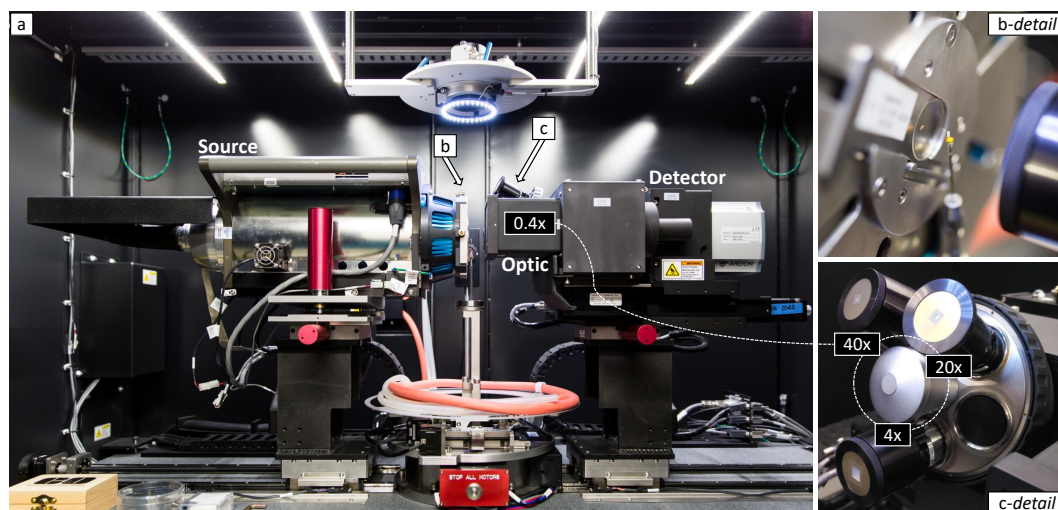


Figure 4.2: X-ray microscopic setup with (a) the overall view with the X-ray source (left), the sample (middle), and the detector (right). Also (b) the detailed sample mounting also showing the applied source-filter covering the aperture. Furthermore (c) the detailed X-ray microscopic optic with different magnification steps, which are either 0.4x(a), 4x, 20x, or 40x.

4.4.2 Source Filter

As already mentioned in Sec. 3.2.1, the X-ray radiation is filtered naturally by air in the system and artificially before reaching the sample by applying filters. This is done to cut off low energy parts of the polychromatic spectrum to increase transmission for high X-ray attenuating materials and to reduce artefacts. Fig. 4.3-a shows the aperture of the X-ray source with empty filter slot.

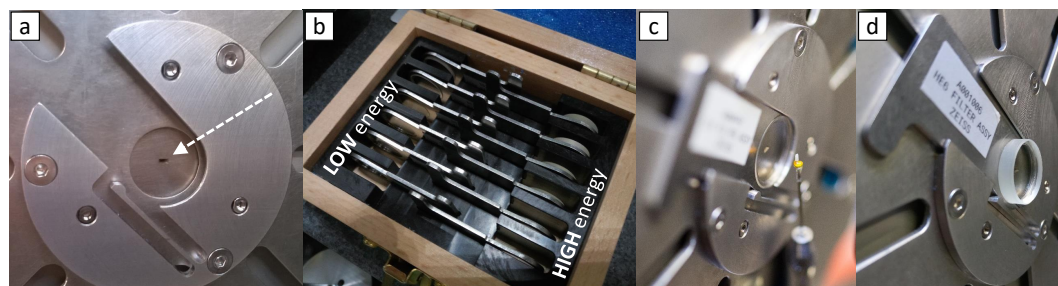


Figure 4.3: X-ray filtering to avoid the BH artefact: (a) Aperture (indicated by arrow) with empty filter slot, (b) filter collection for two different energy ranges and (c) applied filter elements for low-energy (LE) and (d) high-energy (HE) filters. Note that the filter thickness correlates with filter strength; (c)→LE1, (d)→HE6.

The available filter collection for low energies (LE, 30 to 80 keV) and high energies (HE, up to 160 keV) can be seen in Fig. 4.3-b. Mounted LE and HE filters are shown in Fig. 4.3-c and Fig. 4.3-d, respectively. Note the increasing material⁴³ thickness, most apparent in the case of HE filters. The filters are selected according to the energy range, which in turn depends on the selected optical magnification. The referring guideline for the filter selection is given in Tab. 10.1 in the Appendix 10.5.

A reference image is taken when the sample is set up. From this, a transmission range for the sample is estimated and compared with tabulated values depending on the selected energy and optical magnification. If the measurement time is suf-

⁴³ The filter material is optically transparent with unknown composition. Probably a synthetic crystal structure, which shows specific absorption properties by doping with foreign atoms in addition to the variable thickness, see also Appendix 10.3.

ficient, filtering is done rather conservatively. It is better to use a filter one class higher, especially to avoid BH artefacts. Note that moderate filtering does not have an influence on the initial beam shape but significant influence on the number of generated VIS photons represented by detector counts.

In addition, Fig. 4.4-a to Fig. 4.4-c show sample projections of the same particle sample at different energy levels and without filtering 30 keV/2 W, 80 keV/7 W, and 120 keV/10 W respectively. Note the slow fading due to higher transmission at higher energies. More and more photons are passing the sample without generating an absorption contrast. This is of course a minor problem to single phase systems, because a distinction between different materials is not necessary here. But insufficient contrast could lead to a significant loss of image information when dealing with low-absorbing material and multiphase systems, see also Sec. 5.1.

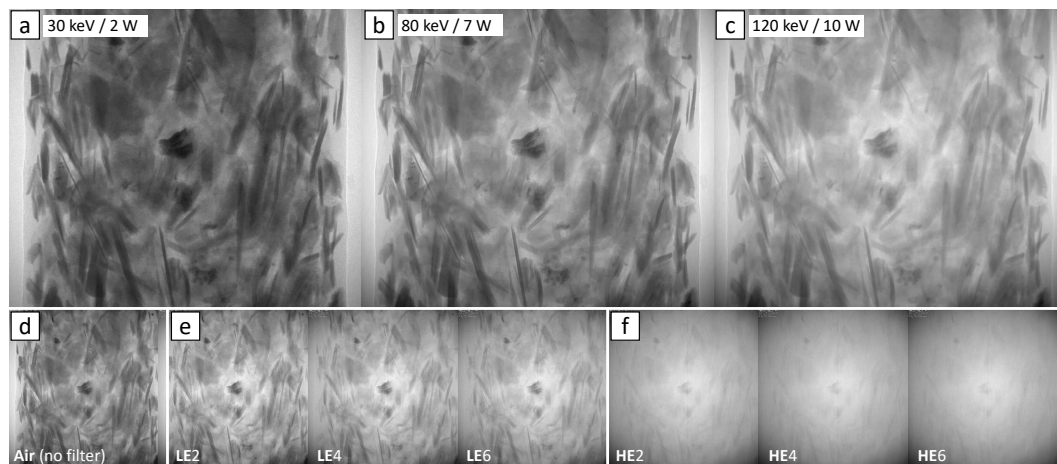


Figure 4.4: X-ray source settings starting from (a) low energy to (b,c) higher energies. As photon energy increases, the sample gets increasingly X-ray transparent—structures slightly disappear but remain sharp. The effect of filtering manifests in a fading of the whole structural information, shown here (d) without filter (e) with low-energy (LE) and (f) high-energy (HE) filters. Note that together with this also the photon number decreases significantly. So, to achieve reasonable scanning times, filtering cannot be applied independently from the samples properties.

4.4.3 Detector Binning

Binning detector pixels to “virtual” pixels is comparable to the *ISO*⁴⁴ value, which represents the light sensitivity in the analogue photography. By virtually combining a certain number of detector pixels n_{px} in XRM⁴⁵, exposure time t_{ex} can be dramatically decreased:

$$t_{\text{ex}} = \frac{1}{n_{\text{px}}^2} \quad (4.1)$$

Fig. 4.5 shows the binning modifications related to the projection images. Note that with higher binning also the image pixel size increases while the number of effective pixels decreases. In the example given in Fig. 4.5 this means for binning 1 an effective pixel number of 1954^2 pixels⁴⁶, and for binning 8 an effective pixel number of only 240^2 pixels. So, binning makes the image “grainy”, which can be seen in Fig. 4.5-e.

⁴⁴ Analogue films are available in fixed ISO levels. low-ISO values, starting with ISO 50 and 100 high light situations (outside with sun), and high-ISO values for situations with less light (in-room).

⁴⁵ For the used detector these are 2, 4, or 8.

⁴⁶ Note that the physical pixel number is 2048^2 , but DRR reduces this number to an effective pixel number after reconstruction. For more details see Sec. 4.4.6

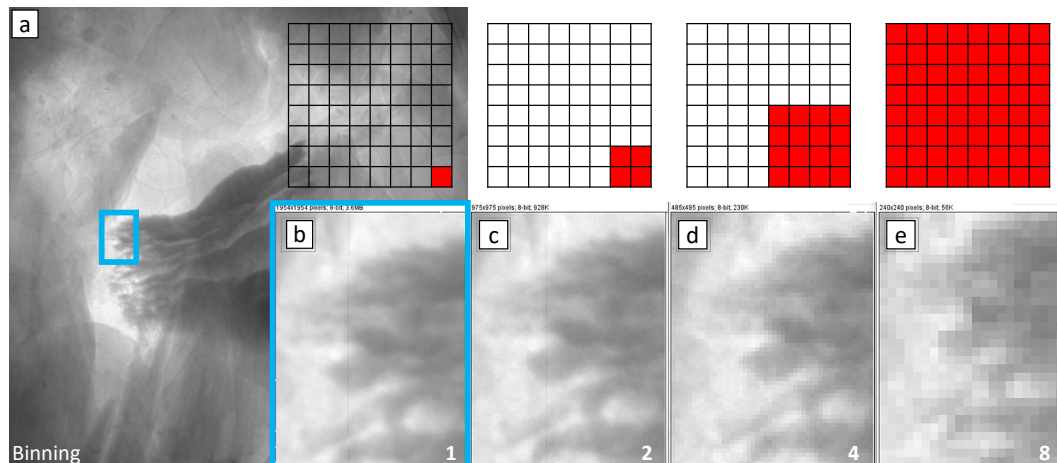


Figure 4.5: Binning of the detector pixels in projection image (a) shown by detail enlargements (b to e). The eight by eight matrix is filled with red pixels representing the final size of the binned (virtual) pixel. Note the appearing pixel structure in with binning eight in (e). As the pixel size stays constant, the image size decreases by the referring binning factor.

4.4.4 Cone Beam Artefact Compensation

As described in Sec. 3.4.3, the conical-shaped X-ray beam produces artefacts, which leads to a *grey value gradient*, *blurring*, and *distortion*. All three effects are possible causes for particle segmentation errors. Fig. 4.6 shows a possible way to analyse this quantitatively for individual samples.

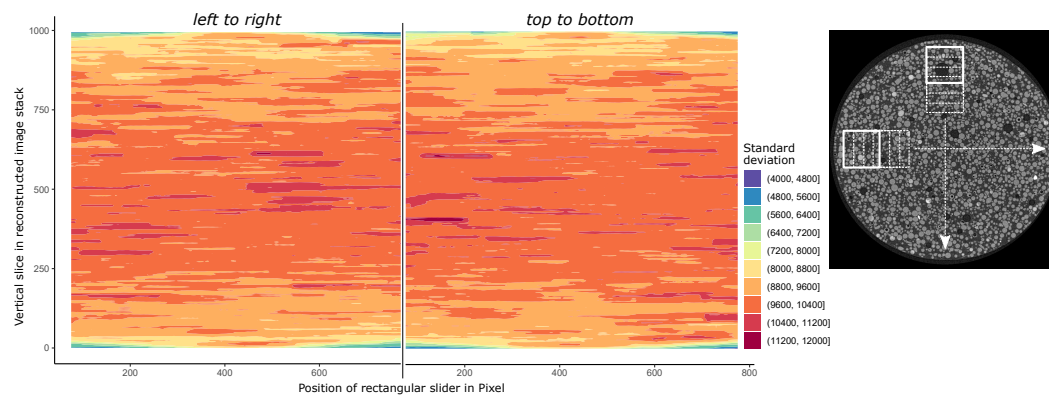


Figure 4.6: Visualization of the cone beam artefact (left) by determining the standard deviation of a small rectangular area “sliding” over each tomographic section from left to right and from top to bottom (right). Note that a higher standard deviation (red) indicates structural features of high, a lower (green, blue) of low contrast.

A square geometry is slid over the image surface from left to right and from top to bottom with an offset of one pixel for each iterative step. All pixels within each square are aggregated to determine the standard deviation, which, as shown in Fig. 4.6, has then been colour-coded. Artefacts that are “destroying” image information should be represented by a lower contrast (see Sec. 5.1) and a lower standard deviation. This can be clearly seen on the top and bottom of the standard deviation maps for both directions. A practical question now is how many sections are influenced and have to be removed from the initial dataset to prevent errors in the subsequent image processing workflow. A straightforward solution is to calculate

the *projection angle*⁴⁷, which is determined by the FOV and the distance between the X-ray source and the sample that is in this case referred to as xs . As can be seen in Fig. 4.7-a, there are regions on the top and on the bottom of the FOV that are illuminated by X-rays but not projected on the scintillator (and then captured on the CCD). The tangent of the projection angle α equals:

$$\tan(\alpha) = \frac{FOV}{2 \cdot xs} \quad (4.2)$$

with FOV as the field of view. Via the corresponding alternating angle (b), the opposite cathetus ex converted into a number of sections N_{ex} results in:

$$N_{ex} = \tan(\alpha) \cdot \frac{FOV}{2} \cdot \frac{1}{\text{voxelsize}} = \frac{FOV^2}{4 \cdot xs \cdot \text{voxelsize}} \quad (4.3)$$

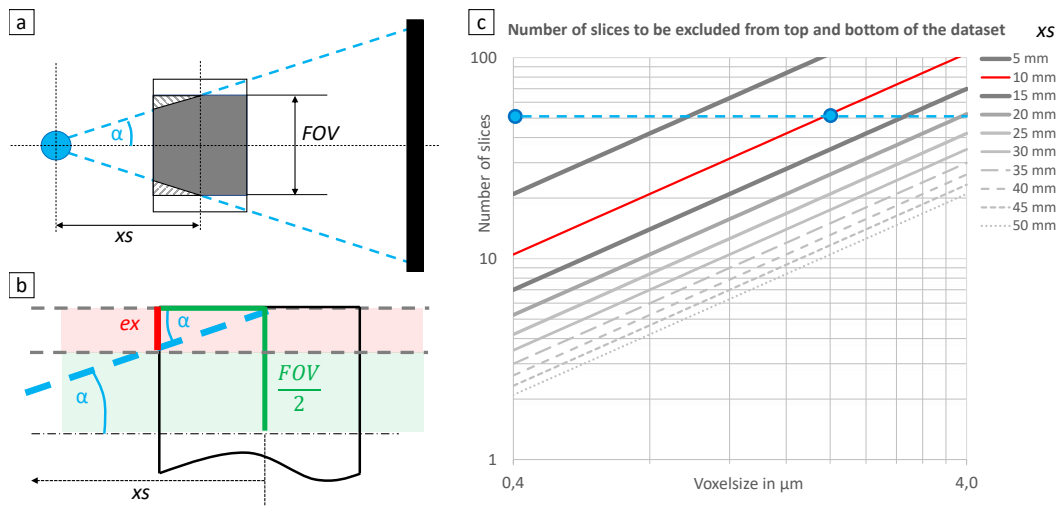


Figure 4.7: Quantification of the cone beam artefact: (a) non-projected areas on the top and bottom of the FOV suggest an estimation by (b) triangulation to calculate (c) the number of sections that have to be excluded from a quantitative analysis. Note that the red line indicates the fixed source-sample distance that was used in the studies to guarantee a comparable projection angle.

Fig. 4.7-c shows the corresponding number of sections that have to be excluded from the dataset due to the cone beam artefact. Both measurement points for this work are marked in blue. The corresponding source-sample distance xs of 10 mm used in this work⁴⁸ is marked in red. The high-resolution scans with the 40x objective with the corresponding FOV of approx. 400 μm requires 10, the low-resolution scan with the 4x objective and the corresponding FOV of approx. 2 mm requires 50 sections to be removed on top and on the bottom of the FOV⁴⁹. Fig. 4.8 shows the effect for a sample dataset from **Paper C**.

4.4.5 Center Shift Correction

Mostly done in automatic mode, the center is shifted iteratively by searching for a maximum in image contrast. Fig. 4.9 shows an example of a quartz particle sample embedded in a wax matrix. The misalignment is evident in the ring-shaped artefacts, which become elliptical for elongated objects.

⁴⁷ Note that this angle is often referred to as *cone angle* or *cone beam angle*. This term is deliberately not used in this work, as it conveys a direct reference to the beam shape and considers this to be the causal variable for the artefacts. However, the artefact arises during the back projection over the object space and can be minimized by other reconstruction methods [142].

⁴⁸ This distance is kept constant to guarantee a fixed projection angle for all measurements of this study.

⁴⁹ Note that the corresponding measurements were performed with binning 2. In case of binning 1, the number of sections has to be doubled.

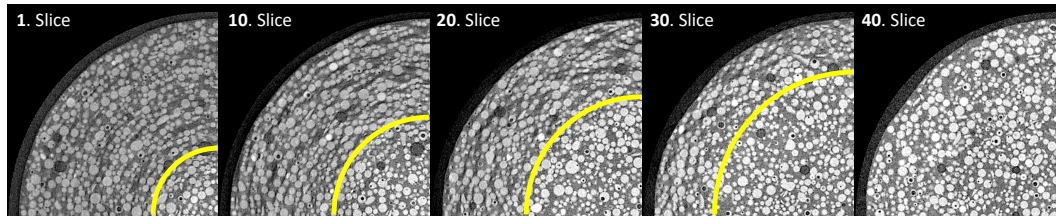


Figure 4.8: Verification of the cone beam artefact: Clearly visible in the first section (left) but disappearing after approx. 40 sections (right). Note that the region of the unaffected area, which is enclosed by a yellow circle, increases slightly, not volatile.

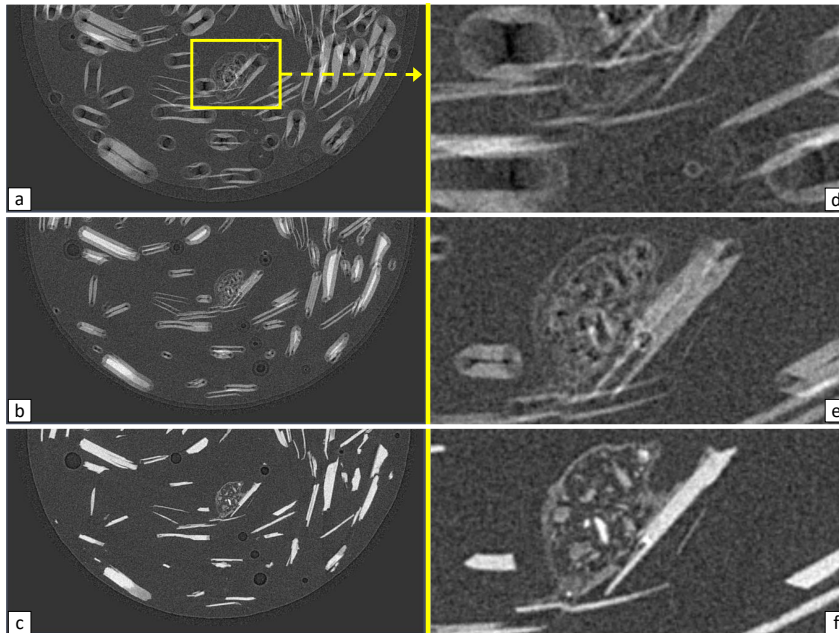


Figure 4.9: Exemplary sections of a quartz particle sample image stack starting from misalignment, where no correction is applied, to a suitable center shift correction (from a to c) and respective magnified details (from d to f).

Of course, these artefacts have a considerable influence on the identification of the shape and size of objects and is not always as clearly visible as in the example shown. It also has to be mentioned that the center shift correction is always connected to the applied drift (see Sec. 3.4.6) correction of the series of projection images. That means after changing the drift correction mode, a new center shift has to be calculated for the altered dataset.

4.4.6 Dynamic Ring Removal

Fig. 4.10 shows an example of a ring structure (details of this effect see Sec. 3.4.8) appearing when no random-like shift of the flat panel detector is applied. The sample is a small cut-out of a periodic filter cloth structure provided by the subproject A7⁵⁰ (cross-flow filtration) of the SPP 2045. Rings are only visible in the top view of the projection image stack, see Fig. 4.10-b. Part Fig. 4.10-c shows the ring structure from the side view. Ring formation is visualized in Fig. 4.10-d.

Note that the lateral shift within the projection plane has to be corrected by an automated alignment of the projection image series, the so-called dynamic ring

⁵⁰ Details regarding this and all other projects of the Priority Programme SPP2045 can be found on the website: <https://tu-freiberg.de/fakult4/mvtat/SPP2045/Projekte>.

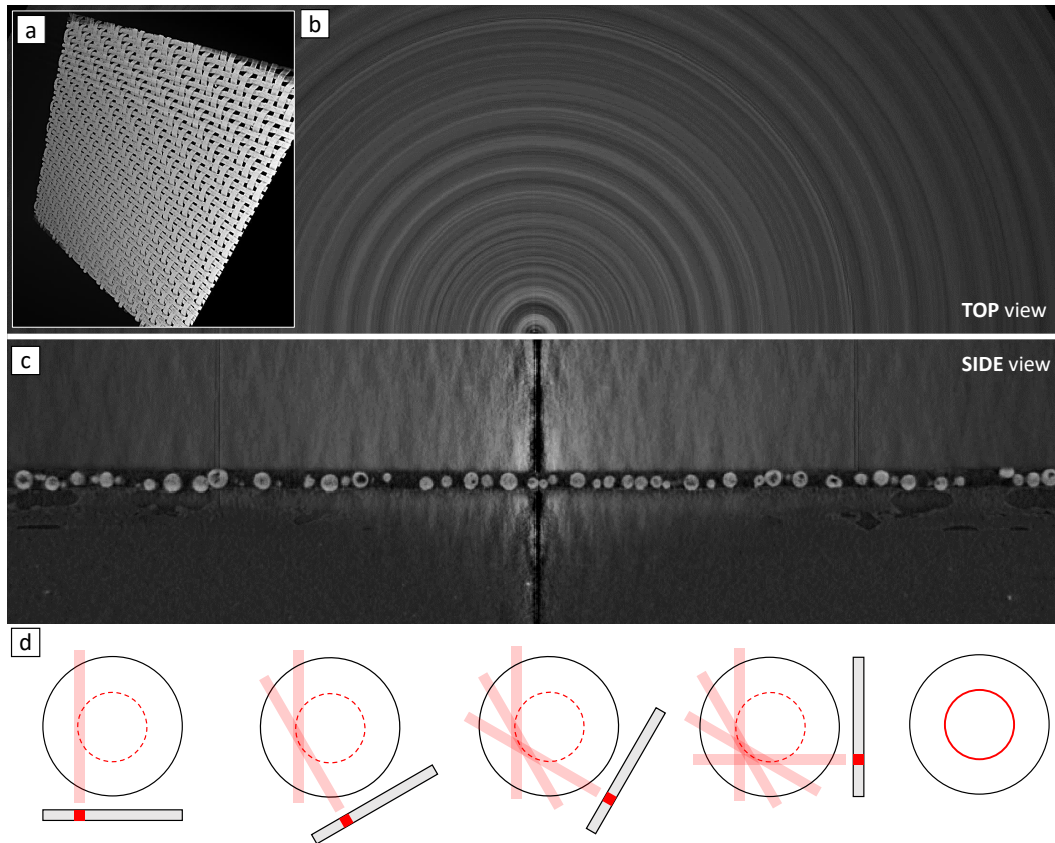


Figure 4.10: Example of a ring artefact without random-like detector shift (see Sec. 3.4.8). (a) A periodic mesh structure is (b) generating concentric rings in the projection top view, that (c) appears as distortions in the side views. The origin of the circular shape is (d) shown exemplarily at a back-projected defective detector pixel represented by a black pixel in the projection image. Note again that for illustrative purposes the dimension is reduced to two dimensions here, resulting in a 1D projection image giving a 2D reconstruction.

removal (DRR). If one puts all images on top of each other, there is no clear border. It's like a stack of paper that has to be realigned after falling down. However, since the anchor point is inside the border, the excess border must be cut off so that all images are the same size again. This leads to a final pixel number not of 1024^2 but of 995^2 to 999^2 pixels. Of course, since the system works with isotropic voxels, the number of sections in the reconstructed image stack is also reduced. Also note that there are measurement situations where DRR is not a good choice because of additional stage movement that could cause physical sample drift. One example is given by Santini et al. [143] who did 3D contact angle measurements with a single droplet on a surface structure. Another example here is given in the Appendix 10.2.

It should be mentioned here that the correction can also be done after the measurement. One approach is to apply algorithms to reduce the artefacts directly within the object space but with a coupled degrading of image information. Since a ring in object space is a line in the sinogram (details see Sec. 3.3.4), it can be removed more easily but also with loss of information. A more detailed presentation on the removal of artefacts is beyond the scope of this paper. A promising approach is provided by Yoon et al. [144].

5 Image Analysis

Most image analyses based on tomography data are of qualitative nature. Sometimes, the main focus is only the three-dimensional visualization of objects, which is not wrong. But considering the potential of the measurement methodology, the focus should be on a quantitative analysis of the tomographic datasets. In most cases, this requires a distinction between different features (structures, phases, particles). Starting with a stack of grey scale images from the reconstructed dataset, a huge pool of image processing strategies and algorithms is available, each one altering the image itself, and thus, producing an error. Single pixels have no “memory”. Without knowing the image processing workflow, which is documented in detail in **Papers A, C, D**, it is very difficult to evaluate quantitative image analysis data. The best case scenario would be to store raw image data and workflow separately. In modern image processing software this is done by applying layers. Each layer represents a reversible step, leading to the final result.

One reasonable scenario for tomographic datasets is presented in **Paper E**. In the following Sec. 5.1, the most relevant parameters determining image quality are introduced followed by a brief discussion of two possible workflows for image processing with the focus on particle segmentation in Sec. 5.2. The threshold-based segmentation, which is used in **Paper A**, and the machine-learning assisted segmentation, which is used in **Paper C**.

5.1 Image Quality

As focus should be on gaining best image quality, one has to define what quality means when dealing with pixel-based image data. A suitable way of describing the image data is required that allows not only analysis but also the comparison of different images.

5.1.1 Grey Value Histogram

The grey value histogram is the frequency distribution of all grey values of an image, plotted against the grey value itself. In other words, it shows the number of pixels assigned to one distinct grey value from the given value range of all possible grey values. It is determined by the X-ray spectrum, e.g. photon energy distribution and integral intensity, the hardware setup of the tomographic device, e.g. number of detector pixels, objectives and finally, the properties of the sample itself, e.g. diameter and X-ray absorption coefficient.

The most important descriptors for particle analysis are briefly explained below. It should be noted that the image quality cannot be assessed with the human eye in every case. For example, high overall sharpness and contrast can be counterproductive for particle segmentation. In quantitative analysis, the properties have to be considered in a much more diversified way. To stay with the example of particle

segmentation, a slight blurring within equal phases (noise reduction and prevention of over-segmentation) combined with sharp edges is ideal for optimal results.

In all cases, a visualization method is needed that makes it possible to evaluate even very small differences. A histogram of all grey values is the proper graph used in image analysis. This visualization method collects distinct grey values of all pixel in bins of equal size. Depending on the data type, the available number of grey values can be interpreted as third axis, the “bit depth” (8 bit, 16 bit or 32 bit). Fig. 5.1-a shows an exemplary section maximized to pixel level. Each pixel grey value of the image is a distinct selection within this grey scale (Fig. 5.1, marked red).

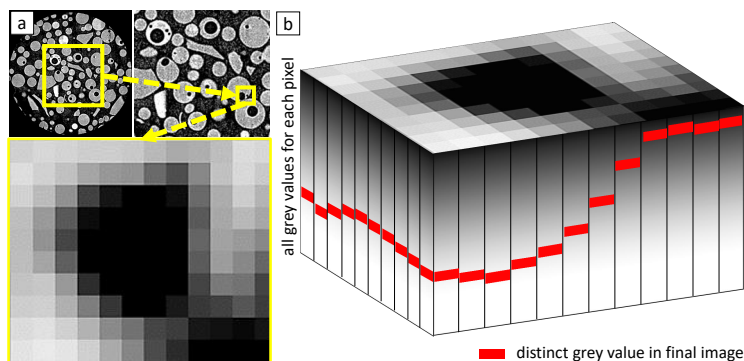


Figure 5.1: Visualization of a grey scale histogram’s origin: (a) reconstructed section from a spherical soda-lime glass particle sample magnified twice to a resolution where the pixels are clearly visible. Every pixel has a certain number of available grey values represented (b) by a third axis where the actual value in the image is marked in red. Note that due to the finite number of possible grey values determined by the number of bits within the file this axis is not continuous but distinct.

Fig. 5.2 shows three pairs of example histograms. On the left, the reference state, which is compared with a different state on the right. Note that the grey value 0 refers to black (the image frame) and maximum value 255 refers to white. Changes are discussed based on the referring histograms:

1. One rectangle with a specific grey value on the left is supplemented by eight further rectangles on the right, see Fig. 5.2-a. The position of the bars (the grey value) remains the same, only the height of the rectangle’s grey value increases⁵¹, see Fig. 5.2-b.
2. Four different shapes (rectangle, triangle, circle, needle) in the upper left corner on the left are distributed in all four corners of the rectangle on the right, see Fig. 5.2-c. No change can be observed. Same slope in both cases as can be seen in Fig. 5.2-d. The grey scale histogram does not depend on the location of shapes in the image.
3. The four rectangles, each with a unique grey value, are supplemented by five additional rectangles, each also with a unique grey value, see Fig. 5.2-e. In the histogram, five more bars of the same size are added at the respective grey value positions, see Fig. 5.2-f.

So it can be seen that the histogram representation is well suited to capture the essence of an image, independent of the actual 2D-projected structures. But without further calibration, it cannot serve as a quantitative measure.

⁵¹ As the same amount of voxels turning to grey are not white anymore, the histogram bar of 255, representing white, is decreasing. Due to the logarithmic scale, which is chosen for visualization purposes, this is not clearly visible. Note that this effect refers also to (3), but not to (2), because the area covered by the objects remains the same.

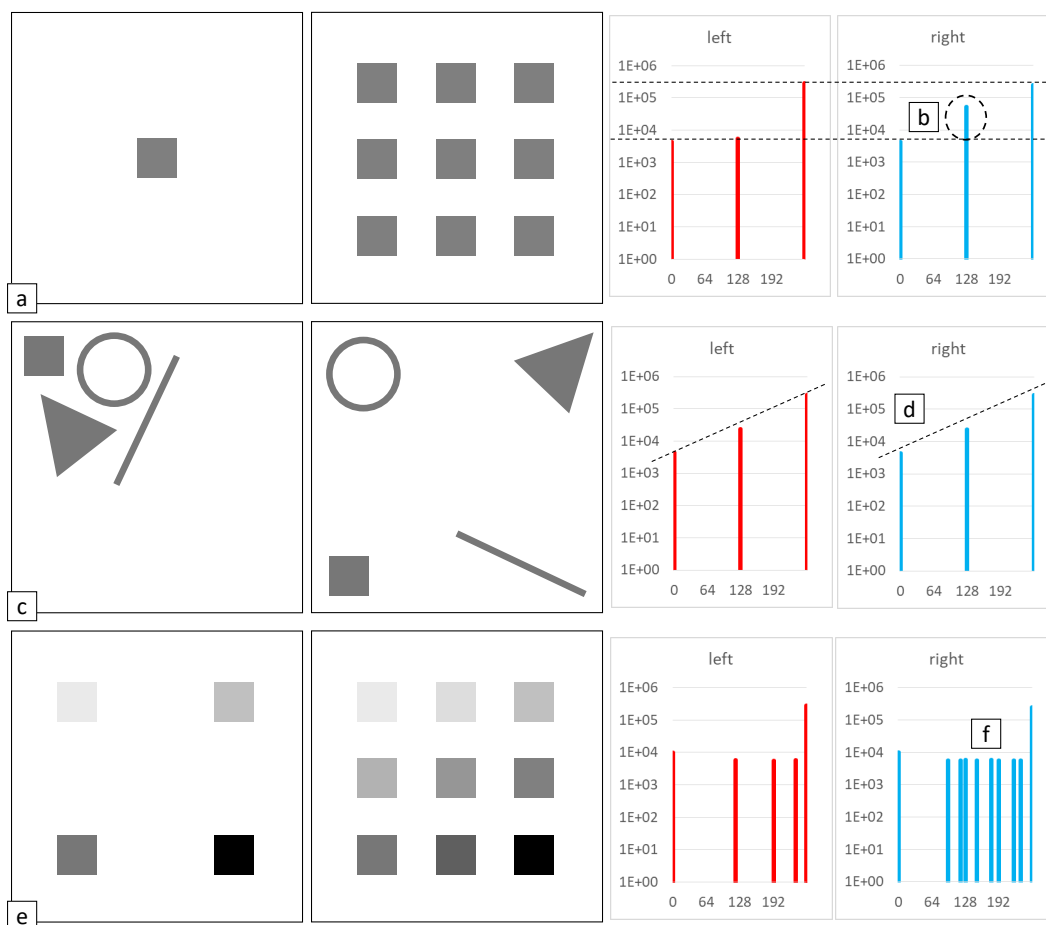


Figure 5.2: Image objects and their relation to the grey value histogram: (a) a larger number of pixels assigned to a specific grey value results in (b) a higher peak in the histogram. In contrast, (c) the position of objects at a constant pixel number has (d) no effect on the histogram's values. Note that even the shape and the number of objects in the image are of no interest here. The only thing that matters is the number of pixels assigned to a certain grey value. (e) This number of distinct grey values in the image is (f) directly transferred to the histogram. Note that the dotted lines in (b) and (d) are only to guide the eye for direct comparison.

5.1.2 Resolution

Why is there a need for a second optical magnification step⁵² and why should it be kept variable to apply different steps? Fig. 5.3 shows a projection image of a filament-like structure that was captured at highest reasonable magnification inside a particle, resulting in a final voxel size of about 400 nm⁵³.

By adapting the sample-detector distance for magnifications Fig 5.3-a 40, Fig 5.3-b 20x, and Fig 5.3-c 4x, the product of geometrical and optical magnification keeps constant. But even when adjusting the exposure time, it is not possible to maintain the spatial resolution. This becomes most obvious when comparing the zoomed part from Fig 5.3-a with Fig 5.3-c. The further one moves away from the sample with the detector, the more geometric invariances of the cone beam become apparent. In addition, the quantum yield decreases dramatically due to the quadratic decrease in the number of photons, which leads to additional blurring at significantly longer exposure times. Tab. 5.1 summarizes all numbers for the example from Fig 5.3 with constant source-sample distance.

⁵² Note that a test without additional optical magnification is not possible in the current measurement setup. In addition, the detector would have to be moved away from the sample by nearly 1 m, which the instrument dimensions do not allow.

⁵³ From a purely mechanical point of view, a smaller voxel size would be conceivable by increasing the sample-detector distance at the highest optical magnification to one tenth, i.e. 40 nm. Practically, it is strongly limited mainly by the size of the focal spot (penumbral blurring, see Sec. 3.4) and the homogeneity of the scintillator material.

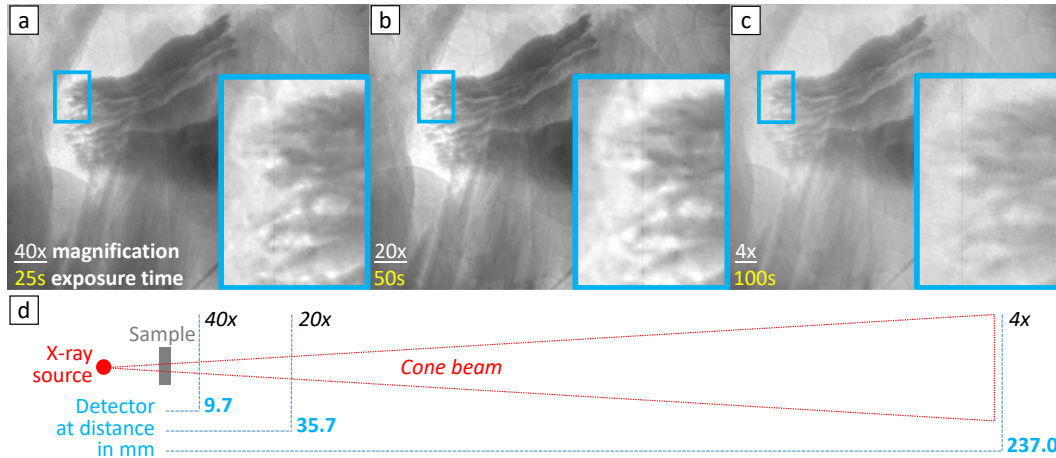


Figure 5.3: Influence of different magnification levels for identical voxel size, in this case 400 nm, on the quality of the related projection image: (a) A filament structure inside a mineral particle with 40x magnification, same for (b) 20x and (c) 4x. As the enlarged image part shows, the details and the contrast decrease dramatically when going to a lower magnification, while at the same time the needed exposure time per each projection increases. This can be explained by (d) the larger distances for lower optical magnification as the total magnification has to stay constant to guarantee the same voxel size. The larger the distance the higher arising errors, which are e.g. penumbral blurring, detailed discussed in Sec. 3.4. The calculated values are summarized in Tab. 5.1. Note that also the scintillator thickness has an influence on reachable resolution limits. Because this value is fixed and cannot be changed it will be assigned to the overall optical system and not of further concern here.

The geometric magnification $M_{\text{geometric}}$ is determined by calculating the object size on the scintillator screen with known source–detector distance and cone beam angle by applying the arcus tangens. Then, the object size in the sample is calculated by applying the intercept theorem. Dividing the latter by the source–detector distance gives the geometric magnification. The total magnification M_{total} is calculated as follows:

$$M_{\text{total}} = M_{\text{geometric}} \cdot M_{\text{optical}} \quad (5.1)$$

As can be seen in Tab. 5.1, apart from smaller variations due to rounding error and inaccurate angle indication, the products of all three magnification levels are almost the same.

Table 5.1: Calculated total magnification as the product of geometrical and additional optical magnification on basis of the example from Fig. 5.3. Differences in total magnification (they should be exactly the same) are due to rounding errors and inaccurate angle indication (projection angle in this case is between 0.75 and 0.77 degrees).

Distances in mm		Object sizes in mm			Magnification		
Source-Sample	Sample-Detector	Source-Detector	on scintillator	inside sample	Geometric	Optical	Total
15	237.0	252.0	1.69	0.10	16.8	4	67.2
15	35.7	50.7	0.34	0.10	3.4	20	67.6
15	9.7	24.7	0.17	0.10	1.6	40	65.9

5.1.3 Signal-to-Noise Ratio

van Daatselaar et al. [145] give a medical example, where mainly the influence of the number of available projection images on the signal-to-noise ratio (SNR) is investigated. Projection images must therefore not only be exposed long enough, but also be available in a sufficiently large number⁵⁴ to minimize the final noise in the reconstructed cross section.

As already discussed in Sec.3.4.9, a minimum number of 5,000 VIS photons is needed per projection image to guarantee a good SNR. Strictly speaking, the SNR should be evaluated separately for projection and reconstruction. This distinction is omitted here, since with the applied FBP reconstruction algorithm used in this study⁵⁵ it can be assumed that the noise propagates from the projection to the reconstruction without decreasing. To guarantee a sufficient high SNR for each reconstructed section, the projection must be as low-noise as possible. In the following the term SNR refers to the projection image only. Fig. 5.4 shows the overview and the detail image of a single particle measurement. Counts per exposure increase from Fig. 5.4-a to Fig. 5.4-c.

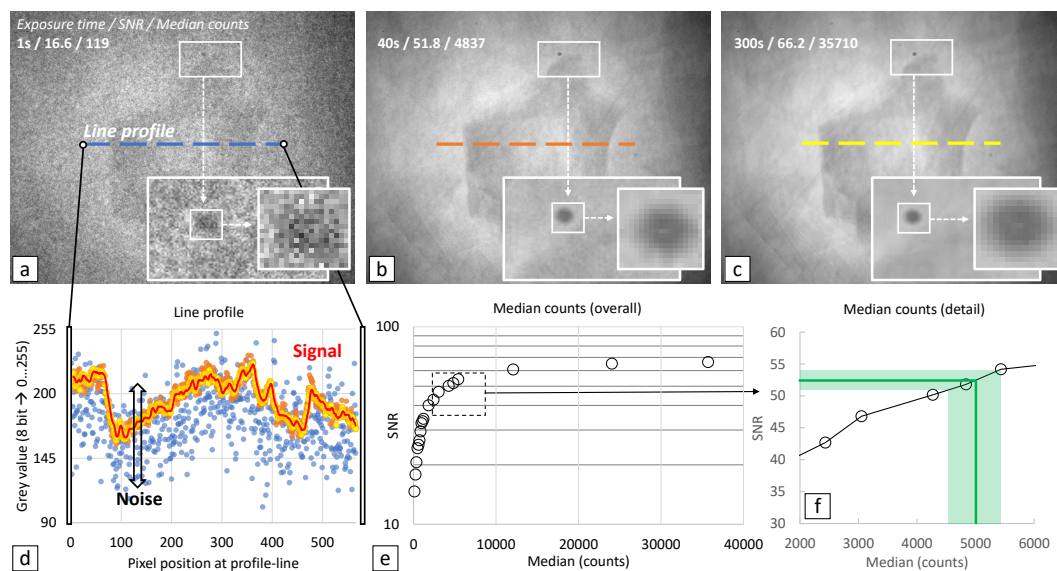


Figure 5.4: Influence of the exposure time on the SNR: (a) Projection image of a particle, where the number of photons, with a median value of approx. 100, is much below the minimum of 5,000 for the given detector. The enlarged image parts clearly show image noise. Structural information is lost. (b) one order of magnitude higher, at the given minimum, structures became visible. The advantage of (c) the increase by a further order of magnitude can no longer be assessed visually. (d) shows the referring grey value line profiles marked in (a to c). The decrease of the fluctuation range with increasing photon number is clearly recognisable. (e) shows the SNR, calculated with Eq. 5.2. As expected, the SNR does not increase linearly but asymptotically. The enlarged part (f) shows a corridor of $\pm 2.5\%$ relative error, meaning that a slight undercut of the minimum photon count will not decrease SNR dramatically. Note that the source-sample distance is 15 mm in every case.

Although the 100 counts from Fig. 5.4-a are clearly below the recommended limit, the actual structure can already be recognized and, at least for overview scans, one has a good first impression of the sample. The visible image noise, on the other hand, already disappears significantly in Fig. 5.4-b.

There are multiple ways to define the SNR based on different assumptions for

⁵⁴ The author gain good results with 180 projections which seems very low. Recalling the rule of thumb by Kyrieleis et al. [88] (compare Sec.3.3), best image quality using FBP would be approx. 520 projections. But as the overall goal in medical radiography is to minimize the dosage penetrating living tissue, this is perhaps a good middle ground.

⁵⁵ Note that there are methods to reduce SNR, e.g. by smoothing the sinogram [89], or by applying another reconstruction algorithm [108], e.g. iterative.

the *signal* and the *noise*. One possible way is to use the reciprocal of the coefficient of variation, which means the ratio of the average to the standard deviation of a distribution [74]:

$$SNR = \frac{\text{Signal}}{\text{Noise}} = \frac{\mu}{s} = \frac{\mu}{\sqrt{\frac{1}{n-1} \sum_{i=1}^n (\text{greyval}_i - \overline{\text{greyval}}_{10})^2}} \quad (5.2)$$

The original grey values from a line profile of Fig. 5.4-a to Fig. 5.4-c are visualised in Fig. 5.4-d. Going from very short (blue) to long exposure times (yellow), the variation of the data points, representing the noise, decreases significantly. As can be seen in Fig. 5.4-e, as expected, a higher exposure time, meaning higher photon counts on the CCD detector, results in a higher SNR. This effect is not linear, but converges asymptotically, meaning much longer exposure times will not increase the SNR significantly. As illustrated in the magnification in Fig. 5.4-c, the structure even gets more blurry compared to the same magnified area in Fig. 5.4-b, which can be explained by penumbral blurring and temperature drift of the X-ray beam.

Looking at the proposed minimum photon count of 5,000 photons per exposure, see Fig. 5.4-d, this number refers to a SNR of approx. 52.5. As can be seen in Fig. 5.4-e, assuming a 2.5% relative deviation from this value, this gives a SNR of 50, which is a photon count of about 4,500. So, going slightly below the 5,000 limit is possible with an acceptable error. This small difference is only of interest for highly absorbent phases and time-critical test series. In addition, it must be noted that in case of samples, which are smaller than the FOV, vertical areas outside at the top and the bottom of the FOV are considered to be not critical in case of a low SNR, since the signal, and so the noise too, is only “smeared” horizontally over the object space by the FBP algorithm. The corresponding sections of vertical areas without object information can be removed after reconstruction. In contrast, extending the exposure time from 35 s to 300 s, i.e. almost a ninefold increase, only leads to an increase in SNR to 66, see Fig. 5.4-f. As the example shows, a balancing process is necessary here. Note that this method is only a very rough estimation for SNR quantification. Another approach for the SNR quantification *without* having a reference is given by Thong et al. [146] who uses an *autocorrelation function* to separate signal from noise, as it is known from signal processing [147].

5.1.4 Contrast and Dynamic Range

In the tomographic sample, one weakest and one strongest absorbing point exists. These maxima form the so-called *contrast* range of the projection images, and thus also of the later reconstructed volume. The *dynamic range* is the ratio between the smallest and largest value, in this case given by a certain detector⁵⁶. The question is, how the contrast, which is in our case needed to create a reasonable projection image of the particle sample, fits to this dynamic range. If the contrast range exceeds the dynamic range, the details at the upper or lower end of this spectrum are lost. In the following, the focus will be on the dynamic range, as it is a detector property that is directly related to the X-ray attenuation of the material.

The dynamic range indicates the ratio of the largest measurable signal to the smallest signal distinguishable from the background noise. The overall system must be designed in such a way that the scintillator efficiency matches the dynamic range

⁵⁶ The human eye is also some kind of detector. As it works logarithmically, we are able to see something in a dark room and also on a sunny day outside. Note that the dynamic range is also used in audio and video applications.

of the VIS CCD detector [86]. As in optical photography, the aim is to capture as much of the structural information as possible during a single exposure. There are strongly X-ray absorbing phases, like metals, with a few detector counts, and weakly absorbing phases, like air, with many detector counts. If this can only be realized by combining measurements taken at different energies, this is called high dynamic range (HDR) imaging. In X-ray tomography this is realized by varying tube voltage [148] but is not part of the presented studies.

Same like in photography, an excessive number of photons⁵⁷ can lead to a significant or total loss of contrast and so, a picture carrying no information. In case of X-ray tomography this means, that too many VIS photons will generate so many electrons in the CCD pixel that the associated electronics will be overloaded. This over-exposure is prevented by an over-exposure test before each measurement by adjusting the exposure time accordingly.

Fig.5.5 shows the sample material becomes more and more transparent with increasing exposure time (Fig.5.5-a to Fig.5.5-d)—its contrast and information vanishes. The ring shape of the growing area of over-exposure is related to the cone beam (illustrated by the beam profile in Fig. 5.5-e, details see Sec. 3.4.3). The structures inside this ring⁵⁸ is the projection of the structure of the scintillator material probably caused by diffractive photons generating a phase contrast.

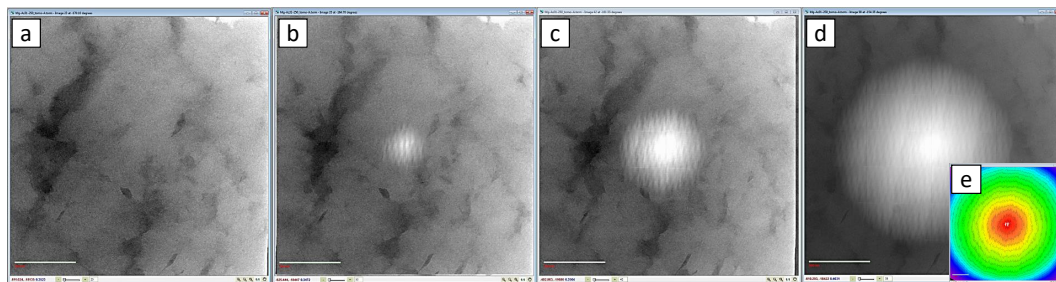


Figure 5.5: Overexposure of a projection image caused by increasing exposure time from (a) to (d). The white circular area, which gradually shows up, is caused by (e) the conical shape of the beam with highest intensity in the center (marked red).

5.1.5 Sharpness

As demonstrated above and visualized in Fig. 5.3, a certain magnification is achievable with different lenses, even with low magnification. But due to the system inherent blurring⁵⁹, which increases with geometric distance, these are so-called empty magnifications—the spatial resolution is not equally increased with increasing geometrical magnification.

5.1.6 Summary

As discussed in the previous sections, image quality is essential to perform reasonable quantitative image analysis. All errors that show up in the projection image manifest themselves to a higher or lesser extent in the reconstructed tomogram. Fig. 5.6 summarizes all previously mentioned factors influencing image quality.

The particle sample, discussed in Sec. 4.1, the measurement, discussed in Sec. 4.4, which is influenced by the system's configuration, and the image artefacts, discussed

⁵⁷ In case of the ZEISS Xradia VERSA 510 these are 60,000 photons per exposure and pixel.

⁵⁸ Of course, this structure is always included in the image information, but it is removed from the final projection by taking a reference without a sample.

⁵⁹ Blurring is induced by different mechanisms already described in Sec. 3.4: temperature drift, penumbral blurring, cone beam, sample motion, partial volume.

in Sec. 3.4, are connected in multiple ways. If these can be controlled as precisely as possible, errors in the following image segmentation steps can be reduced significantly.

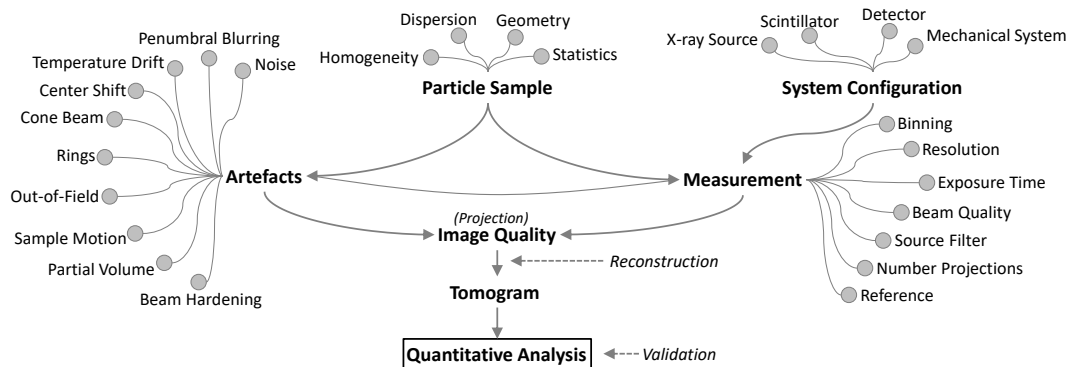


Figure 5.6: Summary of factors influencing the quantitative image data evaluation. Corresponding to already presented sections, main parts are here the system's configuration, which directly influences the measurement. The measurement and the particle sample can create artefacts, all together having impact on the quality of the projection image. The reconstruction can alter the image quality of the final tomogram used for the quantitative analyse.

5.2 Basic Image Processing Strategies

The image quality is decisively determined by the resolution, image sharpness, image noise, contrast and dynamic range of the projection image and thus also of the reconstructed image stack. Based on the grey value histogram, different image pre-processing steps can be applied to create an optimal starting point for further image segmentation. Schlüter et al. [149] give a review on possible strategies for multiphase images obtained by XRM. The underlying image processing strategies are described in detail in **Papers A, C and D**. In the following, only the main part of the image processing routine will be explained by using the example of image segmentation. Fig. 5.7 shows two possible image segmentation strategies based on single grey value thresholding and machine learning algorithms. The embedded particle sample, see Fig. 5.7-a, is reconstructed to a three dimensional volume as can be seen in Fig. 5.7-b. For easier explanation, the image processing workflow is reduced to two dimensions only. In a real case scenario, image processing is categorized in 2D, mainly for image quality enhancement, and 3D methods, mainly for all processing steps regarding the final particle segmentation. The overall goal is to separate all particles within the image into distinct features that can be analyzed to generate quantitative data.

5.2.1 Threshold-Based Segmentation

In threshold-based segmentation⁶⁰, one grey value is determined that divides the particle phase, which is light, from background, which is dark, see Fig. 5.7-d, a process which is called binarization. Depending on the used algorithm this is working more or less well, e.g. there are a lot of remaining noise-pixels, sometimes called speckles, see Fig. 5.7-e. Artefacts are therefore removed using appropriate filters, see Fig. 5.7-f. To calculate particle dimensions correctly, holes inside the particles are

⁶⁰ Due to the observer dependency this is a critical and non-trivial step [150].

filled with white pixels, see Fig. 5.7-g belonging to the particle phase. Particles that are very close to each other sometimes get in direct contact and are not separated by at least one background pixel (black) layer⁶¹.

In this case a watershed algorithm [151] is applied that treats the image like a topographic map separating adjacent drainage basins. Simple watershed is extremely sensitive to noise pixels, which are black pixels inside white particle areas after applying a binarization algorithm. It is also not working properly for elongated non-compact particles. In both cases, it can occur that the particle is divided into parts, a phenomenon called oversegmentation⁶². Finally, these particles are recognized as connected and externally delimited areas of particle phase against the background (marked light blue with unique identifier). In case of ROI-tomography, all particles that are not completely within the FOV are discarded from subsequent analysis. All steps of the threshold-based method have to be optimized for each new particle system. In case of multiphase particles, the workflow gets more complicated, e.g. the need for multiple thresholds or grey scale-based methods without prior binarization. Note that the workflow in Fig. 5.7 is idealised. Sometimes there have to be additional image pre-processing steps or other information from the original image has to be taken into account, like grey value gradients [152] for the generation of particle-discrete markers [153, 154] that work as a kind of seed for the segmentation algorithm.

5.2.2 Machine Learning Assisted Segmentation

Supervised machine learning assisted segmentation, also called *feature-based* segmentation [155], in this example the trainable waikato environment for knowledge analysis (WEKA) segmentation algorithm [156, 157], is based on a solid and representative selection of images, as can be seen in Fig. 5.7-A. These images are used for feature selection, in our case particle and background. Features are marked manually, indicated by yellow and green, see Fig. 5.7-B. This marking is done by shapes and lines with different sizes and thicknesses, depending on the features. Very thin lines between particles, for example, represent a characteristic that is used by the algorithm to classify them as background. The algorithm learns on basis of rules how to divide distinct features, see Fig. 5.7-C, step by step. As can be seen in Fig. 5.7-D, the outcome is very similar to the threshold-based approach, but without additional image processing and resulting artefacts.

Although this sounds like an attractive alternative, the quality of the segmentation result is crucially dependent on the training data set which includes the manual markers. The chosen approach of machine learning, as in the present case of the decision trees, is theoretically easy to understand, but due to the large number of decision trees and splits within the respective tree structures, it is no longer easily verifiable. For a quantitative evaluation, the segmentation results are compared to a manually segmented one that is considered to be correct. This dataset is also referred to as *ground truth*. More details on this topic are given in **Paper C**, regarding the used WEKA trainable segmentation algorithm, and in **Paper D**, regarding the neural network approach, which was chosen here as an alternative.

Like it is described in Sec. 4.3, it is always good to use an additional validation step, which was done in both the methodological papers and the case studies. Note that a detailed description of the image processing workflow is given in all papers with the corresponding sources.

⁶¹ In the optimal case, this effect has to be avoided by a proper sample preparation strategy, see Sec. 4.1

⁶² Modern image processing workflows that are using watershed algorithms can avoid this, for example, by merging oversegmented particle parts with the help of Neuronal Networks [9]

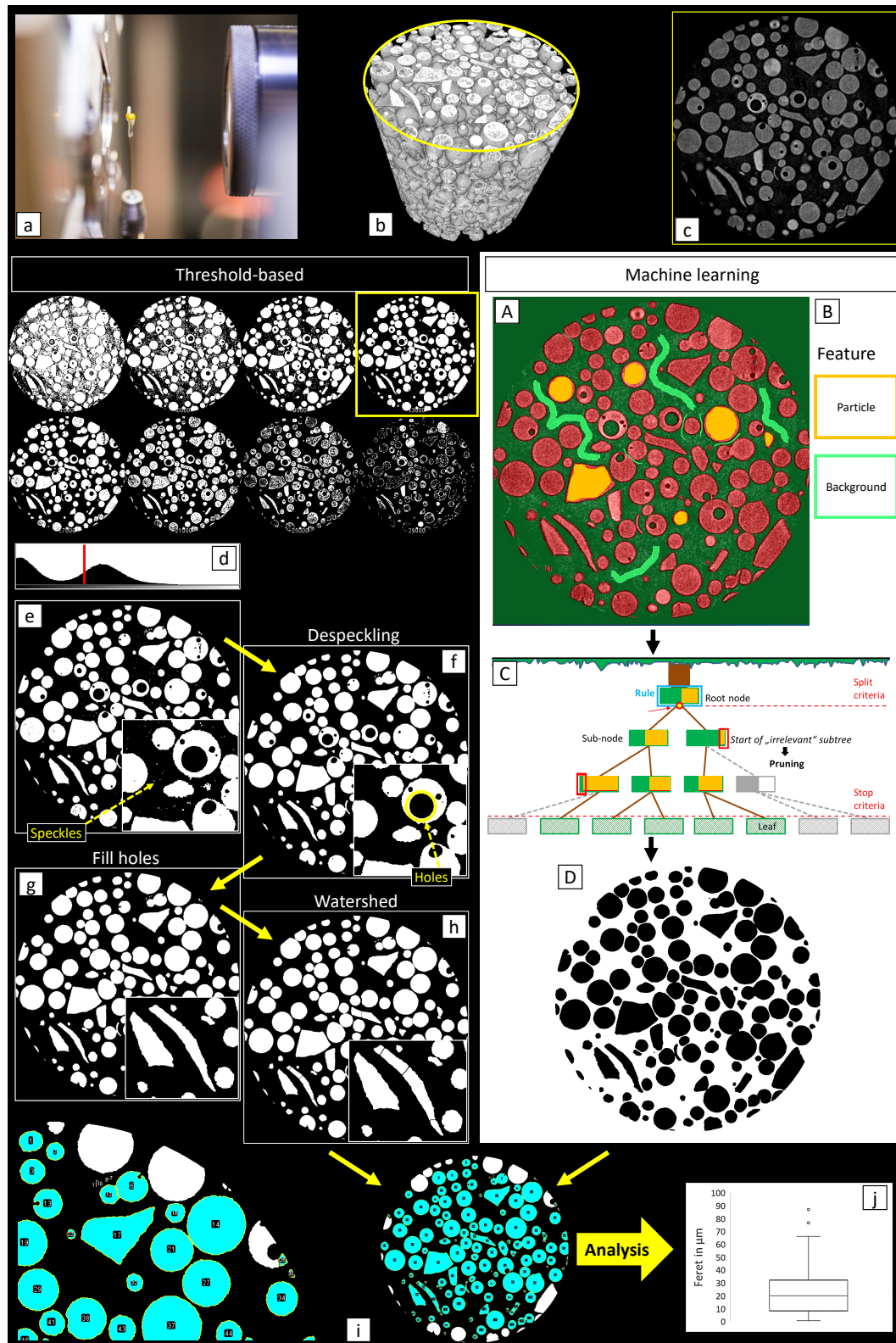


Figure 5.7: Comparison of two possible particle segmentation strategies: (a) Acquisition of the sample volume, (b) reconstruction to get the tomographic dataset, (c) represented by vertical sections. Threshold-based strategy to (d) separate particle and background phase. (e) Image processing to determine the optimal threshold including (f) despeckling, (g) fill holes, and (h) subsequent watershed, resulting in (i) a particle-discrete data set for quantitative analysis. In comparison (A) a machine learning strategy with (B) feature selection, (C) learning algorithm and (D) subsequent classification result after additional application of fill-holes algorithm.

6 Correlative Tomography

Correlative tomography mainly concerns a correlation of measurement results of the same and/or other measurement methods within one or across several size scales⁶³. Reviewing the recent literature, a possible categorisation can be made as follows:

1. A *scouting approach*, where the correlation is used for scale bridging. The intermediate measurement steps are only a tool. Just the result of the highest magnification is of interest. This approach is used in **Papers A, C** and also by Morales et al. [159]. A short introduction is given in Sec. 6.1.
2. A *multiscale approach*, where correlating is done mainly with the aim of connecting multiple scales of the same measurement method. Here, two or more scales are of interest, not only the highest magnification. This approach is used in **Paper D** and also by Burnett et al. [160], see also Sec. 6.2.
3. A *multidisciplinary approach*, where the main focus is on the connection of other measurement methods, supporting and validating the actual measurement result, and, more interesting here, to provide additional information, which was not accessible via one method alone. This approach is used by Cnudde et al. [161] and Furat et al. [9]. A short introduction is given in Sec. 6.3.

Complex characterization tasks require a mixture of these approaches [162]. Ideally, the full range of possibilities would be used in every tomographic analysis, but this is not feasible for a practical workflow due to monetary and time constraints and sometimes it would only be of academic interest. Important in this context is the sample preparation strategy described in Sec. 4.1. If the sample volume can be reduced between the steps, like it is realized in **Paper D**, acquisition time can be significantly optimized, or, as in the case of nano-tomography, this is what makes a measurement even possible at all.

The principle tools for the correlation procedure are basically known from 2D imaging [162] where it is called *digital image correlation (DIC)*. One example is optical microscopy where DIC is used to find a ROI for SEM analysis. The extension to 3D is called *digital volume correlation (DVC)*. Here, an example is the usage of the XRM to find the ROI for a TEM analysis [159]. In this case, the new workflow is a significant improvement over the established method, which would require up to 20 iteration cycles of manual cutting despite careful alignment for high-resolution TEM measurement. The method is also applicable to generate displacement fields in structures, which are, for example, captured before and after a defined load on porous structures [163], or compressed particle beds [164].

The following examples show that the three different categories cannot be clearly distinguished from each other. The decisive factor is the objective of the measurement. The more clearly this is defined, the more likely it is that unnecessary measurement time can be saved. For example, the tomograms in the following section could be imaged with the same high resolution, but if the objective is not defined, only an unnecessarily large amount of data will be generated here, the potential of which will not be used. Follow-up measurements are the better alternative here.

⁶³ Note that correlative tomography sometimes also refers a change of the sample over time, called *time-laps tomography* or *4D tomography* with time as the 4th dimension. One example here is given by Paz-Garcia et al. who investigate microstructural changes in electrode material within the charge cycle of a Li-ion battery [158]. The correlation of the measurement volume over time is essential to track changes and perform quantitative analysis. This kind of correlative approach should not be of further concern here.

6.1 Scouting Approach

As already explained in the previous sections, there is a fixed relationship between the FOV and the achievable voxel resolution, which is given by the number of available pixels on the detector, minimized by additional binning if necessary. If scanning times are to be minimized and artefacts caused by ROI tomography are to be avoided, the size of the sample must be adapted, see Sec. 3.3.5 and Sec. 4.1 respectively. The higher the resolution becomes, the smaller is the FOV and thus the sample volume. In practice, the adaptation of the sample size is not possible in every case. Sometimes samples have a given size and destruction should be avoided because they will be used in other analysis methods or in cyclically in repeated tests like it is shown in the fracture analysis example in Appendix 10.1, where the sample is used between the scans to perform an ultra sonic fatigue test (USFT). Another example is given in Fig. 6.1, where relatively large fibres from a filtration experiment had to be embedded to avoid motion artefacts (see Sec. 3.4.6).

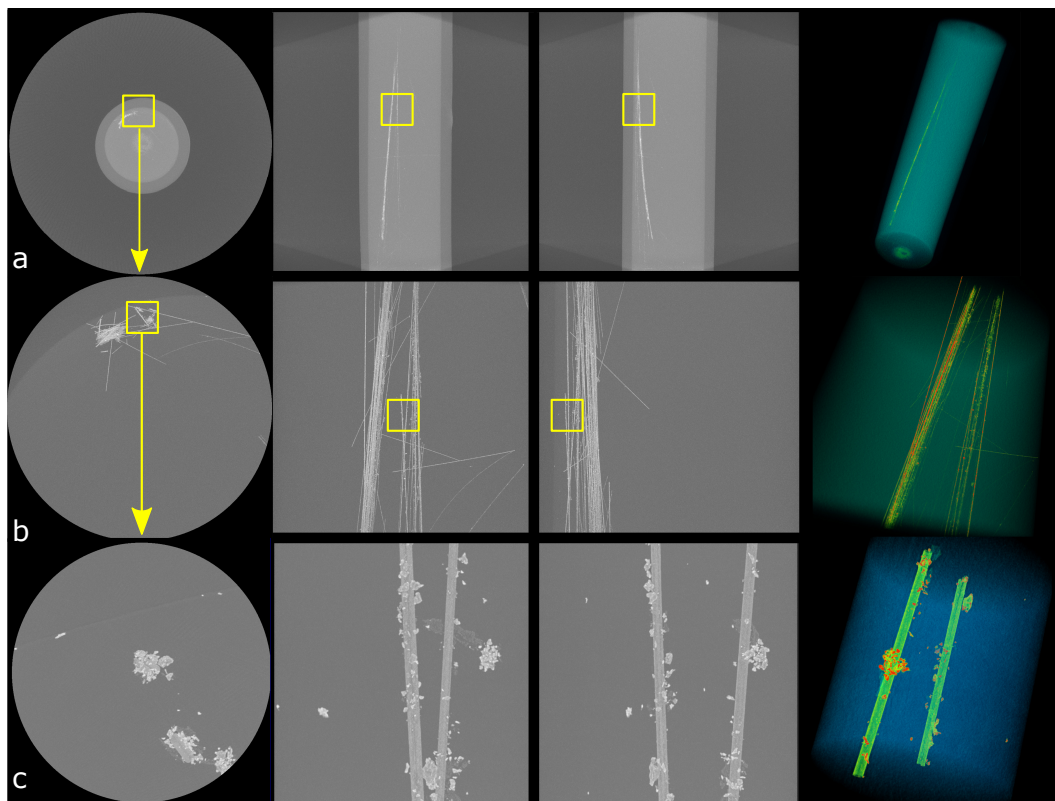


Figure 6.1: Analysis of aluminium oxide fibres from a filtration process with the goal of locating filtered particles loosely attached to the fibre surface. (a) First scan with lowest magnification, followed by (b) the next zoom step with higher magnification, resulting in (c) a high resolution scan. All three scans are illustrated with a top view (left), two corresponding side views (middle) and a 3D visualization (right). Note that the pre-scans used for scouting can be captured with very less projections, captured very quickly with bad quality but showing sufficient details to re-locate the next scan step.

But the embedding had to be done very carefully with minimal mechanical impact, as particles had been deposited on the fibres and it was essential to prevent them from falling off. On the one hand the small diameter (approx. $10\ \mu\text{m}$) makes single fibres invisible in the projection image with lowest magnification. Highest

magnification, on the other hand, makes alignment for scanning the same fibre within the very small FOV nearly impossible. So, a low resolution scan with the 0.4x objective was performed, capturing only 201 projection images in a very short time, see Fig. 6.1-a⁶⁴. With the new coordinates, a new scan with the 4x objective was performed with the same goal, see Fig. 6.1-b. The last scan with the highest magnification, see Fig. 6.1-c, here a 40x objective, was then performed with a sufficient number of projection images (according to Eq. 3.2), which was in this case 1601. However, since the focus here is on finding a partial section, the intermediate steps are deliberately driven to the limit so that a meaningful correlative analysis is no longer possible.

6.2 Multiscale Approach

In the field of tomographic particle characterization discussed here, there are two main tasks that require an analysis method over multiple scales. First is to be able to analyse two (or more) characteristics, like a disperse particle collective with particle fractions on different orders of magnitude. This is done in **Paper D** with a mixture of fibres, several 100 μm in length, together with spherical particles in the range below 10 μm in diameter. When adapting the FOV to capture the fibre length, the voxel size would be reduced in such a way that the spherical system could only be partially mapped, the fines would be much below the voxel size. In contrast, a high resolution scan of the spherical fines not reveal the longest dimension of the fibres. Only by combining two magnification steps, the characterization of the full system is possible. Another example is given in Fig. 6.2-a, where a low-resolution scan from the Zeiss Xradia 510 Versa, which is used in this thesis, is combined with a scan of higher resolution from the same and from another micro-CT⁶⁵.

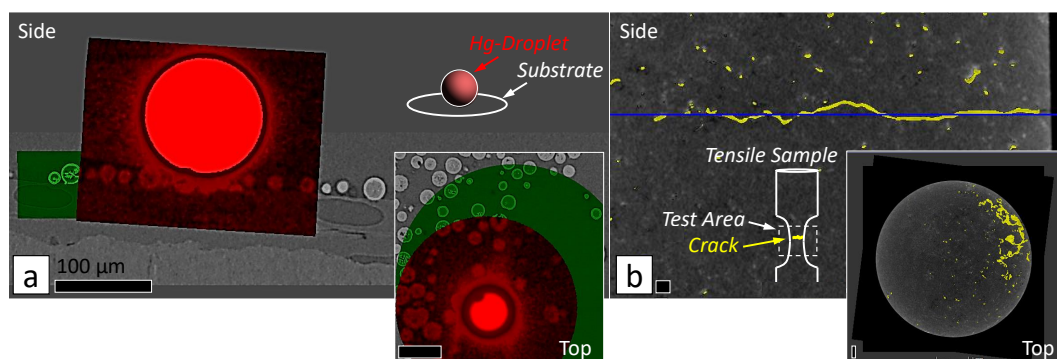


Figure 6.2: Examples for (a) multiscale approach capturing a mercury droplet on a substrate to investigate the contact angle distribution in 3D, here scans from different devices at two different energies where combined. Another example (b) for the multidisciplinary approach showing two correlated measurements before and after USFT. Here, scans were supplemented with later SEM analysis of polished sections [6]. Note that the scale bars are all referring to a length of 100 μm .

Note that only by using two different energies, the very strongly X-ray absorbing mercury droplet could be imaged together with the much weaker absorbing aluminium oxide substrate. The dynamic range of a single measurement would not have been sufficient (see also Sec. 5.1.4). The example is discussed in detail in Appendix 10.2.

⁶⁴ This means that in this case, no consideration is given to the lower limit of the photon counts either. The image is therefore very noisy, but after contrast maximisation, the structures necessary for finding the coordinates can still be recognised in the tomogram.

⁶⁵ The second device has no additional magnifying optic, so it is not an X-ray microscope (XRM).

The second task is one (or more) disperse particle collective(s) of the same order of magnitude with different characteristics to be analysed. These characteristics are for example particle size, that can be scanned with low-resolution, and particle shape, that can be scanned with high-resolution to image fine details.

6.3 Multidisciplinary Approach

Since X-ray attenuation as described in Sec. 3.2 and Sec. 3.3 is able to perform structural analyses non-destructively, but is only suitable to a limited extent for describing samples quantitatively in terms of their composition, additional analytical methods are required that have to be correlated with tomography measurements.

As already discussed in Sec. 4.1, avoiding sample motion, except for rotation, is even more essential when correlating volumes of different resolution. Parlanti et al. [98] states that it is at least beneficial to align the sample as accurately as possible and maintain the alignment for all measurement methods to be correlated. Basically trivial, but an important consideration for the sample preparation⁶⁶. When interconnecting measuring systems from a single manufacturer, this can be realised via corresponding hardware and software interfaces [165]. In any case, it is essential to know the exact distance to the surface in order to correlate, for example, 2D methods that are done via manual cuts. This was realized with overview scans in **Paper D** to identify a proper FOV for high resolution nano-CT scans.

Here, the quality of the digital volume correlation (DVC) strongly depends on the image quality and the used algorithms [102]. DVC can be performed discretely following distinct features like particles or continuously tracking the movement of random structures in the material [164, 103]⁶⁷. Here, the minimum size of a representative volume element is related to the material and the property of interest [166]. All captured feature movements between different tomograms are summarized as displacement field. Here, the resolution has to be much better than the voxel size to get reasonable information of shift errors [163].

Note that this section is deliberately kept very short as this approach is the subject of current research but is not included in the own publications referenced here. Nonetheless, in Sec. 8 Outlook on Further Research Activities, the current status of the study on the correlative material analysis of multiphase particle systems is described. Additionally, Fig. 6.2-b shows another example of cast alumina samples before and after ultra sonic fatigue test (USFT) to identify cracks within the matrix, their propagation being a function of the material phases [14, 6]. This example is discussed in detail in Appendix 10.1.

Both examples are connected to the Collaborative Research Center 920, which is dealing with multi-functional filters for metal melt filtration. Example 1 focuses on the breakage behaviour of cast alumina samples after USFT. Note that this example is not related to particle analysis. In this case the correlation of the volumes would become even more complicated, especially if the particle system does not include special features, that can serve as alignment markers when matching different volumes.

⁶⁶ An important questions is how to mark the sample's initial relative position when it is necessary to unmount it for experiments between two or multiple measurements.

⁶⁷ Features can be highly X-ray attenuating contaminations, intersecting fibres in the particle system of **Paper D** or entrapped air voids in case of the epoxy embedding method from **Paper C**, which is applied in the ongoing studies, presented in Sec. 8

7 Data Management

Data is generated, stored, filtered, accounted for and aggregated. Raw data is increasingly abstracted, an essential process, especially with very large amounts of data, to be able to capture condensed information. In order to produce scientifically reproducible results, each of these intermediate data-modifying steps must be stored as metadata together with the referring measurement data. Fig. 7.1 shows a tomographic imaging workflow generating data on different aggregation levels.

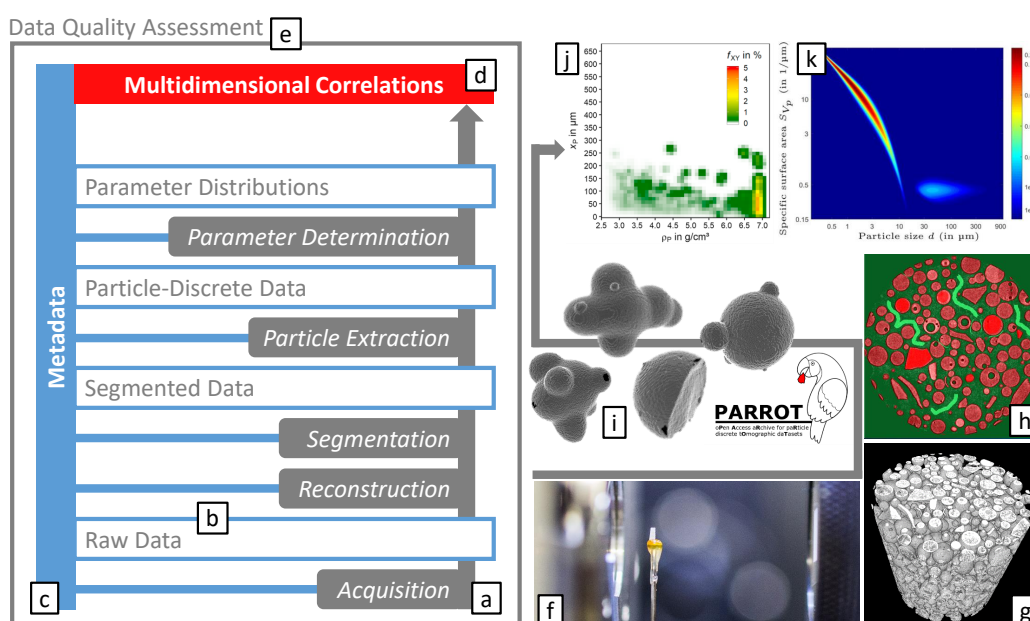


Figure 7.1: All (a) data generating steps within a typical tomographic data acquisition workflow used in this thesis. All these steps are generating (b) data and (c) metadata, which is used for the final (d) multidimensional correlation. (e) Assessing data quality is a crucial step here. Note that on the right side the examples from the previous sections are visualizing the data representations, with (f) a mounted particle sample, (g) the reconstructed tomographic dataset, (h) a classified slice, (i) extracted particle-discrete data, offering the possibility to perform a multidimensional correlation, e.g. with (j) KDE, or (k) Copula.

The following part gives insight into the data processing methods used in this thesis with focus on ensuring data quality, followed by the treatment of particle-discrete datasets, stored within the PARROT database [5]. Note that this section does not claim to be a sufficiently detailed introduction to the topic of a reasonable data processing strategy, including data collection, data assessment and data cleaning, and finally model estimation, interpretation, and conclusion—the so-called *data mining*⁶⁸. The interested reader is referred to [168, 169].

⁶⁸ A more general approach is given by the cross-industry standard process for data mining (CRISP-DM) [167], which will not be of further concern here.

7.1 Data Quality

The basis of a well-founded data analysis is reliable raw measurement data. It is not important that the data is free of errors from the very beginning, but that the overall scatter can be explained as far as possible from the documented metadata. For example, defective pixels on the detector or, as explained in Sec. 3.4, the fluctuation of the electron excitation bulb on the target inevitably lead to blurring in the system. Events which are recorded in log files but are only stored and are not included in any automatic or manual evaluation can be problematic.

Most modern measurement devices are equipped with an automatic capturing of the current status of hardware and software components, usually called *logging*. These log files are stored on the system and in most cases are only read out when an acute error occurs. This is the most obvious application but often leaves out a much more important aspect. The real potential of such log files is the statistical analysis of the numerous entries. To do this, the log file has to be passed through line by line and separated into logical units, in most cases strings, which is called *parsing*. These strings can be grouped afterwards to be analysed statistically. The referring parsing tool was programmed in C# within the .NET framework, the related graphical user interface and the code-snippets can be found in Appendix 10.6. Doing such an analysis in regular intervals, enables one to look for developments that may cause problems in the future. This forward-thinking method is referred to as *predictive maintenance*. Certainly, the little program is only the first step. Predictive maintenance is not just the collection and evaluation of data, but involves extensive analysis and, above all, the creation of prediction models, some of which are quite complex.

7.2 Data Availability

Storing the data in a reasonable way is a crucial step. Storing all of the data is in most cases possible but not necessarily the best solution. Careful data management is very important but often neglected due to the high time effort. Besides the *local* data management, a *global* perspective is increasingly important for interconnected scientific work. Providing the data to other working groups is essential to solve today's challenges in an efficient and reasonable way. The next short sections cannot cover this topic in total but will provide some information on how the data is handled in the referring publications.

7.2.1 Tomographic Datasets

The tomographic datasets consist of a raw datafile in a Zeiss proprietary format (32 bit, **.txrm*), which holds all relevant metadata. These files are stored on a local backup-secured filesystem. Because this datatype is not easily accessible by third party software, the reconstructed image stack (16 bit, **.tif*) together with relevant metadata is uploaded to an online open access repository and archive of the TU Dresden and TU Bergakademie Freiberg, called *OpARA*. Here, the related datasets get a digital object identifier (DOI) and can so be referenced within the related publications and can also be used as a direct database link, as it is realized within the particle database *PARROT*, see **Paper E**, which will be discussed in the following section.

7.2.2 Particle Database

The focus of this thesis is the generation of particle–discrete tomographic data. Storing this data within an open access database allows the provision of filtered datasets worldwide. Not only for correlating the data, but also to develop and evaluate own image processing workflows and use the 3D datasets as a starting point for process modelling purposes, to name just one possible example here. Sharing such datasets gives other researchers the chance to reuse the data without the need for appropriate measurement equipment and resources.

The structure of this database in pilot stage is described in detail in **Paper E**. Six particle systems with relevant measures and 3D representations are stored within this database. Additionally, there are three use cases presented which show possible applications of particle–discrete datasets, from 3D particle analysis, statistical analysis and multivariate parametric modelling, and numerical process modelling. Based on a relational model, the database can easily be supplemented with additional information by inserting new columns in existing tables, or by creating new tables, with proper primary keys for joining. Note that with this concept it is also possible to supplement data to existing datasets or to link other databases as well.

Like the DOI from the OpARA system is used as a unique identifier for the tomographic dataset, also other unique keys could easily be utilized. The main work lies in defining and maintaining the interfaces. Depending on the type, number and amount of measurement data, this can take a lot of time. For this reason, among others, the number of data sets and parameters was deliberately limited in the pilot phase. The interfaces are based on manually created and automatically exported text files. If the structure of these interface files is retained, they can be converted to automatic filling in a later phase. Further details on implementation, scalability, maintenance and performance can be found in **Paper E** and the corresponding supplementary material.

Note that, with the current database design, it would also be possible to include single high–resolution particle information. Fig. 7.2 shows reconstructed sections of three different dolomite particles, which are embedded in epoxy resin.

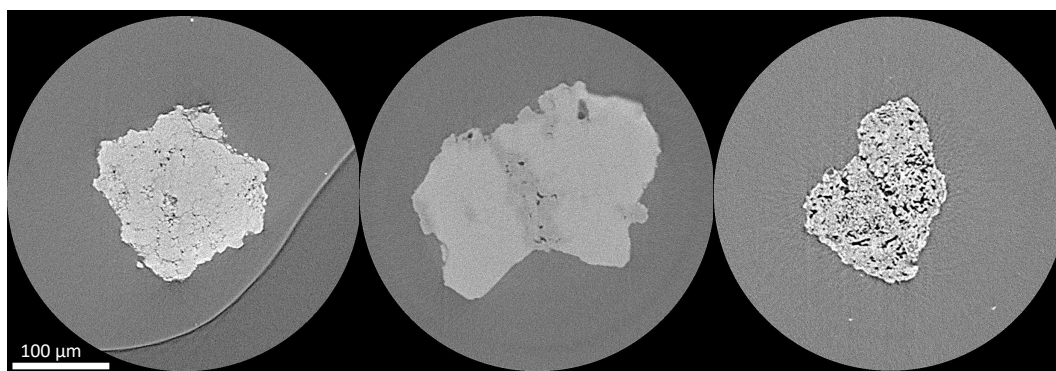


Figure 7.2: Exemplary sections from three different dolomite particles embedded in epoxy resin with various internal structures. Note that the particle on the left is located at the phase boundary to the air, which is clearly marked by a line.

Considering that these are particles of the same type of rock⁶⁹, the potential in terms of revealing the internal structure becomes apparent. For example, the proportion of different phases, the crack or pore size distribution could be of interest.

⁶⁹ Dolomite is a carbonate rock mainly consisting of $\text{CaMg}(\text{CO}_3)_2$.

8 Outlook on Further Research Activities

As already shown in Fig. 1.2 of the Outline Sec. 1, the next challenge is the extension of the methodology towards multiphase particle samples in three dimensions. Note that the following workflow combines state-of-the-art measuring devices and is thus most likely a reasonable approach for laboratories with already existing equipment. Another approach is to build new equipment. This can be done either by using established methods, like it is done by Boone et al. [170] with a combination of CT and X-ray fluorescence (XRF), or by using new techniques, like it is done by Godinho et al. [171] with a combination of a polychromatic X-ray source with a multichannel detector⁷⁰, a so-called *spectral CT*. These other approaches should be not of further concern here.

The adaption of the wax sample preparation method, which is presented in **Paper A**, by using a combination of epoxy resin with nano graphite spacer particles, see **Paper C**, makes the application of the high-energy particle radiation required for elemental analysis possible at all. Fig. 8.1 shows an exemplary workflow.

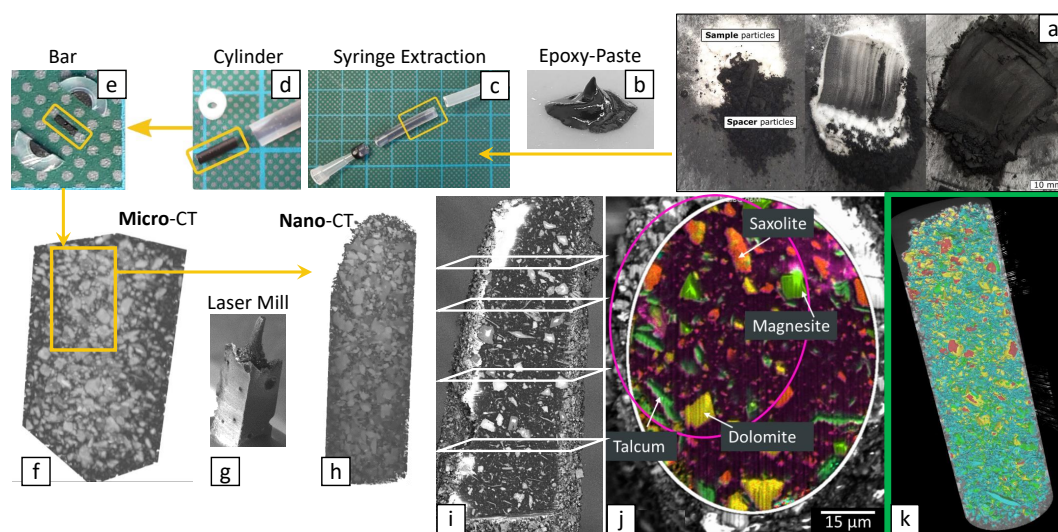


Figure 8.1: X-ray tomographic workflow for element-specific analysis with (a) adapted sample preparation method [3] generating (b) an epoxy paste that (c) can be extracted with a syringe to (d) form a cylinder sample. (e) Cut to a bar, the sample can (f) be captured in high-resolution mode with the micro-CT. A (g) laser mill is used to generate a sample cylinder suitable for (h) nano-CT measurement and (i) correlated measurements on sections in different heights with the FIB-SEM, which are able to (j) identify different mineral phases, indicated by different colours, (k) to map the whole 3D volume. Note that this figure is based on a presentation at ECCE/ECAB 2021 [11] and M&M 2021 [12]

Here, a mixture of two mineralogical phases, Saxolite (CaCO_3) and Talc (magnesia derivatives, such as Dolomite, Magnesite and Talcum), with comparable size and density, are classified by a combination of a deflector wheel classifier and an electrostatic separator using the different triboelectric charging properties of the two materials.

⁷⁰ With a multichannel detector it is possible to determine the X-ray photon energy within fixed bins, for example 128 [171]. The analysis of the resulting energy spectrum allows the identification of transmission changes at defined energies, which are specific of each element.

Since the X-ray absorption contrast, both of the polychromatic radiation of the micro-CT and of the nearly monochromatic radiation of the nano-CT⁷¹, as described in Sec. 3.2 and Sec. 3.3, cannot be used directly for material identification. The multi-scale workflow presented in **Paper D** has to be supplemented by (correlated with) a destructive measurement technique, in this example focused ion beam (FIB), which is able to slice the sample very precisely to create a defined surface for techniques for elemental identification. In other words, this technique is an extension of the 2D MLA, which is working on polished sections, into high-resolution 3D.

In the FIB process, ions are accelerated in a defined manner, directed with high kinetic energy onto a surface and lead to local ablation of the sample. The SEM, which is connected and works in parallel, provides the image data for the respective section plane. Additional detectors, such as electron backscatter diffraction (EBSD) and energy-dispersive X-ray spectroscopy (EDXS), can be used for the acquisition of local chemical information. Where classical etching and sputtering methods remove material in the micrometer range, the FIB delivers much more precise results and is able to work in the range of several atomic layers. The distances between the cutting planes are in the range of the local two-dimensional resolution and thus enable a vertical voxel dimension of 100 nm to 10 nm. However, due to the long scan time of a high-resolution SEM image, the creation of a larger 3D volume, a stack of a multiple of such images, is not practical and has to be replaced by the analysis of representative sections as it has already been published for a combination of micro-CT and representative sections from MLA by Furat et al. [9]. Nonetheless, FIB nano tomography not only makes element identification possible, but also closes the gap between nano-CT and the atomic resolution of the transmission electron microscopy (TEM) [173, 174].

Before applying the high-resolution measurements, the sample diameter, the same size as in **Paper D**, has to be further reduced, now with a laser mill⁷² to a cylinder, see Fig. 8.1-g, which, as discussed in Sec. 4.1, is an ideal shape for the nano-CT, see Fig. 8.1-h. After the 3D capturing, the focused ion beam (FIB) is used to perform a vertical cut that allows the identification of the height for a suitable horizontal cut, see Fig. 8.1-i, for a following scanning electron microscopy (SEM) analysis [176]. After the measurement, the additional element-specific data has to be correlated with the existing data set to create a 3D volume of combined particle-discrete and mineral-discrete⁷³ information. In the presented workflow, this is realized by using parametric copulas, see also Sec. 2.3 and the already published work by Furat et al. [68].

First results of this ongoing work were already presented at the *ECCE/ECAB 2021–13th European Congress of Chemical Engineering and 6th European Congress of Applied Biotechnology* by Ditscherlein et al. [11] and at *Microscopy & Microanalysis 2021* by Englisch et al. [12] and will be published soon.

As the discussion of this thesis in combination with the referenced publications has hopefully shown, X-ray computed tomography offers an immense potential to complement existing established measurement methods of particle characterisation or makes some approaches possible in the first place. Due to the constant further development of hardware, especially X-ray sources and detector sensors, and software, especially reconstruction algorithms, we are certainly only at the beginning here.

⁷¹ A detailed introduction to the specifics of nano-CT imaging are beyond the scope of this work. Some details can be found in the materials and methods section of **Paper D** and its supplementary, where the measurement setups of both, micro-CT and nano-CT, are compared with each other. In this study a Zeiss Xradia 810 Ultra was used. The interested reader is also referred to a summary of nano-CT technology by Withers [172].

⁷² Laser milling, also called laser ablation, uses a well-defined monochromatic laser beam for direct layer-by-layer material removal that is performed by a CNC machine [175]. Due to the laser beam's shape, the resulting cylinder is slightly conical, which is no problem for the measurement principles used here.

⁷³ Note that this information can also be interpreted as an extension of the property vector of the particle-discrete information.

Bibliography

- [1] R. Ditscherlein, T. Leißner, and U. A. Peuker. Preparation techniques for micron-sized particulate samples in X-ray microtomography. *Powder Technology*, 360:989–997, jun 2019. doi: 10.1016/j.powtec.2019.06.001.
- [2] R. Ditscherlein, T. Leißner, and U. A. Peuker. Self-constructed automated syringe for preparation of micron-sized particulate samples in X-ray microtomography. *MethodsX*, jan 2020. doi: 10.1016/j.mex.2019.11.030.
- [3] R. Ditscherlein, T. Leißner, and U. A. Peuker. Preparation strategy for statistically significant micrometer-sized particle systems suitable for correlative 3D imaging workflows on the example of X-ray microtomography. *Powder Technology*, 395: 235–242, jan 2022. doi: 10.1016/j.powtec.2021.09.038.
- [4] R. Ditscherlein, O. Furat, M. de Langlard, J. Martins de Souza e Silva, J. Sygusch, M. Rudolph, T. Leißner, V. Schmidt, and U. A. Peuker. Multiscale tomographic analysis for micron-sized particulate samples. *Microscopy and Microanalysis*, 26(4):676–688, jul 2020. doi: 10.1017/s1431927620001737.
- [5] R. Ditscherlein, O. Furat, E. Löwer, R. Mehnert, R. Trunk, T. Leißner, M. J. Krause, V. Schmidt, and U. A. Peuker. PARROT: A pilot study on the open access provision of particle-discrete tomographic datasets. *Microscopy and Microanalysis*, page 1–11, 2022. doi: 10.1017/S143192762101391X.
- [6] R. Wagner, M. Seleznev, H. Fischer, R. Ditscherlein, H. Becker, B. G. Dietrich, A. Keßler, T. Leißner, G. Wolf, A. Leineweber, U. A. Peuker, H. Biermann, and A. Weidner. Impact of melt conditioning and filtration on iron-rich β phase in AlSi9Cu3 and its fatigue life studied by μ CT. *Materials Characterization*, 174:111039, apr 2021. doi: 10.1016/j.matchar.2021.111039.
- [7] D. Hoppach, E. Werzner, C. Demuth, E. Löwer, H. Lehmann, L. Ditscherlein, R. Ditscherlein, U. A. Peuker, and S. Ray. Experimental investigations of the depth filtration inside open-cell foam filters supported by high-resolution computed tomography scanning and pore-scale numerical simulations. *Advanced Engineering Materials*, page 1900761, oct 2019. doi: 10.1002/adem.201900761.
- [8] T. Leißner, A. Diener, E. Löwer, R. Ditscherlein, K. Krüger, A. Kwade, and U. A. Peuker. 3D ex-situ and in-situ X-ray CT process studies in particle technology—A perspective. *Advanced Powder Technology*, oct 2019. doi: 10.1016/j.apt.2019.09.038.
- [9] O. Furat, T. Leißner, R. Ditscherlein, O. Šedivý, M. Weber, K. Bachmann, J. Gutzmer, U. A. Peuker, and V. Schmidt. Description of ore particles from X-ray microtomography (XMT) images, supported by scanning electron microscope (SEM)-based image analysis. *Microscopy and Microanalysis*, 24(5):461–470, oct 2018. doi: 10.1017/s1431927618015076.
- [10] C. Voigt, J. Hubáľková, L. Ditscherlein, R. Ditscherlein, U. A. Peuker, H. Giesche, and C. G. Aneziris. Characterization of reticulated ceramic foams with mercury intrusion porosimetry and mercury probe atomic force microscopy. *Ceramics International*, 44 (18):22963 – 22975, 2018. doi: 10.1016/j.ceramint.2018.09.094.
- [11] R. Ditscherlein, S. Englisch, O. Furat, L. Hansen, A. Weber, T. Leißner, V. Schmidt, E. Spiecker, and U. A. Peuker. Correlative measurement and multidimensional characterization of fine particle systems. In *ECCE/ECAB 2021 – 13th European Congress of Chemical Engineering and 6th European Congress of Applied Biotechnology*, September 2021.
- [12] S. Englisch, R. Ditscherlein, O. Furat, L. Hansen, D. Drobek, J. Wirth, S. Carl, T. Leissner, B. A. Zubiri, A. Weber, V. Schmidt, U. A. Peuker, and E. Spiecker. Comprehensive, multidimensional and correlative particle characterization of a saxolite and talcum compound to support the understanding of complex separation processes. In *Microscopy & Microanalysis*, August 2021.
- [13] J. Schreier, R. Ditscherlein, T. Leißner, U. A. Peuker, and U. Bröckel. Mikroröntgentomographie zur Charakterisierung des Trennerfolgs bei der mehrdimensionalen formselektiven Umbenetzungsagglomeration. In *Online Jahrestreffen der ProcessNet-Fachgruppen Mechanische Flüssigkeitsabtrennung, Zerkleinern und Klassieren sowie Agglomerations- und Schüttguttechnik*, March 2021.
- [14] R. Wagner, A. Weidner, M. Seleznev, H. Fischer, H. Biermann, R. Ditscherlein, T. Leissner, U. A. Peuker, B. Dietrich, A. Kessler, and G. Wolf. μ CT-Untersuchungen zum Einfluss einer Schmelzekonditionierung und -filtration auf die eisenreiche β -Phase in AlSi9Cu3 und deren Ermüdungsverhalten. In *38. Vortrags- und Diskussionstagung Werkstoffprüfung*, December 2020.
- [15] R. Ditscherlein, O. Furat, M. de Langlard, J. Martins de Souza e Silva, J. Sygusch, M. Rudolph, T. Leißner, V. Schmidt, and U. A. Peuker. Multi-Skalen Ansatz für die röntgentomographische Analyse partikulärer Proben im Bereich kleiner 10 μ m. In *Hybrides Jahrestreffen der ProcessNet-Fachgruppe Partikelmesstechnik und des Arbeitsausschusses Feinstäube*, March 2020.
- [16] R. Ditscherlein, T. Leissner, O. Furat, J. Martins de Souza e Silva, J. Sygusch, M. Rudolph, V. Schmidt, and U. A. Peuker. Multi-scale particle analysis. In *ZEISS XEN 7th X-ray microscopy european network user workshop*, January 2019.
- [17] R. Ditscherlein, T. Leissner, O. Furat, V. Schmidt, and U. A. Peuker. Segmentation-optimized preparation method for particulate samples in micro-CT analysis. In *International Congress on Particle Technology-PARTEC*, April 2019.
- [18] J. Baruchel, J.-Y. Buffiere, E. Maire, P. Merle, and

- G. Peix. *X-Ray Tomography in Material Science*. Hermes Science Publications, 2000. ISBN 2-7462-0115-1.
- [19] S. R. Stock. Recent advances in X-ray microtomography applied to materials. *International Materials Reviews*, 53(3):129–181, may 2008. doi: 10.1179/174328008x277803.
- [20] R. Mizutani and Y. Suzuki. X-ray microtomography in biology. *Micron*, 43(2–3):104–115, feb 2012. doi: 10.1016/j.micron.2011.10.002.
- [21] D. Wildenschild, C. M. P. Vaz, M. L. Rivers, D. Rikard, and B. S. B. Christensen. Using X-ray computed tomography in hydrology: Systems, resolutions, and limitations. *Journal of Hydrology*, 267(3–4):285–297, oct 2002. doi: 10.1016/S0022-1694(02)00157-9.
- [22] R. A. Ketcham and W. D. Carlson. Acquisition, optimization and interpretation of X-ray computed tomographic imagery: Applications to the geosciences. *Computers and Geosciences*, 27(4):381–400, 2001. doi: 10.1016/S0098-3004(00)00116-3.
- [23] D. J. Brown, G. T. Vickers, A. P. Collier, and G. K. Reynolds. Measurement of the size, shape and orientation of convex bodies. *Chemical Engineering Science*, 60(1):289–292, jan 2005. doi: 10.1016/j.ces.2004.07.056.
- [24] E. Zschech, W. Yun, and G. Schneider. High-resolution X-ray imaging—a powerful nondestructive technique for applications in semiconductor industry. *Applied Physics A*, 92(3):423–429, may 2008. doi: 10.1007/s00339-008-4551-x.
- [25] C. L. Lin, J. D. Miller, and A. Cortes. Applications of X-ray computed tomography in particulate systems. *KONA Powder and Particle Journal*, 10(0):88–95, 1992. doi: 10.14356/kona.1992013.
- [26] J. D. Miller, C. L. Lin, and A. B. Cortes. A review of X-ray computed tomography and its applications in mineral processing. *Mineral Processing and Extractive Metallurgy Review*, 7(1):1–18, mar 1990. doi: 10.1080/08827509008952663.
- [27] J. D. Miller and C. L. Lin. Treatment of polished section data for detailed liberation analysis. *International Journal of Mineral Processing*, 22(1–4):41–58, apr 1988. doi: 10.1016/0301-7516(88)90055-5.
- [28] S. T. Erdoğan, E. T. Garboczi, and D. W. Fowler. Shape and size of microfine aggregates: X-ray microcomputed tomography vs. laser diffraction. *Powder Technology*, 177(2):53–63, aug 2007. doi: 10.1016/j.powtec.2007.02.016.
- [29] J. E. Spowart. Automated serial sectioning for 3-D analysis of microstructures. *Scripta Materialia*, 55(1):5–10, jul 2006. doi: 10.1016/j.scriptamat.2006.01.019.
- [30] T. L. Burnett, R. Kelley, B. Winiarski, L. Contreras, M. Daly, A. Gholinia, M. G. Burke, and P. J. Withers. Large volume serial section tomography by Xe plasma FIB dual beam microscopy. *Ultramicroscopy*, 161:119–129, feb 2016. doi: 10.1016/j.ultramicro.2015.11.001.
- [31] J. D. Miller, C.-L. Lin, L. Hupka, and M. I. Al-Wakeel. Liberation-limited grade/recovery curves from X-ray micro CT analysis of feed material for the evaluation of separation efficiency. *International Journal of Mineral Processing*, 93(1):48–53, 2009. doi: 10.1016/j.minpro.2009.05.009.
- [32] S. L. Gay and R. D. Morrison. Using two dimensional sectional distributions to infer three dimensional volumetric distributions—validation using tomography. *Particle & Particle Systems Characterization*, 23(3–4):246–253, oct 2006. doi: 10.1002/ppsc.200601056.
- [33] W.-A. Kahl, N. Dilissen, K. Hidas, C. J. Garrido, V. Vizcaino, and M. J. Román-Alpiste. 3-D microstructure of olivine in complex geological materials reconstructed by correlative X-ray micro-CT and EBSD analysis. *Journal of Microscopy*, 268(2):193–207, jul 2017. doi: 10.1111/jmi.12598.
- [34] T. Ueda, T. Oki, and S. Koyanaka. Experimental analysis of mineral liberation and stereological bias based on X-ray computed tomography and artificial binary particles. *Advanced Powder Technology*, 29(3):462–470, mar 2018. doi: 10.1016/j.appt.2017.11.004.
- [35] T. Heinig, K. Bachmann, R. Tolosana-Delgado, G. van den Boogaart, and J. Gutzmer. Monitoring gravitational and particle shape settling effects on MLA sample preparation. In *IAMG Conference, Freiberg, Germany*, September 2015.
- [36] R. Cepuritis, E. J. Garboczi, S. Jacobsen, and K. A. Snyder. Comparison of 2-D and 3-D shape analysis of concrete aggregate fines from VSI crushing. *Powder Technology*, 309:110–125, mar 2017. doi: 10.1016/j.powtec.2016.12.037.
- [37] O. Macho, J. Kabát, L. Gabrišová, P. Peciar, M. Juriga, R. Fekete, P. Galbavá, J. Blaško, and M. Peciar. Dimensionless criteria as a tool for creation of a model for predicting the size of granules in high-shear granulation. *Particulate Science and Technology*, 38(3):381–390, jan 2019. doi: 10.1080/02726351.2018.1548531.
- [38] M. Buchmann, E. Schach, R. Tolosana-Delgado, T. Leifšner, J. Astoveza, M. Kern, R. Möckel, D. Ebert, M. Rudolph, G. van den Boogaart, and U. A. Peuker. Evaluation of magnetic separation efficiency on a cassiterite-bearing skarn ore by means of integrative SEM-based image and XRF-XRD data analysis. *Minerals*, 8(9):390, sep 2018. doi: 10.3390/min8090390.
- [39] C. L. Evans, E. M. Wightman, and X. Yuan. Quantifying mineral grain size distributions for process modelling using X-ray micro-tomography. *Minerals Engineering*, 82:78–83, oct 2015. doi: 10.1016/j.mineng.2015.03.026.
- [40] J. D. Miller and C. L. Lin. X-ray tomography for mineral processing technology 3D particle characterization from mine to mill. *Minerals & Metallurgical Processing*, 35(1):1–12, feb 2018. doi: 10.19150/mmp.8052.
- [41] T. Lowe, R. S. Bradley, S. Yue, K. Barii, J. Gelb, N. Rohbeck, J. Turner, and P. J. Withers. Microstructural analysis of TRISO particles using multi-scale X-ray computed tomography. *Journal of Nuclear Materials*, 461:29–36, jun 2015. doi: 10.1016/j.jnucmat.2015.02.034.
- [42] D. Garcia, C. L. Lin, and J. D. Miller. Quantitative analysis of grain boundary fracture in the breakage of single multiphase particles using X-ray microtomography procedures. *Minerals Engineering*, 22(3):236–243, 2009. doi: 10.1016/j.mineng.2008.07.005.
- [43] Y. Ghorbani, M. Becker, J. Petersen, S. H. Morar, A. Mainza, and J.-P. Franzidis. Use of X-ray computed tomography to investigate crack distribution and mineral dissemination in sphalerite ore particles. *Minerals Engineering*, 24(12):1249–1257, oct 2011. doi: 10.1016/j.mineng.2011.04.008.
- [44] G. Bagheri and C. Bonadonna. On the drag

- of freely falling non-spherical particles. *Powder Technology*, 301:526–544, nov 2016. doi: 10.1016/j.powtec.2016.06.015.
- [45] Y. Liu, F. Gong, Z. You, and H. Wang. Aggregate morphological characterization with 3D optical scanner versus X-ray computed tomography. *Journal of Materials in Civil Engineering*, 30(1):04017248, jan 2018. doi: 10.1061/(asce)mt.1943-5533.0002091.
- [46] A. Marmottant, L. Salvo, C. L. Martin, and A. Mortensen. Coordination measurements in compacted NaCl irregular powders using X-ray microtomography. *Journal of the European Ceramic Society*, 28(13):2441–2449, sep 2008. doi: 10.1016/j.jeurceramsoc.2008.03.041.
- [47] E. Löwer, T. H. Pham, T. Leißner, and U. A. Peuker. Study on the influence of solids volume fraction on filter cake structures using micro tomography. *Powder Technology*, 363:286–299, mar 2020. doi: 10.1016/j.powtec.2019.12.054.
- [48] E. J. Garboczi, K. A. Riding, and M. Mirzahassemi. Particle shape effects on particle size measurement for crushed waste glass. *Advanced Powder Technology*, 28(2):648–657, feb 2017. doi: 10.1016/j.apt.2016.12.002.
- [49] E. J. Garboczi. Three-dimensional mathematical analysis of particle shape using X-ray tomography and spherical harmonics: Application to aggregates used in concrete. *Cement and Concrete Research*, 32(10):1621–1638, oct 2002. doi: 10.1016/S0008-8846(02)00836-0.
- [50] C. L. Lin and J. D. Miller. 3D characterization and analysis of particle shape using X-ray microtomography (XMT). *Powder Technology*, 154(1):61–69, jun 2005. doi: 10.1016/j.powtec.2005.04.031.
- [51] E. Masad, S. Saadeh, T. Al-Rousan, E. Garboczi, and D. Little. Computations of particle surface characteristics using optical and X-ray CT images. *Computational Materials Science*, 34(4):406–424, dec 2005. doi: 10.1016/j.commatsci.2005.01.010.
- [52] J. D. Orford and W. B. Whalley. The use of the fractal dimension to quantify the morphology of irregular-shaped particles. *Sedimentology*, 30(5):655–668, oct 1983. doi: 10.1111/j.1365-3091.1983.tb00700.x.
- [53] S. Arasan, S. Akbulut, and A. S. Hasiloglu. The relationship between the fractal dimension and shape properties of particles. *KSCE Journal of Civil Engineering*, 15(7):1219–1225, sep 2011. doi: 10.1007/s12205-011-1310-x.
- [54] E. J. Garboczi and J. W. Bullard. 3D analytical mathematical models of random star-shape particles via a combination of X-ray computed microtomography and spherical harmonic analysis. *Advanced Powder Technology*, 28(2):325–339, feb 2017. doi: 10.1016/j.apt.2016.10.014.
- [55] D. Su and W. M. Yan. 3D characterization of general-shape sand particles using microfocus X-ray computed tomography and spherical harmonic functions, and particle regeneration using multivariate random vector. *Powder Technology*, 323:8–23, jan 2018. doi: 10.1016/j.powtec.2017.09.030.
- [56] F. J. Anscombe. Graphs in statistical analysis. *The American Statistician*, 27(1):17–21, feb 1973. doi: 10.1080/00031305.1973.10478966.
- [57] B. W. Silverman. *Density Estimation for Statistics and Data Analysis*. Chapman & Hall/CRC Monographs on Statistics & Applied Probability. Taylor & Francis, 1986. ISBN 9780412246203.
- [58] D. W. Scott. *Multivariate Density Estimation*. Wiley, aug 1992. doi: 10.1002/9780470316849.
- [59] E. Schach, M. Buchmann, R. Tolosana-Delgado, T. Leißner, M. Kern, G. van den Boogaart, M. Rudolph, and U. A. Peuker. Multidimensional characterization of separation processes—Part 1: Introducing kernel methods and entropy in the context of mineral processing using SEM-based image analysis. *Minerals Engineering*, 137:78–86, jun 2019. doi: 10.1016/j.mineng.2019.03.026.
- [60] P. Hall, S. J. Sheather, M. C. Jones, and J. S. Marron. On optimal data-based bandwidth selection in kernel density estimation. *Biometrika*, 78(2):263–269, 1991. doi: 10.1093/biomet/78.2.263.
- [61] M. Buchmann, E. Schach, T. Leißner, M. Kern, T. Mütze, M. Rudolph, U. A. Peuker, and R. Tolosana-Delgado. Multidimensional characterization of separation processes—Part 2: Comparability of separation efficiency. *Minerals Engineering*, 150:106284, may 2020. doi: 10.1016/j.mineng.2020.106284.
- [62] R. Bellman and E. S. Page. In *Adaptive Control Processes: A Guided Tour.*, 1961. doi: 10.1515/9781400874668.
- [63] M. Di Marzio and G. Lafratta. Reducing dimensionality effects on kernel density estimation: The bivariate gaussian case. In *Classification and Data Analysis*, pages 287–294. Springer, 1999. ISBN 978-3-642-60126-2. doi: 10.1007/978-3-642-60126-2_36.
- [64] B. Efron and R. J. Tibshirani. *An Introduction to the Bootstrap*. Chapman and Hall/CRC, may 1994. doi: 10.1201/9780429246593.
- [65] R. B. Nelsen. *An Introduction to Copulas*. Springer, 2006. ISBN 978-0-387-28678-5.
- [66] Harry Joe. *Dependence Modeling with Copulas*. CRC Press, 2014.
- [67] Fabrizio Durante and Carlo Sempi. *Principles of Copula Theory*. Chapman and Hall/CRC, 2015.
- [68] O. Furat, T. Leißner, K. Bachmann, J. Gutzmer, U. A. Peuker, and V. Schmidt. Stochastic modeling of multidimensional particle properties using parametric copulas. *Microscopy and Microanalysis*, 25(3):720–734, apr 2019. doi: 10.1017/s1431927619000321.
- [69] Rico Fischer. *Modellierung von Abhängigkeiten mit Hilfe von Copulas: Anwendung bei der Bestimmung des Value at Risk*. Logos-Verlag, Berlin, February 2009. ISBN 3832521429.
- [70] J. Radon. Über die Bestimmung von Funktionen durch ihre Integralwerte längs gewisser Mannigfaltigkeiten. In *Berichte über die Verhandlungen der Königlich Sächsischen Gesellschaft der Wissenschaften zu Leipzig*, volume Mathematisch-Physische Klasse 69, pages 262–277, 1917.
- [71] G. Hounsfield. Computerized transverse axial tomography. *British Journal of Radiology*, 46(542):148–149, dec 1973. doi: 10.1259/0007-1285-46-552-1016.
- [72] J. Vega, U. Diaz, G. B. Castrom, J. J. San Martin Luque, V. Corbalan, and P. Chimeno Herrero. Sir Godfrey Hounsfield and the history of computer tomography. In *European Society of Radiology 2017*, 2017.
- [73] G. Hounsfield. *Computed medical imaging*. In *Noble Lecture*, Londong, England, 1979. Medical Systems Department of Central Research Laboratories EMI.

- [74] T. M. Buzug. *Computed tomography from photon statistics to modern cone-beam CT*. Springer, Germany, 2008. doi: 10.1007/978-3-540-39408-2.
- [75] I. Han, L. Demir, and M. Şahin. Determination of mass attenuation coefficients, effective atomic and electron numbers for some natural minerals. *Radiation Physics and Chemistry*, 78(9):760–764, sep 2009. doi: 10.1016/j.radphyschem.2009.03.077.
- [76] C. T. Chantler. Detailed tabulation of atomic form factors, photoelectric absorption and scattering cross section, and mass attenuation coefficients in the vicinity of absorption edges in the soft X-ray ($Z=30\text{--}36, Z=60\text{--}89, E=0.1\text{--}10$ keV)—addressing convergence issues of earlier work. *Journal of Synchrotron Radiation*, 8(4):1124–1124, jun 2001. doi: 10.1107/s0909049501008305.
- [77] G. V. Pavlinsky. *Fundamentals of X-ray Physics*. Cambridge International Science Publishing, 2008. ISBN 1904602649.
- [78] P. Russo. *Handbook of X-ray Imaging*. CRC Press, 2018. ISBN 9781498741521.
- [79] P. M. Jenneson, R. D. Luggar, E. J. Morton, O. Gundogdu, and U. Tüzün. Examining nanoparticle assemblies using high spatial resolution X-ray microtomography. *Journal of Applied Physics*, 96(5):2889–2894, 2004. doi: 10.1063/1.1776635.
- [80] Y. Zhang, P. Mostaghimi, and R. T. Armstrong. On the challenges of grayscale-based quantifications using X-ray computed microtomography. *Journal of Microscopy*, may 2019. doi: 10.1111/jmi.12805.
- [81] C. K. Egan, S. D. M. Jacques, M. D. Wilson, M. C. Veale, P. Seller, A. M. Beale, R. A. D. Patrick, P. J. Withers, and R. J. Cernik. 3D chemical imaging in the laboratory by hyperspectral X-ray computed tomography. *Scientific Reports*, 5(1), oct 2015. doi: 10.1038/srep15979.
- [82] M. L. Hill, J. G. Mainprize, G. E. Mawdsley, and M. J. Yaffe. A solid iodinated phantom material for use in tomographic X-ray imaging. *Medical Physics*, 36(10):4409–4420, 2009. doi: 10.1118/1.3213516.
- [83] W. Ludwig, A. King, P. Reischig, M. Herbig, E. M. Lauridsen, S. Schmidt, H. Proudhon, S. Forest, P. Cloetens, S. R. du Roscoat, J. Y. Buffière, T. J. Marrow, and H. F. Poulsen. New opportunities for 3D materials science of polycrystalline materials at the micrometre lengthscale by combined use of X-ray diffraction and X-ray imaging. *Materials Science and Engineering: A*, 524(1–2):69–76, oct 2009. doi: 10.1016/j.msea.2009.04.009.
- [84] R. Ditscherlein. This radiograph is actually my own teeth.
- [85] M. Nikl. Scintillation detectors for X-rays. *Measurement Science and Technology*, 17(4):R37–R54, feb 2006. doi: 10.1088/0957-0233/17/4/r01.
- [86] T. Martin, A. Koch, and M. Nikl. Scintillator materials for X-ray detectors and beam monitors. *MRS Bulletin*, 42(06):451–457, jun 2017. doi: 10.1557/mrs.2017.116.
- [87] R. A. Crowther, D. J. DeRosier, and A. Klug. The reconstruction of a three-dimensional structure from projections and its application to electron microscopy. *Proceedings of the Royal Society of London. A. Mathematical and Physical Sciences*, 317(1530):319–340, jun 1970. doi: 10.1098/rspa.1970.0119.
- [88] A. Kyrieleis, V. Titarenko, M. Ibson, T. Connolley, and P. J. Withers. Region-of-interest tomography using filtered backprojection: Assessing the practical limits. *Journal of Microscopy*, 241(1):69–82, dec 2010. doi: 10.1111/j.1365-2818.2010.03408.x.
- [89] P. J. La Riviere and D. M. Billmire. Reduction of noise-induced streak artifacts in X-ray computed tomography through spline-based penalized-likelihood sinogram smoothing. *IEEE Transactions on Medical Imaging*, 24(1):105–111, jan 2005. doi: 10.1109/tmi.2004.838324.
- [90] B. R. Pauw. Live Fourier Transformation Program (<https://lookingatnothing.com>). Technical report, BAM Federal Institute for Materials Research and Testing, 2014.
- [91] X. Pan, E. Y. Sidky, and M. Vannier. Why do commercial CT scanners still employ traditional, filtered back-projection for image reconstruction? *Inverse Problems*, 25(12):123009, dec 2009. doi: 10.1088/0266-5611/25/12/123009.
- [92] D. M. Pelt, D. Gürsoy, W. J. Palenstijn, J. Sibbers, F. De Carlo, and K. J. Batenburg. Integration of TomoPy and the ASTRA toolbox for advanced processing and reconstruction of tomographic synchrotron data. *Journal of Synchrotron Radiation*, 23(3):842–849, apr 2016. doi: 10.1107/s1600577516005658.
- [93] T. M. Buzug. *Einführung in die Computertomographie, Mathematisch-physikalische Grundlagen der Bildrekonstruktion*, volume 1. Springer, 2004.
- [94] D. T. Ginat and R. Gupta. Advances in computed tomography imaging technology. *Annual Review of Biomedical Engineering*, 16(1):431–453, jul 2014. doi: 10.1146/annurev-bioeng-121813-113601.
- [95] D. Wu, K. Kim, G. E. Fakhri, and Q. Li. Iterative low-dose CT reconstruction with priors trained by artificial neural network. *IEEE Transactions on Medical Imaging*, 36(12):2479–2486, dec 2017. doi: 10.1109/tmi.2017.2753138.
- [96] A. Katsumata, A. Hirukawa, S. Okumura, M. Naitoh, M. Fujishita, E. Arijii, and R. P. Langlais. Effects of image artifacts on gray-value density in limited-volume cone-beam computerized tomography. *Oral Surgery, Oral Medicine, Oral Pathology, Oral Radiology, and Endodontology*, 104(6):829–836, dec 2007. doi: 10.1016/j.tripleo.2006.12.005.
- [97] X. Xiao, F. De Carlo, and S. Stock. Practical error estimation in zoom-in and truncated tomography reconstructions. *Review of Scientific Instruments*, 78(6):063705, jun 2007. doi: 10.1063/1.2744224.
- [98] P. Parlanti, V. Cappello, F. Brun, G. Tromba, R. Rigolio, I. Tonazzini, M. Cecchini, V. Piazza, and M. Gemmi. Size and specimen-dependent strategy for X-ray micro-CT and TEM correlative analysis of nervous system samples. *Scientific Reports*, 7(1), jun 2017. doi: 10.1038/s41598-017-02998-1.
- [99] M. N. Boone, J. Vlassenbroeck, S. Peetermans, D. Van Loo, M. Dierick, and L. Van Hoorebeke. Secondary radiation in transmission-type X-ray tubes: Simulation, practical issues and solution in the context of X-ray microtomography. *Nuclear Instruments and Methods in Physics Research, Section A: Accelerators, Spectrometers, Detectors and Associated Equipment*, 661(1):7–12, jan 2012. doi: 10.1016/j.nima.2011.09.046.
- [100] P. L. Salmon, X. Liu, and A. Sasov. A post-scan method for correcting artefacts of slow geometry changes during micro-tomographic scans. *Journal of X-Ray Science and Technology*, 17(2):161–174, 2009. doi: 10.3233/XST-2009-0220. cited By 21.
- [101] G. Probst, B. Boeckmans, J.-P. Kruth, and

- W. Dewulf. Compensation of drift in an industrial computed tomography system. In *6th Conference on Industrial Computed Tomography*, 2016.
- [102] B. Wang, B. Pan, R. Tao, and G. Lubineau. Systematic errors in digital volume correlation due to the self-heating effect of a laboratory X-ray CT scanner. *Measurement Science and Technology*, 28(5):055402, mar 2017. doi: 10.1088/1361-6501/aa60ad.
- [103] N. Limodin, J. Réthoré, J. Adrien, J.-Y. Buffière, F. Hild, and S. Roux. Analysis and artifact correction for volume correlation measurements using tomographic images from a laboratory X-ray source. *Experimental Mechanics*, 51(6):959–970, aug 2010. doi: 10.1007/s11340-010-9397-4.
- [104] N. Fusi and J. Martinez-Martinez. Mercury porosimetry as a tool for improving quality of micro-CT images in low porosity carbonate rocks. *Engineering Geology*, 166:272–282, 2013. doi: 10.1016/j.enggeo.2013.10.002.
- [105] W. Dewulf, Y. Tan, and K. Kiekens. Sense and non-sense of beam hardening correction in CT metrology. *CIRP Annals*, 61(1):495–498, 2012. doi: 10.1016/j.cirp.2012.03.013.
- [106] E. Maire and P. J. Withers. Quantitative X-ray tomography. *International Materials Reviews*, 59(1):1–43, 2014. doi: 10.1179/1743280413Y.0000000023.
- [107] G. R. Davis and J. C. Elliott. Artefacts in X-ray microtomography of materials. *Materials Science and Technology*, 22(9):1011–1018, 2006. doi: 10.1179/174328406X114117.
- [108] F. E. Boas and D. Fleischmann. CT artifacts: Causes and reduction techniques. *Imaging in Medicine*, 4(2):229–240, 2012. doi: 10.2217/im.12.13.
- [109] Q. Zhang, Y.-C. Hu, F. Liu, K. Goodman, K. E. Rosenzweig, and G. S. Mageras. Correction of motion artifacts in cone-beam CT using a patient-specific respiratory motion model. *Medical Physics*, 37(6Part1):2901–2909, may 2010. doi: 10.1118/1.3397460.
- [110] J. F. Barrett and N. Keat. Artifacts in CT: Recognition and avoidance. *RadioGraphics*, 24(6):1679–1691, nov 2004. doi: 10.1148/rg.246045065.
- [111] P. Echlin. *Handbook of Sample Preparation for Scanning Electron Microscopy and X-Ray Microanalysis*. Springer, Cambridge Analytical Microscopy, UK, 2009. ISBN 978-0-387-85731-2.
- [112] R. Eslahpazir, M. Kupsta, Q. Liu, and D. G. Ivey. Sample preparation method for characterization of fine solids in athabasca oil sands by electron microscopy. *Energy & Fuels*, 25(11):5158–5164, nov 2011. doi: 10.1021/ef200994a.
- [113] Jeanne Ayache, Luc Beaunier, Jacqueline Boumendil, Gabrielle Ehret, and Danièle Laub. *Sample Preparation Handbook for Transmission Electron Microscopy*, volume Techniques. Springer, 2010.
- [114] J. I. Goldstein, D. E. Newbury, P. Echlin, D. C. Joy, C. E. Lyman, E. Lifshin, L. Sawyer, and J. R. Michael. *Specimen Preparation of Hard Materials: Metals, Ceramics, Rocks, Minerals, Microelectronics and Packed Devices, Particles and Fibres*, page 690. Springer, 3 edition, 2003. doi: 10.1007/978-1-4615-0215-9_11.
- [115] A. du Plessis, C. Broeckhoven, A. Guelpa, and S. G. le Roux. Laboratory X-ray micro-computed tomography: A user guideline for biological samples. *GigaScience*, 6(6), apr 2017. doi: 10.1093/gigascience/gix027.
- [116] K. E. B. Doncom, L. D. Blackman, D. B. Wright, M. I. Gibson, and R. K. O'Reilly. Dispersity effects in polymer self-assemblies: a matter of hierarchical control. *Chemical Society Reviews*, 46(14):4119–4134, 2017. doi: 10.1039/c6cs00818f.
- [117] G. A. Moore. Is quantitative metallography quantitative? In *Applications of Modern Metallographic Techniques*, pages 3–3–46. ASTM International, 1970. doi: 10.1520/stp32072s.
- [118] Z. P. Luo and J. H. Koo. Quantifying the dispersion of mixture microstructures. *Journal of Microscopy*, 225(2):118–125, feb 2007. doi: 10.1111/j.1365-2818.2007.01722.x.
- [119] M. Rudolph, K. Bauer, and U. A. Peuker. Phase-contrast atomic force microscopy for the characterization of the distribution of nanoparticles in composite materials. *Chemie Ingenieur Technik*, 82(12):2189–2195, nov 2010. doi: 10.1002/cite.201000090.
- [120] H. Nolte, C. Schilde, and A. Kwade. Determination of particle size distributions and the degree of dispersion in nanocomposites. *Composites Science and Technology*, 72(9):948–958, may 2012. doi: 10.1016/j.compscitech.2012.03.010.
- [121] A.-X. Wu, B.-H. Yang, Y. Xi, and H.-C. Jiang. Pore structure of ore granular media by computerized tomography image processing. *Journal of Central South University of Technology*, 14(2):220–224, 2007. doi: 10.1007/s11771-007-0074-5.
- [122] C. L. Lin and J. D. Miller. Network analysis of filter cake pore structure by high resolution X-ray microtomography. *Chemical Engineering Journal*, 77(1–2):79–86, 2000. doi: 10.1016/S1385-8947(99)00149-7.
- [123] M. Tuceryan and A. K. Jain. Texture segmentation using voronoi polygons. *IEEE Transactions on Pattern Analysis and Machine Intelligence*, 12(2):211–216, 1990. doi: 10.1109/34.44407.
- [124] A. Crouter and L. Briens. Methods to assess mixing of pharmaceutical powders. *AAPS PharmSciTech*, 20(2), jan 2019. doi: 10.1208/s12249-018-1286-7.
- [125] P. M. Gy. The sampling of particulate materials—A general theory. *International Journal of Mineral Processing*, 3(4):289–312, 1976. doi: 10.1016/0301-7516(76)90020-X.
- [126] P. M. Gy. *Practical Implementation of the Theoretical Results—Correct Selection*, volume 4, book section 22, page 29. Elsevier Scientific Publishing Company, 1979.
- [127] I. U. Bhuiyan, J. Mouzon, F. Forsberg, S. P. E. Forsmo, M. Sjö Dahl, and J. Hedlund. Consideration of X-ray microtomography to quantitatively determine the size distribution of bubble cavities in iron ore pellets. *Powder Technology*, 233:312–318, 2013. doi: 10.1016/j.powtec.2012.09.012.
- [128] F. Sondej, A. Bück, K. Koslowsky, P. Bachmann, M. Jacob, and E. Tsotsas. Investigation of coating layer morphology by micro-computed X-ray tomography. *Powder Technology*, 273:165–175, mar 2015. doi: 10.1016/j.powtec.2014.12.050.
- [129] A. R. Videla, C. L. Lin, and J. D. Miller. 3D characterization of individual multiphase particles in packed particle beds by X-ray microtomography (XMT). *International Journal of Mineral Processing*, 84(1–4):321–326, 2007. doi: 10.1016/j.minpro.2006.07.009.
- [130] J. Sittner, J. R. Da Assuncao Godinho, A. Renno,

- V. Cnudde, M. Boone, T. de Schryver, D. van Loo, M. Merkulova, A. Roine, and J. Liipo. Spectral x-ray computed micro tomography: 3-dimensional chemical imaging, oct 2020.
- [131] M. Alizadeh, A. Hassanpour, M. Pasha, M. Ghadiri, and A. Bayly. The effect of particle shape on predicted segregation in binary powder mixtures. *Powder Technology*, 319:313–322, sep 2017. doi: 10.1016/j.powtec.2017.06.059.
- [132] K. E. Thompson, C. S. Willson, and W. Zhang. Quantitative computer reconstruction of particulate materials from microtomography images. *Powder Technology*, 163(3):169–182, apr 2006. doi: 10.1016/j.powtec.2005.12.016.
- [133] L. Babout, K. Grudzień, J. JWiacek, M. Niedostatkiewicz, B. Karpiński, and M. Szkodo. Selection of material for X-ray tomography analysis and DEM simulations: comparison between granular materials of biological and non-biological origins. *Granular Matter*, 20(3), jun 2018. doi: 10.1007/s10035-018-0809-y.
- [134] R. Cepuritis, E. J. Garboczi, C. F. Ferraris, S. Jacobsen, and B. E. Sørensen. Measurement of particle size distribution and specific surface area for crushed concrete aggregate fines. *Advanced Powder Technology*, 28(3):706–720, mar 2017. doi: 10.1016/j.apt.2016.11.018.
- [135] X. Fu, M. Dutt, A. C. Bentham, B. C. Hancock, R. E. Cameron, and J. A. Elliott. Investigation of particle packing in model pharmaceutical powders using X-ray microtomography and discrete element method. *Powder Technology*, 167(3):134–140, sep 2006. doi: 10.1016/j.powtec.2006.06.011.
- [136] F. Bernier, R. Tahara, and M. Gendron. Additive manufacturing powder feedstock characterization using X-ray tomography. *Metal Powder Report*, 73(3):158–162, may 2018. doi: 10.1016/j.mprp.2018.01.002.
- [137] H. Masuda and K. Iinoya. Theoretical study of the scatter of experimental data due to particle-size-distribution. *Journal of Chemical Engineering of Japan*, 4(1):60–66, 1971. doi: 10.1252/jcej.4.60.
- [138] H. Masuda and K. Gotoh. Study on the sample size required for the estimation of mean particle diameter. *Advanced Powder Technology*, 10(2):159–173, jan 1999. doi: 10.1016/s0921-8831(08)60447-1.
- [139] M. W. Wedd. Procedure for predicting a minimum volume or mass of sample to provide a given size parameter precision. *Particle & Particle Systems Characterization*, 18(3):109, oct 2001. doi: 10.1002/1521-4117(200110)18:3<109::aid-ppsc109>3.0.co;2-b.
- [140] P. Kanovsky and R. Srinivasan. An approach to the construction of parametric confidence bands on cumulative distribution functions. *Biometrika*, 59(3):623–631, 1972. doi: 10.1093/biomet/59.3.623.
- [141] R. C. H. Cheng and T. C. Iles. Confidence bands for cumulative distribution functions of continuous random variables. *Technometrics*, 25(1):77–86, feb 1983. doi: 10.1080/00401706.1983.10487822.
- [142] S. Magkos, A. Kupsch, and G. Bruno. Suppression of cone-beam artefacts with direct iterative reconstruction computed tomography trajectories (DIRECTT). *Journal of Imaging*, 7(8):147, aug 2021. doi: 10.3390/jimaging7080147.
- [143] M. Santini, M. Guilizzoni, and S. Fest-Santini. X-ray computed microtomography for drop shape analysis and contact angle measurement. *Journal of Colloid and Interface Science*, 409:204–210, nov 2013. doi: 10.1016/j.jcis.2013.06.036.
- [144] J. Yoon, Y. G. Lee, K. Kim, and Y. G. Shin. An automated sinogram-space ring artifact reduction method in computed tomography. In *6th Conference on Industrial Computed Tomography*, Wels, Austria, 2016.
- [145] A. N. van Daatselaar, P. F. van der Stelt, and J. Weenen. Effect of number of projections on image quality of local CT. *Dentomaxillofacial Radiology*, 33(6):361–369, nov 2004. doi: 10.1259/dmfr/23496562.
- [146] J. T. L. Thong, K. S. Sim, and J. C. H. Phang. Single-image signal-to-noise ratio estimation. *Scanning*, 23(5):328–336, dec 2006. doi: 10.1002/sca.4950230506.
- [147] Z. A. Lomnicki and S. K. Zaremba. On the estimation of autocorrelation in time series. *The Annals of Mathematical Statistics*, 28(1):140–158, 1957. doi: 10.1214/aoms/1177707042.
- [148] P. Chen, Y. Han, and J. Pan. High-dynamic-range CT reconstruction based on varying tube-voltage imaging. *PLOS ONE*, 10(11):e0141789, nov 2015. doi: 10.1371/journal.pone.0141789.
- [149] S. Schlüter, A. Sheppard, K. Brown, and D. Wildenschild. Image processing of multiphase images obtained via X-ray microtomography: A review. *Water Resources Research*, 50(4):3615–3639, apr 2014. doi: 10.1002/2014wr015256.
- [150] P. C. Baveye, M. Laba, W. Otten, L. Bouckaert, P. Dello Sterpaio, R. R. Goswami, D. Grinev, A. Houston, Y. Hu, J. Liu, S. Mooney, R. Pajor, S. Sleutel, A. Tarquis, W. Wang, Q. Wei, and M. Sezgin. Observer-dependent variability of the thresholding step in the quantitative analysis of soil images and X-ray microtomography data. *Geoderma*, 157(1-2):51–63, jun 2010. doi: 10.1016/j.geoderma.2010.03.015.
- [151] F. Meyer and S. Beucher. Morphological segmentation. *Journal of Visual Communication and Image Representation*, 1(1):21–46, sep 1990. doi: 10.1016/1047-3203(90)90014-m.
- [152] S. Schlüter, U. Weller, and H.-J. Vogel. Segmentation of X-ray microtomography images of soil using gradient masks. *Computers & Geosciences*, 36(10):1246–1251, oct 2010. doi: 10.1016/j.cageo.2010.02.007.
- [153] Y. Wang, C. L. Lin, and J. D. Miller. Improved 3D image segmentation for X-ray tomographic analysis of packed particle beds. *Minerals Engineering*, 83:185–191, nov 2015. doi: 10.1016/j.mineng.2015.09.007.
- [154] M. Alam and A. Asadul Haque. A new cluster analysis-marker-controlled watershed method for separating particles of granular soils. *Materials*, 10(10):1195, oct 2017. doi: 10.3390/ma10101195.
- [155] P. I. Guntoro, G. Tiu, Y. Ghorbani, C. Lund, and J. Rosenkranz. Application of machine learning techniques in mineral phase segmentation for X-ray microcomputed tomography (CT) data. *Minerals Engineering*, 142:105882, oct 2019. doi: 10.1016/j.mineng.2019.105882.
- [156] A. Madra, N. E. Hajj, and M. Benzeggagh. X-ray microtomography applications for quantitative and qualitative analysis of porosity in woven glass fiber reinforced thermoplastic. *Composites Science and Technology*, 95:50–58, may 2014. doi: 10.1016/j.compscitech.2014.02.009.
- [157] I. Arganda-Carreras, V. Kaynig, C. Rueden, K. W.

- Eliceiri, J. Schindelin, A. Cardona, and H. S. Seung. Trainable weka segmentation: A machine learning tool for microscopy pixel classification. *Bioinformatics*, 33(15):2424–2426, mar 2017. doi: 10.1093/bioinformatics/btx180.
- [158] J. M. Paz-Garcia, O. O. Taiwo, E. Tudisco, D. P. Finegan, P. R. Shearing, D. J. L. Brett, and S. A. Hall. 4D analysis of the microstructural evolution of Si-based electrodes during lithiation: Time-lapse X-ray imaging and digital volume correlation. *Journal of Power Sources*, 320:196–203, jul 2016. doi: 10.1016/j.jpowsour.2016.04.076.
- [159] A. G. Morales, E. S. Stempinski, X. Xiao, A. Patel, A. Panna, K. N. Olivier, P. J. McShane, C. Robinson, A. J. George, D. R. Donahue, P. Chen, and H. Wen. Micro-CT scouting for transmission electron microscopy of human tissue specimens. *Journal of Microscopy*, 263(1):113–117, feb 2016. doi: 10.1111/jmi.12385.
- [160] T. L. Burnett, S. A. McDonald, A. Gholinia, R. Geurts, M. Janus, T. Slater, S. J. Haigh, C. Ornek, F. Almuaili, D. L. Engelberg, G. E. Thompson, and P. J. Withers. Correlative tomography. *Scientific Reports*, 4(1), apr 2014. doi: 10.1038/srep04711.
- [161] V. Cnudde, G. Silversmit, M. Boone, J. Dewanckele, B. De Samber, T. Schoonjans, D. Van Loo, Y. De Witte, M. Elburg, L. Vincze, L. Van Hoorebeke, and P. Jacobs. Multi-disciplinary characterisation of a sandstone surface crust. *Science of The Total Environment*, 407(20):5417–5427, oct 2009. doi: 10.1016/j.scitotenv.2009.06.040.
- [162] J. Caplan, M. Niethammer, R. M. Taylor, and K. J. Czymmek. The power of correlative microscopy: Multi-modal, multi-scale, multi-dimensional. *Current Opinion in Structural Biology*, 21(5):686–693, oct 2011. doi: 10.1016/j.sbi.2011.06.010.
- [163] B. K. Bay, T. S. Smith, D. P. Fyhrie, and M. Saad. Digital volume correlation: Three-dimensional strain mapping using X-ray tomography. *Experimental Mechanics*, 39(3):217–226, sep 1999. doi: 10.1007/BF02323555.
- [164] M. Sjö Dahl, C. R. Siviour, and F. Forsberg. Digital volume correlation applied to compaction of granular materials. *Procedia IUTAM*, 4:179–195, 2012. doi: 10.1016/j.piutam.2012.05.020.
- [165] J. Gelb, D. P. Finegan, D. J. L. Brett, and P. R. Shearing. Multi-scale 3D investigations of a commercial 18650 Li-ion battery with correlative electron- and X-ray microscopy. *Journal of Power Sources*, 357:77–86, jul 2017. doi: 10.1016/j.jpowsour.2017.04.102.
- [166] C. Liu. On the minimum size of representative volume element: An experimental investigation. *Experimental Mechanics*, 45(3):238–243, jun 2005. doi: 10.1007/bf02427947.
- [167] C. Shearer. The CRISP-DM model: The new blueprint for data mining. *Journal of Data Warehousing*, 5(4), 2000.
- [168] I. H. Witten, E. Frank, and M. A. Hall. *Data Mining: Practical Machine Learning Tools and Techniques*. Elsevier, 3 edition, 2011. doi: 10.1016/c2009-0-19715-5.
- [169] J. Han, M. Kamber, and J. Pei. *Data Mining: Concepts and Techniques*. Elsevier, 3 edition, 2012. doi: 10.1016/c2009-0-61819-5.
- [170] M. N. Boone, J. Dewanckele, V. Cnudde, G. Silversmit, L. Van Hoorebeke, L. Vincze, and P. Jacobs. Combination of laboratory micro-CT and micro-XRF on geological objects. In *Advances in Computed Tomography for Geomaterials*, pages 205–212. John Wiley & Sons, Inc., jan 2013. doi: 10.1002/9781118557723.ch25.
- [171] J. R. A. Godinho, G. Westaway-Heaven, M. A. Boone, and A. D. Renno. Spectral tomography for 3D element detection and mineral analysis. *Minerals*, 11(6):598, jun 2021. doi: 10.3390/min11060598.
- [172] P. J. Withers. X-ray nanotomography. *Materials Today*, 10(12):26–34, dec 2007. doi: 10.1016/s1369-7021(07)70305-x.
- [173] B. J. Inkson, M. Mulvihill, and G. Möbus. 3D determination of grain shape in a FeAl-based nanocomposite by 3D FIB tomography. *Scripta Materialia*, 45(7):753–758, oct 2001. doi: 10.1016/s1359-6462(01)01090-9.
- [174] L. Holzer, B. Muench, M. Wegmann, P. Gasser, and R. J. Flatt. FIB-nanotomography of particulate systems—Part I: Particle shape and topology of interfaces. *Journal of the American Ceramic Society*, 89(8):2577–2585, aug 2006. doi: 10.1111/j.1551-2916.2006.00974.x.
- [175] D. T. Pham, S. S. Dimov, P. V. Petkov, and S. P. Petkov. Laser milling. *Proceedings of the Institution of Mechanical Engineers, Part B: Journal of Engineering Manufacture*, 216(5):657–667, may 2002. doi: 10.1243/0954405021520265.
- [176] C. E. Lyman, J. I. Goldstein, A. D. Romig, P. Echlin, D. C. Joy, D. E. Newbury, D. B. Williams, J. T. Armstrong, C. E. Fiori, E. Lifshin, and K.-R. Peters. *Scanning Electron Microscopy, X-Ray Microanalysis, and Analytical Electron Microscopy*. Springer US, 1990. doi: 10.1007/978-1-4613-0635-1.
- [177] F. Forsberg and C. R. Siviour. 3D deformation and strain analysis in compacted sugar using X-ray microtomography and digital volume correlation. *Measurement Science and Technology*, 20(9):095703, jul 2009. doi: 10.1088/0957-0233/20/9/095703.
- [178] W. Xu, N. Dhawan, C.-L. Lin, and J. D. Miller. Further study of grain boundary fracture in the breakage of single multiphase particles using X-ray microtomography procedures. *Minerals Engineering*, 46-47:89–94, 2013. doi: 10.1016/j.mineng.2013.03.016.
- [179] M. Daly, T. L. Burnett, E. J. Pickering, O. C. G. Tuck, F. Léonard, R. Kelley, P. J. Withers, and A. H. Sherry. A multi-scale correlative investigation of ductile fracture. *Acta Materialia*, 130:56–68, may 2017. doi: 10.1016/j.actamat.2017.03.028.
- [180] Zeiss. *Xradia Versa Manual*. Technical Report A003030, Rev. A, Carl Zeiss X-ray Microscopy, Inc., 2014.

9 Publications

9.1 Copyright Declaration

Elsevier

This concerns the articles from the journals MethodsX and Powder Technology

Authors publishing in Elsevier journals have wide rights to use their works for non-commercial teaching and scholarly purposes without needing to seek extra permission. According to the "Author User Rights"-document (https://www.elsevier.com/__data/assets/pdf_file/0007/55654/AuthorUserRights.pdf, downloaded December 2020), the author has the right to insert a version of the published journal article into his dissertation.

Cambridge University Press

This concerns the articles from the journal Microscopy and Microanalysis

As stated in the *License To Publish*-document <https://www.cambridge.org/core/services/aop-file-manager/file/5d3eee3fc941e8c208ac58e9/CAN-ctf>, signed by the author in May 2020 and January 2022, authors publishing in journals of Cambridge University Press under the Gold Open Access Standard under the Creative Common License with Attribution 4.0 International, in this specific case CC BY 4.0, have the right to share, copy and redistribute the considered material in any medium or format without extra permission. This fully covers the inclusion into this dissertation.

9.2 Overview

Again, see Fig. 9.1 as a contextual reference for the work as a whole.

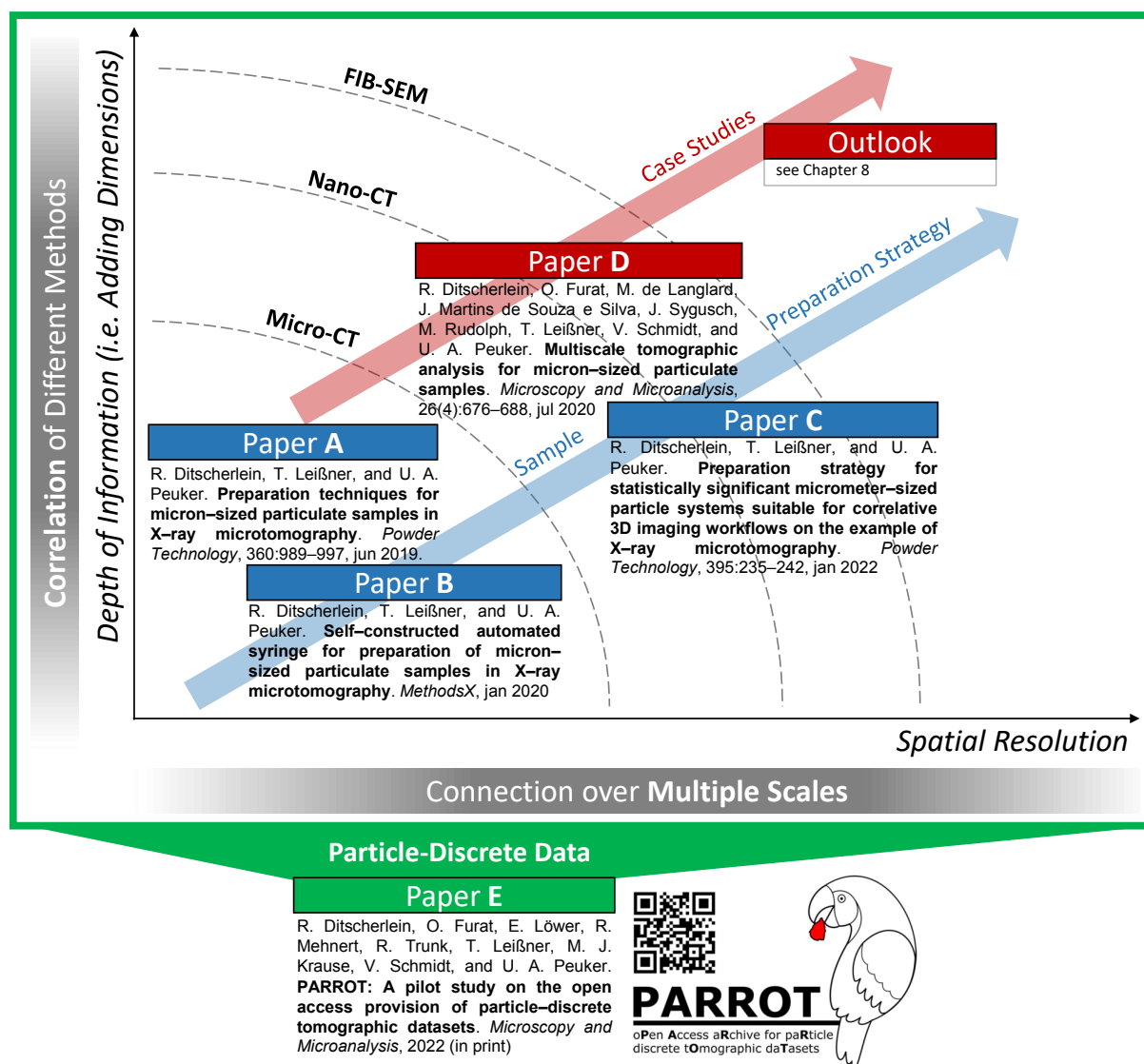


Figure 9.1: Overview of the publications that are part of this thesis.

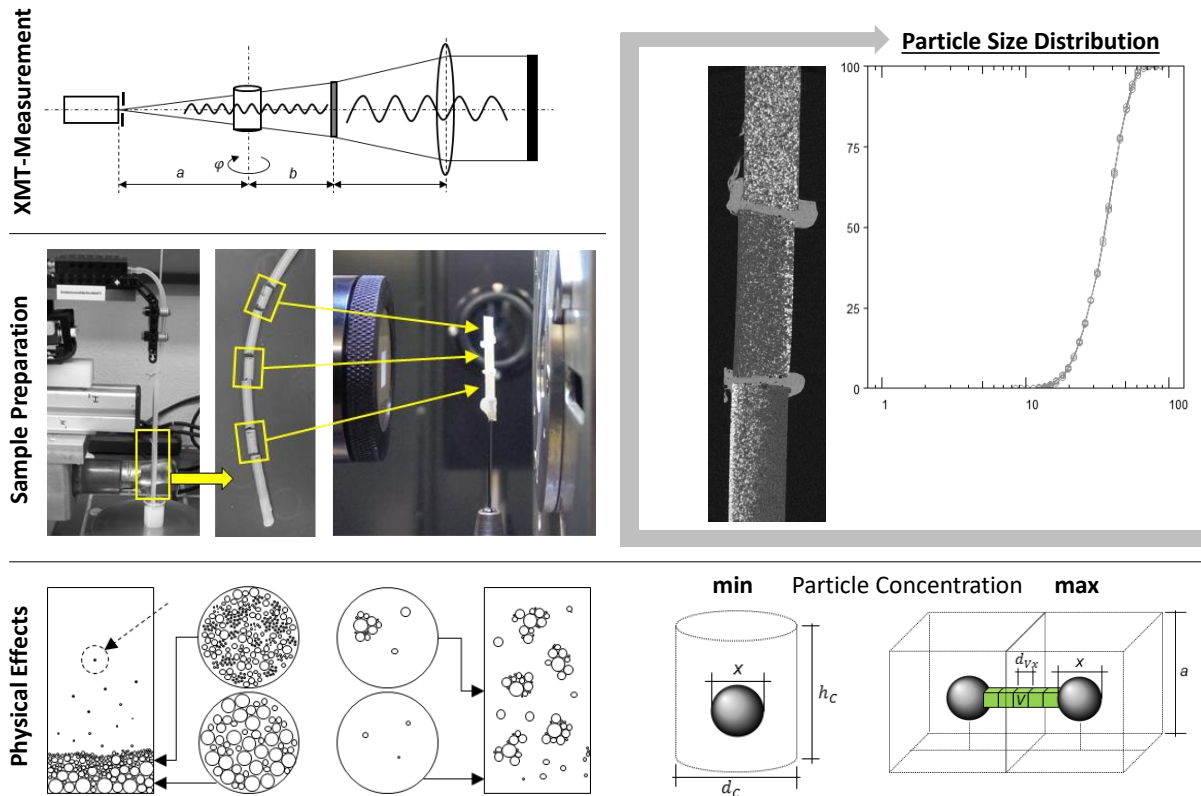
9.3 List of Publications

The following pages list the publications of this thesis, each introduced by a graphical abstract and the highlights. Note that each publication is followed by the respective supplementary material.

Paper A

Powder Technology, June 2019
Preparation Techniques for Micron-Sized Particulate Samples
in X-Ray Microtomography

Graphical Abstract



Highlights

- Calculation of representative number of particles per sample based on statistics
- Determination of sample volume by particle number and volume concentration
- Preparation of homogeneous particle samples using low X-ray attenuating wax
- Validation of reproducible particle size distribution measurement via XMT



Contents lists available at ScienceDirect

Powder Technology

journal homepage: www.elsevier.com/locate/powtec

Preparation techniques for micron-sized particulate samples in X-ray microtomography

Ralf Ditscherlein*, Thomas Leißner, Urs A. Peuker

Institute of Mechanical Process Engineering and Mineral Processing, Technische Universität Bergakademie Freiberg, Agricolastraße 1, D-09599 Freiberg, Germany



ARTICLE INFO

Article history:

Received 12 February 2019
 Received in revised form 15 April 2019
 Accepted 2 June 2019
 Available online 6 June 2019

Keywords:

Particle characterization
 Sample preparation
 X-ray microtomography
 XMT
 XRM

ABSTRACT

New application fields of particle technology, e.g. coatings, pharmaceuticals or electronic components require more and more highly defined particles in the lower micrometer range. In this case the particle size distribution (PSD) is no longer sufficient to define the specifications alone. The particle system has to be described by further distributed properties, which are for instance particle shape or particle composition. Tomographic particle characterization is one key methodology to provide the data, required to quantify these specifications. The tomogram of a representative particle sample contains information on the size and shape of each individual particle. The data of X-ray absorption furthermore gives hints about the material properties and structure of intergrown or composite structures. One central challenge in the tomography of a particle sample is the segmentation of the image data. When the particles in the sample are too close to each other, the algorithm is not able to separate individuals. On the other hand, oversegmentation can occur, when a particle is separated into two or more individuals during the image processing. Therefore, the physical sample preparation, which keeps the particles at a defined distance, strongly facilitates any automated segmentation.

The established techniques known from SEM, TEM or automated mineralogy (MLA) cannot be transferred to X-ray microtomography (XMT), because they only have to provide a representative 2D-measuring plane. The 3D-sample preparation introduced here is able to provide a homogeneous particle sample immobilized within a matrix material with low X-ray absorption. In the sample, all particles have a minimum distance which amounts to more than a defined minimum multitude of the voxel size. The carrier matrix is a wax structure, that is shock frozen within a small polymeric tube with inner diameter from 0.5 mm to 2 mm. This corresponds to the requested sample size for the tomographic measurements (X-ray microscopy system Zeiss VERSA 510), which is 1024 times voxel size ($\approx 0.5 \mu\text{m}$), allowing multi-dimensional characterization of particles from $5 \mu\text{m}$ to $50 \mu\text{m}$ in size and shape.

© 2019 Elsevier B.V. All rights reserved.

1. Introduction

1.1. Particle characterization

Distributed particle properties are of great interest when describing processes from the micro- to the macro-scale. The easiest way is to spread particles on an object carrier and performing a two-dimensional (2D) analysis with optical or, if higher resolutions are

needed, electron microscopy [1,2]. When sections of particulate systems need to be analysed, particles are embedded in a matrix that can be polished to a defined roughness that is suitable for the analysis method (e.g. coupled methods such as SEM-EDS or SEM-EBSD [3,4]). To prevent stereological errors when deducing three-dimensional (3D) characteristics from 2D measurements, sectioning methods like the focused ion beam (FIB) combined with scanning electron microscopy (SEM) allow quasi-3D-characterization — but with high effort and not for all materials. Tomography, that comprises all imaging methods that slice an object to reveal its interior structure, gives a much better statistic in terms of particle number. A good summary of the 3D characterization of particle shapes is given by Lin and Miller [5]. This study will focus on size distribution analysis only.

1.2. Sampling theory

Cy [6] described the sampling of particulate material as a combination of sample extraction and sample preparation — both generating

Abbreviation: B-D, Binomial distribution; EBSD, Electron backscatter diffraction (SEM-EBSD); EC, Elementary cell; EDS, Energy dispersive spectroscopy (SEM-EDS); EP, Extraction point (sampling); ESD, Equivalent spherical diameter; FBP, Filtered back projection (algorithm); FIB, Focused ion beam; FOV, Field of view; K-S, Kolmogorov-Smirnov (statistics); LOESS, Locally weighted scatterplot smoothing; MLA, Mineral liberation analysis; PSD, Particle size distribution; SEM, Scanning electron microscopy; TEH, Tube extraction height (sampling); TEM, Transmission electron microscopy; XMT, X-ray microtomography; XRM, X-ray microscope.

* Corresponding author.

E-mail address: ralf.ditscherlein@mvtat.tu-freiberg.de (R. Ditscherlein).

their specific errors. This model was developed for mixtures of valuables in waste material and is empirically described by tabulated factors depending on mineralogical composition, liberation, particle size and shape.

Hutschenreiter [7,8] developed a sampling model especially adapted for the analysis of particle size distributions (PSD). The basis is a statistical urn model. An important requirement is that every bin of the PSD is representative, proportional to its mass fraction in the basic population. Especially the largest ones, because of their small number in the sampled volume.

A more practical approach, especially for micron-sized particle systems, is given by Koglin et al. [9] and Vigneau et al. [10], who calculate a minimum particle number based on statistical models.

1.3. Sample preparation

The preparation method for particulate samples in XMT-analysis depends on the particle size and the parameters of interest. The easiest case is a packed particle bed where, however, particles are not prevented from moving while scanning. Also direct particle-particle contact can cause problems in particle software segmentation. To fix the particles, an embedding matrix is used - in most cases epoxy resin, because it is well machinable and transparent for optical analysis. A good summary of miniaturized alternatives to conventional sample preparation techniques for solid samples can be found in [11].

If the setting velocity of the particles is not negligible, segregation leads to different compositions of vertical sections. While sedimenting, particles get in direct contact as is the case in a packed bed. Both effects can be problematic in software segmentation due to non-separated particles and different grey-scale histograms (Fig. 1-C/D). Below 50 μm , strongly increased particle-particle interactions can cause agglomeration of particles which also influences the quality of particle segmentation (with/without agglomerates - Fig. 1-E/F).

To prevent sedimentation, the hardening time of the epoxy resin needs to be significantly reduced. This can be achieved by replacing it with wax. Waxes are used for tissue preparation in optical microscopy because of its histological compatibility. A good summary of existing methods for biological sample preparation and their applications in X-ray microtomography is given by Strotton et al. [12]. They are characterized by melting points around 60°C, negligible shrinkage while hardening, good cutting properties and low X-ray attenuation coefficients (comparable to resin). They are also suitable for volume samples. In 3D particle analysis, wax embedding methods for particulate material are rarely mentioned. One example is given by Van Meel et al. [13].

1.4. X-ray microtomography (XMT)

Particle-dependent distributions (e.g. size, shape) give insight in how mechanical processes work and how they are connected to related micro-processes. Only in three dimensions, a reliable description of distributed volumetric particle properties is made possible [5]. This

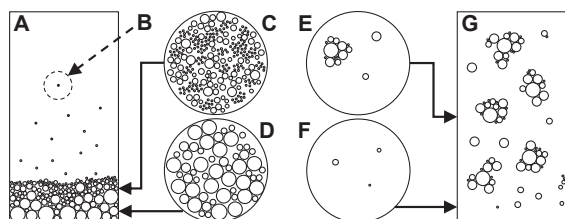


Fig. 1. Samples embedded in resin (A, G), free particle that froze while resin hardening (B); Horizontal sections with small (C) and large (D) particles due to sedimentation; Sections with agglomerated (E) and free (F) particles of an embedded sample without sedimentation.

without unwanted uncertainties caused by stereologically corrected 2D analysis methods and with the possibility to quantitatively investigate particle collectives [14] and their structural characteristics [15] or the inverse pore network between the particles [16].

In conventional radiological 2D imaging, all attenuation coefficients along one line through the sample volume form one sum signal. This equals one specific grey value of overlapping structures, which are located in succession in the beam path. So they cannot be analysed separately. By scanning a specific field of view (FOV) of the sample under different angles, a 3D-volume can be created by applying a mathematical reconstruction algorithm. Extracted sections from this volume are no longer a sum signal but a real volume-slice with grey values proportional to the attenuation coefficients of the material.

State-of-the-art scanners for micro-scale analysis are designed with cone-beam geometry and flat-panel detectors in combination with a magnifying optic (sometimes called an X-ray microscope). A detailed description of the evolutionary steps can be found in [17]. Besides the application in material science [18], there are multiple implementations in the field of process engineering - regarded by the 4 typical macro-processes:

- 1) Comminution: liberation analysis [19], particle breakage analysis in grinding processes [20], grain boundary fracture [21] and random fracture [22] analysis
- 2) Agglomeration: sintering of raw material in iron ore processing [23] and of nano-particles in pharmacy [24]
- 3) Separation: analysis of exposed grain surface area in flotation processes [25], pore network analysis [26,27]
- 4) Mixing: physical separation processes in silo storages [28] and 3D particle bed characterization [29]

In-situ measurements become more and more interesting in all application fields due to decreasing scan-times and increasing computational power. Analyses that were formally only possible in synchrotron experiments become now available for lab-based X-ray systems. A very good summary of quantitative X-ray tomography applications is given by Maire and Withers [30].

2. Material and methods

2.1. Particle system

As idealized sample, a spherical soda-lime glass-particle system (SiLibeads, type S from Sigmund Lindner) with particle sizes below 50 μm was chosen (72.3% SiO_2 , 13.3% Na_2O , 8.9% CaO , 4.0% MgO , 1.5% others). To have a defined range in the PSD, the material (upper specification limit 50 μm) was classified with a separator type ALPINE Multi-Plex 100 MZR classifier above 5 μm particle size. The PSD was determined with laser diffraction, Beckman Coulter LS13320 XR, with dry- and wet-dispersion unit - with and without pre-dispersion in an ultrasonic bath (240 W). The results of the repeated determination can be seen in Table 1.

In Fig. 2 one can see some examples of irregular shaped particles, which are present in the material. These particles account for less than

Table 1
Results of the laser-diffraction measurement given in characteristic quantiles for three different measurement modes and two replicates each.

Method	Run	$x_{10}/\mu\text{m}$	$x_{50}/\mu\text{m}$	$x_{90}/\mu\text{m}$
Dry	1	22.8	37.5	55.4
	2	22.9	37.0	54.5
Wet	1	23.1	38.1	57.8
	2	23.0	38.1	57.7
Wet, Dispersed	1	22.8	38.2	58.7
	2	22.8	38.1	58.5

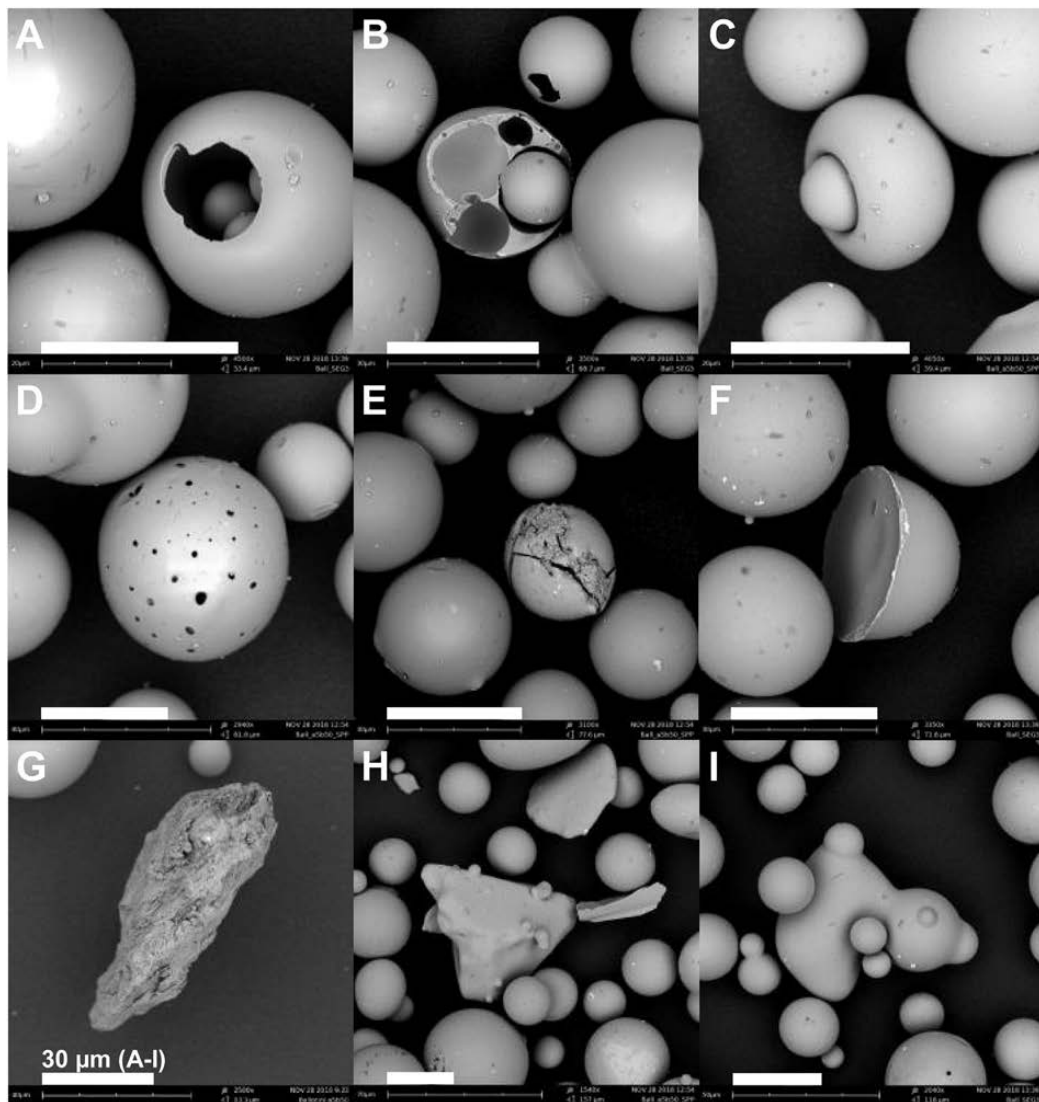


Fig. 2. Extraordinary shapes in spherical SiO_2 -particle fraction below 50 characterized with SEM: (A) hollow and (B) massive spheres including small spheres, (C) doughnut-shaped particle, (D) sphere with small surface-holes, (E) irregular and (F) regular broken spheres, (G) sharp-edged contamination, (H,I) irregular-shaped particles with sintered satellites.

<5% of the sample mass. Thus, using ESD as descriptor for particle size seems to be reasonable.

2.2. Representative sample

The model approach of Gy and Hutschenreiter has to be supplemented, because in case of tomographic imaging it is sometimes not possible to get all sampled particles into the FOV and thus in the measured volume. A second sampling step has to be taken into account, which leads to the question how many particles are needed to get a representative sample — presumed that there are no segregation.

Vigneau et al. [10] proposed the Kolmogorov-Smirnov (K-S) test statistics [31] (1-dimensional) to determine the required number of particles to reach a certain confidence interval. Mathematical derivation and proof can be found in [32,33]. For a large number of particles ($n > 40$) and for a specific level of significance α ($0 < \alpha < 0.2$), the variation \pm

$\delta_\alpha(n)$ of the number based distribution function Q_0 (confidence band) is given by:

$$\delta_\alpha(n) = \sqrt{-\frac{1}{2n} \ln\left(\frac{\alpha}{2}\right)} \quad (1)$$

With this, one can calculate the needed number of particles n at a given confidence band width. Significance α is the probability that the determined Q_0 sticks out of the confidence band. With decreasing α the confidence band is widened up. To compensate for, n has to grow. Because the K-S test statistics is based on the assumption that every particle has the same weight in the overall distribution, Eq. (1) is only valid for number based distribution Q_0 .

Koglin et al. [9] proposed a model which is based on the binomial distribution (B-D). The resulting equation depends on the t -value

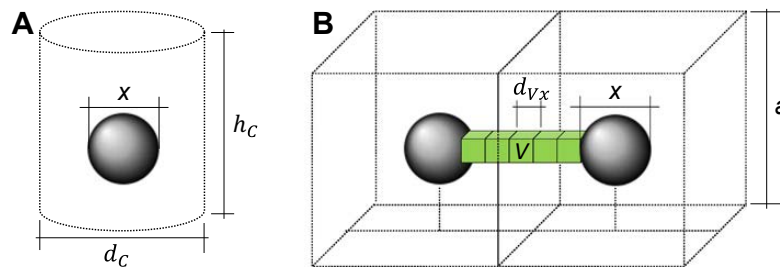


Fig. 3. Minimum concentration estimation: particle inside surrounding matrix cylinder (equivalent to sample geometry) with diameter d_C and height h_C (A), maximum concentration estimation: two particles with diameter x in the centre of the surrounding matrix cubes (wax) with side length a and a specific number of separating voxels V with voxel size d_{Vx} (B).

(student-t distribution) for a given probability P to avoid making a mistake:

$$f_P(n) = \sqrt{\frac{t^2}{n}} \cdot Q_0(1-Q_0) \quad (2)$$

Q_0 is practically chosen between 0.2 and 0.8 (0.5 for selecting the median as characteristic value for the given distribution).

2.3. Sample preparation

The initial sample is divided into sub-samples of 640 mg using rotating sample splitters. Two sub-samples were selected for concentrations of 10% and three for 15% (combined as analysis sample). The sample was extracted with a self-designed computer-controlled syringe. A detailed description can be found in MethodX.

A histological wax (PHC9061, PothHille) with a melting point between 59°C and 61°C was used as embedding matrix. The suspension of dispersed particles and wax was then sampled using a pre-heated plastic tube of 2 mm inner diameter. Pre-heating is required to prevent uncontrolled solidification of the wax before sampling is finished. This will be discussed in the results section.

2.3.1. Minimum concentration estimation

With the estimations from Koglin et al. and Vigneau et al. regarding the minimum particle number for a representative sample, one can calculate the minimum particle concentration c_{min} by relating the volume $V_{Particle}$ of all particles $n_{Particle}$ to the volume of the sample cylinder

$V_{Cylinder}$:

$$c_{min} = \frac{V_{Particle}}{V_{Cylinder}} = \frac{n_{Particle} \cdot \frac{4}{3}\pi \cdot x^3}{n_{Stitch} \cdot \pi \left(\frac{d_C}{2}\right)^2 \cdot h_C} \quad (3)$$

with particle size x , sample cylinder diameter d_C and height h_C . Stitching offers the possibility to virtually combine multiple scans to extend the observed volume by n_{Stitch} .

2.3.2. Maximum concentration estimation

To estimate the maximum particle concentration under ideal conditions (no agglomeration/sedimentation), one can define a cube with side length a in which a particle with size x is centred (Fig. 3-A). Two particles are separated by a number of voxels $n_{Voxel, sep}$ with voxel size d_{Vx} . The concentration of this model “elementary cell” (EC) is then given by:

$$c = \frac{V_{Particle}}{V_{Cube}} = \frac{\frac{4}{3}\pi \cdot \left(\frac{x}{2}\right)^3}{a^3} \quad (4)$$

The number of separating voxels $n_{Voxel, sep}$ can be calculated with:

$$n_{Voxel, sep} = \frac{2 \cdot \left(\frac{a-x}{2}\right)}{d_{Vx}} \quad (5)$$

Rearranging Eq. (5) to the cube side length a and applying this to Eq. (4), one can calculate the maximum particle concentration c_{max} which is

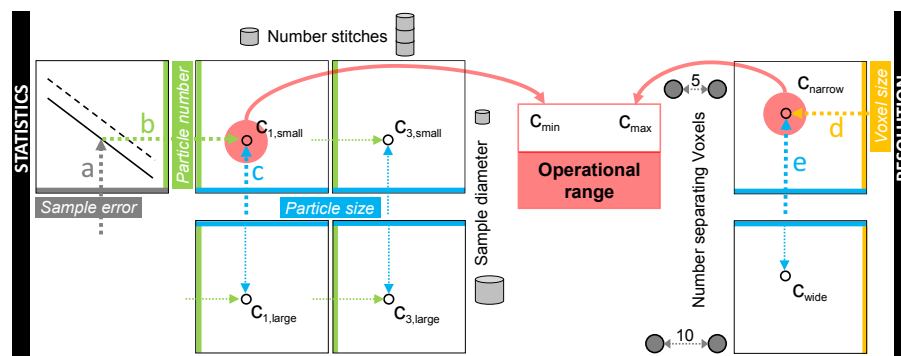


Fig. 4. Workflow to determine the operational range for particle concentration by using the minimum and maximum estimation. A given sample error (a) determines the needed number of particles (b), with a rough particle size estimation from particle system characterization (c) c_{min} can be calculated with Eq. (3); c_{max} can be calculated from the particle size (e), the voxel-resolution (d) and the needed number of separating voxels.

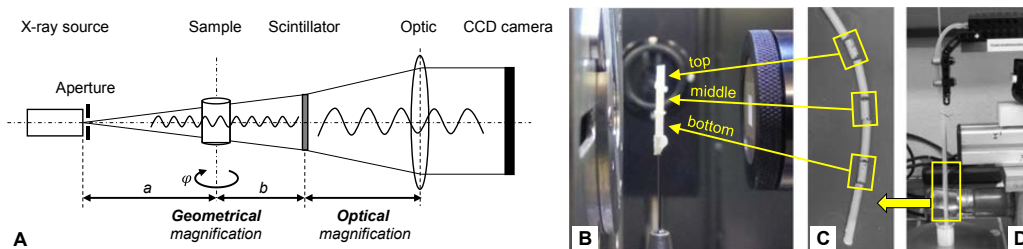


Fig. 5. Principle of CT-measurement with two step magnification (A), mounted sample stack between source and detector (B), cutted tube with positions top, middle and bottom (C) probed tube part from fluid-extraction-unit setup (D).

no longer dependent from the EC:

$$C_{\max} = \frac{4}{3} \pi \left(\frac{\chi}{2} \right)^3 \frac{1}{(n_{\text{Voxel,sep}} \cdot d_{\text{Vx}} + \chi)^3} \quad (6)$$

With given particle size (representative value) and sample volume, C_{\max} is only dependent on the user defined needed minimum voxel number to separate particles from each other. Both estimations are summarized in Fig. 4.

2.3.3. Aspiration speed

To prevent segregation effects, aspiration speed has to be much higher than the stationary setting velocity of the particles. The required dynamic viscosity was measured with Discovery Hybrid Rheometer DHR 1 by TA Instruments at 70°C, 80°C and 90°C. The overall average is 24 mPas. With the Stokes-equation one can calculate the setting velocity of the largest particle (will sink the fastest) with diameter 50 μm –0.4 mm s^{-1} at a *Re*-number of 7×10^{-4} that indicates Stokes flow. To prevent segregation (stationary setting velocity of smallest particle diameter 5 μm \rightarrow 0.004 mm s^{-1} , factor 100 slower) and sedimentation effects (tube not perfectly vertical), one has to adjust the aspiration speed much higher (with tube inner diameter of 2 mm, aspiration height of 160 mm and aspiration time of 2 s \rightarrow 80 mm s^{-1}).

2.3.4. Error estimation

Errors for sample splitting are (1) losses by emitting dust and loosing fine fraction of the particulate sample that will influence the PSD, (2) the entry of impurities caused by abrasion or dust which can influence the XMT-measurement due to high absorption coefficients (see subsection 1.4) and (3) forming of agglomerates that will alter the system from the initial state. To prevent agglomeration, the sub-samples where put in the stirred pre-melted wax very slowly. The rotation speed was increased after adding new sub-samples starting from

400 min^{-1} to 1000 min^{-1} . The goal is to suppress the formation of a vortex that would significantly lower stirring efficiency.

2.4. XMT-measurement

The analysis was carried out with an XMT (Zeiss, type VERSA 510) with a polychromatic X-ray source, a rotating tungsten target, a maximum acceleration voltage of 160 keV and a maximum power of 10 W. Compared to a conventional X-ray micro-computed tomography set-up, the optical system increases magnification by factor of 10. Fig. 5-A shows the principle of the 2-step-magnification. The minimum voxel size of the system is 0.3 μm . One voxel is a volume pixel element in the final tomographic reconstruction with the same edge length in x, y (area - normal pixel/2D) and z (depth - volume pixel/3D). The following primary effects determine the practically attainable optical resolution of the system:

- 1) pixel-resolution of the CCD-sensor (2048 \times 2048) Px,
- 2) optical magnification (0.4 \times , 4 \times , 20 \times , 40 \times),
- 3) mechanical stability of the system and
- 4) thermal stability of the system and the sample.

Secondary effects due to system resolution are for example the X-ray tube itself [34], the cone-beam and the scintillator [35] [36]. Especially when measuring at high resolutions, the influence of these effects can increase rapidly. Further information regarding the technology of the XMT and its fields of application are summarized in [30,37]. Further information regarding the physical mechanisms and X-ray physics in general can be found in [17,38]. A collection of known artefacts in X-ray tomographic analysis is summarized by Boas and Fleischmann [35] and by Davis and Elliott [36]. Table 2 shows all relevant scanning parameters.

2.5. Volume reconstruction

The reconstruction was done with the Scout&Scan Reconstructor Version 11.1.8043 from Zeiss with the standard filtered back projection

Table 2
Parameters for measurement (Meas.) and subsequent reconstruction (Recon.)

	Parameter	Value	
Meas.	Sample size/mm	2	
	Field of View (FOV)/mm	2	
	Acceleration voltage/keV	80	
	Electrical power/W	7	
	Source filter (Zeiss standard)	LE4	
	Exposure time/s	1	
	Optical magnification	4	
	Number projections	2001	
	Angle range/deg	360	
	Voxel size/ μm	2	
	Binning	2	
	Recon.	Algorithm	FBP
		Smoothing (Gauß)	0.7
Beam Hardening Correction		0.05	

Table 3
Image-processing workflow in Fiji (ImageJ 1.51w) with used parameters and references.

	Method	Parameter	Reference
2D pre-processing	Enhance Contrast	s 0.35	
	Unsharp Mask	r 5, m 0.4	
	Non-loc. M. Denoising	s 15, sf 1, a	[42]
	8 bit conversion	–	
	Auto Local Threshold	Bernsen, r 15	[43]
			p 40, p2 0, w
3D	Despeckle		
	Fill Holes		
	3D Watershed Split	s auto, r 2	[44]
	3D Objects Counter		[39]

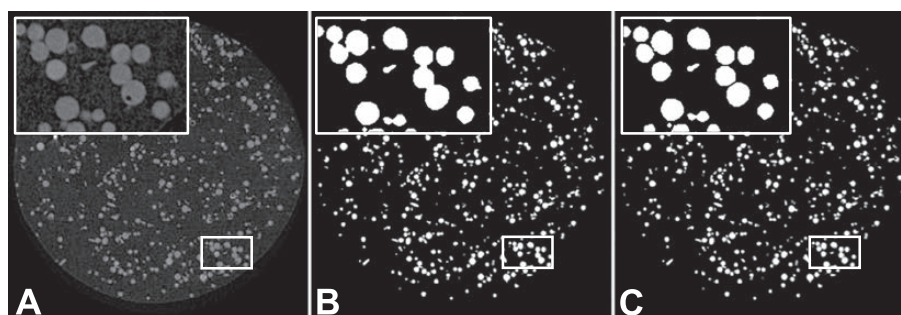


Fig. 6. Reconstructed slices (A), after 2D pre-processing (B) and 3D segmentation (C) with corresponding detail enlargement.

(FBP) algorithm. Reconstruction settings are summarized in Table 2. Due to the absence of high attenuating phases, no beam-hardening was found, except in case of sample contamination. Due to the cone-beam artefact, 50 slices at the top and at the bottom where excluded from the dataset before image post-processing. With regard to 995 slices in total these are approx. 10% of the full dataset.

2.6. Image processing

Image processing was done with Fiji (ImageJ 1.51w). All related parameters are listed in Table 3 (workflow from top to bottom). Due to the cone-beam setup and resulting overall grey-scale differences, Auto Local Threshold is essential for good segmentation results. Here the threshold is computed for each pixel in a defined radius. So it is more independent from grey-level variations and sticks more to the structure (in this case particles). The parameters of the underlying algorithm (in this case Bernsen) can vary depending on object size, contrast and shape and have to be carefully selected for a given segmentation task. Non-optimal parameter selection can lead to artefacts in the final binary image that can make segmentation much more challenging. Despeckling is used to reduce black pixels inside particles that would lead to oversegmentation artefacts. Fig. 6 shows an example for workflow results - (A) raw, (B) binarized and (C) segmented.

As shown in Fig. 2-A some particles are hollow. When calculating the equivalent spherical diameter (ESD) (see Subsection 2.7) this would distort the outcome due to much lower particle-related voxel volumes. The Fill Holes algorithm is one method to solve this issue by filling closed lines with white pixels (related to particle).

Table 4

Aggregated results for the particle size distribution (average, standard deviation) from all measurements; For experiments tube extraction height-validation (TEH) and extraction point-validation (EP) with given target particle concentration and average number of particles N per experiment.

Quantile	Avg/ μm		EP	Stddev/ μm		
	TEH	15%		TEH	15%	10%
Exp.						
Conc.	10%	15%	10%	10%	15%	10%
0.01	10.3	10.0	10.0	0.5	2.4	1.0
0.05	15.8	15.8	16.1	0.8	2.5	1.3
0.10	19.2	19.7	19.7	1.0	1.6	1.4
0.25	24.8	25.0	25.0	0.9	1.0	1.1
0.50	30.6	30.6	30.7	0.8	1.0	1.0
0.75	37.6	37.6	37.5	0.7	1.2	1.0
0.90	44.6	44.4	44.4	0.6	1.1	1.0
0.95	48.3	48.1	48.1	0.6	0.9	1.0
0.99	53.5	53.4	53.4	0.6	0.7	0.8
N (avg)	25,580	35,220	24,770			

2.7. Image analysis

Qualitatively, reconstructed sections themselves have a lot of valuable information. Quantitative analysis needs much more precise work in acquisition (e.g. voxel-resolution \rightarrow object surface), image pre-processing (e.g. beam-hardening correction \rightarrow artefacts), image processing (e.g. oversegmentation) and in post-processing, especially when developing macros for slice-per-slice operations (processing one slice after another with the same sequence of image processing steps).

Due to the spherical shape of the particles, the equivalent spherical diameter was chosen as representative measure for particle size. After particle identification, ImageJ 3D Objects Counter [39] calculates the voxel-volume for each particle (as sum of all particle-related voxels). This volume, regarded as sphere, gives the corresponding diameter. To determine the concentration of the particles in the wax matrix, an ImageJ-macro steps through the slices and determines the ratio of white (particle) and black (matrix) pixels.

3. Results and discussion

3.1. Sampling

To verify the influence of the tube extraction height (TEH) on the PSD (selective aspiration), samples on top, middle and bottom position - vertically centred - where extracted and combined to a sample stack (see Fig. 5-C/B). The sample stack reduces scan time (warmup) and minimizes variability between different scans.

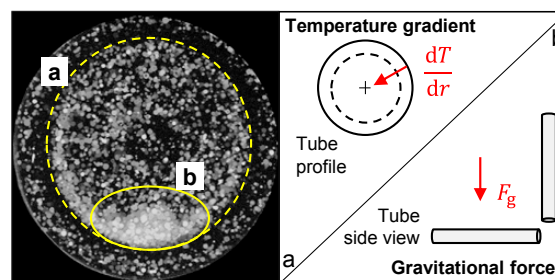


Fig. 7. Results from first wax sample preparation tests; Vertically aggregated slices with 2 artefacts: (a) formation of a cylinder inside the sample tube due to temperature gradient, (b) accumulation of particles on the bottom due to gravitational effects.

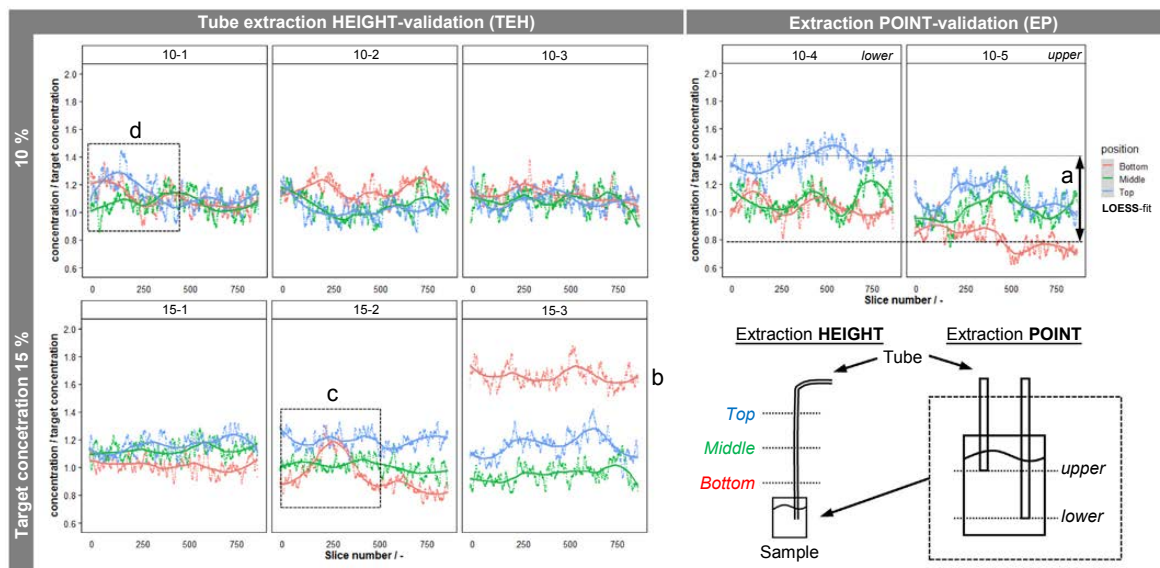


Fig. 8. Calculated concentrations for target concentrations 10% (top) and 15% (bottom); Left shows the validation of the extraction height (top, middle, bottom) of the suction-tube and right the validation of the extraction point from the sample volume; Fitting curves are generated with LOESS-approach [40]. High differences in extraction point validation (a), outlier (b) and indication of agglomerate (c, d).

To verify the influence of the extraction point (EP) in the sample vessel, two different positions (close to the top/bottom) were investigated. Equally to TEH, the tube was placed outside of the rotation centre of the fluid to guarantee optimal mixing conditions.

The minimum number of particles per scanned volume are 18,400 for the Vigneau-approach (Eq. (1) – confidence level $\alpha = 0.05$) and 9600 for the Koglin-approach (Eq. (2) – acceptable sampling error $f_p = 0.05$). The chosen Vigneau-approach results in a theoretical minimum target particle concentration of 10%. In the experiments this results in an average particle number of approx. 25,000 for target concentration 10% and approx. 35,000 for 15% (Table 4).

3.2. Sedimentation

In preliminary studies of the wax preparation method, two side-effects were observed. First, the reconstructed volume shows an inner cylinder of the tube (silicone, temperature range from 60 °C to 200 °C). This can be explained by the temperature gradient between the tube-hull (room temperature) and the hot wax ($T \approx 80$ °C). The inner tube-hull is wetted by the first wax volume that gets in contact. The wax hardened (together with the contained particles) and becomes the new interface to the next wax volume elements (Fig. 7 - a). The higher the gradient, the thicker the layer. The image was generated by

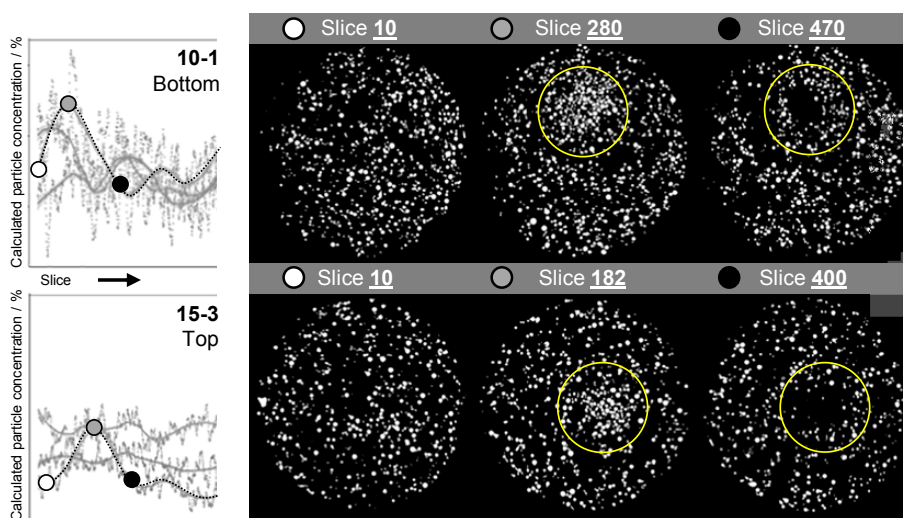


Fig. 9. Reconstructed slices from different sample heights for target concentrations 10% (10-1/bottom) and 15% (15-2/top) before (white), with (grey) and after the agglomerate (black) with marked agglomerate and void.

996

R. Ditscherlein et al. / Powder Technology 360 (2020) 989–997

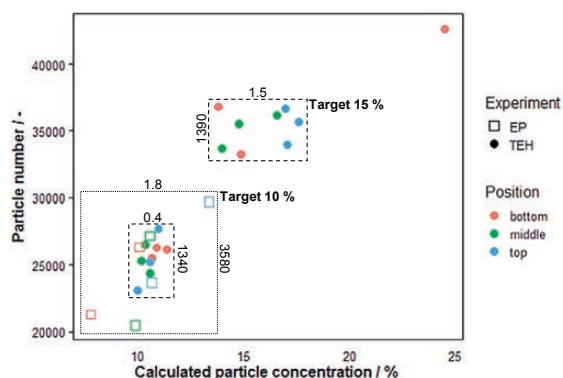


Fig. 10. Particle number vs. target particle concentration for experiments tube extraction height (TEH) and extraction point (EP) for positions bottom, middle and top with given standard deviations.

the aggregation of the minima in all slices (ImageJ 1.51w, operation: Image/Stacks/Z Projection/Max Intensity).

The second effect was induced by unintentional tilting of the tube. Vertical sedimentation effects due to gravitational force are suppressed by the flow-induced force in the opposite direction. Horizontally placed, F_g is perpendicular to the flow direction - particles accumulate at the bottom of the inner-hull (Fig. 7 - b). To avoid these two effects, a tube-heating system and an automated fluid extraction unit was constructed that guarantees a defined aspiration speed in vertical alignment without critical temperature gradient.

3.3. Concentration

For the experiments, two concentrations were chosen that lay within the theoretically calculated c_{\min} (Eq. (3)) and c_{\max} (Eq. (6)), defining an operational range (Fig. 4) from 10% to 15%. All data points in Fig. 8 are fitted with the locally weighted scatterplot smoothing (LOESS) by Jacoby [40] (stiffness 0.4 \rightarrow empirically chosen in comparison with image data, confidence interval for each curve 0.95), that is a simple nonparametric curve-fitting to empirical data.

The target concentrations are in good agreement with the calculated values with tendency to higher concentrations, except 10–4–Top from the lower and 10–5–Bottom from the upper extraction point. At 15%

target concentration 15–3–Bottom shows a much higher concentration of about 25%. One can see that for TEH the variation of the particle number is comparable for target concentrations 10% and 15%, contrary the variation of the calculated particle concentration is 4 times higher when going from 10% to 15%.

Peaks in the approximation (LOESS) curve (Fig. 8-c,d) result from not perfectly wax-dispersed particle sample. In the reconstructed slices agglomerates are visible that are followed by sections where no particles are present (voids). While suctioning, the agglomerated particle collective pull a wake behind that pushes away particles out of this volume element. Fig. 9 shows two examples for target concentrations 10% and 15% with coloured matching positions in the particle concentration curves (Fig. 8-d,c).

When plotting the particle number against the concentration (Fig. 10) 15–3–Bottom can be identified as outlier and is so excluded from the aggregated results of the particle size distribution (Table 4). Corresponding standard deviations are labelled on the boxes that mark target concentration 10% for TEH and EP and 15% for TEH. Target concentration 10% for TEH has nearly the same variation of particle number but the smallest variation of calculated particle concentration compared to 15%.

3.4. Particle size distribution

In Fig. 11, one can see the distributions of the equivalent spherical diameter for target-concentrations of 10% and 15% for tube-extraction heights bottom, middle and top. Although the boxes are on comparable levels Table 4 shows increasing standard deviations in TEH when going to lower quantiles. Higher concentrations cause a higher probability of agglomerated particles. In this case, oversegmentation generates smaller particles compared to well-dispersed systems - variance increases.

4. Conclusions

X-ray microtomography is a powerful tool to determine particle size distributions. The paper discusses (1) what points have to be considered when preparing small-scale particle samples for XMT-measurement. The sample has to be representative and has to fit to the desired voxel size, which determines the FOV. (2) Wax embedding was successfully validated as preparation method for spherical particle systems for XMT-measurement. (3) Target particle concentration should be in proximity of the minimum concentration (Eq. (3)) to get statistically verified number of particles but to minimize the risk of agglomeration (Fig. 9). (4) The extraction point should be in the vertical centre of the sample vessel and always outside of the rotation axis to guarantee a good blending. (5) The particle system should always be pre-characterized with 2D-methods (e.g. SEM, optical microscopy) to verify binarization results (e.g. hollow particles or binarization artefacts).

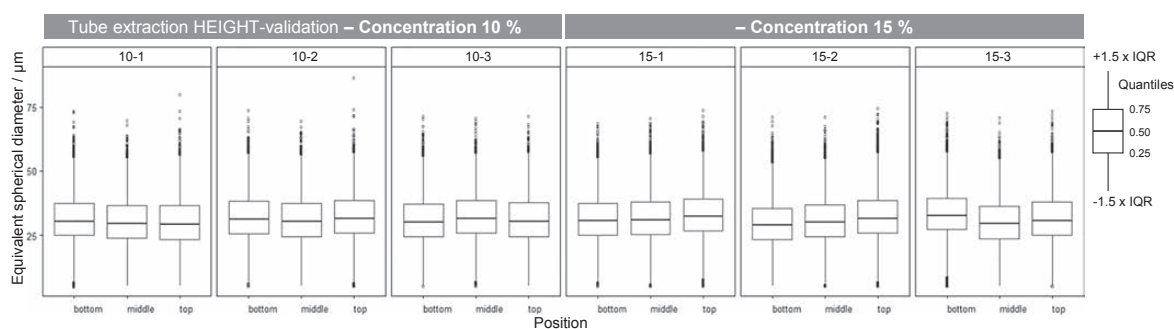


Fig. 11. Equivalent spherical diameter for target-concentrations of 10% and 15% for tube-extraction heights bottom, middle and top; Box-plots with upper (0.75) and lower (0.25) quartile as box, divided by median and whiskers at $\pm 1.5 \times$ inter-quartile-range (Quantile 0.75 - Quantile 0.25) times 1.5.

Future work will focus on dispersion grade in each volume over the sample (for a better measure for preparation quality) and particle systems with various particle shapes. This will set new requirements to statistics (higher dimensional K-S) and maximum particle concentrations. The presented segmentation algorithms are expected to be not sufficient for these systems (particle detection - oversegmentation) and will have to be replaced by supervised learning algorithms (e.g. neural networks [41]).

Raw-data files (Zeiss-format) and reconstructed slices can be requested from the corresponding author.

Acknowledgements

We would like to thank the German Research Foundation (DFG) for supporting the project as part of the priority programme SPP2045 (313858373). We would also like to thank A. Kästner for supporting the sample-handling, T. Hantusch for constructing the rack for the extraction unit, E. Löwer, M. Buchmann and L. Ditscherlein for discussions regarding the data analysis and T. Buchwald for proof-reading.

References

- [1] J.I. Goldstein, D.E. Newbury, P. Echlin, D.C. Joy, C.E. Lyman, E. Lifshin, L. Sawyer, J.R. Michael, Specimen Preparation of Hard Materials: Metals, Ceramics, Rocks, Minerals, Microelectronics and Packed Devices, Particles and Fibres, Book Section 11, 3rd ed. vol. 690, Springer, 2003.
- [2] J. Ayache, L. Beaudier, J. Boumendil, G. Ehret, D. Laub, Sample Preparation Handbook for Transmission Electron Microscopy, Techniques Springer, 2010.
- [3] R. Fandrich, Y. Gu, D. Burrows, K. Moeller, Modern SEM-based mineral liberation analysis, Int. J. Miner. Process. 84 (1–4) (2007) 310–320.
- [4] M. Buchmann, E. Schach, R. Tolosana-Delgado, T. Leiner, J. Astoveza, M. Kern, R. Mckel, D. Ebert, M. Rudolph, K. van den Boogaart, U. Peuker, Evaluation of magnetic separation efficiency on a Cassiterite-bearing Skarn ore by means of integrative SEM-based image and XRF/XRD data analysis, Minerals 8 (9) (2018) 390 (ISSN 2075-163X).
- [5] C.L. Lin, J.D. Miller, 3D characterization and analysis of particle shape using X-ray microtomography (XMT), Powder Technol. 154 (1) (2005) 61–69.
- [6] P.M. Gy, The sampling of particulate materials - a general theory, Int. J. Miner. Process. 3 (4) (1976) 289–312.
- [7] W. Hutschenreiter, Fehlerfortpflanzung bei der Probenahme, Bergakademie Jahrgang, 1965 6 17 (Heft 9).
- [8] W. Hutschenreiter, Fehlerrechnung und Optimierung bei der Probenahme, Freiburger Forschungshefte A 531 (1975) 8.
- [9] B. Koglin, K. Leschonski, W. Alex, Teilchengrößenanalyse, Chemie Ingenieur Technik 46 (7) (1974) 289–292.
- [10] E. Vigneau, C. Loisel, M.F. Devaux, P. Cantoni, Number of particles for the determination of size distribution from microscopic images, Powder Technol. 107 (3) (2000) 243–250.
- [11] F. Pena-Pereira, Miniaturized Alternatives to Conventional Sample Preparation Techniques for Solid Samples, Book Section 7, vol. 108, De Gruyter Open, 2014.
- [12] M.C. Strotton, A.J. Bodey, K. Wanelik, M.C. Darrow, E. Medina, C. Hobbs, C. Rau, E.J. Bradbury, Optimising complementary soft tissue synchrotron X-ray microtomography for reversibly-stained central nervous system samples, Sci. Rep. 8 (2017).
- [13] K. Van Meel, A. Smekens, M. Behets, P. Kazandjian, R. Van Grieken, Determination of platinum, palladium, and rhodium in automotive catalysts using high-energy secondary target X-ray fluorescence spectrometry, Anal. Chem. 79 (16) (2007) 6383–6389.
- [14] K.E. Thompson, C.S. Willson, W. Zhang, Quantitative computer reconstruction of particulate materials from microtomography images, Powder Technol. 163 (3) (2006) 169–182.
- [15] L. Handl, L. Torbahn, A. Spettl, V. Schmidt, A. Kwade, Structural analysis and tracking of micron-sized glass particles during shear deformation: a study based on time-resolved tomographic data, Adv. Powder Technol. 28 (8) (2017) 1920–1929.
- [16] W.B. Lindquist, Quantitative analysis of three dimensional X-ray tomographic images, in: proceedings of SPIE - the, Int. Soc. Opt. Eng. 4503 (2001) 103–115.
- [17] P.D.T.M. Buzug, Einführung in die Computertomographie, Mathematisch-physikalische Grundlagen der Bildrekonstruktion, vol. 1, Springer, 2004.
- [18] S.R. Stock, X-ray microtomography of materials, Int. Mater. Rev. 44 (4) (1999) 141–164.
- [19] J.D. Miller, C.-L. Lin, L. Hupka, M.I. Al-Wakeel, Liberation-limited grade/recovery curves from X-ray micro CT analysis of feed material for the evaluation of separation efficiency, Int. J. Miner. Process. 93 (1) (2009) 48–53.
- [20] P. Kodali, N. Dhawan, T. Depci, C.L. Lin, J.D. Miller, Particle damage and exposure analysis in HPCR crushing of selected copper ores for column leaching, Miner. Eng. 24 (13) (2011) 1478–1487.
- [21] W. Xu, N. Dhawan, C.-L. Lin, J.D. Miller, Further study of grain boundary fracture in the breakage of single multiphase particles using X-ray microtomography procedures, Miner. Eng. 46–47 (2013) 89–94.
- [22] D. Garcia, C.L. Lin, J.D. Miller, Quantitative analysis of grain boundary fracture in the breakage of single multiphase particles using X-ray microtomography procedures, Miner. Eng. 22 (3) (2009) 236–243.
- [23] V. Shatokha, I. Korobeynikov, E. Maire, L. Grmillard, J. Adrien, Iron ore sinter porosity characterisation with application of 3D X-ray tomography, Ironmak. Steelmak. 37 (5) (2010) 313–319.
- [24] P.M. Jenneson, R.D. Luggar, E.J. Morton, O. Gundogdu, U. Tzn, Examining nanoparticle assemblies using high spatial resolution x-ray microtomography, J. Appl. Phys. 96 (5) (2004) 2889–2894.
- [25] Y. Wang, C.L. Lin, J.D. Miller, Quantitative analysis of exposed grain surface area for multiphase particles using X-ray microtomography, Powder Technol. 308 (2017) 368–377.
- [26] G. Kerckhofs, J. Schrooten, T. Van Cleynebreugel, S. V. Lomov, M. Wevers, Validation of x-ray microfocus computed tomography as an imaging tool for porous structures, Rev. Sci. Instrum. 79 (013711).
- [27] N. Fusi, J. Martinez-Martinez, Mercury porosimetry as a tool for improving quality of micro-CT images in low porosity carbonate rocks, Eng. Geol. 166 (2013) 272–282.
- [28] L. Babout, K. Grudzien, E. Maire, P.J. Withers, Influence of wall roughness and packing density on stagnant zone formation during funnel flow discharge from a silo: an X-ray imaging study, Chem. Eng. Sci. 97 (2013) 210–224.
- [29] A.R. Videla, C.L. Lin, J.D. Miller, 3D characterization of individual multiphase particles in packed particle beds by X-ray microtomography (XMT), Int. J. Miner. Process. 84 (1–4) (2007) 321–326.
- [30] E. Maire, P.J. Withers, Quantitative X-ray tomography, Int. Mater. Rev. 59 (1) (2014) 1–43.
- [31] J. Massey, F. J., The Kolmogorov-Smirnov test for goodness of fit, J. Am. Stat. Assoc. 46 (253) (1951) 68–78.
- [32] P. Massart, The tight constant in the dvoretzky-kiefer-wolfowitz inequality, Ann. Probab. 18 (3) (1990) 15.
- [33] D. Khoshnevisan, Empirical Processes and the Kolmogorov-Smirnov Statistic, 2014.
- [34] M.N. Boone, J. Vlassenbroeck, S. Peetermans, D.V. Loo, M. Dierick, L.V. Hoorebeke, Secondary radiation in transmission-type X-ray tubes: simulation, practical issues and solution in the context of X-ray microtomography, Nucl. Inst. Meth. Phys. Res. Sec. A 661 (1) (2012) 7–12 (doi:|et|@temp|bibinfo@X@doi|0.1016/j.nima.2011.09.046).
- [35] F.E. Boas, D. Fleischmann, CT artifacts: causes and reduction techniques, Imaging. Med. 4 (2) (2012) 229–240.
- [36] G.R. Davis, J.C. Elliott, Artefacts in X-ray microtomography of materials, Mater. Sci. Technol. 22 (9) (2006) 1011–1018.
- [37] V. Cnudde, M.N. Boone, High-resolution X-ray computed tomography in geosciences: a review of the current technology and applications, Earth Sci. Rev. 123 (2013) 1–17.
- [38] G.V. Pavlinsky, Fundamentals of X-Ray Physics, Cambridge International Science Publishing, 2008.
- [39] F.P. Bolte, S. Cordelières, A guided tour into subcellular colocalization analysis in light microscopy, J. Microsc. 224 (3) (2006) 213–232.
- [40] W.G. Jacoby, Loess: a nonparametric, graphical tool for depicting relationships between variables, Elect. Stud. 19 (4) (2000) 577–613.
- [41] O. Furat, T. Leißner, R. Ditscherlein, O. Sedivy, M. Weber, K. Bachmann, U. Peuker, V. Schmidt, Description of Ore Particles from CT Images Supported by 2D Mineral Liberation Analysis, Microscopy and Microanalysis, 2018.
- [42] A. Buades, B. Coll, Jean-Michel Morel, Non-Local Means Denoising, Image Processing on Line, 2011.
- [43] J. Bernsen, Dynamic thresholding of grey-level images, Proc. Int. Conf. Pattern Recogn. (1986) 1251–1255.
- [44] J. Ollion, J. Cochenne, F. Loll, C. Escud, Boudier, TANGO: a generic tool for high-throughput 3D image analysis for studying nuclear organization, Bioinformatics 29 (14) (2013 Jul 15) 1840 (–1, 2013).

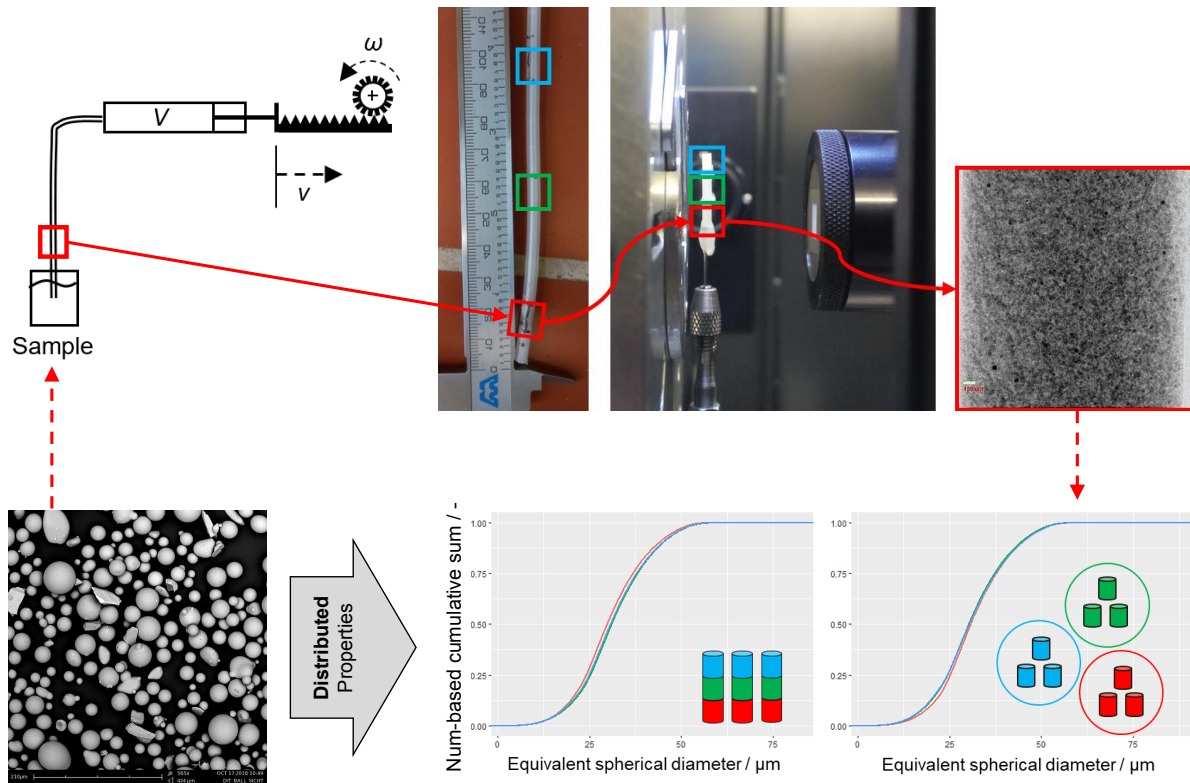
Nomenclature

- Symbol*: Meaning (Unit)
- a : Cube side length (c_{max} estimation) (m)
- α : Confidence interval (%)
- c_{min} : Minimum particle concentration (vol-%)
- c_{max} : Maximum particle concentration (vol-%)
- d_c : Sample cylinder diameter (m)
- d_{Vx} : Voxel size (m)
- δ_{Q_0} : Variation of Q_0 (%)
- f_p : Sampling error (%)
- h_c : Sample cylinder height (m)
- n : Number of elements of distribution (–)
- $n_{Particle}$: Number particles (–)
- n_{Stitch} : Number of stitches (scan) (–)
- $n_{Voxel, sep}$: Number of separating voxels (c_{max} estimation) (–)
- P : Probability (%)
- Q_0 : Number based distribution function (%)
- t : t-Value from student-t distribution (–)
- $V_{Cylinder}$: Volume of sample cylinder (m³)
- $V_{Particle}$: Volume of particles $n_{Particle}$ (m³)
- x : Particle size (m)

Paper B

MethodsX, January 2020 (open access)
Self-Constructed Automated Syringe
for Preparation of Micron-Sized Particulate Samples
in X-ray Microtomography

Graphical Abstract



Highlights

- Self-constructed low-cost automated syringe
- Easily to adapt to different measurement geometries
- Controlled suctioning speed and volume
- Programmable ramp to avoid entry of air-bubbles in matrix

Contents lists available at [ScienceDirect](#)**MethodsX**journal homepage: www.elsevier.com/locate/mex

Method Article

Self-constructed automated syringe for preparation of micron-sized particulate samples in x-ray microtomography

Ralf Ditscherlein*, Thomas Leißner, Urs A. Peuker

TU Bergakademie Freiberg, Agricolastraße 1, 09599 Freiberg, Germany

A B S T R A C T

In X-ray microtomography the sample has to meet special requirements regarding (1) mechanical stability (blurring), (2) geometry (FOV - field of view, rotational symmetry) and (3) composition (high attenuating phases). When analyzing micron-sized particulate material (e.g. powders), the particles in the FOV have to be (4) statistically representative and fixation (embedding matrix) becomes a critical issue due to segregation and agglomeration effects. The authors describe a self-constructed, low-cost automated syringe that allows controlling aspiration speed and suctioning volume. The carrier matrix is a wax structure that is shock frozen within a small polymeric tube. With this, the authors could successfully validate the method to determine particle size distributions (PSD). The described method is used in a related study by Ditscherlein et al. (2019).

- Low-cost automated syringe constructed with LEGO-parts and automatized with Arduino-microcontroller.
- Particle sample embedded within a shock-frozen wax matrix.
- Reproducibility successfully demonstrated by determining particle size distributions.

© 2019 The Authors. Published by Elsevier B.V. This is an open access article under the CC BY license (<http://creativecommons.org/licenses/by/4.0/>).

A R T I C L E I N F O

Method name: Micron-sized particle sample preparation for XMT-analysis

Keywords: Particle characterization, Sample preparation, X-ray microtomography, XMT, Automated syringe

Article history: Received 26 July 2019; Accepted 28 November 2019; Available online 10 January 2020

DOI of original article: <http://dx.doi.org/10.1016/j.powtec.2019.06.001>

* Corresponding author.

E-mail address: ralf.ditscherlein@mvtat.tu-freiberg.de (R. Ditscherlein).

<http://dx.doi.org/10.1016/j.mex.2019.11.030>

2215-0161/© 2019 The Authors. Published by Elsevier B.V. This is an open access article under the CC BY license (<http://creativecommons.org/licenses/by/4.0/>).

Specifications Table

Subject Area:	Engineering
More specific subject area:	Particle Characterization
Method name:	Micron-sized particle sample preparation for XMT-analysis
Name and reference of original method:	Please see bib-keys at the end of the document
Resource availability:	<p>Hardware-part https://store.wayneandlayne.com/products/bricktronics-shield-kit.html LEGO Digital Designer https://www.lego.com/de-de/ldd/download LEGO Digital Designer File FluidExtractionUnit.lxf Arduino Script FluidExtractionUnit.ino</p>

Method details

Motivation

New application fields of particle technology, e.g. coatings, pharmaceuticals or electronic components require more and more highly defined particles in the lower micrometer range. In this case, the particle size distribution (PSD) is no longer sufficient to define the specifications alone. The particle system has to be described by the PSD, but also by further distributed properties, which are for instance the particle shape distribution or the particle composition distribution. Tomographic particle characterization is one key methodology to provide the data, required to quantify these specifications. The tomogram of a representative particle sample contains information on the size and shape of each individual particle. The data of X-ray absorption furthermore gives hints on the material properties and structure of intergrown or composite structures.

One central task in the tomography of a particle sample is the segmentation of the image data. When the particles in the sample are too close to each other, separating individuals can be challenging (one possible approach for segmentation algorithms for aggregated particles is given by Münch et al. [2]). On the other hand, oversegmentation can occur, when a particle is separated into two or more individuals during the image processing. In both cases, the physical sample preparation, which keeps the particles at a defined distance, is a key factor to minimize image segmentation errors.

The established techniques known from SEM, TEM or automated mineralogy (MLA) cannot be transferred to X-ray tomography, because they only have to provide a representative 2D-measuring plane. The 3D-sample preparation introduced here, is able to provide a homogeneous particle sample immobilized (minimization of segregation and agglomeration: Fig. 1-A, B) within a matrix material with low X-ray absorption that fits the required geometrical demands. This is (1) the rotational symmetry of the sample to ensure comparable X-ray-penetrated lengths (Fig. 1-C). (2) the sample has to fit to the desired field of view (FOV) to avoid region of interest tomography inside the sample that would increase exposure time (due to sample thickness and higher number of needed projections) and the probability of artefacts generated by material outside the FOV (Fig. 1-D).

To create such samples, there are already several syringes on the market starting at approx. 1300 €, but only for infusion. Dual systems for infusion and withdrawal starting at approx. 2300 €. They are offering multiple additional features and precision that is much too high for this application, which makes the equipment very expensive. The system described here reduces these costs by factor 10–15.

Materials & methods

Using wax as embedding matrix

Normal procedure for fixation of particles for volumetric scans is to embed them into a matrix that meets the requirements of the used measurement technique. In case of X-ray tomography, epoxy is a

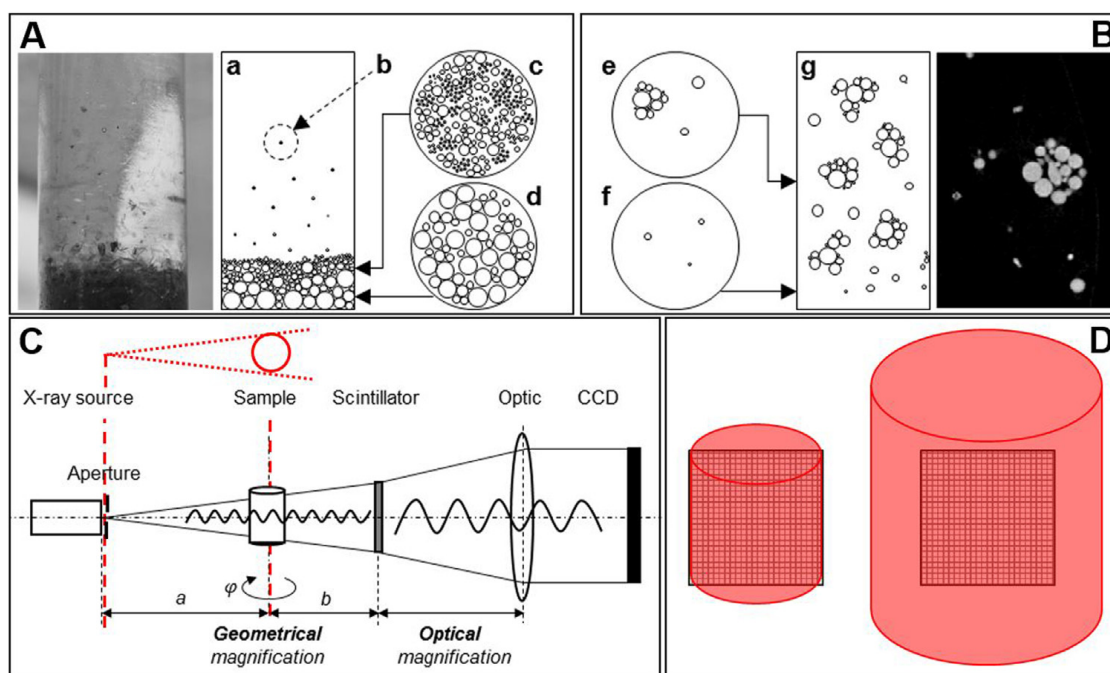


Fig. 1. Segregation (A) and agglomeration (B) effects while embedding particulate samples in matrix, geometrical requirements for the sample: rotational symmetry (C) and appropriate sample size fitting to the field of view (D), adapted from [1].

known standard adapted from 2D-methods like mineralogical analysis. It has a low X-ray attenuation coefficient and is stable at room temperature. In case of particles in the lower micrometer range, the settling velocity of the particles is not negligible. Due to the hardening time of the resin, segregation leads to a different composition of vertical sections. Direct particle contact can lead to a challenging segmentation procedure, especially in case of irregular shapes.

In recent studies, gel-like matrixes have been used for particle sample preparation that are stable at room temperature (e.g. Agar investigated by [3]), but not good machinable. The focus of this study is to create a sample that is stable over a long period of time and is good machinable (e.g. for correlative analysis where sub-samples have to be cut out to reduce the FOV or to prepare 2D sections). Histological wax is an alternative that is known from biological sample preparation due to the good compatibility of matrix and investigated structures. Also positive is a negligible shrinkage rate while hardening, good cutting properties and a low X-ray attenuation coefficient that is comparable to resin. A good summary of miniaturized alternatives to conventional sample preparation techniques

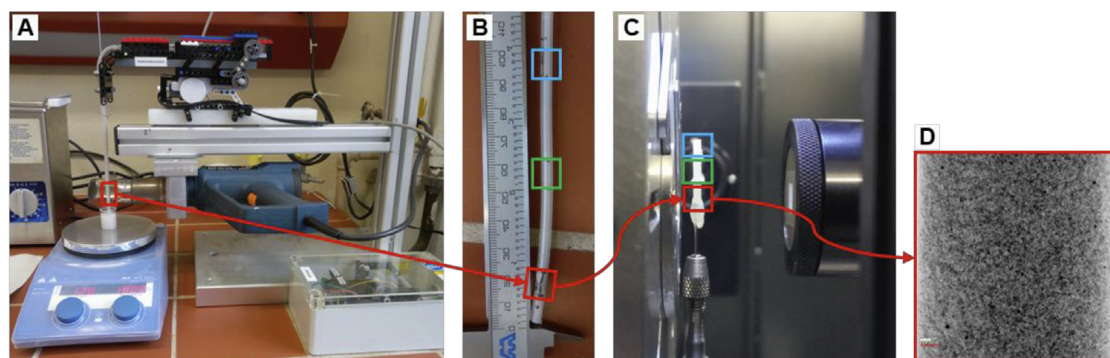


Fig. 2. Sample preparation rack with extraction unit and heating gun (A), polymeric tube with solidified wax after shock freezing (B), sample stack with sub-samples from 3 different positions (top, middle, bottom) (C) and projection image from one sub-sample from sample stack (D).

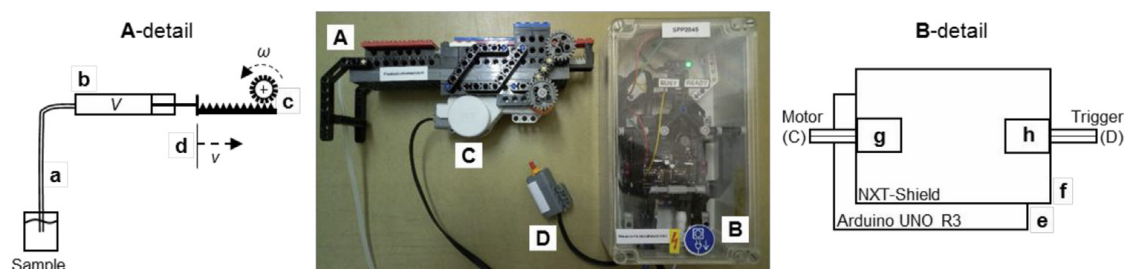


Fig. 3. Fluid extraction unit (A) with controller (B), motor (C) and trigger (D), A-detail: flexible tube (a) mounted on a syringe (b) with a dynamic suction volume V which is increased by transforming rotational motion of a gear (c) in translation (d) with the speed v , B-detail: Arduino UNO R3 as basis (e) with a NXT-Shield (f) as extension to connect LEGO-motor (g, C) and trigger (h, D).

for solid samples is given by Pena-Pereira [4]. A good summary of existing methods for biological sample preparation and their applications in X-ray microtomography is given by Strotton [5]. In 3D particle analysis, wax embedding methods are rarely mentioned. One example is given by Van Meel et al. [6], where wax is used as binder for tablets.

Only using wax does not solve the problem of segregation. For this, the wax is additionally shock frozen within a small polymeric tube (Fig. 1-E, F). The experimental setup with a mounted validation sample is shown in Fig. 2.

Specifications

The authors used a histological wax from PothHille (PHC9061) with a melting point between 59 and 61 °C. The silicone tube has an inner diameter of 2 mm, which corresponds to the requested sample size for the tomographic measurements (X-ray microscopy system ZEISS Xradia VERSA 510, 2048 pixel detector, camera binning 2, 80 keV, 7 W).

Automated syringe

The automated syringe is shown in Fig. 3. For the construction, LEGO Digital Designer¹ was used. To connect the Arduino-Board (AB) to the LEGO-NXT motors and sensors, a circuit board from Wayne & Lane² was used. The high torque of the NXT-motors can move the piston of the syringe accurately and with low voltages of the AB, which saves additional circuit boards and power sources. The AB offers the chance to program individual movement paths, adapted to the specific needs of the sampled material, e.g. a controlled start-up to prevent abrupt changes of motion, which can cause unwanted mechanical stress. The LEGO-parts are listed in Table 1. Fig. 4-A shows the assembled syringe mounting with tube connection (a), syringe (b) and rack (c). Fig. 4-B shows the 3D construction model from LEGO Digital Designer. The corresponding file and the Arduino-Script can be found in the supplemental material.³

Method validation

As idealized sample, a spherical soda-lime glass-particle system (SiLibeads, type S from Sigmund Lindner) with particle sizes below 50 μm was chosen (72.3% SiO₂, 13.3% Na₂O, 8.9% CaO, 4.0% MgO, 1.5% others). The number based cumulative distribution at sample positions top, middle and bottom (with regard to their extraction height from the polymeric tube) and the characteristic quantiles show no significant differences (data basis: 3 replicates for each extraction position). Detailed results are

¹ <https://www.lego.com/de-de/ldd/download>.

² <https://store.wayneandlayne.com/products/bricktronics-shield-kit.html>.

³ [FluidExtractionUnit.lxf](#), [FluidExtractionUnit.ino](#).

Table 1

LEGO part list with brick number, name and quantity.

Brick	Name	Quantity
300526	BRICK 1 × 1	2
300426	BRICK 1 × 2	1
300326	BRICK 2 × 2	4
654126	TECHNIC BRICK 1 × 1	6
370026	TECHNIC BRICK 1 × 2, Ø4,9	1
3200026	BRICK 1 × 2 M. 2 HOLES Ø 4,87	1
370126	TECHNIC BRICK 1 × 4, Ø4,9	6
389426	TECHNIC BRICK 1 × 6, Ø4,9	2
370226	TECHNIC BRICK 1 × 8	2
273026	TECHNIC BRICK 1 × 10 Ø4,9	2
389526	TECHNIC BRICK 1 × 12, Ø4,9	5
302421	PLATE 1 × 1	2
302326	PLATE 1 × 2	3
379426	PLATE 1 × 2 W. 1 KNOB	16
243123	FLAT TILE 1 × 4	6
306821	FLAT TILE 2 × 2	3
306823	FLAT TILE 2 × 2	7
302226	PLATE 2 × 2	1
371026	PLATE 1 × 4	2
366626	PLATE 1 × 6	5
302026	PLATE 2 × 4	2
4514845	PLATE 1 × 12	6
303126	PLATE 4 × 4	5
303521	PLATE 4 × 8	2
428226	PLATE 2 × 16	1
428221	PLATE 2 × 16	1
4211114	PLATE 6 × 10	3
4210720	PLATE 6 × 14	3
4180508	RIGHT PLATE 2 × 3 W/ANGLE	1
4180536	LEFT PLATE 2 × 3 W/ANGLE	1
4297185	CABLE 0,5 M	2
4296929	Push sensor	1
4297008	Tacho Motor	1
4142822	TECHNIC 3 M BEAM	1
3227126	TECHNIC ANGULAR BEAM 3 × 7	2
662926	TECHNIC ANGULAR BEAM 4 × 6	4
4107578	DOUBLE ANGULAR BEAM 3 × 7 45°	2
663226	TECHNIC LEVER 3 M	2
4211573	1/2 BUSH	2
4211483	CONNECTOR PEG W. KNOB	2
4142865	2M CROSS AXLE W. GROOVE	1
273621	BALL W. CROSS AXLE	2
4129886	CONNECTOR PEG	23
4225927	CONNECTOR PEG/CROSS AXLE	13
4211622	BUSH FOR CROSS AXLE	2
4514553	CONNECTOR PEG W. FRICTION 3 M	3
4211086	CROSSAXLE 3 M WITH KNOB	4
4210810	DOUBLE CROSS BLOCK	2
370726	CROSS AXLE 8M	1
373726	CROSS AXLE 10M	1
4120102	GEAR WHEEL T = 8, M = 1	5
374323	TOOTHED BAR M = 1, Z = 10	6
4142825	GEAR WHEEL Z24	2
393826	PLATE 1 × 2 (ROCKING)	3
393726	ROCKER BEARING 1 × 2	3

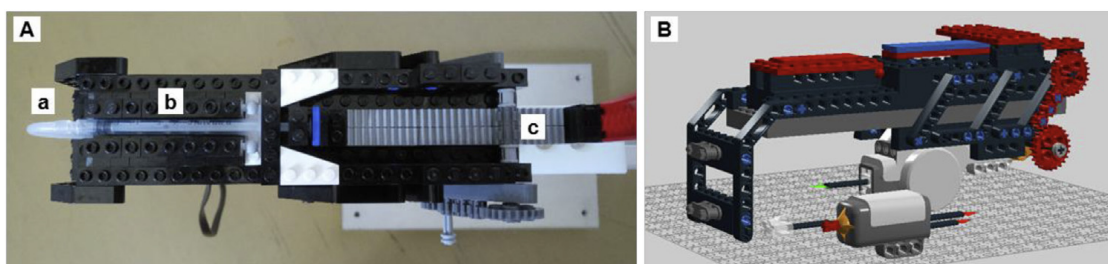


Fig. 4. Syringe mounting (A) with tube connection (a), syringe (b) and rack (c); 3D construction model in LEGO Digital Designer (B).

Table 2

Aggregated results particle size distribution (average, standard deviation) from all measurements; For experiments tube extraction height-validation (TEH) and extraction point-validation (EP) with given target particle concentration and average number of particles N per experiment.

Quantile	avg / μm			stddev / μm		
	TEH		EP	TEH		EP
	10%	15%	10%	10%	15%	10%
0.01	10.3	10.0	10.0	0.5	2.4	1.0
0.05	15.8	15.8	16.1	0.8	2.5	1.3
0.10	19.2	19.7	19.7	1.0	1.6	1.4
0.25	24.8	25.0	25.0	0.9	1.0	1.1
0.50	30.6	30.6	30.7	0.8	1.0	1.0
0.75	37.6	37.6	37.5	0.7	1.2	1.0
0.90	44.6	44.4	44.4	0.6	1.1	1.0
0.95	48.3	48.1	48.1	0.6	0.9	1.0
0.99	53.5	53.4	53.4	0.6	0.7	0.8
N (avg)	25580	35220	24770			

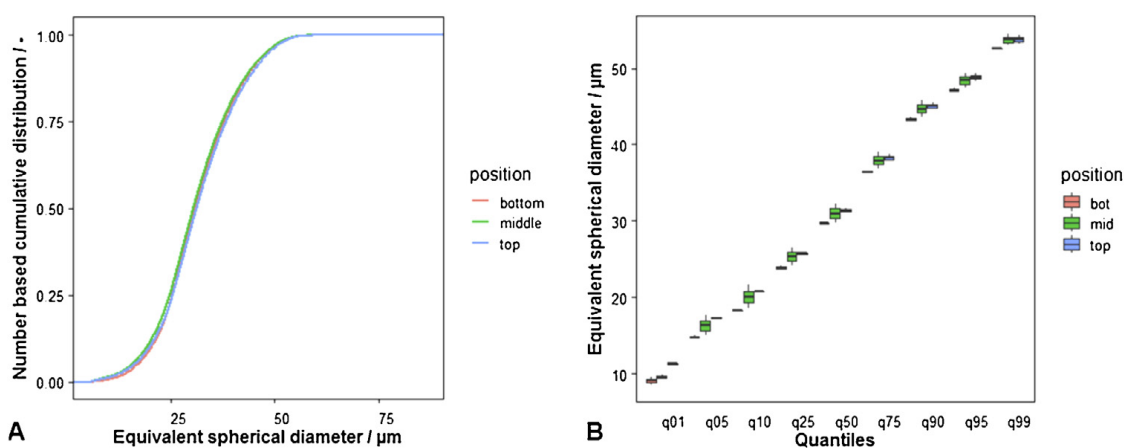


Fig. 5. Number based cumulative distribution of the equivalent spherical diameter (ESD) of a spherical particle sample (5 ... 50 μm) for 3 different extraction points from the sample tube (A), quantiles of the ESD at the same positions for variation-analyses (B).

summarized in Table 2. Number based cumulative distributions and summarizing box-plots of all extraction heights are shown in Fig. 5. More details can be found in Ref. [1].

Declaration of Competing Interest

The authors certify that they have NO affiliations with or involvement in any organization or entity with any financial interest (such as honoraria; educational grants; participation in speakers' bureaus; membership, employment, consultancies, stock ownership, or other equity interest; and expert testimony or patent-licensing arrangements), or non-financial interest (such as personal or professional relationships, affiliations, knowledge or beliefs) in the subject matter or materials discussed in this manuscript.

Acknowledgements

The authors would like to thank the German Research Foundation (DFG) for supporting the project as part of the priority program SPP2045 (313858373). Also the technical staff of the institute for giving many good ideas to optimize the experimental set-up.

References

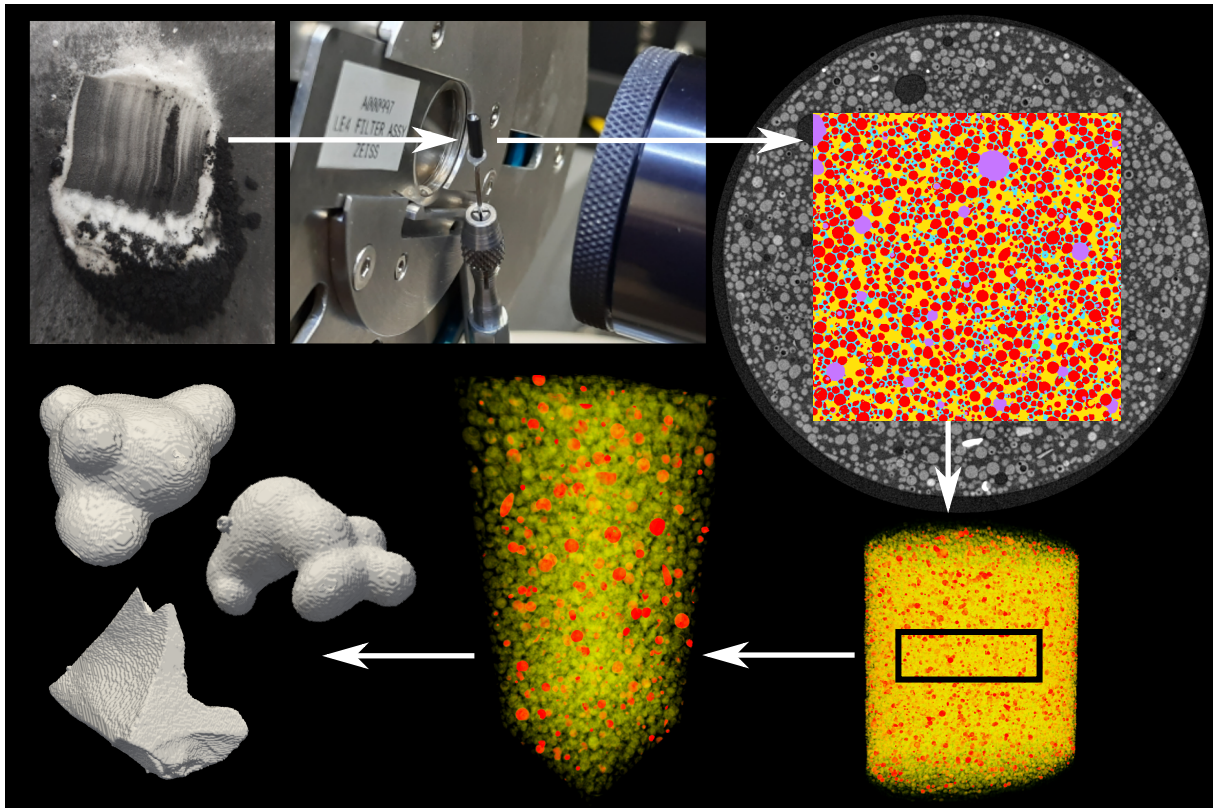
- [1] R. Ditscherlein, T. Leißner, U.A. Peuker, Preparation techniques for micron-sized particulate samples in X-ray microtomography, *Powder Technol.* (2019), doi:<http://dx.doi.org/10.1016/j.powtec.2019.06.001>.
- [2] B. Münch, P. Gasser, L. Holzer, R. Flatt, FIB-nanotomography of particulate systems - Part II: particle recognition and effect of boundary truncation, *J. Am. Ceram. Soc.* 89 (8) (2006) 2586–2595, doi:<http://dx.doi.org/10.1111/j.1551-2916.2006.01121.x>.
- [3] K. Ashrafi, Y. Tang, H. Britton, O. Domenge, D. Blino, A.J. Bushby, et al., Characterization of a novel intrinsically radiopaque Drug-eluting Bead for image-guided therapy: DC Bead LUMI™, *J. Control. Release* 250 (2017) 36–47, doi:<http://dx.doi.org/10.1016/j.jconrel.2017.02.001>.
- [4] F. Pena-Pereira, Miniaturized alternatives to conventional sample preparation techniques for solid samples, *De Gruyter Open*, (2014) .
- [5] M.C. Strotton, A.J. Bodey, K. Wanelik, M.C. Darrow, E. Medina, C. Hobbs, et al., Optimising complementary soft tissue synchrotron X-ray microtomography for reversibly-stained central nervous system samples, *Sci. Rep.* 8 (12017) (2018).
- [6] K. Van Meel, A. Smekens, M. Behets, P. Kazandjian, R. Van Grieken, Determination of platinum, palladium, and rhodium in automotive catalysts using high-energy secondary target X-ray fluorescence spectrometry, *Anal. Chem.* 79 (16) (2007) 6383–6389.

Paper C

Powder Technology, September 2020

Preparation strategy for statistically significant micrometer-sized particle systems suitable for correlative 3D imaging workflows on the example of X-ray microtomography

Graphical Abstract



Note that the nano particles used in the following publication are made of carbon black, which is amorphous carbon, but are incorrectly described as graphite, crystalline carbon. However, with regard to the low absorption properties used for X-rays, the difference is irrelevant.

Highlights

- Preparation of homogeneous particle samples using a low X-ray attenuating matrix
- Forced distancing by addition of low X-ray attenuating graphite nanoparticles
- Generation of particle-discrete datasets by machine learning assisted segmentation
- Validation of reproducible particle size measurement via X-ray microtomography



Preparation strategy for statistically significant micrometer-sized particle systems suitable for correlative 3D imaging workflows on the example of X-ray microtomography

Ralf Ditscherlein*, Thomas Leißner, Urs A. Peuker

Institute of Mechanical Process Engineering and Mineral Processing, Technische Universität Bergakademie Freiberg, Agricolastraße 1, D-09599 Freiberg, Germany



ARTICLE INFO

Article history:

Received 28 July 2021

Received in revised form 14 September 2021

Accepted 15 September 2021

Available online 21 September 2021

Keywords:

Particle characterization

Sample preparation

X-ray microtomography

XRM

Machine learning assisted segmentation

ABSTRACT

The characterization of multidimensional particle property distributions through computed tomography requires an adapted sample preparation strategy. This strategy should both generate as many spatially separated particles as possible in the smallest achievable volumes and also enable mechanically and vacuum-stable samples that are suitable for correlative measurement, for example with high-energy ion beam methods. In the present study an epoxy-based method is presented that minimizes the negative influence of particle sedimentation by adding very low X-ray absorbing graphite nanoparticles as spacer. A machine learning-based method is presented to discretize the particle system. Results are compared with data from 2D SEM validation measurements and data of a previous study.

© 2021 Elsevier B.V. All rights reserved.

1. Introduction

Characterizing multidimensional particle-discrete properties is a key challenge in modern process design and development. As X-ray Microtomography (XMT) has become one of the main non-destructive and non-intrusive three-dimensional (3D) characterization methods in engineering [1,2] and materials science [3], it is used to capture 3D particle samples to generate distributions of particle properties.

Since the X-ray Microscope (XRM) detector used in this study is non-energy-dispersive, all photons are summed only by their number. The correlation of material composition and 3D information is not possible by XMT alone, because the X-ray spectrum of each line path through the sample is “lost” after the transformation in the scintillator material. Additional information from other analysis methods must be correlated. As proposed [4] for mineral particles in the particle size range above 300 μm . In this study, we extend this method down to micrometer-sized particles as a supplement to the successfully validated wax preparation method presented [5].

To create valid 3D datasets, a minimum number of particle-discrete values is needed to obtain a statistically representative sample [6,7]. “Particle-discrete” means that the scanned volume, also referred to as

Field of View (FOV), consists of distinct objects, each one consisting of a defined number of voxels. The challenge now is to have as many particles as possible in the scan volume while at the same time creating enough space between them, so as not to compromise the subsequent segmentation into individual volumes. This becomes even more important when it is necessary to reduce the sample volume when correlating other methods such as Focused Ion Beam (FIB)-Scanning Electron Microscopy (SEM), which then allows shifting scales from micro- down to nanometer resolution.

Fig. 1 shows different preparation strategies for particulate samples to prevent particle movement while scanning. Particles in the millimeter and upper micrometer range are usually fixed as bulk, e.g. by a foam structure (a), embedded in epoxy (b), or spread on an adhesive polymer sheet which is rolled to a cylinder (e) [8]. In all cases, the fixation should be designed to prevent direct particle-particle contacts to avoid the need of complex image segmentation tasks caused by the Partial Volume Effect (PVE). In tomographic imaging, the PVE is caused by structures below voxel resolution producing voxels consisting of more than one phase. The output is an unclear non-linearly averaged grey value, depending on the phase shares. Possible solutions to prevent direct particle-particle contact can be epoxy hardened under rotation to minimize the influence of gravity (d) [9] or shock freezing of pre-dispersed particles in molten wax (f) where the latter technique was chosen for Part 1 of the study [5,10]. Bridging analysis technologies to higher magnification levels, sub-volumes have to be extracted physically, e.g. by FIB-SEM or virtually, e.g. with Region of Interest (ROI)-

* Corresponding author.

E-mail address: ralf.ditscherlein@mvtat.tu-freiberg.de (R. Ditscherlein).

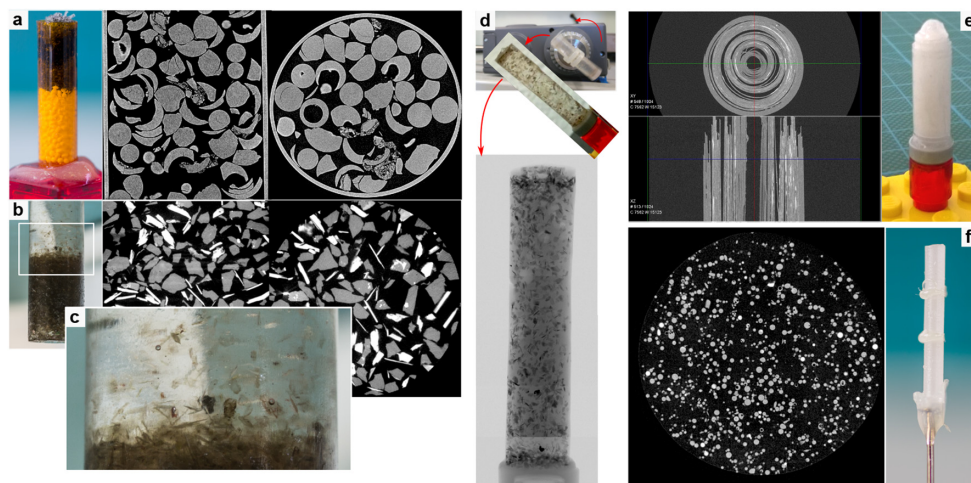


Fig. 1. Particle sample preparation methods with corresponding reconstructed slices: (a) Loose bulk of particles with a foam fixation on top, (b) particles embedded in epoxy with (c) significant segregation during solidification, (d) epoxy sample rotating while curing, (e) particles spread on a rolled adhesive polymer sheet, (f) particles embedded in a shock-frozen wax matrix [5].

tomography. Physically or virtually, the volume fraction of the particles in the matrix should be high enough to guarantee a sufficient number of particles in the sub-volume, much higher than in conventional embedding workflows. Additionally, the matrix material itself must be vacuum-stable and must not break down into critical components under the influence of high energy, e.g. the application of an ion beam in case of FIB-SEM, that would contaminate the vacuum chamber. All these requirements place the focus back on the application of epoxy.

The epoxy method presented in this work is intended to minimize direct particle-particle contacts. This is done by pre-dispersing the particles of interest with the help of another particle system consisting of low X-ray absorbing material below the targeted voxel size, in this case nanographite. After embedding this mixture into epoxy, hardening time is not critical anymore, because the additional particles together with the resin work as spacers between the particles of interest. Realized already for mineralogical two-dimensional (2D) analysis [11,12], this method is now adapted and validated for 3D tomographic experiments in the present paper. Although we will discuss the application in X-ray tomographic analysis in the following, the presented method is also applicable for laser milling [13] and serial sectioning purposes [14]. Note that the method in the following will be referred to as Epoxy-Nanographite (ENaG).

As proposed in the first part of this study [5], we now use a machine learning algorithm for the image processing workflow, in our case Waikato Environment for Knowledge Analysis (WEKA) [15], a free software package developed at the University of Waikato, New Zealand, which is available as a plugin for Fiji [16] (<https://imagej.net/plugins/tws/>), a derivative of the commonly known ImageJ environment. To ensure comparability, the datasets of the wax method are evaluated again in the same way and compared with the ENaG method.

The paper is organized as follows: first, starting with alternative preparation methods to the wax method, second, a methodological description of the preferred ENaG method and evaluation of four independent samples, followed by a short explanation of the utilized machine learning procedure and the application to the datasets of the wax method in order to compare both.

2. Materials & methods

2.1. Particle system

For this study, we use a spherical soda-lime glass-particle system (SiLibeads, type S from Sigmund Lindner GmbH) with particle sizes below $50\ \mu\text{m}$ (72.3% SiO_2 , 13.3% Na_2O , 8.9% CaO , 4.0% MgO , 1.5% others). To have a defined particle size distribution, the material was classified to cut off particles of sizes below $5\ \mu\text{m}$. A detailed description of the particle system is given in the previous study.

2.2. Sample preparation

The FOV and the sample size are firmly linked via the finite number of pixels on the CCD detector of the XRM. Optimally, the overall sample should fit to the FOV to avoid long scanning times caused by a large number of required projections [17] and large radiated lengths. In addition, particulate samples in the lower micrometer range make the following demands on the sample preparation: (i) Analysis particles should be well dispersed with sufficient distance to avoid PVE in the particle-matrix-particle transition region, which simplifies the subsequent image segmentation step; (ii) the matrix material/composition should consist of a low X-ray absorbing material to guarantee good contrast and optimal scanning times; (iii) for correlative analyses, the sample should be mechanically and vacuum-stable to avoid contamination of process compartments.

A good degree of dispersion can be achieved by inserting the particle sample in a fluid or by rubbing the sample mechanically. In both cases, the dispersed phase has to be fixed to avoid particle motion while scanning. The present paper deals with a vacuum stable epoxy (EpoThin 2, Buehler). As mentioned above, the hardening time of the resin is not short enough to avoid particle sedimentation in the sample volume. Even extremely fast curing resins, e.g. photo-initiated thermal frontal polymerization, have an average curing time of more than 10 s [18]. One possible solution is the addition of a third phase, which in combination with the epoxy portion serves only as a spacer to keep analysis particles at distance. Therefore, we use graphite nanoparticles (Carbon black powder, Lamp black 101, Orion, average particle size 95 nm).

These particles are nearly X-ray transparent in the energy regime used during measurements (80 keV) and their size is many times below the voxel resolution used in this study (2 μm).

Fig. 2 shows the dry dispersion process in detail. All steps are performed with a rubber spatula (a) on a sheet of paper (b), which is pretreated with nanoparticles to “pre-coat” the surface of the paper. The particles of interest (white) and spacer particles (black) (c) are constantly stressed by the spatula in different directions with only light pressure (d). In order to prevent the sample from spreading over an increasingly large area, it is swept together at regular intervals with the spatula followed by continued rubbing. In the experiment, this procedure was applied for about 10 min for each sample until no white stripes, which would indicate remaining macroscopic agglomerates, are visible and the sample is assumed to be sufficiently well dispersed (e).

In the next step, the pre-dispersed particles are mixed with epoxy. In both mixing procedures (resin & hardener, final resin & pre-dispersed particle sample) slow vertical stirring prevents the introduction of air bubbles. Preliminary studies have shown that only large air bubbles (larger than 1 mm) near the fluid surface have a chance to disappear under vacuum. Smaller bubbles are incorporated into the matrix during solidification. Fig. 3 visualizes the manufacturing procedure of the final sample for XRM-scans. At the beginning, the paste-like mixture of nanographite, particles, and epoxy (a) is sucked with a syringe into a small polymeric tube (2 mm inner diameter) and closed on the top end (b). After curing between 6 and 9 h, the sample is cut out of the tube (c) and formed (d). For low-resolution scans, the resulting sample cylinder is glued onto a needle pin (e) for sample mounting. For high-resolution scans, a disk is cut from the sample cylinder which is cut a second time into a sample bar with approx. 500 μm in width (f). Then, the sample bar is also glued onto a needle pin (g).

2.3. XRM measurements

Details on the XRM measurements and related artefacts can be found in [5]. A short introduction on the application of tomography measurements in particle technology is given by Leißner et al. [19]. Details regarding the XRM measurement are given in [Appendix A of the Supplementary Material](#).

In this study, we use a 4 \times magnification that gives a voxel size of 2 μm . It should be emphasised here that histogram adjustment during reconstruction (byte scaling) should only be carried out moderately. That means that areas assigned to the air and the matrix and do not seem to be of interest at first glance should not be masked out by cropping, as this deletes useful features for further image processing. A subsequent evaluation of the distribution, for example of the air bubbles in the

sample volume, can also no longer be carried out in this way, as the grey values for air and epoxy are unified by too much byte scaling and can no longer be distinguished afterwards.

2.4. Trainable WEKA segmentation

In this study, we used version v3.2.34 of the 3D trainable WEKA segmentation plugin. The applied method here is called supervised learning as the user utilises a part of the dataset to train a machine learning algorithm, the result of which is in turn evaluated by the user himself. Although quality measures are available, e.g. an Out of Bag (OOB) error, they are not objectively comparable in general and depend strongly on the selected objects in the training dataset. On reflection, however, it becomes clear that this is the case in almost every quantitative assessment of image data and does not represent a disadvantage of this method.

The training itself starts with defining reasonable classes for the current dataset. In our case, the limitation to three classes, (i) the particle, (ii) the entrapped air, and (iii) the epoxy matrix (incorporating also the graphite nanoparticles) was considered to be not sufficient to create good results. “Good” in this case means that the resulting classification fits to the underlying structures, which was determined visually. Some highly absorbing particles (appear significantly brighter than an average particle), which have been assigned to the particle class during training, shift the grey value distribution of all class-associated particles towards higher values. The same occurs when PVE areas in the particle-matrix-particle transition region are assigned to the epoxy class. Since PVE areas are similar to the particle class, areas within particles are now often wrongly assigned to the epoxy matrix, to name just one example of misclassification. One possible solution is to add two new classes assigned to highly attenuating particle and PVE-structures, respectively, which are called separators in the following. So, the resulting classes are (i) particles, (ii) air, (iii) epoxy, (iv) highly attenuating particles, and (v) separators. Note that the additional separator category significantly improves the segmentation result, but this effect is limited. Strongly cohesive particle systems that cannot be dispersed by mechanical stress and are still present as aggregates must be pre-dispersed in a different way. The share of PVE is otherwise dominant and ultimately leads to a bias in the particle size distribution.

After the definition, a certain number of objects within the image stack have to be assigned to the classes to prepare a learning basis for the algorithm. In practical terms, this means using different marking tools (circle, freehand shape, line) to mark particles, for example, and assign them to the particle class. An attempt should be made to include different structural characteristics, e.g. not only perfectly round particles

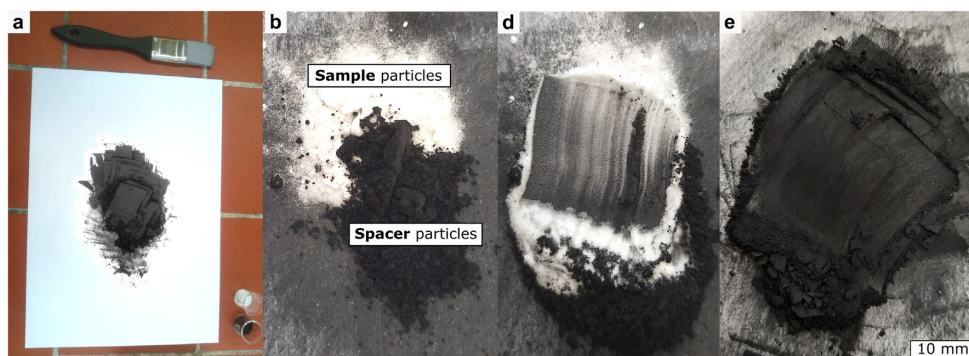


Fig. 2. Dry dispersion of particle sample with graphite nanoparticles: dry dispersion with a rubber spatula (a) on a pretreated sheet of paper (b) with their calculated shares (c), after applying the rubber spatula (d), final state with no visible agglomerates (e).

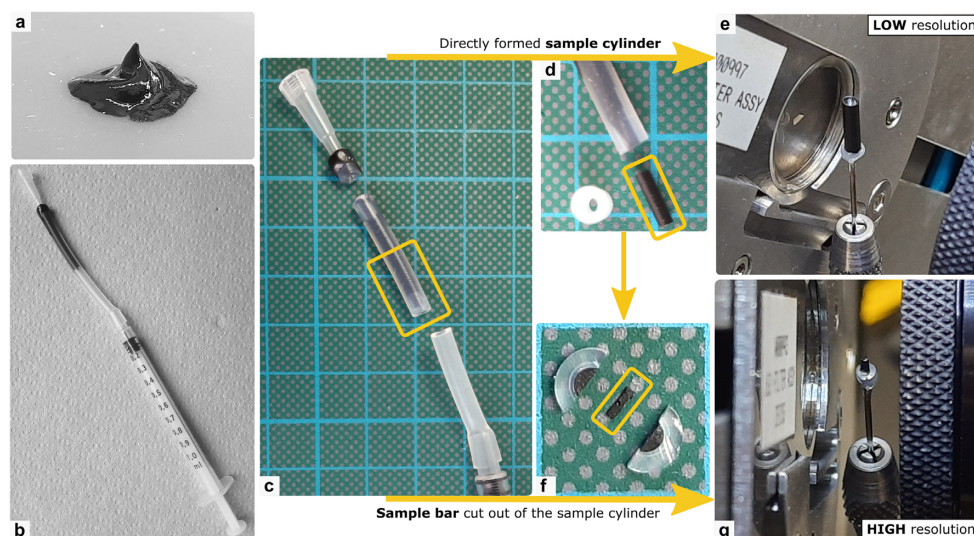


Fig. 3. Paste-like mixture of ENaG matrix and particles (a), extracted with a syringe into a polymeric tube (b), hardened and cut (c), formed (d) and mounted on a sample holder for low-resolution measurement (e), cut into a bar (f) and mounted for high-resolution measurement (g).

with a homogeneous structure, but also irregular, very large/small particles, etc., same with all other classes. To capture potential gray value histogram fluctuations over the height of the image stack, objects should not only be assigned in one slice but at different height regions. Especially in the case of particles, it is beneficial to mark single particles in 2D belonging to the same 3D particle to train also the connection of objects in three dimensions.

We select a decision tree approach (fast random forest model) with a minimum sigma of 1.0 and a maximum sigma of 8.0 and variance, mean and structure as training feature ensemble. A feature here is a measure, which is applied to the marked training structures and used as split criteria for the decision tree. Good results were obtained when having at least 5000 pixels per class, except classes with very rare occurrences in the dataset, e.g. highly attenuating particles. After training on one small dataset, the resulting model was applied to all other datasets. Here, size was set to 600 per 600 Pixels over the full sample height for the test environment implying 128 MB of working memory.

2.5. Determination of the particle size distribution

The WEKA algorithm creates a false colour image, each colour corresponding to one of the five training classes. For quantitative analysis, the particle class and the class of high X-ray attenuating particles were combined to create the initial dataset for 3D segmentation, which is in this case a watershed algorithm. After the discretization of the dataset, the number of voxels is determined for every particle and back-calculated to an equivalent sphere with the corresponding Equivalent Spherical Diameter (ESD). Details regarding the full image processing workflow are given in Table 1. More details on all separate classes concerning the original dataset can be found in Appendix B of the Supplementary Material. For validation purposes, we use a set of 2D SEM images of dispersed particles on an adhesive tape. Here, we measure all particles from the top to the bottom of the image to get a statistically representative particle size distribution. One example is given in the Appendix C of the Supplementary Material. Note that this procedure fits for the 2D data set, but compared to the 3D procedure described above, it can lead to significant deviations especially for irregularly shaped particles, which is commonly referred to as stereological bias.

Table 1

Image processing steps for acquiring the particle size distribution regarding ESD for reasonable method comparison.

Image processing step	Reason	Reference
1. Removing first/last 50 slices	Cone-beam artefact	[20]
2. WEKA classification	–	[15]
3. Removing first/last 25 slices	Misclassification in marginal areas	–
4. Combining class (I) and (IV)	–	–
5. Filling holes of particles	Reasonable comparison with ESD	–
6. 3D Watershed Split	Separation of contacting particles	[21]
7. 3D Objects Counter	Determining particle-discrete voxel-based volumes	[22]

3. Results and discussion

3.1. Particle concentration

The experiments were carried out with mixing ratios of nanoparticles and particles of interest of 60:40, 40:60, and 20:80, with an initial particle mass of 0.64 g. Preliminary experiments showed that a 20:80 mixture is the optimal case in terms of maximization of particle number keeping enough distance between them. For this, assuming a monodisperse bulk of nanoparticles (density 1.8 g cm^{-3}) and a theoretical porosity of 0.5 for a loose bulk of graphite powder, which is in this case only a rough estimate, the calculated mass for the initial sample is 0.38 g (density of epoxy 1.2 g cm^{-3}). Due to the high surface area of the nanographite ($29 \text{ m}^2 \text{ g}^{-1}$), this quantity was slightly increased to guarantee a paste-like suspension that could be sucked into a syringe. The final mass was determined with 0.40 g of epoxy that would result in a particle concentration of 39%. This was validated by applying a macro in Fiji (ImageJ 1.51w), which binarizes each slice of the tomogram (black pixels: matrix, white pixels: particles) and sums up white pixels to give the concentration of particles in the ENaG matrix. Note that previously the influence of air inclusions (Fig. 5a/c) had to be corrected (b/d,e) to determine the correct particle concentration. The code snippet can be found in Appendix D of the Supplementary

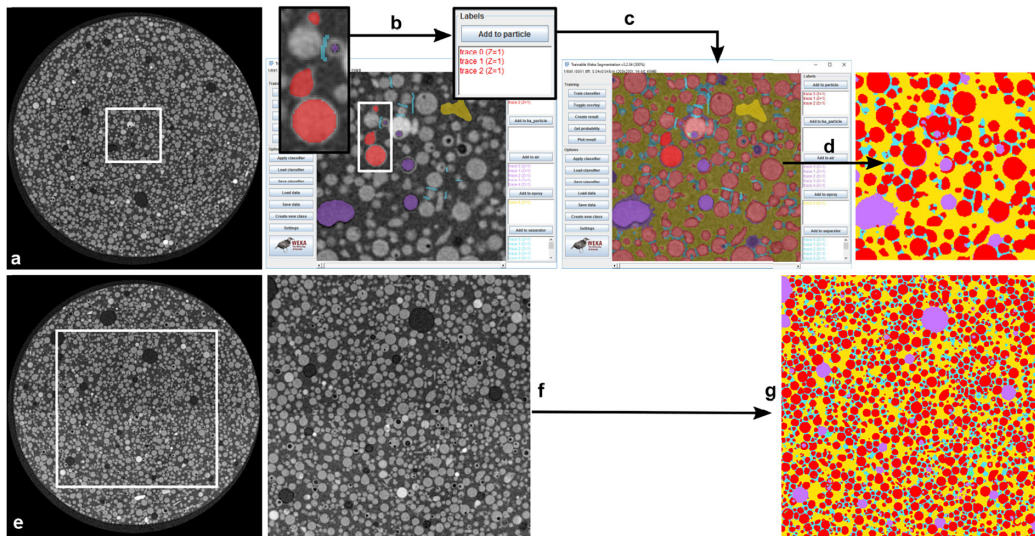


Fig. 4. Application of the trainable WEKA segmentation algorithm. Selection of a cropped training dataset 200 per 200 pixel (a), object assignment to respective classes (b), finally resulting in a model (in this case random forest trees, (c), giving a classified image for validation (d). Application of the model to a larger dataset 600 per 600 pixel (f) to get a classified image (g).

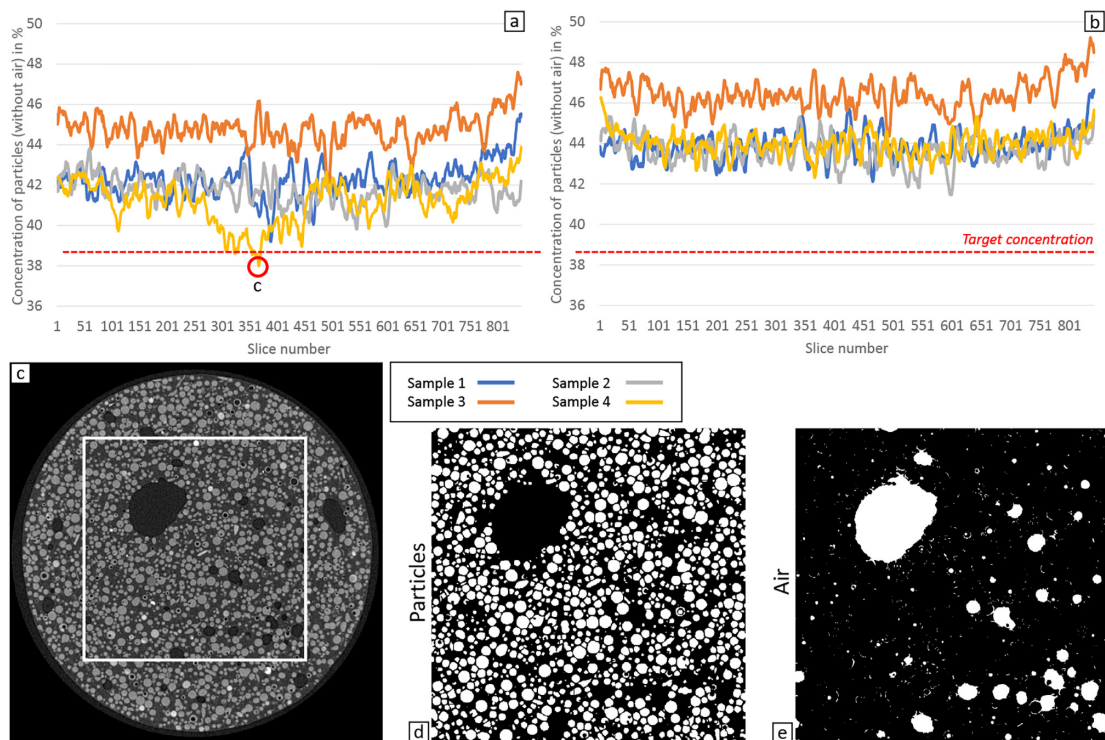


Fig. 5. Concentration of particles in the ENaG matrix for four different samples for (a) without and (b) with correction for air inclusions showing all curves above the theoretical prognosis; (c) one example for air inclusion with binarized section for (d) particles and (e) air.

Material. With 42% to 48%, the calculated value is higher than the target concentration, but close to the expected value considering the very rough porosity estimation. The highest standard deviation is found in Sample 2 with 0.74 vol%, the lowest in Sample 4 with 0.58 vol%.

In figures, there were about 25,000 particles in the analysis volume for the wax method, and about 80,000 particles for the ENaG method. Considering the smaller analysis section of 600 by 600 pixels, an estimated particle number of the total volume of 125,000 is a 5-fold increase compared to the same volume with the wax method.

3.2. Sample homogeneity

The samples' homogeneity was tested by applying the same macro used for the determination of the particle concentration in the previous Section. In contrast to the previously used single thresholding method, the available differentiated segmentation result (see Fig. 4g) now makes it possible to consider all individual classes separately. In a completely homogeneous sample, the proportions would have to be distributed more or less equally over the sample height. Fig. 6 (a) shows all color-coded classes stacked from left to right over the full height of the vertical sample. The share of high attenuating particles is comparably low, which can be seen in a detail magnification (b). The proportions are relatively evenly distributed over the sample height, with Sample 4 showing the largest proportion of air bubbles. Although small variations can be explained by missegmentation, there seems to be a global variation towards the top and bottom of the sample. If we now compare all histograms of the 2D sectional images (macro see Appendix E of the Supplementary Material), we see a clear shift of the histogram peaks very close to the sample edges. This can be explained by the cone beam artefact of the XRM measurement. For the evaluation, the top and bottom 50 slices are removed by default. If we now compare not only the position of the histogram peaks, but also the standard deviation of the grey value distribution per slice, a variation in height emerges here. Since the standard deviation of the grey value distribution of the overall sectional image has been chosen as a training feature in the WEKA algorithm, it quickly becomes clear that a higher standard deviation also affects the variation within individual structures and thus the segmentation result. Since the samples originate from four

independent experiments and were taken at different heights of the tube, an influence of the sampling can be ruled out here. Marginal effects of the segmentation algorithm itself were also examined and evaluated as negligible. Details can be found in Appendix F of the Supplementary Material.

3.3. Particle size distributions

Comparing the distribution densities of the presented ENaG method and the 2D SEM validation there are only minor deviations as can be seen in Fig. 7. These are not restricted to a specific particle size range and are likely the sum of random fluctuations and differences in the particle size determination procedure already described in Section 2. Also, the tomograms of the wax preparation method were classified and segmented in the same way and also show very small deviations. After reconstruction, the wax and the ENaG matrix show nearly the same X-ray attenuation properties, which sounds trivial, but was crucial to successfully apply the same WEKA classification model. Detailed results can be found in Appendix G of the Supplementary Material.

4. Conclusions

As a supplement to the previous study by Ditscherlein et al. [5] based on a shock-frozen wax matrix, we now describe an epoxy-based method for mechanically resistant particle systems. Here, we introduce nanographite particles below the used voxel resolution as spacer to avoid a sedimentation process in the slow-curing epoxy matrix. This method known from 2D automated mineralogy was now validated for 3D tomographic measurements. Since segregation effects no longer play a role, the method is much more suitable for larger particle systems and particle systems of higher density. However, due to the graphite spacer particles used, this only applies to particle systems with an X-ray attenuation coefficient greater than graphite in order to guarantee a sufficiently high contrast in areas of comparable density. The method is also well suited for correlative methods that require mechanically and vacuum stable samples of different sizes. Note again that this method is not suited for brittle particles systems like fibres, because the mechanical treatment would alter the system significantly by particle breakage.

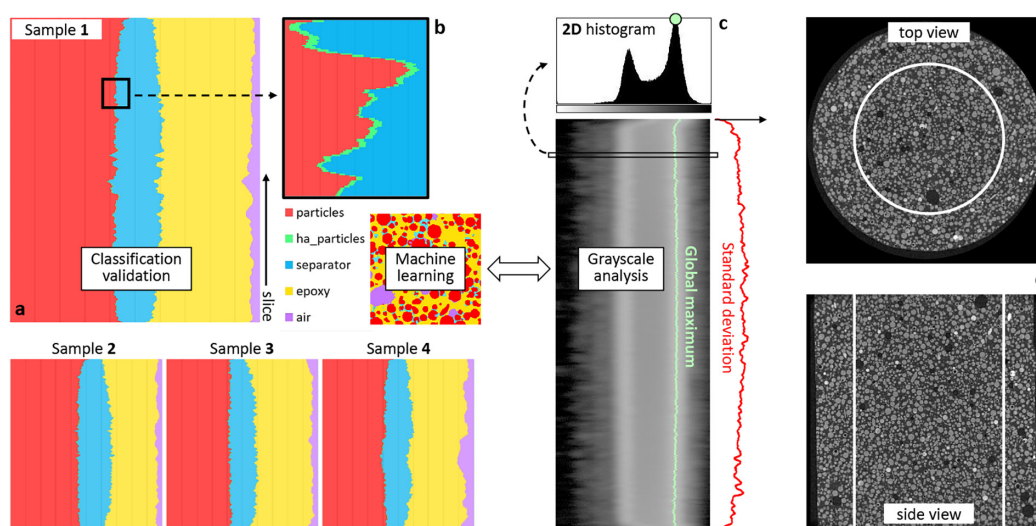


Fig. 6. Verification of the homogeneity of the four samples by stacking the relative proportions of all five classes (a), with magnification to show the very small share of the high attenuating particles (green, b). Additional verification on the stacked 2D histograms (c) acquired from the corresponding 2D slices (d) showing a variation of the standard deviation from the top to the bottom of the stack.

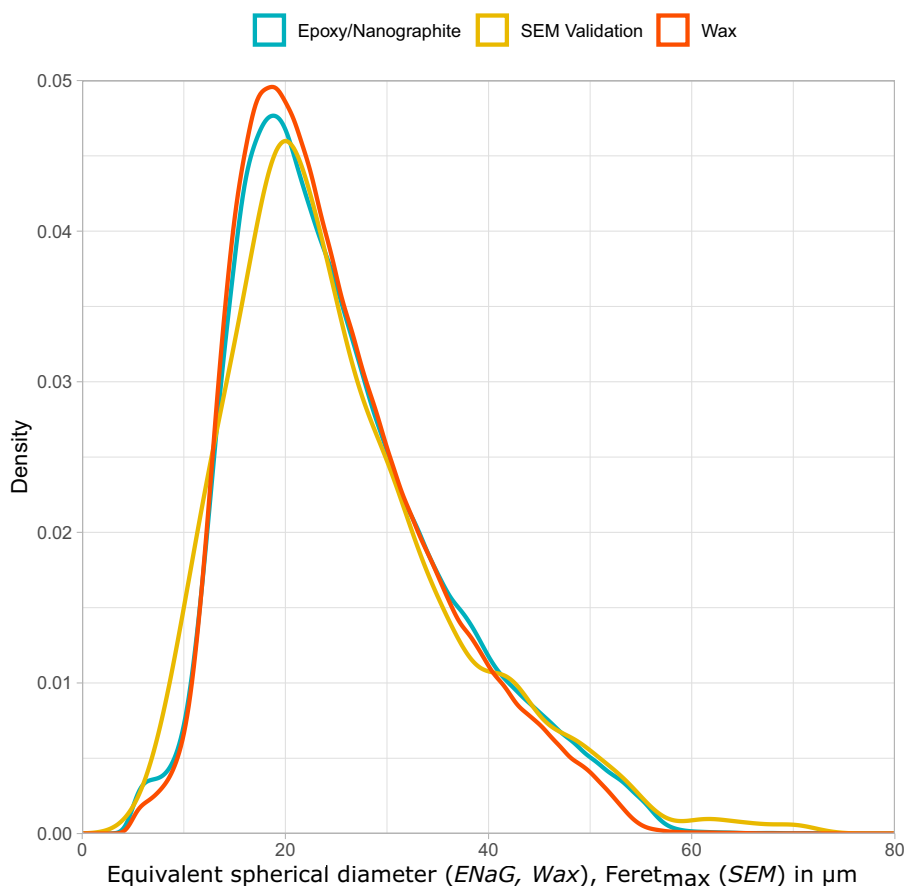


Fig. 7. Comparison of densities originating from the ENaG method, the 2D SEM validation and the re-evaluated wax method from Ditscherlein et al. [5].

The presented approach of WEKA segmentation proves to be promising also for the application for further particle systems even of different preparation methods. A detailed comparison is a reasonable objective for further investigations, but goes far beyond the scope of this paper.

Data availability

Reconstructed TIFF-stacks, acquisition and reconstruction parameters are stored within the scientific data repository of the universities TU Dresden and TU Bergakademie Freiberg with all relevant meta-data [23].

Declaration of Competing Interest

There are no interests to declare in the area of financial and personal relationships.

Acknowledgements

The authors would like to thank the German Research Foundation (DFG) for supporting the project as part of the priority program SPP2045 (313858373), which is dealing with highly specific multidimensional separation of technical ultra-fine particle systems below 10 μm , and the funding of the micro-CT (INST 267/129-1). We would also

like to thank Andreas Bartzsch former group leader of the Erzlabor in Freiberg (laboratory for automated material characterization) for the discussions and the basic procedure know-how and Antje Werner from the Dresden Center for Nanoanalysis for her tips regarding the epoxy sample preparation under vacuum condition. Also Thu Trang Vo, Lisa Ditscherlein and Thomas Buchwald for good ideas and additional proof reading. Erik Löwer for his help in getting started with ImageJ WEKA segmentation.

Appendix A. Supplementary data

Supplementary data to this article can be found online at <http://dx.doi.org/10.1016/j.powtec.2021.09.038>.

References

- [1] J.D. Miller, C.L. Lin, Three-dimensional analysis of particulates in mineral processing systems by cone beam X-ray microtomography, *Mining Metall. Explor.* 21 (2004) 113–124, <https://doi.org/10.1007/bf03403313>.
- [2] E. Maire, P.J. Withers, Quantitative X-ray tomography, *Int. Mater. Rev.* 59 (2013) 1–43, <https://doi.org/10.1179/1743280413Y.0000000023>.
- [3] S.R. Stock, Recent advances in X-ray microtomography applied to materials, *Int. Mater. Rev.* 53 (2008) 129–181, <https://doi.org/10.1179/174328008x277803>.
- [4] O. Furat, T. Leißner, R. Ditscherlein, O. Šedivý, M. Weber, K. Bachmann, J. Gutzmer, U. Peuker, V. Schmidt, Description of ore particles from X-ray microtomography (XMT) images, supported by scanning electron microscope (SEM)-based image

- analysis, *Microsc. Microanal.* 24 (2018) 461–470, <https://doi.org/10.1017/s1431927618015076>.
- [5] R. Ditscherlein, T. Leißner, U.A. Peuker, Preparation techniques for micron-sized particulate samples in X-ray microtomography, *Powder Technol.* 360 (2020) 989–997, <https://doi.org/10.1016/j.powtec.2019.06.001>.
- [6] H. Masuda, K. Gotoh, Study on the sample size required for the estimation of mean particle diameter, *Adv. Powder Technol.* 10 (1999) 159–173, [https://doi.org/10.1016/s0921-8831\(08\)60447-1](https://doi.org/10.1016/s0921-8831(08)60447-1).
- [7] E. Vigneau, C. Loisel, M.F. Devaux, P. Cantoni, Number of particles for the determination of size distribution from microscopic images, *Powder Technol.* 107 (2000) 243–250, [https://doi.org/10.1016/S0032-5910\(99\)00192-8](https://doi.org/10.1016/S0032-5910(99)00192-8).
- [8] E. Garboczi, J. Bullard, 3d analytical mathematical models of random star-shape particles via a combination of X-ray computed microtomography and spherical harmonic analysis, *Adv. Powder Technol.* 28 (2017) 325–339, <https://doi.org/10.1016/j.apt.2016.10.014>.
- [9] S.T. Erdoğan, E.T. Garboczi, D.W. Fowler, Shape and size of microfine aggregates: X-ray microcomputed tomography vs. laser diffraction, *Powder Technol.* 177 (2007) 53–63, <https://doi.org/10.1016/j.powtec.2007.02.016>.
- [10] R. Ditscherlein, T. Leißner, U.A. Peuker, Self-constructed automated syringe for preparation of micron-sized particulate samples in X-ray microtomography, *MethodsX* 7 (2020) 100757, <https://doi.org/10.1016/j.mex.2019.11.030>.
- [11] T. Heinig, K. Bachmann, R. Tolosana-Delgado, G. Boogaart, J. Gutzmer, Monitoring gravitational and particle shape settling effects on MLA sample preparation, IAMG Conference, Freiberg, Germany, 2015.
- [12] E. Schach, M. Buchmann, R. Tolosana-Delgado, T. Leißner, M. Kern, K.G. van den Boogaart, M. Rudolph, U.A. Peuker, Multidimensional characterization of separation processes – Part 1. Introducing kernel methods and entropy in the context of mineral processing using SEM-based image analysis, *Miner. Eng.* 137 (2019) 78–86, <https://doi.org/10.1016/j.mineng.2019.03.026>.
- [13] C. Leone, I. Papa, F. Tagliaferri, V. Lopresto, Investigation of CFRP laser milling using a 30W Q-switched Yb:YAG fiber laser: effect of process parameters on removal mechanisms and HAZ formation, *Composites A* 55 (2013) 129–142, <https://doi.org/10.1016/j.compositesa.2013.08.004>.
- [14] J.E. Spowart, Automated serial sectioning for 3-D analysis of microstructures, *Scr. Mater.* 55 (2006) 5–10, <https://doi.org/10.1016/j.scriptamat.2006.01.019>.
- [15] I. Arganda-Carreras, V. Kaynig, C. Rueden, K. Eliceiri, J. Schindelin, A. Cardona, S. Seung, Trainable Weka Segmentation: a machine learning tool for microscopy pixel classification, *Bioinformatics* 33 (2017) 2424–2426, <https://doi.org/10.1093/bioinformatics/btx180>.
- [16] J. Schindelin, I. Arganda-Carreras, E. Frise, V. Kaynig, M. Longair, T. Pietzsch, S. Preibisch, C. Rueden, S. Saalfeld, B. Schmid, J.-Y. Tinevez, D.J. White, V. Hartenstein, K. Eliceiri, P. Tomancak, A. Cardona, Fiji: an open-source platform for biological-image analysis, *Nat. Methods* 9 (2012) 676–682, <https://doi.org/10.1038/nmeth.2019>.
- [17] A. Kyrieleis, V. Titarenko, M. Ibison, T. Conolly, P.J. Withers, Region-of-interest tomography using filtered backprojection: assessing the practical limits, *J. Microsc.* 241 (2010) 69–82, <https://doi.org/10.1111/j.1365-2818.2010.03408.x>.
- [18] D. Bomze, P. Knaack, R. Liska, Successful radical induced cationic frontal polymerization of epoxy-based monomers by c-c labile compounds, *Polym. Chem.* 6 (2015) 8161–8167, <https://doi.org/10.1039/c5py01451d>.
- [19] T. Leißner, A. Diener, E. “ower, R. Ditscherlein, K. Kr“uger, A. Kwade, U.A. Peuker, 3D ex-situ and in-situ X-ray CT process studies in particle technology – a perspective, *Adv. Powder Technol.* 31 (2020) 78–86, <https://doi.org/10.1016/j.apt.2019.09.038>.
- [20] F.E. Boas, D. Fleischmann, CT artifacts: causes and reduction techniques, *Imaging Med.* 4 (2012) 229–240, <https://doi.org/10.2217/iim.12.13>.
- [21] J. Ollion, J. Cochenec, F. Loll, C. Escudé, T. Boudier, TANGO: a generic tool for high-throughput 3D image analysis for studying nuclear organization, *Bioinformatics* 29 (2013) 1840–1841, <https://doi.org/10.1093/bioinformatics/btt276>.
- [22] F.P. Bolte, S. Cordelières, A guided tour into subcellular colocalization analysis in light microscopy, *J. Microsc.* 224 (2006) 213–232, <https://doi.org/10.1111/j.1365-2818.2006.01706.x>.
- [23] R. Ditscherlein, Different Mixtures (By Volume) of Graphite-Nanoparticles and Analysis Particles, 2020 <https://doi.org/10.25532/OPARA-82>.

Supplementary Material

Preparation strategy for statistically significant micrometer-sized particle systems suitable for correlative 3D imaging workflows on the example of X-ray microtomography

Ralf Ditscherlein^{1,*}, Thomas Leißner¹, and Urs A. Peuker¹

¹Institute of Mechanical Process Engineering and Mineral Processing, Technische Universität Bergakademie Freiberg, D-09599 Freiberg, Germany

*corresponding author: ralf.ditscherlein@mvtat.tu-freiberg.de, phone: +49 3731 39-2714, fax: +49 3731 39-2947

Appendix A: XRM Measurements

In our case, all scans were carried out with an XRM, ZEISS Xradia 510 Versa. Compared to standard micro-CT devices, with an XRM we are able to apply a second magnification step to increase the resolution by a factor of 10. Therefore, after passing the sample, the geometrically magnified signal is projected on a scintillator screen, converted to VIS and magnified a second time with microscopic optics (magnifications 0.4x, 4x, 20x, 40x). So, it is possible to reach a minimum voxel size of about $0.3\ \mu\text{m}$. Table S1 summarizes detailed measurement parameters.

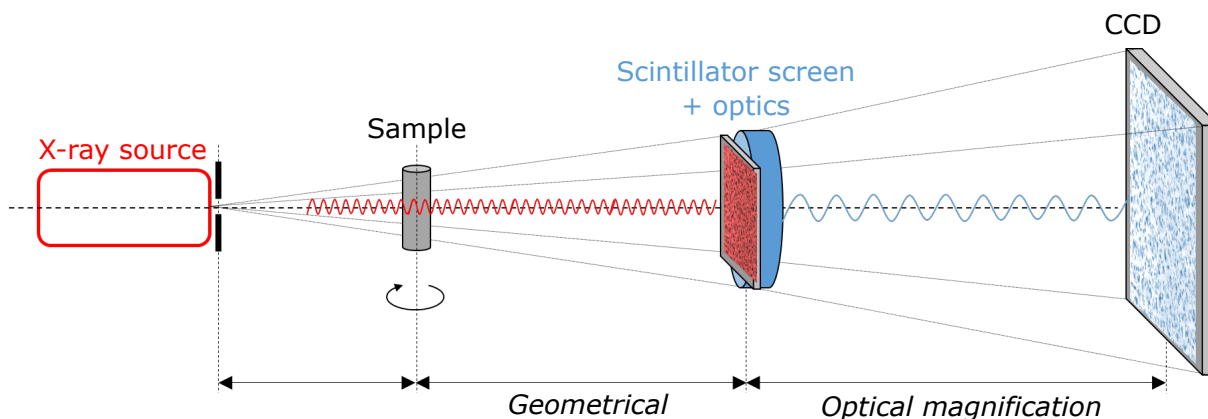


Figure S1: XRM setup with highlighted X-ray cone-beam path (red) and transformed VIS beam path (blue).

Table S1: Parameters for measurement (Meas.) and subsequent reconstruction (Recon.) for both, Low-resolution (Low-res) and High-resolution (High-res) measurements.

	Parameter	Low-res	High-res
Meas.	Sample size / mm	2	0.5
	Field of View (FOV) / mm	2	0.4
	Acceleration voltage / keV	80	80
	Electrical power / W	7	7
	Source filter (Zeiss standard)	LE4	LE2
	Exposure time / s	1	10
	Optical magnification	4	0.4
	Number projections	2001	2001
	Angle range / deg	360	360
	Voxel size / μm	2	0.4
	Binning	2	2
Recon.	Algorithm		FBP
	Smoothing (Gauß)		0.7
	Beam Hardening Correction		0.05

Appendix B: WEKA Feature Extraction

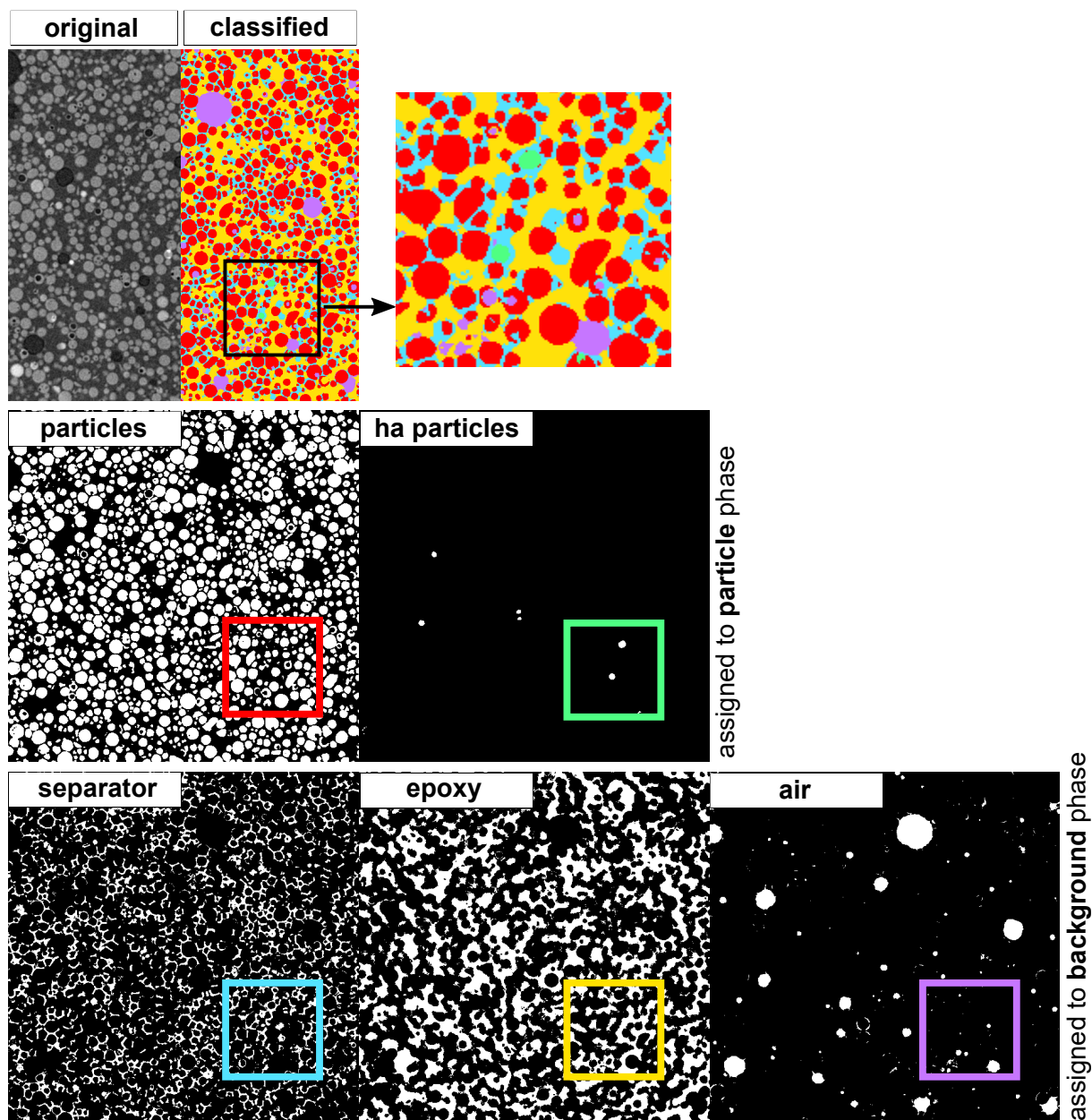


Figure S2: Validation of assignment result to all five distinct classes, which are particles, high attenuating (ha) particles, both assigned to the superior group of the particle phase, separator, epoxy and air, all three assigned to the superior group of the background phase. Note that the markings correspond to the magnification of the segmentation result and the respective colours correspond to the classes.

Appendix C: SEM Validation

As a reasonable validation method, a proper particle sample was dispersed on an object slice. After taking 10 SEM images on 10 random positions, all particles in these images were marked in ImageJ manually and corresponding diameters were summarized as a whole sample of ≈ 1000 particles.

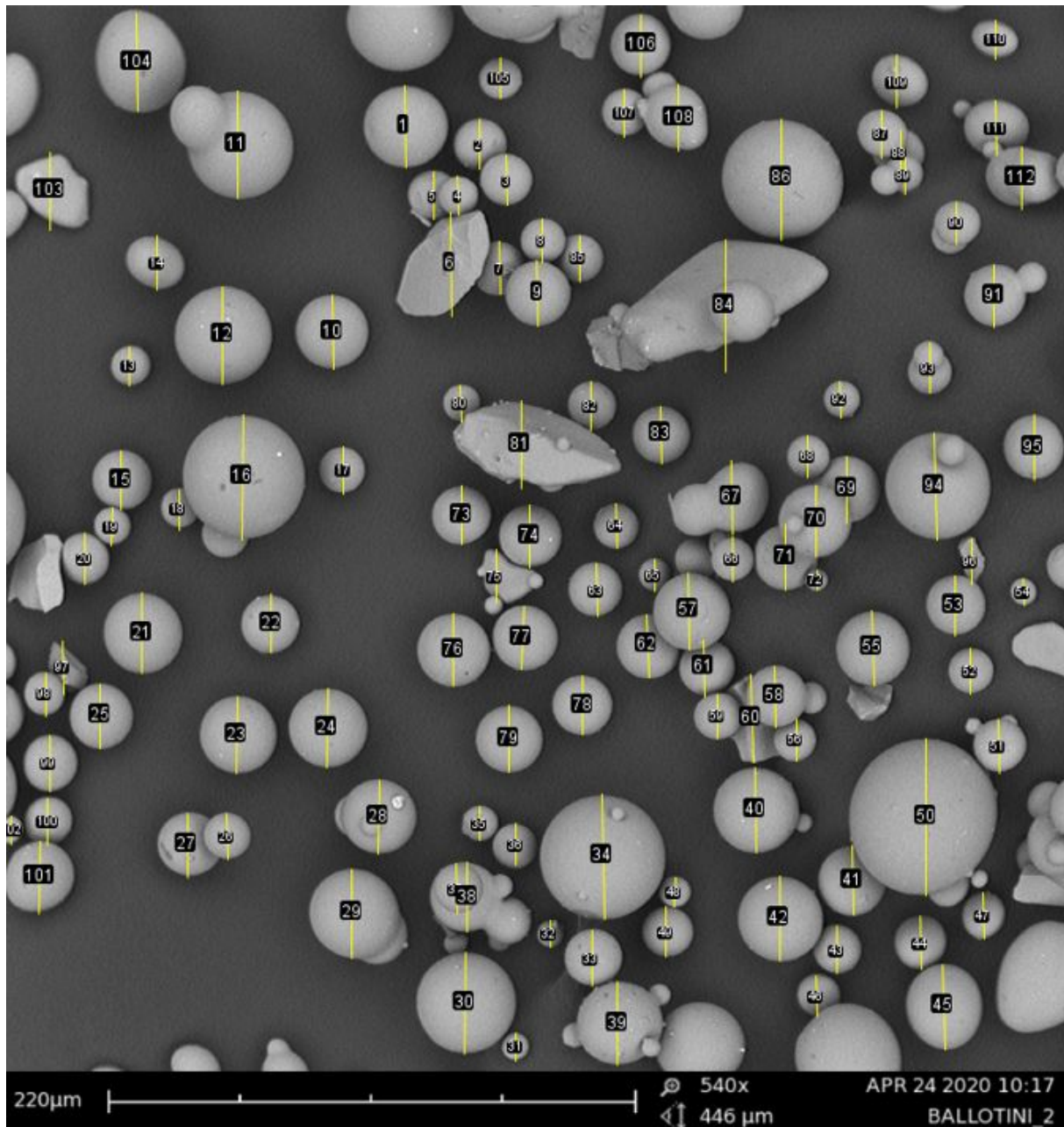


Figure S3: Exemplary SEM image for 2D validation.

Appendix D: ImageJ Macro – Concentration

```
dir = getDirectory("Choose a Directory with BINARY Images (Particles white |  
Background black");  
list = getFileList(dir);
```

```

row = 0;
nBgPxSum = 0;
nPtPxSum = 0;
pC = newArray(list.length+1);
nBgPx = newArray(list.length+1);
nPtPx = newArray(list.length+1);
slice = newArray(list.length+1);

//iterating through the whole image stack
for (f=0; f<list.length; f++) {
  path = dir+list[f];
  if (!endsWith(path, "/")) open(path);
  if (nImages>=1) {
    if (endsWith(path, "f")) {
      t=getTitle();
      s=lastIndexOf(t, '.');
      t=substring(t, 0,s);
      t=replace(t, " ", "_");
      t2= t +'_filtered';

      run("Clear Results");
      nBins = 256;
      getHistogram(values, counts, nBins);
      numberBgPixel = counts[0];
      numberPtPixel = counts[255];
      particleConcentration = numberPtPixel / (numberBgPixel + numberPtPixel) *
        100;

      nBgPxSum = nBgPxSum + numberBgPixel;
      nPtPxSum = nPtPxSum + numberPtPixel;

      slice[row] = list[f];
      nBgPx[row] = numberBgPixel;
      nPtPx[row] = numberPtPixel;
      pC[row] = particleConcentration;

      row++;
      close();
    }
  }
}

particleConcentrationVolume = nPtPxSum / (nBgPxSum + nPtPxSum) * 100;

//writing all results to an array (direct table output not working)
run("Clear Results");
setResult("sliceNumber", 0, "ALL");
setResult("NumberBackgroundPixel", 0, nBgPxSum);
setResult("NumberParticlePixel", 0, nPtPxSum);
setResult("ParticleConcentrationInPct", 0, particleConcentrationVolume);

for (i=1; i<list.length+1; i++) {
  setResult("sliceNumber", i, slice[i]);
  setResult("NumberBackgroundPixel", i, nBgPx[i]);
  setResult("NumberParticlePixel", i, nPtPx[i]);
  setResult("ParticleConcentrationInPct", i, pC[i]);
}

```

```

}

setResult("sliceNumber", list.length+1, dir);

```

Appendix E: ImageJ Macro – Stacked Grey Values

```

dir = getDirectory("Choose a Directory with BINARY Images (Particles white |
    Pores black");
list = getFileList(dir);
//stretching of the log-scale to get "nice" gray scale
logLevel = 50;
row = 0;
newImage("2DHistogram", "8-bit white", 255, 1000, 1);
newImage("MaxCountDistribution", "8-bit black", 255, 1000, 1);

for (f=0; f<list.length; f++) {
    path = dir+list[f];
    if (!endsWith(path, "/")) open(path);
    rename("slice");

    nBins = 256;
    selectImage("slice");
    makeOval(0,0,600,600);
    getHistogram(values, counts, nBins);
    selectImage("2DHistogram");
    maxValueInRow = 0;
    posOfMaxValueInRow = 1;

    for (i = 0; i < 255; i++) {
        //log-transformation of the data
        //log() is the natural log, divided by log(10) it gives the 10-based log
        logCounts = log(counts[i])/log(10) * logLevel;
        if (logCounts > maxValueInRow) {
            maxValueInRow = logCounts;
            posOfMaxValueInRow = i;
        }
        setPixel(i, row, logCounts);
    }
    selectImage("MaxCountDistribution");
    //one pixel before and after the max to enhance visibility
    setPixel(posOfMaxValueInRow-1, row, 255);
    setPixel(posOfMaxValueInRow, row, 255);
    setPixel(posOfMaxValueInRow+1, row, 255);

    //log(0) --> -infinity-value ("1/0") will be changed to "0"
    changeValues(1/0, 1/0, 0);
    close("slice");

    row++;
}

//overlay of max peak over the generated 2D histogram
run("Merge Channels...", "c2=MaxCountDistribution c4=2DHistogram create keep");

```

Appendix F: Potential WEKA Marginal Effects

To investigate potential marginal effects of the machine learning assisted classification algorithm, Sample 1 was artificially divided into three separate datasets. After performing the classification via the WEKA algorithm, the relative differences of the individual datasets to the total dataset were determined. Figure S4 shows only slight variations in the marginal regions, the “contact region” of the individual parts.

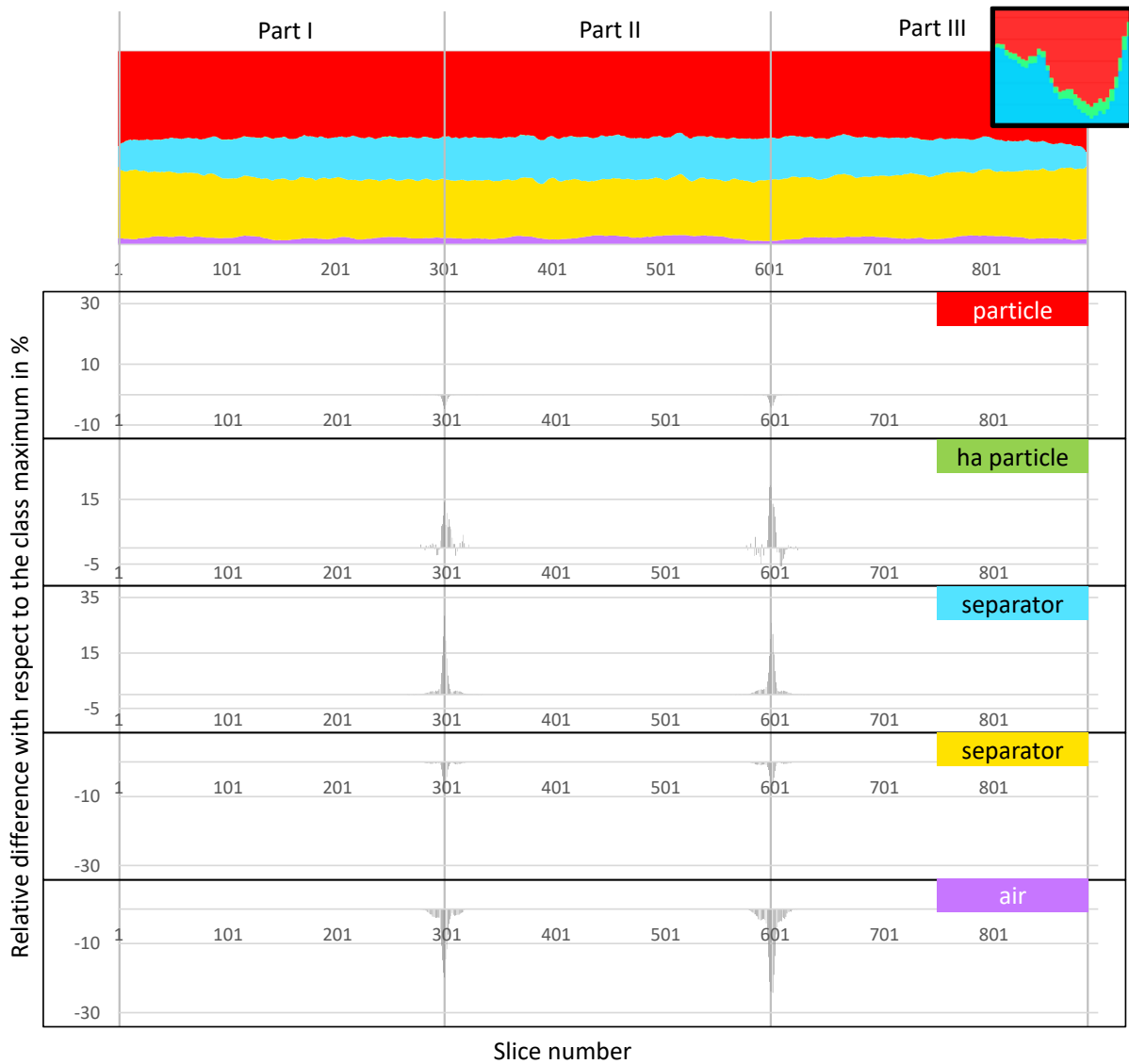


Figure S4: Relative difference between the original dataset and three related subsets.

Appendix G: Detailed Results

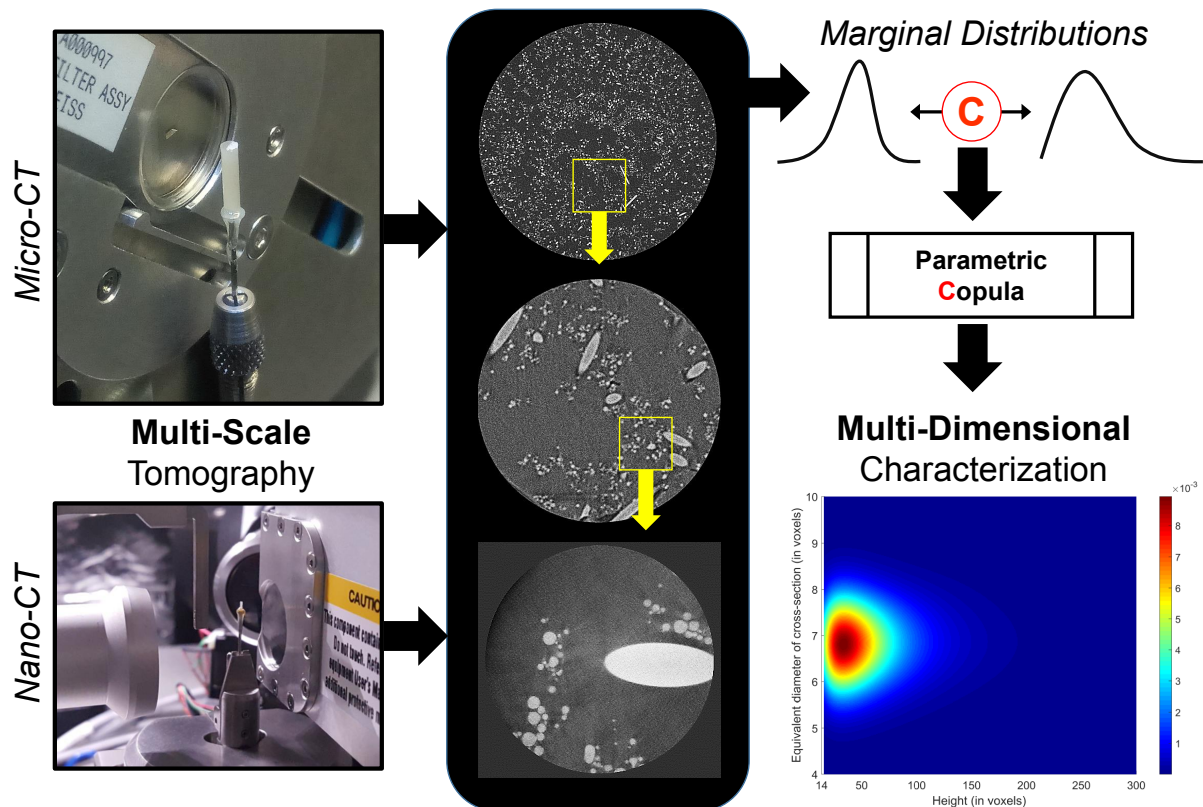
	2D REM	epoxy/nanographite				wax particle conc. 10%								
		1	2	3	4	10-1			10-2			10-3		
<i>in μm</i>						<i>mid</i>	<i>bot</i>	<i>top</i>	<i>mid</i>	<i>bot</i>	<i>top</i>	<i>mid</i>	<i>bot</i>	<i>top</i>
avg	25.42	25.47	25.23	25.68	25.18	25.12	25.36	24.94	24.38	24.55	24.68	24.66	24.80	24.63
stddev		0.20				0.28								
q01	8.35	7.72	7.72	7.99	7.81	8.74	9.64	7.96	8.41	9.07	9.27	8.90	8.74	8.52
q05	11.26	12.33	12.33	12.47	12.36	12.53	13.00	12.11	12.25	12.46	12.53	12.67	12.39	12.36
q10	13.14	14.19	14.16	14.36	14.14	14.28	14.57	14.01	13.87	14.06	14.12	14.31	14.12	14.04
q50	23.14	23.38	23.14	23.69	23.02	23.19	23.53	23.05	22.36	22.60	22.68	22.70	22.79	22.65
q25	17.77	17.76	17.63	18.09	17.58	17.79	18.01	17.60	17.26	17.44	17.42	17.58	17.49	17.38
q75	30.87	31.54	31.16	31.61	17.58	30.88	31.16	30.83	29.91	30.09	30.40	30.17	30.50	30.26
q90	41.79	40.65	40.11	40.76	40.09	39.26	39.28	39.23	38.35	38.49	38.74	38.61	38.99	38.74
q95	47.86	45.91	45.63	46.03	45.53	44.35	44.36	44.40	43.27	43.60	43.79	43.69	43.96	43.91
q99	58.83	53.25	53.03	53.40	53.03	51.33	51.22	51.38	50.29	50.35	50.58	50.53	51.05	50.95
number particles	1034	77,748	84,929	76,468	78,413	21,065	22,717	21,886	22,258	24,782	20,476	21,338	23,077	21,653
...extrapolated (*)		122,064	133,339	120,055	123,108									

wax particle conc. 15%								
15-1			15-2			15-3		
<i>mid</i>	<i>bot</i>	<i>top</i>	<i>mid</i>	<i>bot</i>	<i>top</i>	<i>mid</i>	<i>bot</i>	<i>top</i>
24.92	24.98	25.31	24.37	23.75	24.80	24.33	25.49	24.87
0.50								
8.29	9.27	8.73	9.01	8.74	8.73	22.45	23.60	22.91
12.45	12.87	12.77	12.53	12.32	12.77	8.94	10.44	8.44
14.23	14.44	14.46	14.14	13.92	14.46	12.53	13.34	12.57
23.02	23.10	23.37	22.51	22.03	22.84	14.14	14.88	14.31
17.70	17.75	17.89	17.41	17.20	17.89	17.46	18.28	17.63
30.58	30.68	31.16	29.66	28.81	31.16	29.73	31.17	30.51
39.16	38.85	39.79	37.97	36.43	39.79	37.67	39.43	39.11
44.08	43.77	44.54	43.01	41.31	44.54	42.80	44.12	44.16
51.02	50.52	51.10	49.98	49.04	51.10	50.17	50.86	50.77
32,715	32,658	31,685	31,685	31,051	31,685	30,570	46,247	35,492

Paper D

Microscopy and Microanalysis, June 2020 (open access)
*Multi-Scale Tomographic Analysis for
Micron-Sized Particulate Samples*

Graphical Abstract



Highlights

- Multiscale characterization of two very different particle populations in the micro- and submicrometer range by combining X-ray micro- and nano-CT
- Capturing the multidimensional correlation structure of both systems with statistically representative quantities by using parametric copulas

Original Article

Multiscale Tomographic Analysis for Micron-Sized Particulate Samples

Ralf Ditscherlein^{1*}, Orkun Furat², Mathieu de Langlard², Juliana Martins de Souza e Silva³, Johanna Sygusch⁴, Martin Rudolph⁴, Thomas Leißner¹, Volker Schmidt² and Urs A. Peuker¹

¹Institute of Mechanical Process Engineering and Mineral Processing, Technische Universität Bergakademie Freiberg, D-09599 Freiberg, Germany; ²Institute of Stochastics, Ulm University, D-89069 Ulm, Germany; ³Institute of Physics – mikroMD, Martin Luther University Halle-Wittenberg, D-06120 Halle, Germany and ⁴Helmholtz Institute Freiberg for Resource Technology, D-09599 Freiberg, Germany

Abstract

The three-dimensional characterization of distributed particle properties in the micro- and nanometer range is essential to describe and understand highly specific separation processes in terms of selectivity and yield. Both performance measures play a decisive role in the development and improvement of modern functional materials. In this study, we mixed spherical glass particles (0.4–5.8 μm diameter) with glass fibers (diameter 10 μm , length 18–660 μm) to investigate a borderline case of maximum difference in the aspect ratio and a significant difference in the characteristic length to characterize the system over several size scales. We immobilized the particles within a wax matrix and created sample volumes suitable for computed tomographic (CT) measurements at two different magnification scales (X-ray micro- and nano-CT). Fiber diameter and length could be described well on the basis of the low-resolution micro-CT measurements on the entire sample volume. In contrast, the spherical particle system could only be described with sufficient accuracy by combining micro-CT with high-resolution nano-CT measurements on subvolumes of reduced sample size. We modeled the joint (bivariate) distribution of fiber length and diameter with a parametric copula as a basic example, which is equally suitable for more complex distributions of irregularly shaped particles. This enables us to capture the multidimensional correlation structure of particle systems with statistically representative quantities.

Key words: multidimensional particle characterization, multiscale X-ray tomography, parametric copula, statistical image analysis

(Received 19 March 2020; revised 25 May 2020; accepted 13 June 2020)

Introduction

The characterization of distributed particle properties is a key challenge in chemical engineering to understand the relation between microscopic features and macroscopic effects. Two-dimensional (2D) imaging methods are used to reveal multiple properties at once. Static methods, such as light microscopy, were supplemented by dynamic methods, which represent a significant development, especially with regard to the statistical representativeness of the samples (Brown et al., 2005). Image tracking algorithms were used to compensate for stereological errors from the 2D image description, but only down to particle sizes of around 100 μm (Macho et al., 2019). A complete three-dimensional (3D) description of a collective of particles smaller than 10 μm is not possible with these methods.

Computed tomography (CT) measuring methods, on the other hand, are well-established over length scales from centimeter to

the submicrometer range. Depending on the physical measurement principles and the experimental setup, every measuring method has its limitations, both in analysis volume and spatial resolution. X-ray CT is one of the most common 3D imaging techniques used in the engineering sciences to visualize internal structures of solid-state phases nondestructively (Stock, 1999). The X-rays used are capable of penetrating solid matter, their absorption coefficient being a function of the material density of the sample, the length penetrated, the photon energy, and the atomic number of the compound elements. The measurement parameters are therefore strongly related to the material and its dimensions (Pavlin, 2008). Compared to 2D radiological imaging, the tomography setup offers a chance to analyze the 3D structure of objects in the field of view (FOV) without stereological error. By rotating the sample, a series of projections can be captured—each image with the attenuated sum signal along the beam path. The transformation of the series of 2D images into a 3D volume is based on Fourier, algebraic, or statistical algorithms (Buzug, 2008).

Initially only available at monochromatic synchrotron facilities, state-of-the-art systems are now also available in laboratories, for micrometer (X-ray micro-computed tomography, micro-CT) and submicrometer range imaging (X-ray nano-computed

*Author for correspondence: Ralf Ditscherlein, E-mail: ralf.ditscherlein@mvttat.tu-freiberg.de

Cite this article: Ditscherlein R, Furat O, de Langlard M, Martins de Souza e Silva J, Sygusch J, Rudolph M, Leißner T, Schmidt V, Peuker UA (2020) Multiscale Tomographic Analysis for Micron-Sized Particulate Samples. *Microsc Microanal*. doi:10.1017/S1431927620001737

tomography, nano-CT) (Maire & Withers, 2014). This has opened up the possibility to work on extensive questions from particle measurement technology even without access to measurement time at synchrotron beamlines.

Particles with sizes below the voxel resolution are often used for contrast enhancement of complete phases or as markers of specific regions (Shilo et al., 2012). Alternatively, particles with sizes larger than the voxel resolution can be used directly as alignment markers in 3D imaging (Hagen et al., 2014). Studies on particle properties can be found for single particles (Liu et al., 2016), a limited number (10–100) of free particles (Bagheri et al., 2015), as crystals in mineralogical phases (Kahl et al., 2017) or as macroscopic units with properties like layer thickness (Zhong et al., 2019) or bulk properties (Sjödahl et al., 2012). In contrast, the tomographic analysis of particulate samples of a statistically relevant quantity (more than 1000 particles) with distributed multidimensional properties is rarely mentioned in the literature (Cepuritis et al., 2017).

Since particle systems are, in many cases, composed of particles with size distributions covering more than one size scale, a multiscale approach is a fundamental requirement in order to be able to describe them precisely with respect to their multidimensional properties. Studies often focus on solids to determine material properties like layer composition (Moroni et al., 2016) or micro-processes like crack formation (Burnett et al., 2014). In this study, we investigated a mixture of two particle systems of very different particle sizes. We created a 50/50 (by weight) mixture of spherical glass particles (diameter min $0.4\ \mu\text{m}$, median $1.2\ \mu\text{m}$, max $5.8\ \mu\text{m}$) and glass fibers (diameter $10\ \mu\text{m}$, median length $82\ \mu\text{m}$, longest fiber $660\ \mu\text{m}$) to investigate a borderline case of maximum difference in the aspect ratio and a significant difference in size. Thus, the geometrical properties of spheres and fibers can only be analyzed simultaneously by a combination of tomographic analysis methods on two magnification levels (X-ray micro- and nano-CT).

The basis of a quantitative evaluation of the reconstructed tomography image data is a sequence of individual image processing algorithms that is precisely adapted to the properties of the individual particles in the image (image processing workflow). In our case, we start to identify the fibers and the spheres by segmentation. This is a fundamental step, since the statistical analysis of the particle system strongly depends on the shape and size of the particles and thus on the quality of segmentation. Therefore, we apply the so-called marker-controlled watershed transform, one of the most widely used segmentation algorithms, which has proved to be robust and efficient (Meyer & Beucher, 1990; Soille, 2013). The geometry of a segmented fiber is characterized by its length, specific surface area, and cross-section diameter. A parametric representation of the bivariate distribution of the fiber's length and the specific surface area is obtained using copula theory (Durante & Sempi, 2015). The fitted copula model enables to capture the correlation structure between the length and the specific surface area (the so-called marginal distributions), hence, leading to a more informative description of the fiber system. For the spheres, the volume-equivalent diameter and the specific surface area are used as geometrical criteria, and a copula model is also fitted to this bivariate distribution. Therefore, it is possible to get a full parametric description of the entire particle system by combining the two individual copula models, either using a number- or volume-weighted version of the bivariate probability density functions.

This paper is organized as follows. In the section Materials and Methods, we introduce our sample preparation method, focusing on representativeness and sample size. A summary of the measurement parameters and the description of the image processing procedure then presented. In the section Results and Discussion, we propose a reasonable multidimensional characterization approach, using a copula model and correcting edge effects, to characterize the particulate material composed of fibers and spheres.

Materials and Methods

Preparation of Particulate Samples

A conclusive tomographic analysis of a particulate sample has to meet the following requirements:

1. Enough particles to describe statistically relevant distributed properties.
2. FOV-adjusted sample size to avoid large scanning times and artifacts.
3. Spatially separated particles to avoid segmentation errors.
4. An appropriate voxel size to distinguish interesting features.

These four requirements have to be balanced with respect to the number and the size ranges of particles. The last two requirements are related to the partial volume effect (see Supplementary Appendix B).

Statistical Representativeness

Analyzing particles as a collective with distributed properties requires a representative sample within a scanned volume. Practical approaches to calculate a minimum number of particles based on statistical models are given in the literature (Koglin et al., 1974; Vigneau et al., 2000). We determined the optimal volume concentration of spherical particles, immobilized and embedded in a matrix, in prestudies with 10 vol% (Ditscherlein et al., 2019). The minimum concentration c_{\min} is given by the ratio of the total particle volume V_{Particle} and the volume of the sample cylinder V_{Cylinder} i.e.,

$$c_{\min} = \frac{V_{\text{Particle}}}{V_{\text{Cylinder}}} = \frac{n_{\text{Particle}} \cdot \frac{4}{3} \pi \cdot x^3}{n_{\text{Stitch}} \cdot \pi \left(\frac{d_C}{2}\right)^2 \cdot h_C}, \quad (1)$$

with the number of particles n_{Particle} , equivalent spherical particle diameter x , the number of vertical stitches n_{Stitch} (in this study, equal to 1), diameter d_C , and height h_C of the sample cylinder. In Figure 1, the determined minimum number of particles is shown as a set of ISO-lines going from low particle volume concentrations to a limit concentration for a monodisperse particle fraction (hexagonal close packing, $c \approx 0.74$, see case (b) in Fig. 1). Due to limited machining capabilities for sample preparation, there is also a practical lower limit of the sample size (c). The shift from a large FOV (a-1) to a smaller one (a-2) with constant particle size (equivalent spherical diameter) means that the resulting operating point is near the first ISO-line (10,000 particles) for $c_{\min} = 0.01$. The estimation of the minimum concentration using equation (1) is exact solely in the case of sphere-like particles. The generation of a sufficient fiber statistic is much more challenging when combined with spheres which are two to three scales smaller

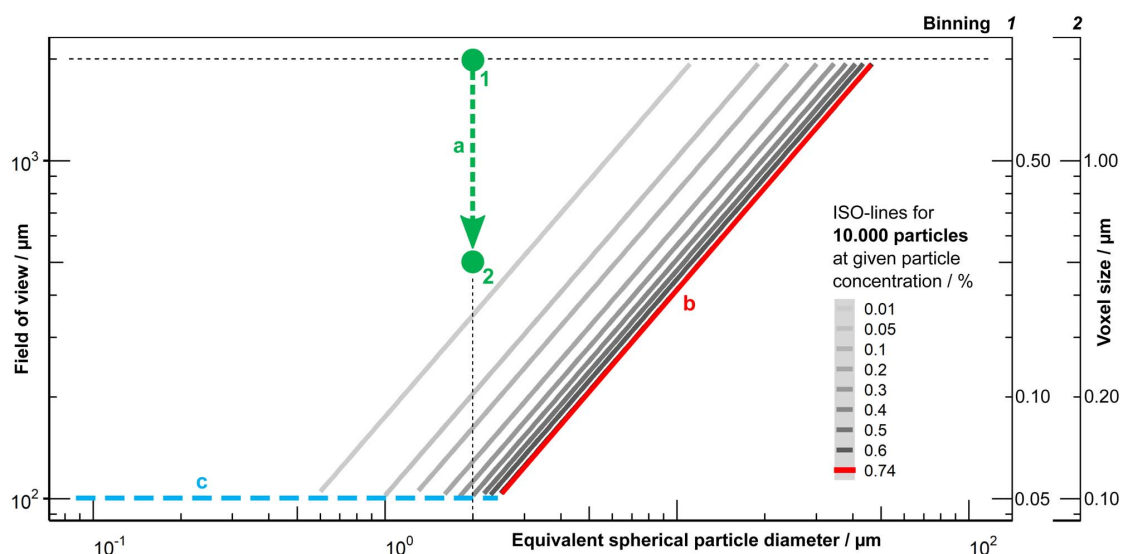


Fig. 1. Possible working area for preparation of particulate samples for a target particle number of 10,000 going from large FOV (a-1) to a smaller FOV (a-2), with concentration limit for spherical monodisperse hexagonal close packing (b) and a minimum FOV due to sample processing (c).

than the longest fiber. In such a situation, the measurement of a suitable sample volume over two different length scales is required.

Sample Size Adjustment

If the required FOV at a chosen magnification is smaller than the biggest lateral dimension of the sample, regions that are only illuminated by penetrating X-rays in certain angle ranges create artifacts in the reconstructed sample volume (Kyrieleis et al., 2010) (especially for highly X-ray absorbing materials). A well-known rule of thumb to determine the needed number of tomographic projections is $n_{\text{Projection}} = \pi/2 \cdot n_{\text{Pixel, Detector}}$. For scans inside the sample (Region of interest tomography, see Supplementary Appendix D), the detector does not cover the entire area of the actual projection image that can lead to artifacts in the final reconstruction. To avoid that, the number of detector pixels $n_{\text{Pixel, Detector}}$ has to be increased to reach the largest lateral dimension of the sample ($n_{\text{Pixel, Sample}}$). This requires a much longer scan time, not only by increasing the number of projection angles but also by the longer X-ray radiation per projection angle. In the case of monochromatic X-rays (nano-CT), the integral energy flux is very low compared with the polychromatic radiation of the micro-CT (for details regarding the CT scanners, see Section Multiscale tomographic measurement or Supplementary Appendix C). Thus, these effects are getting even worse. Reducing sample size (Fig. 2a) is the best way to minimize scan time and to avoid artifacts. Nevertheless, a system of particles with very high aspect ratio (fibers) is a natural limitation. This can only be overcome by measuring on two different scales with two different sample sizes: Large samples for low-resolution (low-res) scans and smaller samples for medium-resolution (med-res) and high-resolution (high-res) scans.

Immobilization by Wax Embedding

The particle system considered in this study was a mixture (50/50 by weight) of two types of glass particle fractions, one being spheres and the other fibers. Spherical soda-lime glass particles were purchased from VELOX, Germany (SG7010, $Q_{0.10}$ 0.62 μm , $Q_{0.50}$ 2.67 μm , $Q_{0.90}$ 4.99 μm), borosilicate-glass fibers from Schwarzwälder Textil-Werke, Germany (FG160/060) with median fiber length of 82 μm , largest fiber length of 660 μm , and narrowly distributed average fiber diameter of 10 μm . Some statistical measures were performed using images acquired from light microscopy and scanning electron microscopy (SEM) and are summarized in Supplementary Appendix A.

To avoid motion artifacts and to ensure the spatial homogeneity of the particles in a sample volume for optimal image segmentation results, the particles must be immobilized. Conventional methods of particle embedding in epoxy-based resins, as used in the preparation of polished sections, e.g., multidimensional particle analysis using Mineral Liberation Analysis (MLA) (an example given by Buchmann et al., 2018), are not suitable here due to the long curing times. Therefore, we have embedded the particles in a histological wax that is normally used for biological sample preparation. We used a target volume concentration of 10%, which we controlled in image segmentation afterwards. Subsequent to drawing of the molten wax particle suspension into a polymer tube, the volume was shock-frozen within the small polymeric tube, resulting in a sample cylinder of approximately 1.6 mm diameter after forming (Ditscherlein et al., 2020). Figure 2a shows the sample preparation procedure beginning with a cylindrical shape (2 mm diameter, a-1) for low-resolution scans, that is manually sliced down (a-3 and a-4) to a bar for medium- and high-resolution scans (≈ 0.5 mm diameter, a-5). In previous studies (Ditscherlein et al., 2019), we showed that the particles are homogeneously distributed over the sample height. Thus, considering two of these different positions from the cylindrical sample was sufficient for the current study.

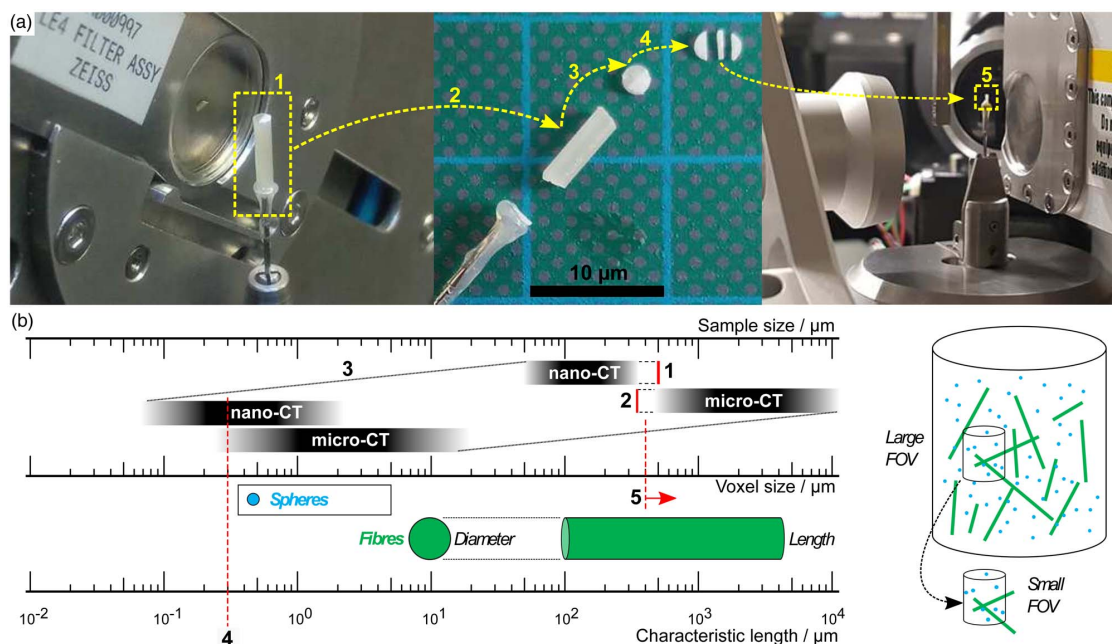


Fig. 2. Large sample mounted on rotating sample stage (a-1), unmounted (a-2) for slicing in small disks (a-3) and sectioning into a small bar (a-4), and remounted for medium- and high-resolution measurements (a-5). Relation between sample size, voxel size, and characteristic particle size—corresponding range marked with a box: extended FOV of nano-CT by ROI measurement (b-1), minimum sample size limited by machining (b-2), fixed correlation between sample and voxel size determined by binning factor (b-3), overlapping measurement field for determining fine particle fraction (b-4), and micro-CT measurement to determine fiber length (b-5).

Multiscale Tomographic Measurements

When handling voxel-based data, it is important to distinguish between voxel and spatial resolution. The voxel resolution only describes the 3D equivalent to the detector pixel resolution (considering the binning to virtual pixels), which is given by the mechanical and optical magnification of the system. This information is insufficient with respect to the effective spatial (structural) resolution, which is a function of the measurement parameters and the properties of the sample itself. Taking this into account, objects smaller than 100 voxels were removed from the data set. In all three resolution modes, the tomograms were exported as a stack of tiff images of approximately 1024×1024 pixels. A comparison of both experimental setups is shown in Supplementary Appendix C. Measurement parameters are summarized in Table 1.

Micro-CT Measurements

Low-resolution and medium-resolution measurements were performed using a micro-CT (Zeiss Xradia VERSA 510) with a polychromatic X-ray source, a rotating tungsten anode, a maximum acceleration voltage of 160 keV, and a maximum power of 10 W. Compared to conventional X-ray micro-CT systems, an additional optical system increases magnification by a factor of 10. This two-step magnification gives a minimum voxel size of $0.3 \mu\text{m}$. Reconstruction was done using the software Zeiss XMReconstructor (Version 11.1.8043) with the aim of minimizing manipulations in preprocessing (smoothing, beam-hardening correction). No beam hardening was visible in the reconstructed slices. Due to the cone beam artifact, 50 slices were removed

from the top and bottom of the data set before image postprocessing. A summary of relevant artifacts related to micro-CT measurements is given by Boas & Fleischmann (2012) and Davis & Elliott (2006).

Nano-CT Measurements

High-resolution imaging was performed using a nano-CT (Zeiss Xradia Ultra 810), which operates at a constant X-ray photon energy of 5.4 keV (monochromatic, no beam-hardening artifacts) with parallel beam geometry (no cone-beam artifacts) and a rotating chromium anode. The minimum voxel size in high-resolution mode is 16 nm. For the experiments, absorption contrast imaging in large field of view mode (minimum voxel size 64 nm) was used. Image reconstruction was performed by means of the software Zeiss XMReconstructor (Version 10.0.3878.16108).

Image Segmentation

Marker-Controlled Watershed Transform

The segmentation procedure for each CT image is based on the *marker-controlled watershed transform*. One of the first papers where the watershed transform was considered is presented by Meyer & Beucher (1990). It takes advantage of the topographic representation of a grayscale image: the parts of the image with low intensities are represented as “valleys,” while the regions with high intensities are assimilated as high altitude reliefs. First, a set of regional minima M of the image has to be determined. Then, the construction of the *watershed lines* can be seen as the result of a flooding process: water starts to rise at a

Table 1. Measurement and Reconstruction Parameters of All Three Resolution Modes—Low-Resolution (low-res), Medium-Resolution (med-res), and High-Resolution (high-res).

Parameter	Micro-CT	Micro-CT	Nano-CT
	Low Resolution	Medium Resolution	High Resolution
Sample size diameter (mm)	1.6	0.5	0.5
Field of view (FOV) (mm)	1.5	0.3	0.065
Acceleration voltage (keV)	80	80	5.4
Electrical power (W)	7	7	900
Target material (-)	Tungsten	Tungsten	Chromium
Source filter (Zeiss standard)	LE4	LE4	*
Exposure time (s)	2	25	60
Optical magnification	4	40	*
Number of projections	3201	3201	901
Angle range (°)	360	360	180
Voxel size (μm)	1.5	0.3	0.064
Binning	2	2	1
Reconstruction algorithm	FBP	FBP	FBP
Smoothing (Gauß)	0.1	0.1	-
Beam hardening correction	0.05	0.05	*

*denotes not applicable for monochromatic measurements.

constant speed from the minima and a dam is constructed if two or more floods from different minima may touch. The resulting dams are the watershed lines and delimit the segmented regions (called *catchment basins*) of the images. For further details on the watershed transform, see Soille (2013), Vincent & Soille (1991), and Gonzalez et al. (2002).

The marker-controlled watershed transform is an adaptation of the classical watershed transform for which the set of minima M is considered as a set of markers. Each marker locates an individual object to be segmented. The ridge lines will then be the contours of the objects. In general, the set M of markers may be difficult to construct. The construction of the markers depends usually on the type of the image and the object properties (shape, size, gradient intensity, etc.).

Segmentation of Low- and Medium-Resolution CT Images

For the low spatial resolution (low-res) CT image, only the fibers are clearly visible. Thus, the segmentation procedure consists of the following main steps:

1. Global thresholding and morphological opening operation to remove small objects.
2. Computation of Euclidean distance transform of the complemented binary image of the fibers.
3. Marker computation: extended-maxima transform of the distance transformation computed in step 2.
4. Application of the marker-controlled watershed transform.

In steps 1 and 2, rather basic image processing operations are performed (Serra, 1983; Gonzalez et al., 2002). Step 3 is a well-known technique (Soille, 2013) to construct a set of markers from the Euclidean distance transform, and step 4 is the application of the marker-controlled watershed transform using these

markers (Soille, 2013). The flowchart in Figure 3 illustrates the application of these steps for a specific slice. Further segmentation results are visualized in Figure 4. The fibers (in blue) are generally well segmented. However, some under segmentation is observed. It is addressed with a postprocessing procedure (described below).

The segmentation of spherical particles for the medium spatial resolution (med-res) CT image is a challenging task as the particles are too small to be clearly visible. After having removed the fibers from the image, the proposed segmentation procedure is the same as for the low-res CT image. The spheres (in blue) are generally highly under-segmented. Indeed, noise and artifacts especially affect the binarization of small objects (for details regarding the partial volume effect, see Supplementary Appendix B).

Segmentation of High-Resolution CT Image

The segmentation procedure for the high spatial resolution (high-res) CT image consists of the following main steps:

1. Intensity adjustment and smoothing with a nonlocal mean filter (using a Gaussian kernel).
2. Performing a morphological ultimate opening operation.
3. Global thresholding. The binary image is further cleaned up with a morphological opening operation: small objects of less than 100 voxels are removed.
4. Computation of Euclidean distance transform of the complemented binary image.
5. Marker computation using the extended-maxima transform.
6. Application of the marker-controlled watershed transform.

Figure 3 illustrates the application of these steps for a specific slice. Steps 1 and 3–6 have already been detailed for the segmentation of the low-res CT image. The ultimate morphological opening (Beucher, 2005, 2007) (step 2) is a less-known technique for

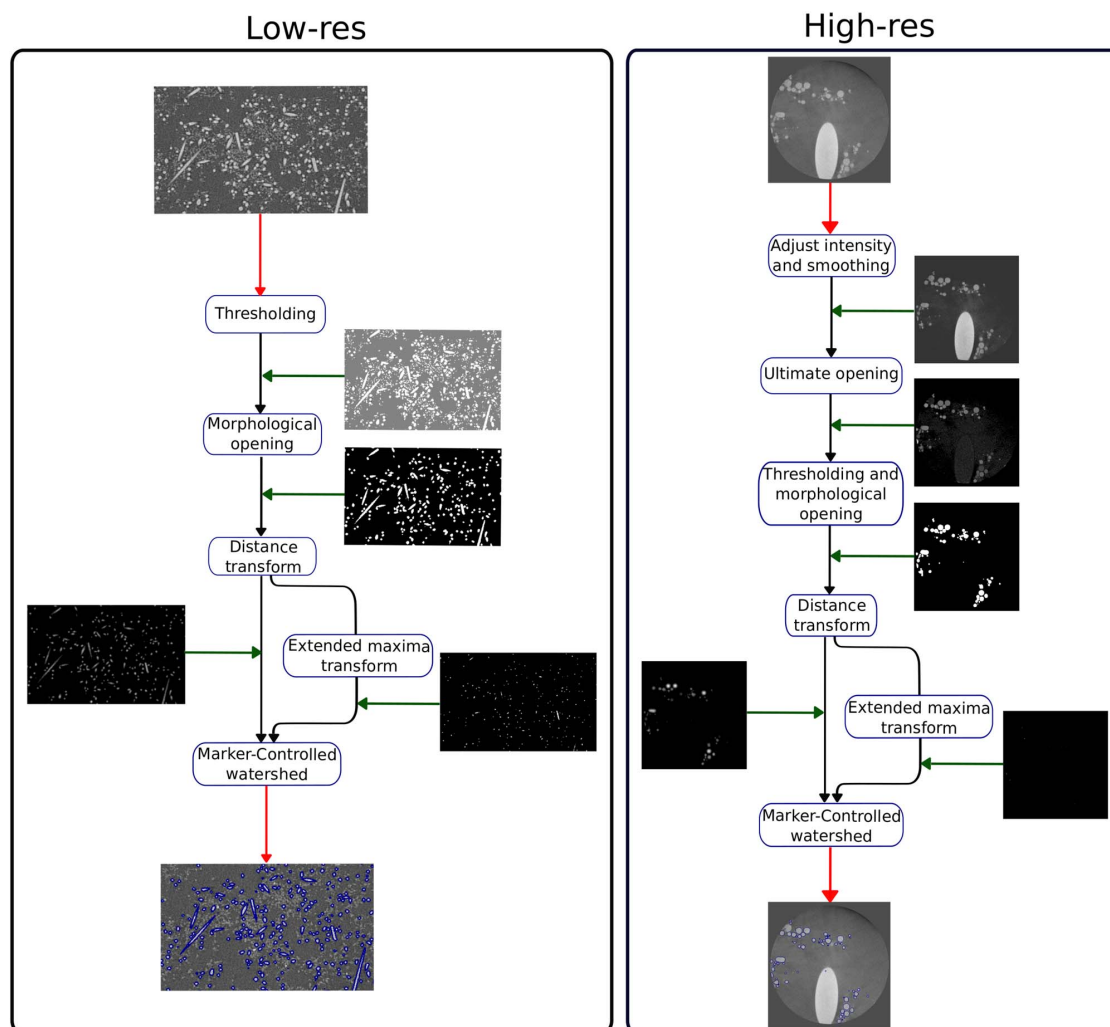


Fig. 3. Segmentation procedure for the CT images. The red arrows correspond to the input and output of the segmentation procedure. The green arrows provide the intermediate results for each of the transformations.

image segmentation. Note that the ultimate opening operator $\theta(v)$ is defined as follows:

$$\theta(v) = \sup_{i \in \{1, \dots, N\}} (\psi_i(v) - \psi_{i+1}(v)) \quad \text{for each } v \in V, \quad (2)$$

where V is the set of voxels, N is some integer, and ψ_i , respectively ψ_{i+1} , is the morphological opening operator for a closed ball of radius i , respectively $i+1$. Then, the voxel intensity values of the resulting image are the largest differences between the voxel intensity values of successive openings. An important consequence is that spherical objects, having the same textural information, are emphasized. Therefore, the binarization of a union of sphere-like particles is easier to undertake after preprocessing the image with the ultimate opening operation. Note that the value of N should be larger than the radius of the biggest sphere within the image. Hence, the main drawback of the ultimate opening is the computation time required to perform openings for balls of important radii. Other applications of the

morphological ultimate opening were considered for text detection (Retornaz & Marcotegui, 2007), for facade segmentation (Hernandez & Marcotegui, 2008), and for detection of microaneurysms on eye fundus images (Zhang et al., 2011).

Postprocessing of Segmented Images

A postprocessing procedure is applied to remove bias due to under or over segmentation. Regarding the segmentation of fibers in the low-res CT image, the following convexity constraint for a segmented object S should be satisfied:

$$\frac{\#S}{\#\text{Conv}(S)} \geq 0.5, \quad (3)$$

where $\#S$ is the number of voxels of S and $\#\text{Conv}(S)$ is the number of voxels of its convex hull. The topological constraint in equation (3) allows the reduction of the bias due to under segmentation, resulting in nonconvex objects (see Fig. 4b).

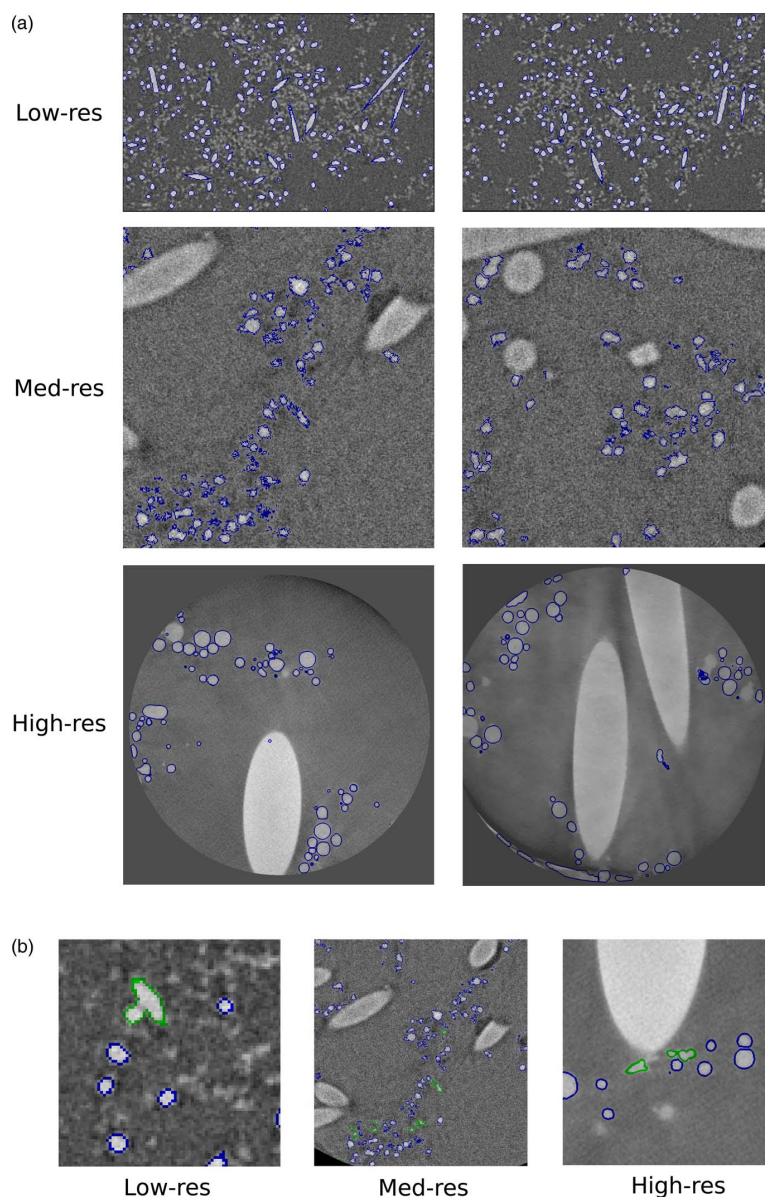


Fig. 4. Examples of segmentation results for each resolution on different slices (a). The boundary of each segmented particles is highlighted in blue. Examples of removed objects (in green) after the postprocessing procedure (b).

For the spherical particles, a constraint on the shape of the segmented objects is used. The *sphericity coefficient* Ψ , defined as the ratio of the surface area of the volume-equivalent sphere divided by the surface area of the corresponding segmented object, quantifies the deviation from the spherical shape (Wadell, 1932; Bailey et al., 2005; Lau et al., 2013). Note that for a segmented object S , its sphericity Ψ_S is given by

$$\Psi_S = \frac{\pi^{1/3}(6V_S)^{2/3}}{S_S}, \quad (4)$$

where V_S and S_S are the volume and the surface area of S , respectively. The closer Ψ_S is to 1, the closer the shape of the segmented object S is to that of a sphere. A standard estimator of V_S is the number of voxels of the segmented object S . The estimator used for the surface area S_S of S is based on the *Crofton formula* of integral geometry (Schneider & Weil, 2008). A formal definition of the estimator can be found in Schladitz et al. (2006). Thus, all particles whose sphericity coefficient is smaller than the threshold of 0.8 and 0.45 for the high-res and med-res CT image, respectively, are removed. The values of these thresholds were fixed empirically by visual inspection.

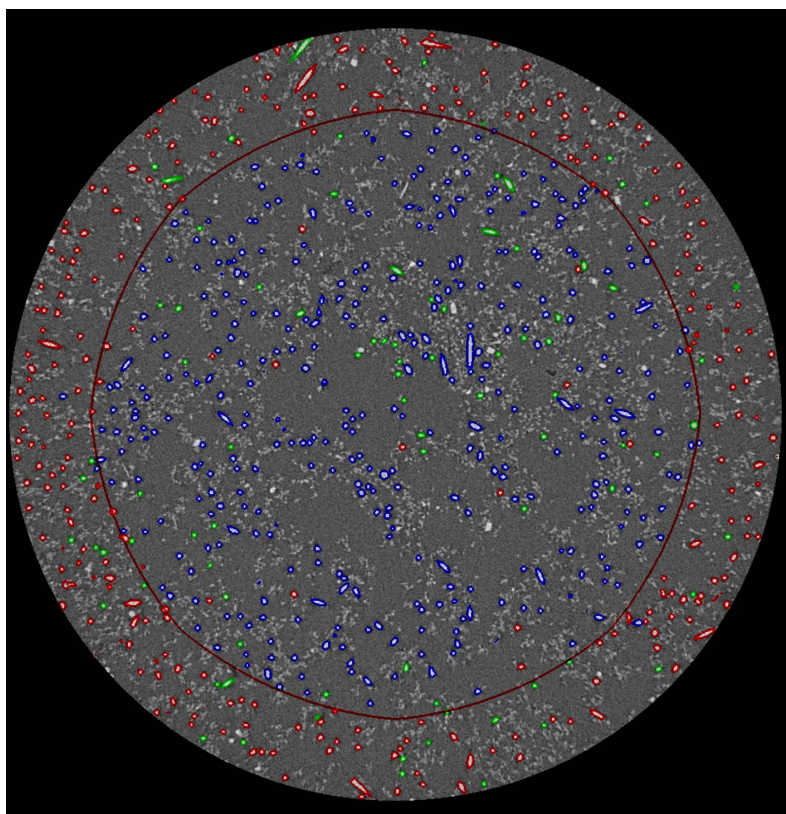


Fig. 5. Minus-sampling technique to remove bias due to edge effects. The red circle is a cross section of the minus-sampling window, i.e., only particles whose centroid is inside this reduced sampling window are sampled. Furthermore, the particles highlighted in red are removed. The particles in green are removed due to the postprocessing technique. Only blue particles are taken into account for the statistical analysis.

Results and Discussion

Correction of Edge Effects

A common problem encountered in spatial statistics is that of *edge effects*. They occur when the estimation of a certain geometrical characteristic requires information from outside of the sampling window. For instance, when determining the lengths of a population of fibers within an image, all fibers that cut the boundary of the sampling window are only partially observed. Taking into consideration only the fully observed fibers leads to a length distribution which is biased because the probability that a long fiber intersects the boundary of the sampling window is higher than the one of a short fiber. In our case, the *minus-sampling* method (Ohser & Schladitz, 2009; Chiu et al., 2013) is used, which consists of taking a sub-window contained in the sampling window such that all particles with nonempty intersection with the sub-window are completely observed in the entire sampling window. Then, considering all particles such that their center of mass is inside the sub-window leads to an unbiased sample of the population of particles.

An illustration how the minus-sampling method is applied in the case of fibers is provided in Figure 5. The gray area visualizes a cross section through the cylindrical sampling window. The sub-window is the cylinder, whose cross section is delimited by the red

circle. All fibers in the sub-window do not intersect the boundary of the entire sampling window. Then, only the fibers (in blue in Fig. 5) whose center of mass is inside the sub-window are considered for the statistical analysis. The fibers highlighted in red are removed by the minus-sampling technique. Note that the minus-sampling technique cannot be used if the sub-window does not include a sufficiently high number of fibers. Analogously, the minus-sampling technique is applied to image data from which the spherical particles are extracted. After applying the minus-sampling method, the remaining segmented particles are the basis for an efficient characterization of the particulate sample, using parametric bivariate distributions of particle properties. First, we fit such distributions to particle properties of spherical particles and fibers individually. Then, the distributions for the individual fractions have been combined to obtain a distribution characterizing the entire sample.

Multidimensional Characterization of Spherical Particles

Univariate Distributions of Particle Size and Specific Surface Area

For each spherical particle, the size d and the specific surface area S_V are computed as geometrical characteristics. In the case of spherical particles, the size d equals the volume-equivalent

diameter d_{eq,V_p} which is given by

$$d_{\text{eq},V_p} = \left(\frac{6V_p}{\pi} \right)^{1/3}, \quad (5)$$

where V_p is the volume of the segmented sphere. The volume V_p is computed by counting the voxels belonging to the particle followed by scaling with a single voxel's volume. Since the spherical particles are not perfect spheres their surface area S cannot be directly computed from their size d_{eq,V_p} . Therefore, we compute the surface area directly from image data using the Crofton formula (Lehmann & Legland, 2012). Then, the specific surface area S_{V_p} is given by

$$S_{V_p} = \frac{S}{V_p}. \quad (6)$$

Supplementary Figure S2 provides histograms of the particle size d for two resolutions. The significant differences between the distributions in the med-res and high-res CT images are not surprising. For the med-res CT images, important under segmentation, due to blurred small spheres or noise/artifacts, was observed. Hence, the distribution is biased toward larger sphere sizes. Moreover, very small spheres, whose volume-equivalent diameters are less than $1.5 \mu\text{m}$, are not detected due to the insufficient resolution of the med-res CT images. In contrast to this, a large fraction of spheres in the nanometer range is correctly segmented and analyzed in the high-res CT images. The high resolution also enables us to overcome the under segmentation problem encountered for the med-res CT images. Consequently, the particle size distribution is right-skewed (see Fig. 6a). Thus, for the analysis of the spherical particles, from hereon, we will solely use two high-res images depicting the spherical particles at spatially different locations. Histograms of the spherical particle's size and specific surface area computed from these images are visualized in Figure 6a.

For validation purposes, we compared the particle size distributions computed from high-res image data and the SEM images (see Fig. 7). The method to derive the particle size distribution from the SEM images is explained in Supplementary Appendix A. We observe an underestimation of the relative frequency for particles with a diameter smaller than $0.6 \mu\text{m}$ in the case of the high-res CT images. This is mainly due to the higher resolution of the SEM images, which allows one to distinguish smaller spheres more clearly. For the high-res CT images, with a resolution that is two times lower, it is hardly possible to segment such small-sized spheres due to noise and artifacts. For bigger particles, the two distributions are consistent, which demonstrates the possibility of using the nano-CT imaging technique in this size range. Note that some overlapping effects appear in the SEM images (see Supplementary Appendix A), which may complicate the segmentation process and bias the volume-equivalent diameter distribution. Besides, the volume fraction of the segmented spheres in one of the high-res images is about 4.4% (sample 1), which is slightly smaller than the expected volume fraction of 5% (see Section Material and Methods). In the other high-res image, the volume fraction of 2.6% deviates significantly more from the target value. The reason for this is the extremely small FOV of the high-res measurement and the nonhomogeneous distribution of the population of spheres within the sample volume. Since this effect is independent of the particle size, the particle size distribution remains unaffected.

Copula Approach

Since univariate histograms of one-dimensional particle characteristics do not provide information about the correlation between the considered characteristics, a more informative description of the particulate system of spheres can be achieved by investigating bivariate distributions. For this purpose, a parametric model can be used to characterize the joint distribution of size d and specific surface area S_{V_p} of the spherical particles. Note that the distribution of d (see Fig. 6a) is clearly not Gaussian, yet the values of d and S_{V_p} are strongly correlated with a correlation coefficient of -0.89 . Thus, standard methods, which approximate the joint distribution of size d and specific surface area S_{V_p} with a product distribution or a bivariate Gaussian distribution, are not applicable in our case. Therefore, the joint distribution will be modeled using copula theory (Durante & Sempi, 2015).

Note that a 2D copula $C: [0,1]^2 \rightarrow [0,1]$ is a cumulative distribution function whose marginal distributions are uniform on the unit interval $[0,1]$. It enables us to characterize the dependency between correlated non-normally distributed random variables. Specifically, in the 2D case, Sklar's theorem (Durante & Sempi, 2015) states that, given two real-valued random variables X_1 and X_2 with cumulative distribution functions F_1 and F_2 , there exists a copula C such that the joint cumulative distribution function F of X_1 and X_2 is given by

$$F(x_1, x_2) = C(F_1(x_1), F_2(x_2)), \quad \text{for each } (x_1, x_2) \in \mathbb{R}^2, \quad (7)$$

where $F(x_1, x_2) = \mathbb{P}(X_1 \leq x_1, X_2 \leq x_2)$. From an easy computation, provided that C , F_1 , and F_2 are differentiable, we find that the joint density f of X_1 and X_2 is given by

$$f(x_1, x_2) = c(F_1(x_1), F_2(x_2)) f_1(x_1) f_2(x_2), \quad (8)$$

for each $(x_1, x_2) \in \mathbb{R}^2$,

where f_1 and f_2 are the marginal densities, and the function c is the probability density function of the copula, i.e.,

$$c(u_1, u_2) = \frac{\partial^2}{\partial u_1 \partial u_2} C(u_1, u_2), \quad \text{for each } (u_1, u_2) \in [0,1]^2. \quad (9)$$

Model Fitting

In order to fit a bivariate probability density f to the observed pairs of size and specific surface area, we first fit the univariate marginal densities f_1 and f_2 . We considered eight possible choices of parametric unimodal distributions, namely the gamma, normal, log-normal, Weibull, generalized extreme value, Rayleigh, Nakagami, and Rician distributions. For each marginal, the best fit is the one with the lowest value resulting from the Akaike information criterion (Akaike, 1998) (AIC). Note that the AIC is a measure of goodness-of-fit which is defined by

$$\text{AIC} = 2k - 2 \log(L), \quad (10)$$

where k is the number of model parameters and L the maximum value of the likelihood function. The best fits were obtained for the inverse Gaussian distribution and the gamma distribution for the size and specific surface area of spherical particles, respectively (see Fig. 6a).

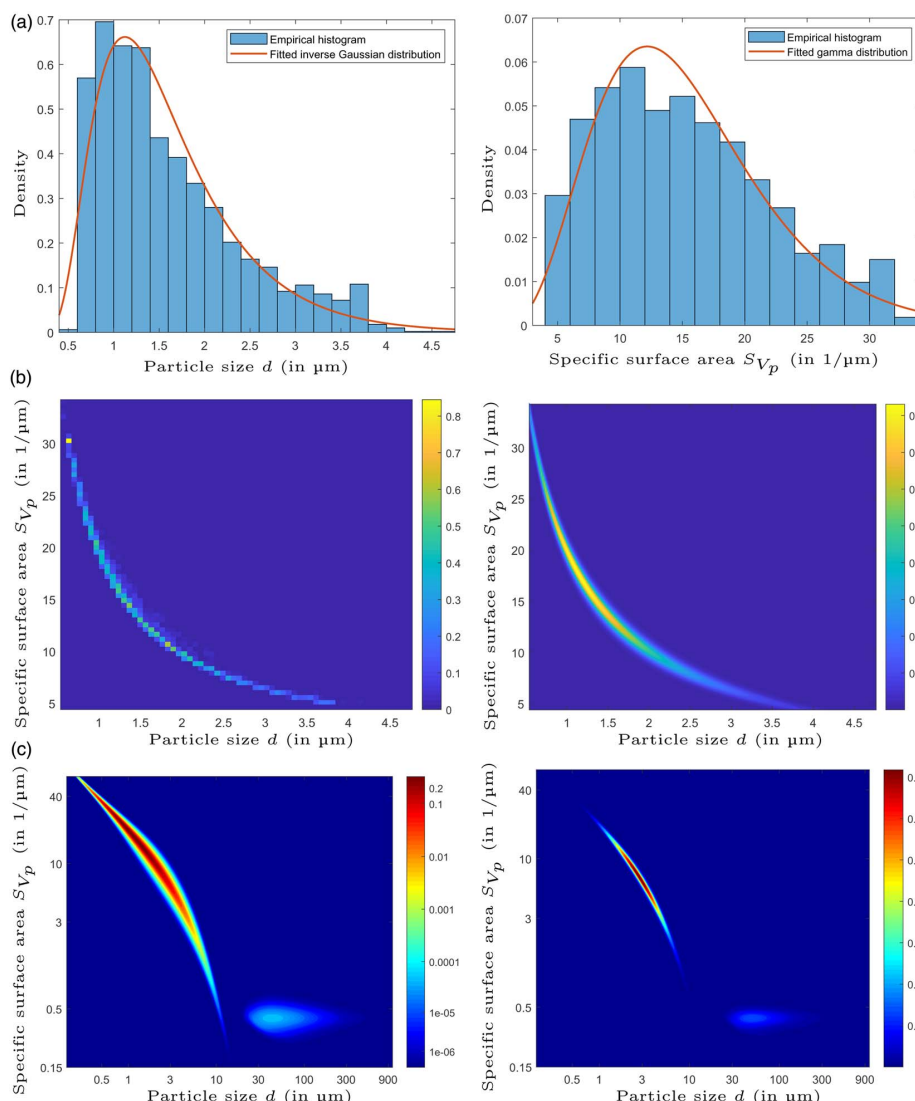


Fig. 6. Statistical analysis of the segmentation results. Fitted parametric (marginal) distributions to size (left) and specific surface area (right) of the spherical particles (a); bivariate histogram (left) and its copula model (right) (b); number-weighted (left) and volume-weighted (right) bivariate probability density of size and specific surface area of the entire particle system (c). Note that the number-weighted visualization has a logarithmically scaled colorbar.

Now, in view of equation (8), the bivariate density f can be fitted by determining a suitable copula density c . Similarly to the univariate case, there are various parametric families of copulas whose parameters can be determined using the maximum likelihood method. More precisely, the bivariate density f was fitted by determining the optimal copula density c from a family of commonly used *Archimedean copulas* (Durante & Sempi, 2015), where the considered Archimedean copulas were the Ali-Mikhail-Haq, Clayton, Frank, Gumbel, Joe, BB1, BB3, BB5, and BB8 copulas (Durante & Sempi, 2015). The best fit, denoted by f_{sphere} , which is the one with the highest maximum likelihood, was obtained for the BB1 copula (see Fig. 6b (right)).

Multidimensional Characterization of Fibers

For each fiber, the size d and the specific surface area S_{V_F} are computed. While the latter is determined in the same manner as for the spherical particles using equation (6), the size d of a fiber is estimated in a different manner. Namely, the size d is the number of voxels along the main directions of the segmented fibers, where a principal component analysis (Pearson, 1901) is used to determine the main direction of a given segmented fiber. Furthermore, for a fiber F , the diameter d_{cross} of its cross section is estimated as the diameter d_{eq,A_F} of the area-equivalent disk which is given by

$$d_{\text{eq},A_F} = \sqrt{\frac{4A_F}{\pi}}, \tag{11}$$

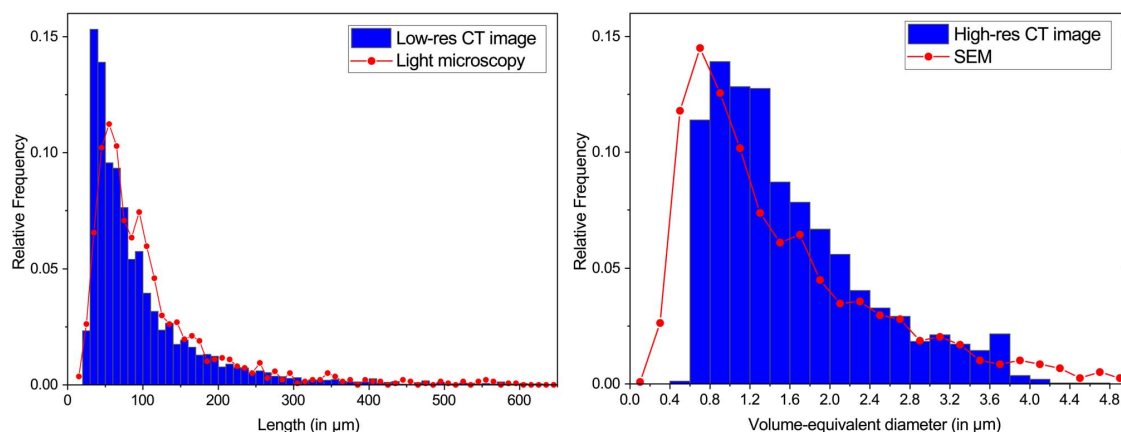


Fig. 7. Comparison of the size distributions computed from the CT images (in blue) and the SEM and light microscopy (in red) images.

where A_F is the area of the cross-section orthogonal to the main axis of the fiber and located at half of the fibers length. Histograms of the size, the specific surface area, and the diameter are provided in Supplementary Figure S7a. We observe that the fiber diameter distribution is concentrated around $10\mu\text{m}$ with a low standard deviation of $1.1\mu\text{m}$, which is consistent with the provider specifications (see Section Materials and Methods). Moreover, we compared the size distributions obtained from the CT image and the light microscopy images (see Fig. 7). The two distributions are consistent, which validates the proposed segmentation procedure for the CT image. Besides, we obtained the following quantiles for the size distribution using the CT image: $Q_{0.10} = 35\mu\text{m}$, $Q_{0.50} = 69\mu\text{m}$, and $Q_{0.90} = 197\mu\text{m}$. These values are slightly lower than the ones derived using light microscopy in the pre-characterization procedure (see Supplementary Appendix A). This deviation is mainly due to some small fibers which were missed during the manual segmentation of the light microscopy images, which then leads to a shift of the size distribution toward longer fibers. Regardless of this manual segmentation incorrectness, the overall size distribution derived from the low-res CT image is consistent with that one of the pre-characterization. Besides, the determined volume fraction of fibers of 4.7% is only slightly smaller than the expected 5% (see Section Materials and Methods).

Similarly, to the approach described in the section Model Fitting, the joint distribution of fiber size and specific surface area can be fitted using parametric copulas. In this manner, we determine the bivariate probability density f_{fiber} , depicted in Supplementary Figure S7b.

Characterization of the Entire Particle System

In the previous sections, we have modeled the bivariate probability densities f_{sphere} and f_{fiber} of particle size and specific surface area for spherical particles and fibers, respectively. While the probability density f_{fiber} was derived using the low-res CT image data, for the density f_{sphere} characterizing the spheres the high-res image data of the same particle system was utilized. Now, we combine these probability densities to obtain a multidimensional, multiscale characterization of the entire particle system. More precisely, the bivariate probability density f_{system} of size and specific

surface area of the entire particle system is given by

$$f_{\text{system}} = \lambda f_{\text{sphere}} + (1 - \lambda) f_{\text{fiber}}, \quad (12)$$

where $\lambda \in [0,1]$ is the (number-based) mixing ratio λ . Since we know that the considered particle mixture is a 50/50 mixture (by weight) of spherical particles and fibers, we can determine the mixing ratio. More precisely, the volume-equality of the fractions is described by

$$\begin{aligned} \lambda \int_0^{\infty} \int_0^{\infty} f_{\text{sphere}}(d,s) V_{\text{sphere}}(d) dd ds \\ = (1 - \lambda) \int_0^{\infty} \int_0^{\infty} f_{\text{fiber}}(d,s) V_{\text{fiber}}(d,s) dd ds, \end{aligned} \quad (13)$$

where $V_{\text{sphere}}(d) = \frac{\pi}{6} d^3$ is the volume of a sphere with diameter d and $V_{\text{fiber}}(d,s)$ is the volume of a fiber with size d and specific surface area s (see Supplementary Appendix E). By solving equation (13) for λ , we obtain the theoretical mixing ratio $\lambda = 0.9995$. The resulting bivariate and bimodal density f_{system} is depicted in Figure 6c (left). If no prior information is available, the mixing ratio λ can be estimated from image data by

$$\lambda = \frac{\frac{n_{\text{sphere}}}{V_{\text{sphere,Cyl}}}}{\frac{n_{\text{sphere}}}{V_{\text{sphere,Cyl}}} + \frac{n_{\text{fiber}}}{V_{\text{fiber,Cyl}}}}, \quad (14)$$

where n_{sphere} is the number of spherical particles observed in the volume $V_{\text{sphere,Cyl}}$ and n_{fiber} is the number of fibers observed in the volume $V_{\text{fiber,Cyl}}$.

Note that the visualization of the number-weighted probability density f_{system} in Figure 6c (left) utilizes, due to the different length scales of the particles, logarithmic axes. Furthermore, due to the relatively large mixing ratio λ , a logarithmically scaled colorbar is required to visualize the second mode corresponding to the fibers. A different representation using the so-called volume-weighted version $f_{\text{system},3}$ of the number-weighted density

f_{system} is given by

$$f_{\text{system},3}(d,s) = \frac{1}{c} \left(\lambda f_{\text{sphere}}(d,s) V_{\text{sphere}}(d) + (1 - \lambda) f_{\text{fiber}}(d,s) V_{\text{fiber}}(d,s) \right), \quad (15)$$

where c is a normalization constant. The volume-weighted probability density $f_{\text{system},3}$ depicted in Figure 6c (right) no longer requires a logarithmically scaled colorbar for visualization purposes.

Both the bivariate number- and volume-weighted probability densities of particle size and specific surface area are important for the characterization and analysis of particle systems. In particular, the first one is of interest when small particles have a significant influence on the distribution of properties of the overall system, e.g., when considering the active surface of a catalyzer material. On the other hand, the volume-weighted probability densities can be of interest when the characterization focuses on the mass of particles, e.g., when investigating the mass of a valuable material after some separation process has been completed.

Conclusions

The combination of micro- and nanotomographic X-ray imaging is a powerful tool for the determination of multidimensional particle properties in the micro- and submicrometer range, capable of bridging several orders of magnitude of particle size. We have shown how to create a sample with a statistically representative number of immobilized particles consisting of two very different particle populations by embedding them into a wax matrix. Furthermore, we emphasized the importance of adapting the sample size to the field of view in order to link X-ray tomography across different scales.

In contrast to the fibers, the size of the spherical particles is at the lower resolution limit of micro-CT. Thus, smaller spherical particles below the micrometer range are not detectable in the reconstructed CT images, hence, leading to a bias in the volume-equivalent diameter distribution. To minimize this well-known phenomenon of voxel size-dependent description of 3D objects, we first minimized the sample size, switched to a better resolution (nano-CT) and, finally, applied suitable image processing algorithms and statistical analysis to characterize the population of spheres. The distributions of the volume-equivalent diameter estimated from the nano-CT and micro-CT images were significantly different, thus, confirming the need to adapt the experiment and the statistical analysis to the size and shape of the particles contained in the same particle system.

The sample volume must be large enough compared to the typical particle size in order to contain a statistically relevant number of particles and to remove edge effects when determining the distributions of their geometrical properties. First, the correlation structure of particle size and specific surface area has been modeled separately for spheres and fibers, using copulas. The fitted copula models provide a complete parametric description of the population of spheres and fibers and are methodologically easily adaptable to more irregularly shaped particles. Finally, by combining these two parametric distributions, we obtained a multidimensional characterization of the entire particle system.

Our proposed workflow (including sample preparation, measurement, image processing, and image analysis) for multidimensional characterization of micro- and nanoscale particle systems is

the starting point for the analyses of products from multidimensional separation processes and will be further discussed in forthcoming studies.

Data availability

Reconstructed TIFF-stacks for high-resolution, medium-resolution, and low-resolution measurements are stored within the scientific data repository of the universities TU Dresden and TU Bergakademie Freiberg with all relevant metadata (Ditscherlein & Martins de Souza e Silva, 2019).

Supplementary material. To view supplementary material for this article, please visit <https://doi.org/10.1017/S1431927620001737>.

Acknowledgments. The authors thank the German Research Foundation (DFG) for supporting the project as part of the priority program SPP2045 (313858373), which is dealing with highly specific multidimensional separation of technical ultra-fine particle systems below 10 μm , the funding of the micro-CT (INST 267/129-1) as well as the nano-CT (WE 4051/21-1).

References

- Akaike H (1998). Information theory and an extension of the maximum likelihood principle. *Selected Papers of Hirotugu Akaike*, pp. 199–213. New York: Springer.
- Bagheri G, Bonadonna C, Manzella I & Vonlanthen P (2015). On the characterization of size and shape of irregular particles. *Powder Technol* **270**, 141–153.
- Bailey M, Gomez C & Finch J (2005). Development and application of an image analysis method for wide bubble size distributions. *Miner Eng* **18**, 1214–1221.
- Beucher S (2005). Numerical residues. In *40 Years on Mathematical Morphology*, pp. 23–32. Dordrecht: Springer.
- Beucher S (2007). Numerical residues. *Image Vis Comput* **25**, 405–415. Berlin, Heidelberg, New York: Springer.
- Boas FE & Fleischmann D (2012). CT artifacts: Causes and reduction techniques. *Imaging Med* **4**, 229–240.
- Brown DJ, Vickers GT, Collier A & Reynolds GK (2005). Measurement of the size, shape and orientation of convex bodies. *Chem Eng Sci* **60**, 289–292.
- Buchmann M, Schach E, Tolosana-Delgado R, Leifner T, Astoveza J, Kern M, Möckel R, Ebert D, Rudolph M, van den Boogaart K & Peuker U (2018). Evaluation of magnetic separation efficiency on a cassiterite-bearing Skarn ore by means of integrative SEM-based image and XRF–XRD data analysis. *Minerals* **8**, 390.
- Burnett TL, McDonald SA, Gholinia A, Geurts R, Janus M, Slater T, Haigh SJ, Ornek C, Almuaili F, Engelberg DL, Thompson GE & Withers PJ (2014). Correlative tomography. *Sci Rep* **4**, 1–6.
- Buzug TM (2008). *Computed Tomography: From Photon Statistics to Modern Cone-beam CT*. Berlin Heidelberg: Springer.
- Cepuritis R, Garboczi EJ, Jacobsen S & Snyder KA (2017). Comparison of 2-D and 3-D shape analysis of concrete aggregate fines from VSI crushing. *Powder Technol* **309**, 110–125.
- Chiu SN, Stoyan D, Kendall WS & Mecke J (2013). *Stochastic Geometry and Its Applications*. United Kingdom: J. Wiley & Sons.
- Davis GR & Elliott JC (2006). Artefacts in X-ray microtomography of materials. *Mater Sci Technol* **22**, 1011–1018.
- Ditscherlein R, Leifner T & Peuker UA (2019). Preparation techniques for micron-sized particulate samples in X-ray microtomography. *Powder Technol* **360**, 989–997.
- Ditscherlein R, Leifner T & Peuker UA (2020). Self-constructed automated syringe for preparation of micron-sized particulate samples in X-ray microtomography. *MethodsX* **7**, 100757.
- Ditscherlein R & Martins de Souza e Silva J (2019). Micro-CT and nano-CT scans of particle systems fibres and spheres. Available at <http://dx.doi.org/10.25532/OPARA-50>.

- Durante F & Sempi C** (2015). *Principles of Copula Theory*. Florida: Chapman and Hall/CRC.
- Gonzalez RC, Woods RE & Eddins S** (2002). *Digital Image Processing*. New Jersey: Prentice Hall.
- Hagen C, Werner S, Carregal-Romero S, Malhas AN, Klupp BG, Guttmann P, Rehbein S, Henzler K, Mettenleiter TC, Vaux DJ, Parak WJ, Schneider G & Grünewald K** (2014). Multimodal nanoparticles as alignment and correlation markers in fluorescence/soft X-ray cryo-microscopy/tomography of nucleoplasmic reticulum and apoptosis in mammalian cells. *Ultramicroscopy* **146**, 46–54.
- Hernandez J & Marcotegui B** (2008). Segmentation of façade images using ultimate opening. *31ème journée ISS*, 1–3.
- Kahl WA, Dilissen N, Hidas K, Garrido C, López-Sánchez-Vizcaíno V & Román-Alpiste M** (2017). 3-D microstructure of olivine in complex geological materials reconstructed by correlative X-ray μ -CT and EBSD analyses. *J Microsc* **268**, 193–207.
- Koglin B, Leschonski K & Alex W** (1974). Teilchengrößenanalyse. *Chem Ing Tech* **46**, 289–292.
- Kyrieleis A, Titarenko V, Ibson M, Connolley T & Withers P** (2010). Region-of-interest tomography using filtered backprojection: Assessing the practical limits. *J Microsc* **241**, 69–82.
- Lau Y, Deen N & Kuipers J** (2013). Development of an image measurement technique for size distribution in dense bubbly flows. *Chem Eng Sci* **94**, 20–29.
- Lehmann G & Legland D** (2012) Efficient N-dimensional surface estimation using Crofton formula and run-length encoding. *Insight J*. <http://hdl.handle.net/10380/3342>.
- Liu Y, Meirer F, Krest CM, Webb S & Weckhuysen BM** (2016). Relating structure and composition with accessibility of a single catalyst particle using correlative 3-dimensional micro-spectroscopy. *Nat Commun* **7**, 1–8.
- Macho O, Kabát J, Gabrišová L, Peciar P, Juriga M, Fekete R, Galbavá P, Blaško J & Peciar M** (2020). Dimensionless criteria as a tool for creation of a model for predicting the size of granules in high-shear granulation. *Particul Sci Technol* **38**, 1–10.
- Maire E & Withers PJ** (2014). Quantitative X-ray tomography. *Int Mater Rev* **59**, 1–43.
- Meyer F & Beucher S** (1990). Morphological segmentation. *J Vis Commun Image Represent* **1**, 21–46.
- Moroni R, Börner M, Zielke L, Schroeder M, Nowak S, Winter M, Manke I, Zengerle R & Thiele S** (2016). Multi-scale correlative tomography of a Li-ion battery composite cathode. *Sci Rep* **6**, 1–6.
- Ohser J & Schladitz K** (2009). *3D Images of Materials Structures: Processing and Analysis*. Weinheim: J. Wiley & Sons.
- Pavlinky GV** (2008). *Fundamentals of X-ray Physics*. United Kingdom: Cambridge International Science Publishing.
- Pearson K** (1901). On lines and planes of closest fit to systems of points in space. *London, Edinburgh, Dublin Philos Mag J Sci* **2**, 559–572.
- Retornaz T & Marcotegui B** (2007). Scene text localization based on the ultimate opening. In *International Symposium on Mathematical Morphology*, vol. 1, pp. 177–188. Rio de Janeiro: MCT/INPE
- Schladitz K, Ohser J & Nagel W** (2006). Measurement of intrinsic volumes of sets observed on lattices. In *13th International Conference on Discrete Geometry for Computer Imagery*, vol. 4245, pp. 247–258. Berlin Heidelberg: Springer.
- Schneider R & Weil W** (2008). *Stochastic and Integral Geometry*. Berlin Heidelberg: Springer.
- Serra J** (1983). *Image Analysis and Mathematical Morphology*. Florida: Academic Press.
- Shilo M, Reuveni T, Motiei M & Popovtzer R** (2012). Nanoparticles as computed tomography contrast agents: Current status and future perspectives. *Nanomedicine* **7**, 257–269.
- Sjödahl M, Siviour CR & Forsberg F** (2012). Digital volume correlation applied to compaction of granular materials. *Procedia IUTAM* **4**, 179–195.
- Soille P** (2013). *Morphological Image Analysis: Principles and Applications*. Berlin Heidelberg: Springer.
- Stock SR** (1999). X-ray microtomography of materials. *Int Mater Rev* **44**, 141–164.
- Vigneau E, Loisel C, Devaux MF & Cantoni P** (2000). Number of particles for the determination of size distribution from microscopic images. *Powder Technol* **107**, 243–250.
- Vincent L & Soille P** (1991). Watersheds in digital spaces: An efficient algorithm based on immersion simulations. *IEEE Trans Pattern Anal Mach Intell* **13**, 583–598.
- Wadell H** (1932). Volume, shape, and roundness of rock particles. *J Geol* **40**, 443–451.
- Zhang X, Thibault G & Decencièrre E** (2011). Application of the morphological ultimate opening to the detection of microaneurysms on eye fundus images from a clinical database. In *13th International Congress of Stereology*, pp. 1–6. Beijing: International Society for Stereology.
- Zhong X, Burke MG, Withers PJ, Zhang X, Zhou X, Burnett TL, Liu Y, Lyon SB & Gibbon SR** (2019). Multi-modal plasma focused ion beam serial section tomography of an organic paint coating. *Ultramicroscopy* **197**, 1–10.

Supplementary Material

Multi-scale tomographic analysis for micron-sized particulate samples

Ralf Ditscherlein^{1,*}, Orkun Furat², Mathieu de Langlard², Juliana Martins de Souza e Silva³, Johanna Sygusch⁴, Martin Rudolph⁴, Thomas Leißner¹, Volker Schmidt², and Urs A. Peuker¹

¹Institute of Mechanical Process Engineering and Mineral Processing, Technische Universität Bergakademie Freiberg, D-09599 Freiberg, Germany

²Institute of Stochastics, Ulm University, D-89069 Ulm, Germany

³Institute of Physics - mikroMD, Martin Luther University Halle-Wittenberg, D-06120 Halle, Germany

⁴Helmholtz Institute Freiberg for Resource Technology, D-09599 Freiberg, Germany

* corresponding author: ralf.ditscherlein@mvtat.tu-freiberg.de, phone: +49 3731 39-2714, fax: +49 3731 39-2947

Appendix A: Particle system

For validation purposes in image processing, a detailed preliminary characterization of the particle systems is mandatory. It enables us to quantify the accuracy of the proposed segmentation procedure and to account for eventual bias linked to the image processing workflow. Figure S1 shows cutouts of both analyzed particulate materials.

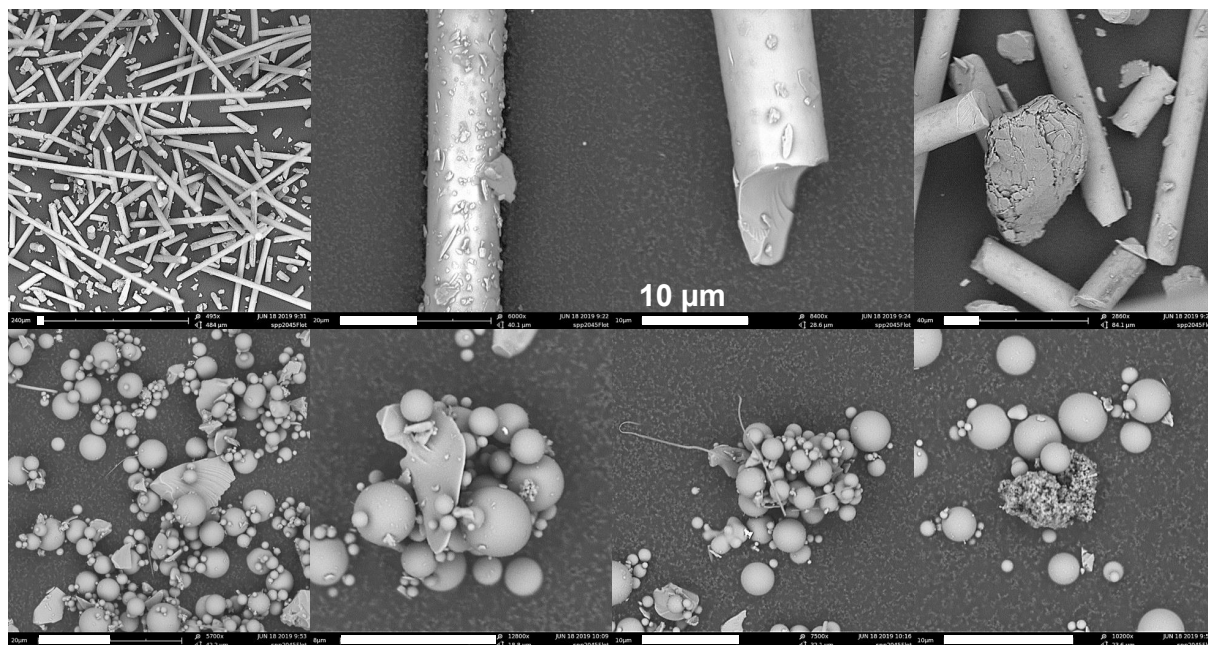


Figure S1: SEM-images of fibres (top) with contamination on the particle surface (organic facening from production process) and spheres (bottom). Note that these images are extreme examples and not representative for the analyzed particle system.

For a reasonable pre-characterization of both particle systems in terms of size (spheres: diameter, fibres: length) we used SEM and light microscopy 2D imaging methods. Integral methods like laser diffraction (in case of spherical systems) are also available but expected to be not comparable due to the different measurement principle. The workflow was as follows: (1) separate the particles on the object carrier, (2) take images at 10 random locations, (3) determine the size of each particle with the ROI-manager of ImageJ (exemplary images of spheres and fibres see Figure S2) and (4) combine all data sets.

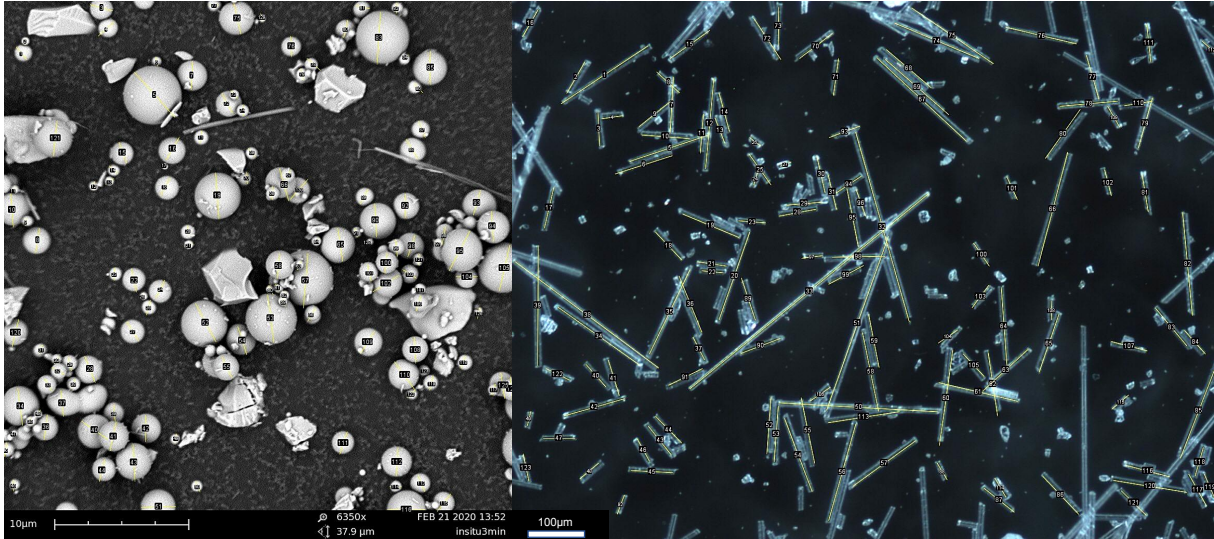


Figure S2: Exemplary SEM image showing the spheres (left) and exemplary image from light microscopy showing the fibres (right)

Table S1: Statistical measures for particle systems determined by 2D image analysis (spheres: SEM, fibres: light microscopy); (*) size is the equivalent spherical diameter, (**) diameter from data sheet specification: 10 μm

Measures	Sphere diameter* <i>in</i> μm	Fibre length** <i>in</i> μm
$Q_{0.10}$	0.6	40.8
$Q_{0.50}$	1.2	81.6
$Q_{0.90}$	2.9	208.7
Min	0.4	17.7
Max	5.8	656.9
Number of particles	1181	1371

The resulting statistical measures of both particle systems are summarized in Table S1. We refrained from automation, since overlay effects in the 2D representation make meaningful binarization and segmentation difficult and, in the case of fibres, lead to over-segmentation. The focus is clearly on 3D analysis.

Appendix B: Partial volume effect

To analyze the particle distribution of our system, we have to distinguish each particle from the background (in this study a wax matrix) and separate the agglomerated particles from each other. The relevant boundary layer (particle-matrix / particle-particle) extends only partially into the surrounding voxel layer. The resulting gray values of these voxels are a mixture between particle and matrix phase depending on their share (partial volume) in the voxel and their specific X-ray attenuation capability. Figure S3 shows an example of a reconstructed CT-image slice of spherical particles (a). Particles are aggregated (b,c-yellow) or physically connected/sintered (b,c-red). Segmenting the particles means finding the proper delimited regions such that each region corresponds to one particle. Gray blend pixels are assigned to either the particle (white) or the matrix (black), which is called binarization by thresholding. In both cases this has an influence on the number, size and shape of the resulting particles (compare d with e).

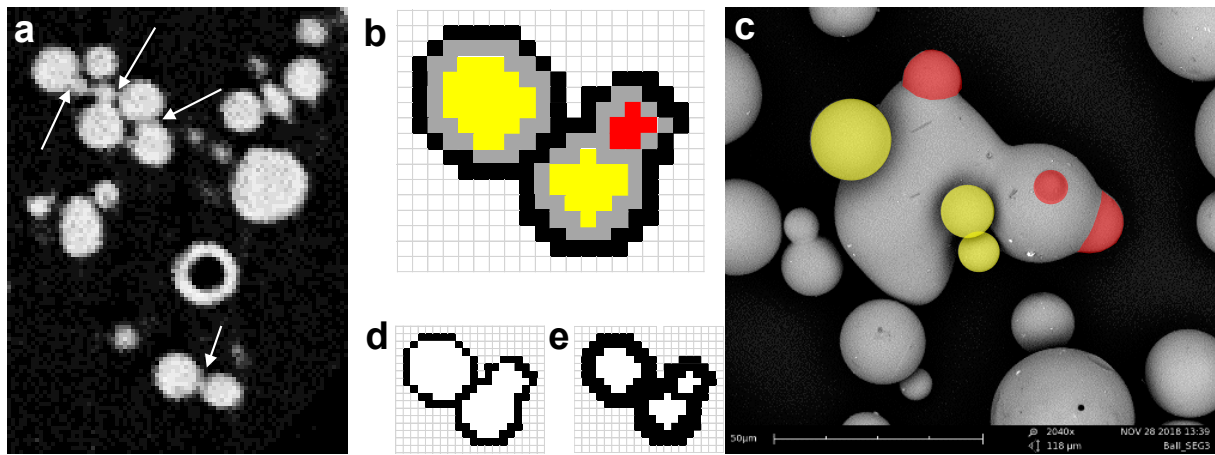


Figure S3: Magnification of a reconstructed tomographic slice (a) where connections between particles are marked (arrow), example of physically connected (b-red) and aggregated particles (b-yellow) with corresponding SEM-image (c), change in particle size, number and shape after thresholding (d,e)

The exemplary analysis of the sphere diameters clearly shows the influence of partial volume effect on the location and shape of the distribution (see Figure S4). Only in the high-resolution CT images are the spherical particles sufficiently well resolved to be able to depict their true size distribution.

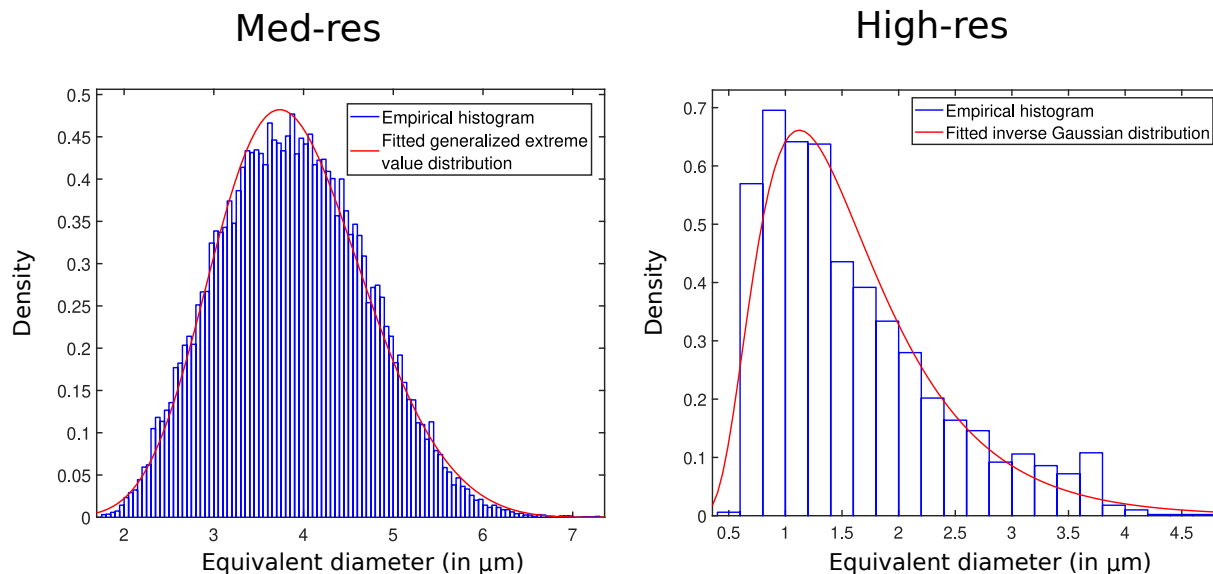


Figure S4: Comparison of the volume-equivalent diameter distributions computed from the med-res and high-res CT images.

Appendix C: Experimental setup

The main difference between micro- and nano-CT is the type of X-rays. In both cases X-rays are generated by the interaction between accelerated electrons with a specific target material (in our case micro-CT/Tungsten, nano-CT/Chromium).

In micro-CT imaging the whole spectrum of X-rays (characteristic and bremsstrahlung) is used as part of a conical beam that is generated by the interaction volume within the target material. So, each individual volume element of the sample material interacts with the whole energy-spectrum of X-rays and alters it. Because the detector is not energy-dispersive, every arriving X-ray photon counts as part of the sum signal. Both, the polychromatic spectrum and the conical beam shape, cause image artefacts.

In nano-CT imaging, a condenser lens filters a specific part of the spectrum and, in this way, creates approximately monochromatic X-rays in a parallel beam. Thus, there are much less artefacts. But because of the lower photon intensity, a much higher exposure time is needed to generate a sufficient signal on the detector. Inside views and corresponding measurement setups of both CT-scanners are visualized in Figure S5.

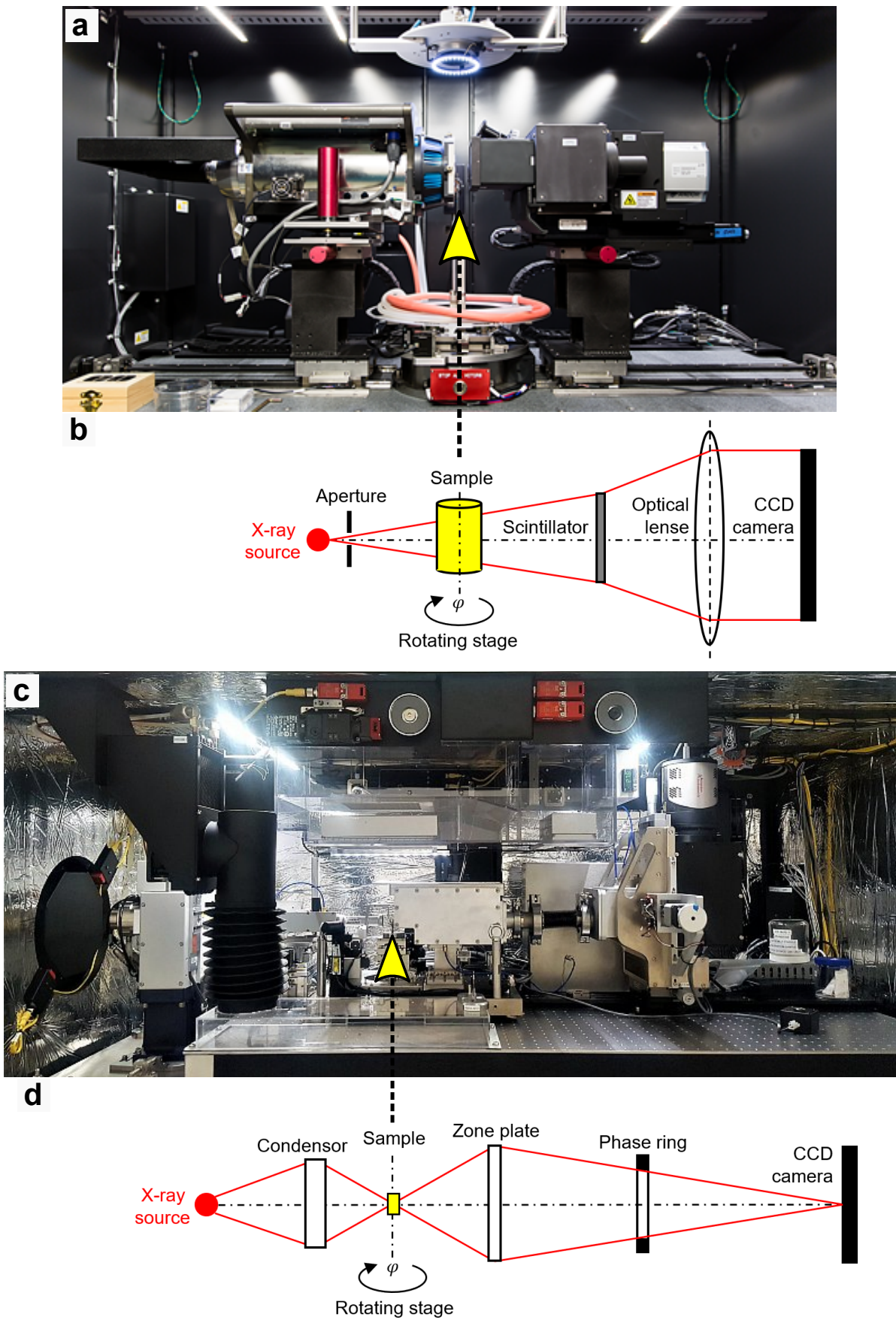


Figure S5: Inside view of micro-CT (a) and nano-CT (c), with corresponding measurement setups (b, d).

Appendix D: Region of interest (ROI) tomography

Ideally, the sample should be a little bit smaller than the field of view (FOV). Thus, when going to higher voxel-resolution, the sample size has to shrink. If this is not possible due to limited machining capabilities or simply because the sample should not be destroyed, the FOV is shifted inside the sample (Figure S6-a). This affects the minimum number of projections, needed for reconstruction, as discussed in the main part of the paper.

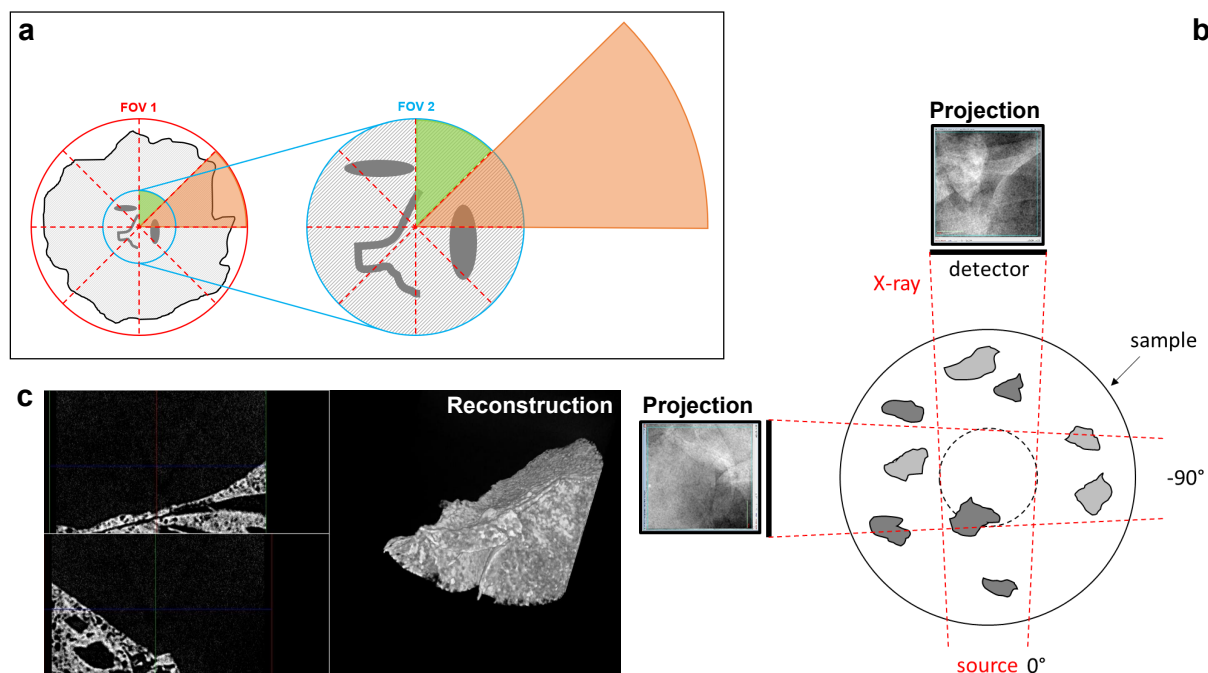


Figure S6: Comparison of two scans of the same sample – whole sample within the field of view (a, FOV1), detail enlargement by ROI (a, FOV2), possible ROI-identification problems (b,c)

ROI-tomography is also challenging in terms of searching for an appropriate scan volume with enough particles in it. Especially when looking for certain structures, the projection image does not tell us, whether the structures are inside the FOV. In this case a common solution is to make a low-quality pre-scan with a limited number of projections to search for the ROI. Afterwards, the determined coordinates are used for a high-resolution scan.

Appendix E: Multidimensional characterization of fibres

A cylindrical fibre is uniquely defined by its size d (height of the cylinder) and its cross-sectional diameter d_{cross} . Another process-relevant characteristic is its specific surface area

$$S_{V_p} = \frac{S}{V_p} = \frac{2d_{\text{cross}} + 4d}{d d_{\text{cross}}}. \quad (1)$$

The histograms of these characteristics and their parametric fits are depicted in Fig. S7a. Furthermore, Fig. S7b. visualizes the bivariate probability density of size and specific surface area using a bivariate histogram (left) and a parametric copula model (right).

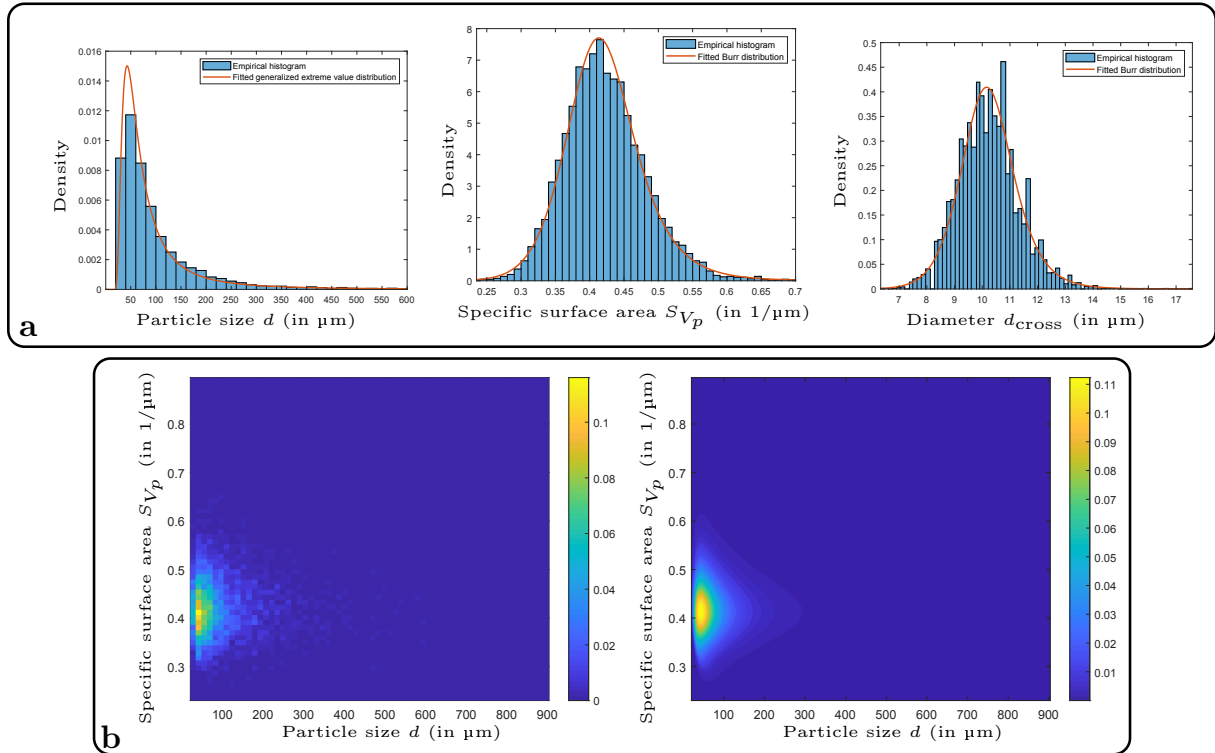


Figure S7: a) Fitted parametric (marginal) distributions to size (left), specific surface area (middle) and diameter (right) of fibres; b) bivariate histogram (left) and the fitted bivariate probability density using a BB8 copula (right).

Note that, instead of the size d and diameter d_{cross} , both the size d and the specific surface area S_{V_p} also uniquely characterize a fibre since

$$d_{\text{cross}} = \frac{4d}{S_{V_p}d - 2}. \quad (2)$$

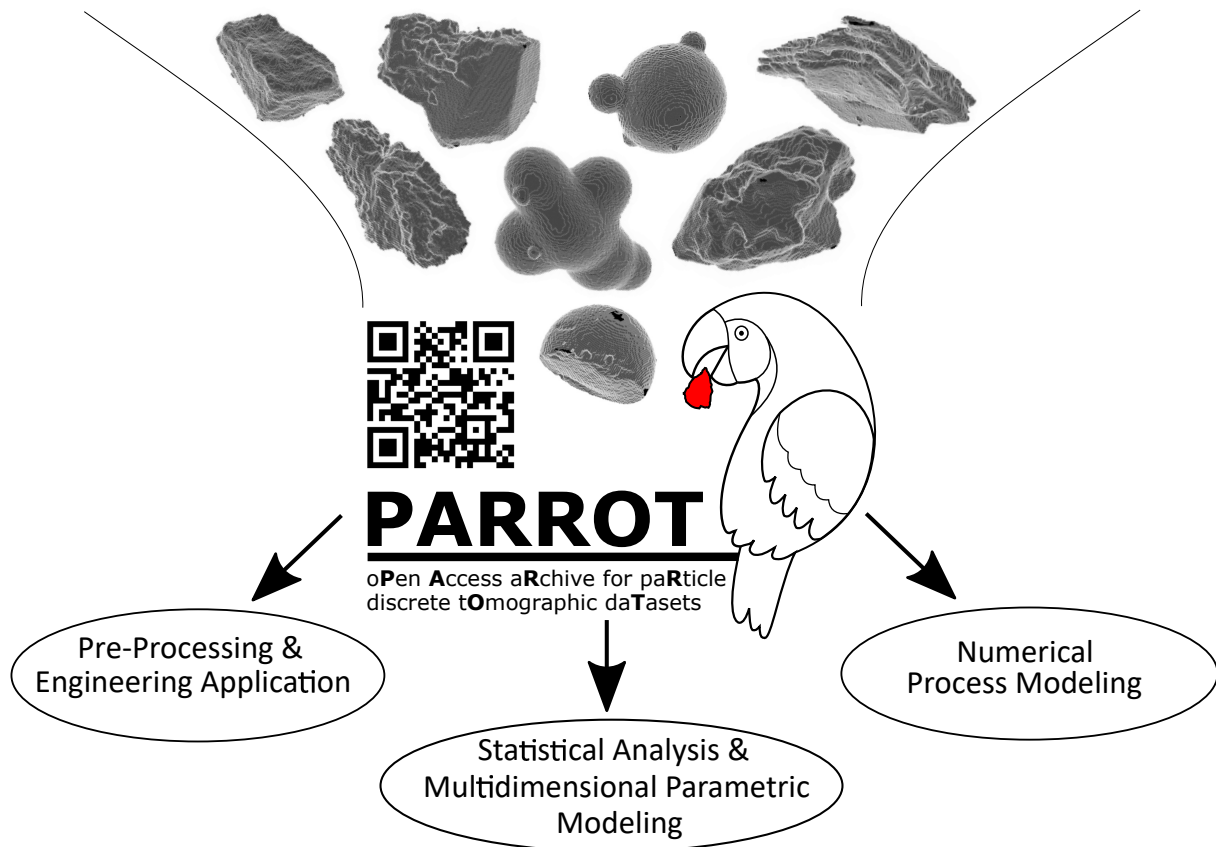
Thus, we can, for example, express the volume V_{fibre} of a fibre as a function of size d and specific surface area S_{V_p} by

$$V_{\text{fibre}}(d, S_{V_p}) = \frac{\pi}{4} d_{\text{cross}}^2 d = \frac{4\pi d^3}{(S_{V_p}d - 2)^2}. \quad (3)$$

Paper E

Microscopy and Microanalysis, January 2022 (open access)
*PARROT: A Pilot Study on the Open Access Provision of
Particle Discrete Tomographic Datasets*

Graphical Abstract




Highlights

- Database solution for handling 3D tomographic particle–discrete datasets of statistically relevant quantities
- Open access web–based user interface for filtering six practically relevant particle systems
- Download of all raw and segmented image stacks, 3D particle–discrete data in ready–to–use format and all related metadata

Original Article

PARROT: A Pilot Study on the Open Access Provision of Particle-Discrete Tomographic Datasets

Ralf Ditscherlein^{1*} , Orkun Furat^{2,†}, Erik Löwer¹, Raik Mehnert³, Robin Trunk⁴, Thomas Leißner¹, Mathias J. Krause⁴, Volker Schmidt² and Urs A. Peuker¹

¹Institute of Mechanical Process Engineering and Mineral Processing, Technische Universität Bergakademie Freiberg, D-09599 Freiberg, Germany; ²Institute of Stochastics, Ulm University, D-89069 Ulm, Germany; ³Mehnert IT Services, Schmiedestraße 7, D-09599 Freiberg, Germany and ⁴Institute of Mechanical Process Engineering and Mechanics, Karlsruhe Institute for Technology (KIT), Straße am Forum 8, D-76131 Karlsruhe, Germany

Abstract

In the present paper, as part of an interdisciplinary research project (Priority Programme SPP2045), we propose a possible way to design an open access archive for particle-discrete tomographic datasets: the PARROT database (<https://parrot.tu-freiberg.de>). This archive is the result of a pilot study in the field of particle technology and three use cases are presented for illustrative purposes. Instead of providing a detailed instruction manual, we focus on the methodologies of such an archive. The presented use cases stem from our working group and are intended to demonstrate the advantage of using such an archive with concise and consistent data for potential and ongoing studies. Data and metadata merely serve as examples and need to be adapted for disciplines not concerned here. Since all datasets within the PARROT database and its source code are freely accessible, this study represents a starting point for similar projects.

Key words: cake filtration, copula-based modeling, fluid flow simulation, multidimensional particle characteristics, particle database, statistical image analysis, X-ray tomography

(Received 31 May 2021; revised 24 November 2021; accepted 16 December 2021)

Introduction

In particle technology, a fundamental understanding of distributed particle characteristics is essential to develop efficient optimization strategies for processes based on particle–particle interactions. For particle sizes below 10 μm , there are numerous established characterization methods that can determine particle characteristics integrally or in a distributed manner (Bagheri et al., 2015). Besides methods like laser diffraction or the measurement of settling velocity, which are based on model assumptions, for example, considering all particles to be perfect spheres, there are methods based on 2D images like optical microscopy, scanning electron microscopy (SEM), or dynamic image analysis (DIA). With the latter, it is even possible to determine the particle morphology for particle sizes above 100 μm by capturing multiple shadow images under random rotation angles (Macho et al., 2019). Although these methods are able to generate distributions of various particle characteristics in 2D, it is not possible to transfer them to 3D without significant stereological bias in case of nonspherical particles (Erdogan et al., 2007; Kahl et al., 2017).

*Corresponding author: Ralf Ditscherlein, E-mail: ralf.ditscherlein@mvmt.tu-freiberg.de

[†]The first two authors contributed equally to this work.

Cite this article: Ditscherlein R, Furat O, Löwer E, Mehnert R, Trunk R, Leißner T, Krause MJ, Schmidt V, Peuker UA (2022) PARROT: A Pilot Study on the Open Access Provision of Particle-Discrete Tomographic Datasets. *Microsc Microanal.* doi:10.1017/S143192762101391X

© The Author(s), 2022. Published by Cambridge University Press on behalf of the Microscopy Society of America. This is an Open Access article, distributed under the terms of the Creative Commons Attribution licence (<https://creativecommons.org/licenses/by/4.0/>), which permits unrestricted re-use, distribution, and reproduction in any medium, provided the original work is properly cited.

Real 3D particle data is needed. In the following sections we would like to briefly motivate why the database solution shown here (Fig. 1) is a benefit in dealing with such 3D data.

3D Characterization of Irregularly Shaped Particles

As the 3D representation of an irregularly shaped soda-lime glass particle shows (Fig. 2, center), a full 3D description of the particle shape cannot be derived from sectional or projection images of 2D microscopy, especially when taking into account that in practice these are not available for each particle simultaneously from different perspectives. Only 3D characterization methods enable to capture multiple particle-discrete characteristics of the 3D particle geometry (Ueda et al., 2018), providing the opportunity to analyze distributions of characteristics on integral and particle-discrete level and to connect them with each other to learn more about the multidimensional interaction of particle characteristics. In this context, particle-discrete means that each particle is described by a vector of characteristics consisting of directly measurable volume pixel (voxel) information, like surface and volume, which are both influenced by the so-called partial volume effect (Soret et al., 2007), and further characteristics derived from this, like various descriptors of size (for example, longest axis, spherical equivalent diameter) and shape (for example, aggregated descriptors as sphericity or functional descriptors as spherical harmonics).

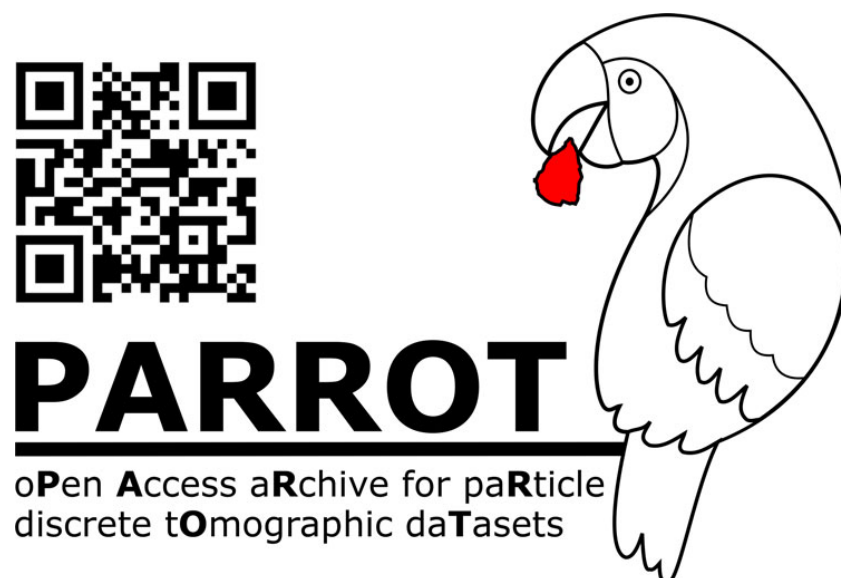


Fig. 1. Logo from <https://parrot.tu-freiberg.de>.

Besides destructive 3D methods like serial sectioning (Zhong et al., 2019), a possible nondestructive 3D characterization method is X-ray microtomography (micro-CT) which is able to capture structural and textural details on the microscale. Here, a series of 2D projection images is used to generate a full 3D representation, a so-called reconstruction, of the sample volume within the field of view (FOV). Micro-CT and setups with additional optical magnification, so-called X-ray microscopes (XRM), have become established laboratory methods in engineering sciences over the last two decades (Stock, 2008; Maire & Withers, 2014). The related application for particle characterization originally comes from the field of geology (Carlson & Denison, 1992; Cnudde & Boone, 2013) but is increasingly used for the analysis of particulate and porous materials in mechanical process engineering (Leißner et al., 2020). Depending on the selected particle system, a reasonable analysis often requires a multiscale approach, for example, for composite particles and/or particles the sizes of which cover various length scales (Ditscherlein et al., 2020a). In

this pilot study, however, we restrict ourselves to single-phase particle systems with a relatively narrow particle size distribution, for which the analysis can be performed without the correlation of measurements on multiple length scales.

Working Areas for Particle-Discrete Image Data

The acquisition and usage of such data is driven by different objectives (Schlüter et al., 2014; Bagheri & Bonadonna, 2016; Cepuritis et al., 2017). In this section, we introduce, as an example, a grouping of working areas from a particle technology perspective into five non-disjoint categories and showcase how these working areas can synergize by using a particle-discrete database. The grouping considered in the present paper consists of (i) a sample preparation strategy, followed by (ii) image acquisition, (iii) image processing, (iv) stochastic modeling of image data, including their simulation to generate virtual image data, so-called digital twins, and (v) numerical process modeling. We

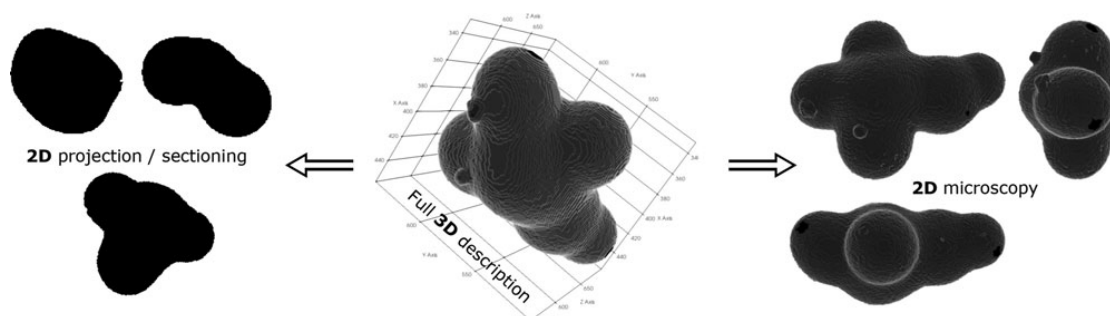


Fig. 2. Possible strategies for the characterization of particle systems shown by the example of a soda-lime glass particle. A visualization of the full 3D description is shown in the middle. Via sectioning or projection measurements 2D data of the particle is obtained (left). Alternatively, 2D microscopy provides top views of the particle, depending on its orientation (right).

Table 1. Working Areas with Corresponding Examples for Database Filling and Query.

	Working Area	Database Filling	Database Query
(i)	Sample preparation	Metadata	–
(ii)	Image acquisition	Metadata and tomographic image stack	–
(iii)	Image processing	Metadata and segmented image stack, 3D particles	Tomographic image stack
(iv)	Stochastic modeling	Metadata and statistical characteristics, virtual particles	Segmented image stack
(v)	Numerical modeling	Metadata and model characteristics	3D particles

believe that close collaborations between various research groups across disciplines regarding their particle-discrete datasets is an important requirement to use synergy effects in all five working areas (i)–(v) mentioned above. In particular, we believe that the development of a multidisciplinary database is an important prerequisite for many future research activities.

Table 1 summarizes some aspects of data exchange between the working areas (i)–(v) within this database, distinguishing between write accesses (database filling) and read accesses (database query). More precisely, the PARROT database will contain metadata on sample preparation procedures (working area (i)) which can depend on the particle system under consideration (including, for example, dry dispersion or extraction only to avoid fragmentation) and the required analysis volume (ideally matching the FOV of the measurement) (Ditscherlein et al., 2020a, 2020b). In addition, the metadata of the image acquisition (working area (ii)) can provide indications of possible artifacts (Boas & Fleischmann, 2012) in the subsequent image processing of the image stack which is uploaded to an external archive (OpARA) and linked via a digital object identifier (DOI) to the PARROT database. For a quantitative analysis of this kind of data (working area (iii)), image processing steps have to be performed, for example, the automated extraction of objects of interest which are, in the context of the present paper, individual particles (Beucher & Meyer, 1993; Burger & Burge, 2016; Westhoff et al., 2017; Ditscherlein et al., 2020a). The resulting segmented version of tomographic image data is also uploaded to OpARA and linked via DOI to the PARROT database. Note that image segmentation using conventional image processing algorithms can be a nontrivial task, which often requires careful calibration of algorithms. This issue can be avoided using methods from machine learning (for example, convolutional neural networks) which have proven their usefulness for image processing tasks in numerous applications (Furat et al., 2018, 2019b; Jiang et al., 2020; Furat et al., 2021a). However, in order to train such methods for image segmentation tasks, pairs of raw data and segmented data are required, where the latter can be difficult to obtain. The PARROT database provides for each tomogram the corresponding segmented 3D image which amounts to thousands of segmented slices. Since recent neural networks can already be trained with just a few slices (Çiçek et al., 2016; Furat et al., 2021a), users of machine learning methods can access an adequate amount of data to train and test their models.

From segmented image data, individual particles can be extracted for the computation of particle characteristics which describe their size, shape, and texture (Burger & Burge, 2016; Furat et al., 2018), see Appendix A-2 of the Supplementary Material. Such particle-discrete vectors of characteristics will be made available within the PARROT database for modeling purposes (working area (iv)). To begin with, particle systems can be efficiently characterized by modeling the distribution of individual particle characteristics using univariate parametric probability distributions (Johnson et al., 1994, 1995). Moreover, the particle-discrete vectors of characteristics allow for the modeling of multivariate distributions which capture the correlation structure of considered characteristics (Ditscherlein et al., 2020a; Furat et al., 2019a), see Appendix A-2 of the Supplementary Material. Besides this, the segmented tomographic image data can be used to calibrate stochastic geometry models. They can be utilized to generate virtual particle systems, so-called digital twins (Prifling et al., 2019; Furat et al., 2021b), which will be made available within the PARROT database in the future. Finally, both segmented and virtual 3D particles within the database can be used for numerical modeling (working area (v)) to compute process-related particle characteristics, like, for example, their settling velocity (Trunk et al., 2018), see Appendix A-3 of the Supplementary Material. Here, both, the immersed boundary method (Uhlmann, 2005) and the lattice Boltzmann method (Trunk et al., 2021) can be utilized to finally assign these additional characteristics to the corresponding particles within the PARROT database—thus, enabling the analysis of structure-property relationships (Stenzel et al., 2017; Neumann et al., 2020; Prifling et al., 2021). With the combination of working areas (i)–(v), a holistic approach to the investigation of such 3D data is provided, from acquisition of image data through their processing and analysis to modeling. Furthermore, the workflow is fully reproducible as all data is made available in open access.

Some Practical Use Cases

Designing type, structure and content of a database is a crucial step and can be done in two ways. The first one is to focus on the data to create a system that can manage it optimally. Relevant key parameters are storage space, minimum redundancies, and retrieval times. The second approach is to focus on the users and the needs for their daily workflows. Users have specific ideas regarding their requirements for the database—so-called use cases (for example, “analysis of particles resulting from a specific comminution process,” “surface characterization of dolomite particles with a minimum voxel volume of 10,000,” etc.). Taking these use cases into account, the data handling becomes intuitive in a certain way. This will be called the user-driven approach. In reality, both approaches go hand in hand and have to be balanced as well as possible. Of course, daily work shows that the working areas presented in the previous section cannot be considered completely independent of each other. Often methods from different working areas are required for the analysis of such image data of particle systems. In the following, we will consider three practical use cases which utilize methods from the introduced working areas and deal, on the basis of a common data source, with different tasks: Acquisition and pre-processing, statistical analysis and multivariate parametric modeling, and numerical process modeling. Note that the use cases illustrate possible applications of the database from the view of particle technology. Nonetheless, applications of further scientific

fields such as geoscience, materials science, or biology that could benefit from such a database are conceivable. For reasons of space, the use cases are only briefly introduced in this paper. A detailed discussion can be found in Appendix A of the Supplementary Material.

Acquisition, Preprocessing, and Analysis of 3D Image Data

The acquisition and analysis of 3D particle-discrete data is the key to obtain valid results regarding the distribution of particle descriptors, especially in the case of irregularly shaped particles. The analysis of such particle systems is described several times in the literature (Cnudde & Boone, 2013). The combination of experimental process engineering with digital computer-based methods helps to predict the behavior of process sequences and their results (Dong et al., 2009; Lin et al., 2010; Yu et al., 2018). For example, in cake-forming filtration (Ruth et al., 1933), the correlation of (measured distributed) particle size and shape characteristics with (measured distributed) descriptors of the 3D morphology of the pore space in the filter cake provides information that can be used to predict process behavior (for example, filter cake dewatering and washing). Querying the database allows users to generate artificial cake structures. These synthetic structures can be used for a large number of simulations, which in turn must be validated by individual experiments. Thus, it is not a replacement of the old methodology, but a significant extension. The case study presented in Appendix A-1 of the Supplementary Material is intended to show how the first step toward this approach is taken using the PARROT database.

Statistical Analysis and Multivariate Parametric Modeling of 3D Image Data

Tomographic image data can provide detailed insight into the 3D microstructure of materials (Maire & Withers, 2014) like, for example, for investigating the active and pore phase of cathode materials (Prifling et al., 2019) or the grain boundary network of polycrystalline materials (Furat et al., 2021a). However, in order to quantitatively investigate tomographic image data, alternative (parametric) representations of this data have to be derived which are easier to interpret. With respect to image data of particle systems, a common approach is the characterization via particle size distributions. This can be done by fitting parametric probability distributions to particle sizes (i.e., volume-equivalent spherical diameters) computed for segmented particles (Handl et al., 2017; Ditscherlein et al., 2020b). However, since tomographic image data gives access to (possibly thousands of) particle-discrete vectors of characteristics, a more informative and efficient approach is to parametrically model the distribution of characteristics in order to describe the particle system. Note that modeling each considered characteristic individually using univariate parametric distributions does not adequately describe the information yielded by the vectors of characteristics. More precisely, univariate distributions do not provide any information on whether and how particle characteristics are correlated with each other (for example, if larger particles are more spherically shaped, etc.). Therefore, we deploy multivariate parametric distributions for modeling the joint distribution of characteristics—thus, capturing the correlation between characteristics (Furat et al., 2019a, 2021a; Ditscherlein et al., 2020a). Then, the considered particle system can be described by just a few model parameters. To illustrate this, we give a possible application of the PARROT database in Appendix A-2 of the Supplementary Material, where we use particle-discrete (vectorial) data to fit

multivariate probability distributions to pairs of characteristics which efficiently characterize systems of particles.

Numerical Process Modeling Based on 3D Image Data

Numerical process modeling is a useful tool to investigate processes or parts of them, which are not easily accessible for measurement devices or require costly equipment for examination (Champion et al., 2007; Kashiwaya et al., 2012). In the literature, many methods and approaches for the simulation of particle behavior have been proposed (Zhu et al., 2008). To keep the required amount of computations at a reasonable level, usually some assumptions and simplifications, especially concerning geometrical particle characteristics, have to be made. However, with increasing computational power, simulations can depict more and more aspects of reality. The declining need for simplifications also leads to a growing need for data. For instance, in particle simulations, it is now possible to describe the real surface of a particle instead of using a spherical approximation. This, however, requires detailed 3D particle datasets with a reasonably exact surface description and an efficient surface representation, which is compatible with currently available simulation software. Users of the PARROT database can download numerous systems of particles as input for numerical simulations by variation of their search-query parameters, see Appendix A-3 of the Supplementary Material. For example, this enables the correlation of geometrical properties of the particle system (for example, multivariate distribution of size/shape characteristics) with physical properties, see Stenzel et al. (2017) and Neumann et al. (2020).

Graphical User Interface

We believe that particle-discrete data is only valuable in combination with metadata which specifies the imaged material, the measurement settings and the performed image processing steps. As such, these should all be provided within the PARROT database and usable as search criteria. The user should be guided through the search and download processes to understand the data in sufficient detail, because otherwise the risk of downloading inappropriate or incomplete data is high. For this reason, the PARROT database is equipped with a web-based graphical user interface (GUI). Input filters can be selected by the user in order to subsequently obtain information on the filtered particle systems and the relevant raw image data. The data corresponding to the search results can be downloaded in a compressed format or, in the case of raw image data, is linked to an external database. Preview images in 2D and 3D illustrate the search results and give a first impression of the data. A short manual explains important terms and provides additional information and is provided on the PARROT website <https://parrot.tu-freiberg.de>.

Outline

The rest of this paper is structured as follows. In section “Materials and Methods,” we introduce some basic methods and give a short overview of the particle systems considered in this paper. In section “Results and Discussion,” we explain some components of the database system and the GUI. This infrastructure is used to query data for the introduced three practical examples of use cases, which are discussed in detail in Appendix A of the Supplementary Material. Section “Conclusion and Outlook” concludes, providing possible

Table 2. Characteristics of the Six Particle Systems Considered in This Study.

	Composition	Manufacturer	Manufacturing Process	Size Range
Aluminum-oxide	Al ₂ O ₃	ALMATIS	Crushing	55–200 μm
Dolomite	Carbonate	Wünschendorfer Dolomitwerk	Calcination and crushing	90–200 μm
Soda-lime glass	Amorphous silicate	Sigmund Lindner	Dry spraying	150–300 μm
Limestone	carbonate	GEOMIN Ergeb. Kalkwerke	Dry milling	55–200 μm
Mica	Silicate	Zinnwald deposit	Comminution and magnet. sep.	90–300 μm
Quartz	Silicate	Strobel Quarzsand	Crushing	<200 μm

guidance for optimizing and maintaining the database as well as scalability beyond the scope of this pilot study.

Note that in this study, we measured six different particle systems of various shapes, from spherical (soda-lime glass particles) to sphere-like (aluminum oxide, dolomite, limestone, and quartz) and clearly nonspherical ones (mica), appropriate examples of particles can be found in Appendix B of the Supplementary Material. We imported the segmented particle-discrete data and related characteristics into the PARROT database. Using the database allows users to filter and query these datasets with respect to distributed characteristics according to specific criteria and, if necessary, match them with corresponding other measurement data. Since the database allows free access worldwide, this is also possible for interested parties who do not yet possess the necessary measurement equipment.

Materials and Methods

Description of Particle Systems

All six particle systems investigated in this study have practical relevance for numerous scientific questions regarding size and shape distributions of particles, their arrangement in the bulk (for example, packed particle bed comminution) and the resulting pore network for fluid flow in filtration experiments. Further information about the characteristics of these particle systems is given in Table 2, whereas examples of SEM images are shown in Figure 3.

Tomographic Measurements Using X-Ray Microscopy

The X-ray microscope (type Xradia VERSA 510 from ZEISS) used in this study has a two step magnification. X-ray photons are

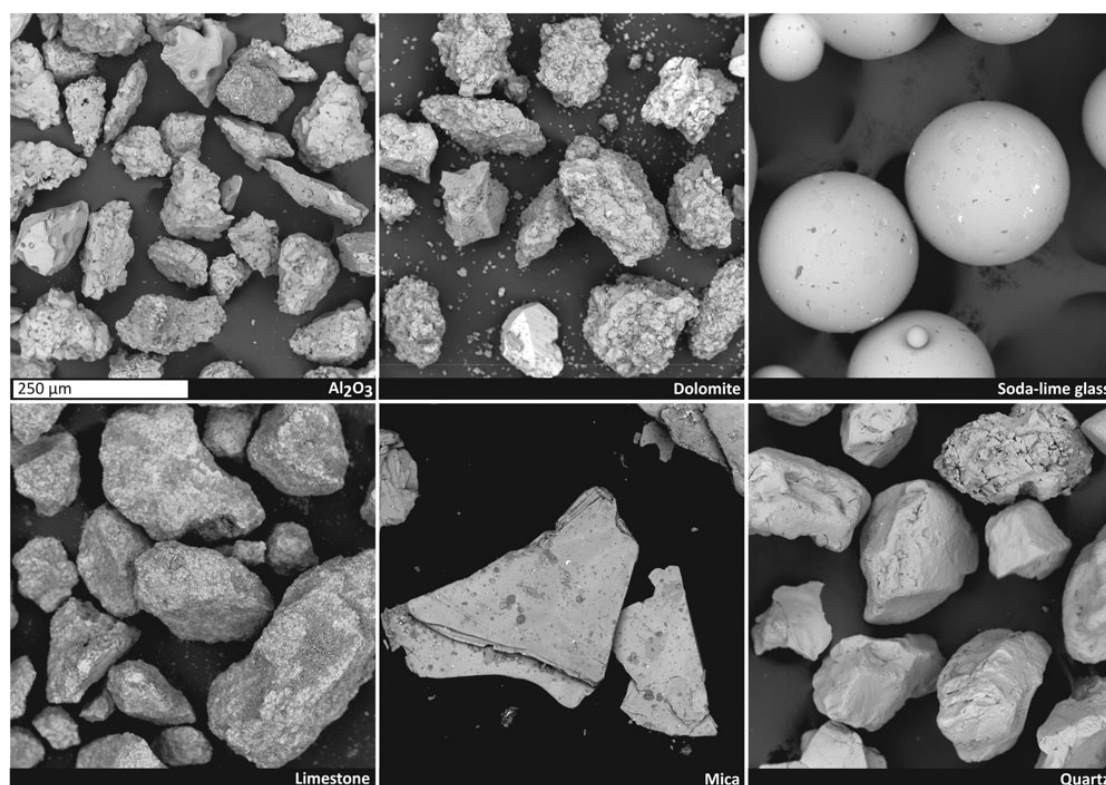


Fig. 3. SEM images of the particle systems considered in this study. The scale bar refers to all systems.

generated in a polychromatic source and projected as a cone beam onto a scintillator screen. This geometrically magnified image is transformed within a scintillating material into photons of visual light (VIS) according to the incoming intensity and energy regime of the X-ray photons, magnified a second time by VIS optical lenses (in this study, we use a magnification factor of four), and projected on a CCD flat panel detector. One tomographic measurement consists of a series of projection images captured over an angular range of at least 180° (in this study 360°), which is mathematically reconstructed into a 3D representative, the so-called tomogram (Buzug, 2008). Artifacts and measurement errors related to tomography will not be discussed here. Interested readers are referred to the literature (Davis & Elliott, 2006; Boas & Fleischmann, 2012). All relevant acquisition parameters can be found in Appendix E of the Supplementary Material.

The starting point for the measurement is to use a well-dispersed particle sample that has to be embedded into a low X-ray attenuating matrix to avoid undesirable motion during the exposure process in the tomography system. Here, the main focus is on a statistically representative sample with sufficiently large space between individual particles to support the image segmentation workflow (Ditscherlein et al., 2020b, 2020c).

Image Segmentation Strategy

To present an example of workflow in an engineering application, we limited ourselves to a simple image segmentation problem using single-threshold binarization with ImageJ (Rueden et al., 2017), described in detail in Appendix C of the Supplementary Material. This strategy works well for nearly spherical particles which are homogeneously distributed within the sample volume. Since this is not always the case in reality, we discover two error causing effects which are well known from image processing: (i) There are particles which are touching each other although they are not physically connected. In this case, the segmentation step (watershed) is not able to separate the particles from each other because of the limited voxel resolution that significantly increases the so-called partial volume effect (PVE; Soret et al., 2007), that is, they are under-segmented. This is the dominant effect, since it affects at least two or more particles in each case. (ii) There are particles which are clearly nonspherical and elongated in one (fibers) or two spatial dimensions (plates). Many conventional segmentation algorithms work similarly in all spatial directions and thus lead to an undesirable artificial splitting along the

longest particle dimension, so-called over-segmentation which can be avoided, for example, by utilizing neural networks for segmenting (Ronneberger et al., 2015; He et al., 2017) or post-processing (Furat et al., 2018). However, this is a minor effect since it affects only one particle in each case (which is then erroneously decomposed into a certain number of fragments). Since both, over- and under-segmentation, alter the particle size and shape significantly, such datasets must not be imported into the database. For the initial datasets in the PARROT database, this was realized by manual sorting to provide reliable datasets. Applied to a very large number of samples with a significantly larger number of particles beyond this pilot study, this procedure needs to be replaced by an automatism that is reliable and offers a possibility to evaluate the quality of an automatic segmentation in order to compare different procedures if necessary. Examples of correctly segmented and discarded particles can be found in Appendix B, whereas the implementation of the segmentation algorithm is given in Appendix D of the Supplementary Material. In particular, the example of mica shows that it is not always obvious to decide which image regions belong to an individual particle. Furthermore, in the case of layered minerals, which can delaminate already during sample preparation, particle segmentation can be difficult and not straightforward. This is the reason why it is absolutely necessary to know the particle system's specialities (metadata) to understand possible unexpected effects when dealing with the data.

Relational Database

Overcome the Large Table Approach

When dealing with datasets, a common approach is utilizing a list/table of values (Fig. 4a). This makes sense as long as all data is part of the same aggregation level (Fig. 4b). If, in contrast, there is data which exists at higher level (meta-level \rightarrow metadata), for example, measurement parameters that are constant for a large number of measurement points (redundant data), the consistency of the database can be compromised. The more parameters are added, the larger this table will get. Searching inside this structure will quickly become confusing and ineffective. In addition, the later addition of new parameters to existing datasets using this structure can only be done with great difficulty. To create a valid database for a large number of particles, which has been the aim in the design of the PARROT database, such redundancies have to be reduced and consistency has to be improved.

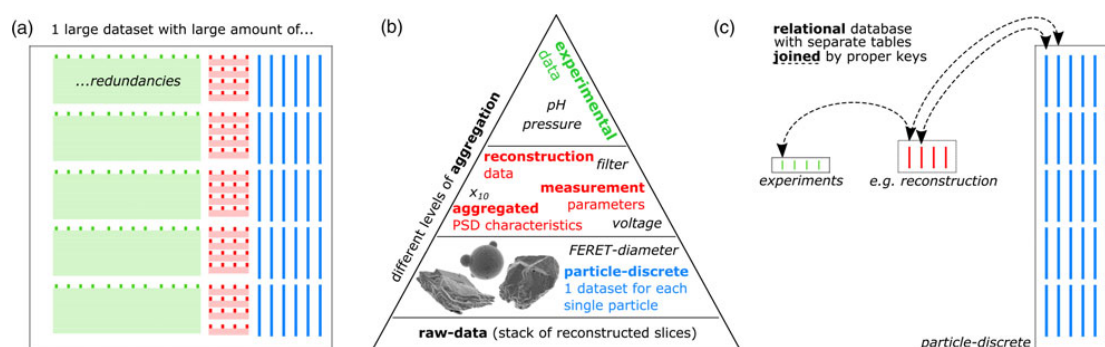


Fig. 4. (a) Different levels of aggregation (b) causes lots of redundancies in a one-table-solution which can be overcome by (c) a relational database approach including the connection (a so-called join) with proper key indices.

One way to this was proposed in 1970 as “A relational model of data for large shared data banks” (Codd, 1970), today generally referred to as relational database.

Database Structure

A relational database compensates for inconsistencies and redundancies by structuring the data according to their aggregation level (see Fig. 4b) and, optimally, within functional groups (Codd, 1982; Paredaens et al., 1989). For example, all data related to an experiment are inserted into a separate experiments table, which is much smaller than the particle table containing particle-discrete data for all particles. On the next aggregation level, there may be data regarding reconstruction and measurement settings or aggregated particle characteristics. This structuring can be done in several steps and is called normalization. A connection between tables is established by so-called key-columns. Every table has a primary key column which has a unique value for every row and can be inserted as a foreign key into another table to establish the relation between both, a so-called join. Joins can be used to link data according to the set theory known from mathematics, for example, datasets belonging to tables A and B at the same time (inner join) or datasets, which only belong to table A but not necessarily to B (left join), etc. This enables us to connect the PARROT database with other relational databases, which contain, for example, results from a laser diffraction measurement of the same particle system, assuming that there are corresponding matching unique keys in both databases. Figure 5 shows the structure of the PARROT database including tables for data and metadata. External connections and automated functionalities are described in the lower left legend. The database itself is embedded in an overall structure that provides all necessary software for database manipulation. This structure is referred to as database management system (DBMS). Besides storing and retrieving data, the system includes

an appropriate security environment. For the PARROT database, we chose MariaDB (Wood, 2018), a widely used community-developed fork of the well-known MySQL DBMS. Its lean design makes it easy to set up for smaller projects, but it is still fully equipped to potentially upscale the DBMS in terms of load and storage. For this pilot study, we use a virtual Windows server with internet access, 1 TB hard disk for the DBMS and the file system, 4 GB RAM and a two core CPU at 2.4 GHz.

The Importance of Metadata

Not knowing the related metadata to our datasets is like knowing the alphabetic letters without their syntax, context, and interconnection. For our case, this means: How is data to be interpreted? Which data types and ranges of values are present? Is the actual data in a raw format or has processing already been performed? In the sense of a holistic view, metadata is essential in order to be able to use findings for specific process optimization. In this context, metadata consists of parameters regarding experiment (pressure, volume flow), measurement (acceleration voltage, exposure time), image analysis (segmentation algorithm) or modeling (model type, basic assumptions). To ensure valid metadata, acquisition should be done automatically whenever possible, for example by using automated extraction from equipment log-files. The integrity and consistency of this type of data is essential for successful data analysis. Within the PARROT database, the import is realized by automated importing routines that are adapted to tab-separated text files suitable to serve as a possible candidate for future interface creation. Since interface implementation is often non-trivial and very device-specific, this general method was chosen as the starting point for the pilot study. Note that the currently available metadata does not claim to be complete. For the pilot study, we have selected the most relevant ones for us at the moment. However, the structure allows further criteria to be added without difficulty.

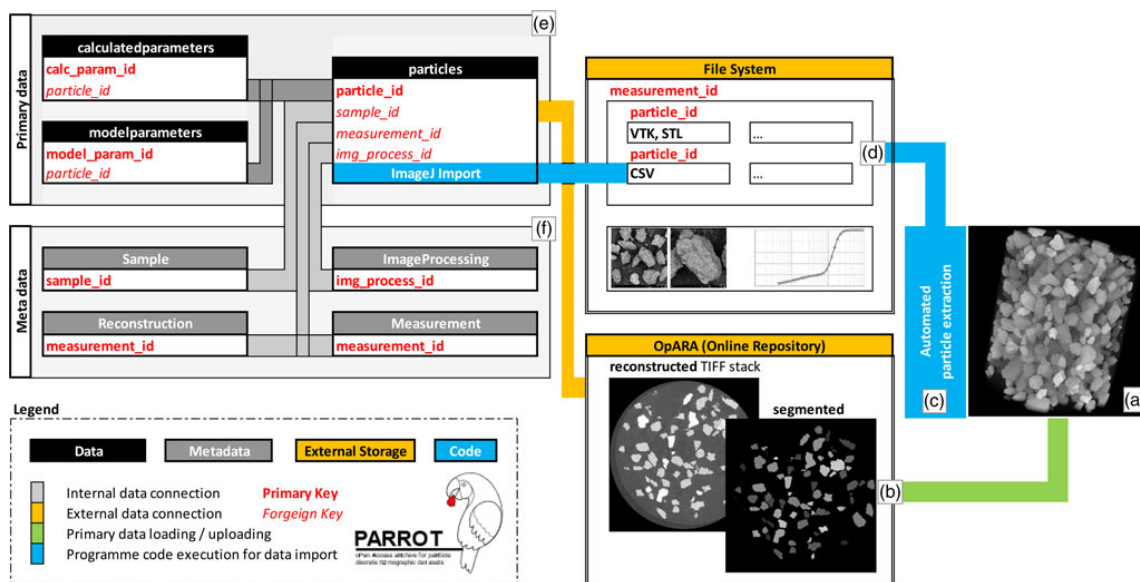


Fig. 5. Structure of the relational database: Starting with (a) the tomographic data that is (b) stored within an online repository and (c) divided into particle-discrete datasets that are (d) stored in a local file system. After import, the database contains (e) primary data and (f) related metadata.

Storage Partitioning

Grouped by memory size, the database holds three general types of data. The first type consists of alphanumeric characters in binary format physically stored within the database, typically allocating only a very small amount of disk space—in our case for 6,000 particles approx. 3 MB. The second type concerns ASCII-files containing particle-discrete data obtained from segmented voxelized image data. The required disk space for the initial dataset of 6,000 particles is approx. 40 GB. This data does not need to be indexed but has to be quickly accessible for compression and downloading. It is thus stored within a local file-system and linked to the database. Provided database-internal special data types, so-called Binary Large Objects (BLOB), would unnecessarily expand the database structure and behave rather unfavorably with regard to efficient resource management by the DBMS. The third type concerns the raw tomography data, consisting of the reconstructed single channel TIFF stacks (for binning 2 with 1024×1024 pixel) and their segmented counterparts. The required disk space for one particle system in compressed format is approx. 2 GB (in total, 12 GB for all six examples). Here, it would also be possible to store the files in the local file system. With regard to scaling the application and high-performance data access, an external solution was preferred. Note that TU Dresden together with TU Bergakademie Freiberg provide an open access repository and archive (OpARA) for storing scientific datasets for a worldwide access via digital object identifier (DOI), which allows linking this external storage via the DOI primary key to the related dataset. Another advantage of this method is that individual datasets can also be directly referenced in the context of scientific publications. The backup of the data is guaranteed by the storage management system of TU Bergakademie Freiberg.

Data Access

Under the assumption of a web-based data access, there are two general design strategies for building the GUI. The data would also be accessible via text input, but this would raise the barrier to widespread use. A GUI should give an intuitive way for selecting and retrieving the data. One way would be to design separate web-pages for each use-case. This approach would get users to their destination, that is, the downloading of filtered data, in the fastest way. However, if important filter substeps are skipped, there is a risk of unintentional virtual mixing of particle-discrete data from different measurements, which mostly makes no sense either in image analysis or in modeling from the application point of view. The second approach is to “guide” all users along the same steps: (i) pre-filtering related to material, measurement, and characteristic, (ii) selecting the particle system; (iii) selecting the related tomographic dataset, and (iv) downloading selected data and metadata. Note that steps (i)–(iv) are all accompanied by a deliberate filtering of the data. This means that in each subsequent step, only the data which match the selected filter criterion are displayed. The filter selection is cached in each step and automatically saved as a text file in the compressed (ZIP-format) download folder, so that it can also be reconstructed afterwards how the filter result was obtained, that is, also by other users who did not query the data themselves.

Results and Discussion

The use cases already introduced in the section “Some practical use cases” are embedded into three different research projects with the following titles: (i) Development of process models

based on 3D information about the multiphase processes in the pore space of a filter cake (funded by DFG, project number: PE 1160/23-1), (ii) Stochastic modeling of multidimensional particle properties with parametric copulas for the investigation of microstructure effects on the fractionation of fine particle systems (funded by DFG through project Z2 of SPP 2045, project number: SCHM 997/27-2), (iii) Two-scale approach for the simulation of multidimensional fractionation of fine particles (funded by DFG through project Z4 of SPP 2045, project number: KR 4259/8-2). For a detailed discussion of all three use cases, the interested reader is referred to Appendix A of the Supplementary Material.

The database itself has been developed in project Z1 of SPP 2045 (project number: PE 1160/22-2) which, in conjunction with projects Z2 and Z4 mentioned above, represents the central part of the SPP 2045 (DFG project number: 313858373) dealing with multidimensional and correlative characterization of particle systems. Further information regarding SPP 2045, including detailed project descriptions, is available online via <https://tu-freiberg.de/fakult4/mvtat/SPP2045>.

Design of the Database System

Due to the broad scope of the topic, not all components of the database can be explained in detail. Since the complete source code of the GUI and the database structure are available in open access, only the most important points will be discussed here.

Data Management

The workflow from gathering data, their analysis, modeling, simulation, and visualization is referred to as data management (Gray et al., 2005). Perhaps one of the most important aspects that completes this process is data sharing. Only when this is possible, that is, when the documentation and provision of metadata has progressed to the point where other workgroups can use the data without difficulty, has the potential been fully exploited. We believe that our approach in implementing the PARROT database is a first step toward reaching this goal on a small scale. It combines fast data access with reasonable storage management and is thus suitable for scientific institutions which do not have sufficient investment funds at their disposal. Open access is an important point in this context. The storage in an online repository (in our case OpARA) only represents an outsourcing of the resources in a broader sense; provided with metadata, an additional added value is generated here, which also benefits the scientific community.

The goal of this pilot study was to develop a working system without requiring a major investment of money or personal resources. We use the noncommercial standard Windows programming environment, called the .NET framework. Within this framework, we use Microsoft Visual Studio with ASP.NET as a programming development environment. The provided model-view-controller architecture (MVC; Leff & Rayfield, 2001) allows a simple set-up of the system. An important aspect in this regard is the language support for querying the database. In most cases, the structured query language (SQL) is used to communicate with the database. Just as in human languages, there are many ways to use this language. Complicated query structures can sometimes produce the same results as simply formulated ones. For an efficient way of using this language, we use a common tool for object-relational mapping (ORM), called

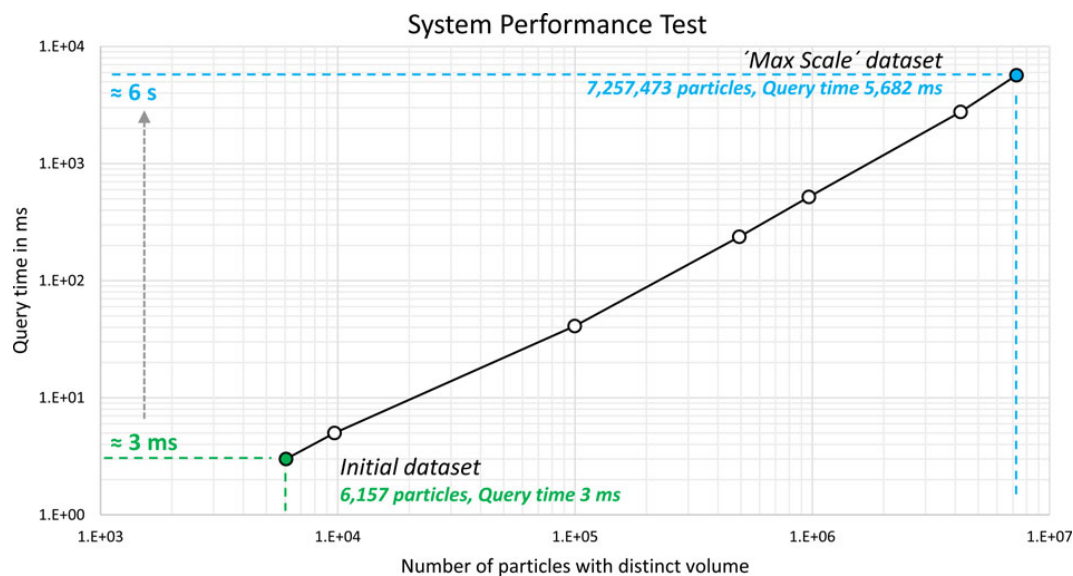


Fig. 6. Performance test using SQL query time as a speed measure over artificially generated discrete particle datasets. Note that unique particle volumes from the total dataset are queried (initially: approx. 6,000 maximum: 10 million particles).

Dapper. This architecture allows easy linking of the input from the web interface to the database, is highly performant and secure against unintentional database manipulation (injections).

Performance

Normally, the performance of a database system is monitored by tools of the DBMS under real conditions during operation. To give an example of such a performance analysis, certain tests with high load were simulated by creating duplicates of the original data in the pilot system.

As a performance measure, we use an SQL query which selects datasets based on distinct bounds specified by the user. As can be seen in Figure 6, querying approximately 7 million particles with unique voxel volume out of a total of 10 million lasts approximately 6 s. The query time of the DBMS itself is therefore in all likelihood not a problem even with very extensive operations. Much more important is the interaction of the DBMS, web server and storage, see section “Maintenance and scalability”.

Maintenance and Scalability

Maintenance is part of the administrative activities that are mandatory for a database system in order to guarantee stability and performance (Mullins, 2002). In the specific example of the PARROT database, this mainly includes the monitoring of database parameters. For example, the load caused by several concurrent database accesses is checked. Since all the individual components (web server, database, storage) interact in a complex way here, it is difficult to predict the real behavior in detail. The administrator must, therefore, statistically evaluate database accesses and optimally balance resources. The system is equipped in such a way that no problems are seen here for the initial phase. It is important that suitable limit values are set in the monitoring tool to alert of bottlenecks in advance, so that the system can be adjusted accordingly at an early stage. Since the system is located on a virtual server, resources can be added quickly after the

shortest downtime and can thus be optimally adapted to the actual requirements.

The used database management system (MariaDB; Tongkaw & Tongkaw, 2016) can be scaled up in data volume, query intensity, and performance by distributing it over a computing cluster, which is commonly known as a “Max Scale” approach (Zaslavskiy et al., 2016). The bottleneck here is rather the web server, which has to handle the parallel accesses. Since no query intensities comparable to other widely used web applications are to be expected in the present case, this is seen as less critical. However, the system should always have enough resources available and, if possible, be designed so that it never runs at full load. As discussed above, this monitoring also falls within the scope of the administrative activities in the pilot phase.

To optimize data and metadata entry for very large datasets, the data import described above would need to be done automatically from a central location. Typically, this is realized by so-called data collectors. These software tools are executed by the server, usually at fixed time intervals, to check whether there is new data in the file system. If this is the case, the corresponding files are read out and imported into the database with corresponding SQL statements, or file paths are linked.

Finally, it is important to emphasize that the general design of the system is critical at this point too. Is there an expert panel that monitors the submission of new datasets or are there mechanisms that automatically check user uploads? How and according to which criteria this can be done is a large complex of topics that cannot be dealt with in the present paper.

Conclusion and Outlook

A complete three-dimensional discrete description of particulate systems is the basis for a wide range of applications from traditional engineering through comprehensive image analysis and microstructure modeling to process modeling. Networking at

the data-level exploits synergies and promotes the exchange of experience. As this study shows, this can be implemented most efficiently by using a relational particle database. Thus, all three use cases presented briefly in this paper and detailed in Appendix A of the Supplementary Material give the possibility to download data according to their requirements. Guided by a simple online web-based graphical user interface, basic understanding of particulate systems is supported, which minimizes potential content errors, like unintentional virtual mixing of different particulate systems.

Note again that this study is not a software package or program library, but rather proposal for a solution that has emerged from the networked work of our research group. In the next step of the project, further particle systems will be added. Moreover, the aim is to make high-resolution image data of individual particles available. Cross-linking between other research groups would also be conceivable to increase the available measurement time, for example, particle systems could be exchanged and scanned during potential equipment standby times. In order to implement this as efficiently as possible and also to be able to comply with the growing demands on the system, the infrastructure and administration would have to be transferred to a superior research institution like the National Research Data Infrastructure (NFDI), funded by the German Research Foundation (DFG).

The authors look forward to a lively use of the PARROT database (<https://parrot.tu-freiberg.de>) and would be grateful for suggestions for improvement and user feedback.

Data availability

The PARROT database is accessible via <https://parrot.tu-freiberg.de>. The complete source code is published in the github repository <https://github.com/ps-igel/OPD> under the GNU General Public License v3.0. Complete raw data (reconstructed and segmented TIFF stacks) of all particle systems considered in this study is available by open access via the OpARA online repository of TU Dresden and TU Bergakademie Freiberg via <http://dx.doi.org/10.25532/OPARA-104> (dolomite), -105 (Al₂O₃), -106 (quartz), -107 (mica), -108 (limestone), and -109 (soda-lime glass). All data is explicitly intended for free use and should help to provide a good starting point for the investigation of similar systems. The authors hope for a vivid exchange of experiences in the future.

Supplementary material. To view supplementary material for this article, please visit <https://doi.org/10.1017/S143192762101391X>.

Acknowledgments. The authors thank the German Research Foundation (DFG) for supporting this study as part of the Priority Program SPP 2045 (DFG project number: 313858373), which is dealing with highly specific multidimensional separation of technical ultra-fine particle systems with particle sizes below 10 μm, for supporting the filtration project regarding the development of process models based on 3D information about the multiphase processes in the pore space of a filter cake (PE 1160/23-1), and for funding of the micro-CT device (INST 267/129-1). Furthermore, we would like to thank Ralf Schünemann as well as the colleagues from the Computer Center of TU Bergakademie Freiberg and the OpARA-team at TU Dresden for their valuable support, Henry Lehmann for his guidance in 3D data processing, Lisa Ditscherlein for providing the SEM images, and Thomas Buchwald for carefully reading the manuscript.

References

Bagheri G & Bonadonna C (2016). On the drag of freely falling non-spherical particles. *Powder Technol* **301**, 526–544.

- Bagheri GH, Bonadonna C, Manzella I & Vonlanthen P (2015). On the characterization of size and shape of irregular particles. *Powder Technol* **270**, 141–153.
- Beucher S & Meyer F (1993). The morphological approach to segmentation: The watershed transformation. In *Mathematical Morphology in Image Processing*, Dougherty ER (Ed.), vol. **34**, pp. 433–481. Boca Raton: Taylor & Francis Group.
- Boas FE & Fleischmann D (2012). CT artifacts: Causes and reduction techniques. *Imaging Med* **4**, 229–240.
- Burger W & Burge MJ (2016). *Digital Image Processing: An Algorithmic Introduction Using Java*. London: Springer.
- Buzug TM (2008). *Computed Tomography: From Photon Statistics to Modern Cone-Beam CT*. Berlin, Heidelberg: Springer.
- Carlson WD & Denison C (1992). Mechanisms of porphyroblast crystallization: Results from high-resolution computed X-ray tomography. *Science* **257**, 1236–1239.
- Cepuritis R, Garboczi EJ, Jacobsen S & Snyder KA (2017). Comparison of 2-D and 3-D shape analysis of concrete aggregate fines from VSI crushing. *Powder Technol* **309**, 110–125.
- Champion JA, Katare YK & Mitragotri S (2007). Particle shape: A new design parameter for micro- and nanoscale drug delivery carriers. *J Control Release* **121**, 3–9.
- Çiçek Ö., Abdulkadir A, Lienkamp SS, Brox T & Ronneberger O (2016). 3D U-Net: Learning dense volumetric segmentation from sparse annotation. In *Proceedings of the International Conference on Medical Image Computing and Computer-Assisted Intervention*, Ourselin S, Joskowicz L, Sabuncu MR, Unal G & Wells W (Eds.), pp. 424–432. Springer.
- Cnudde V & Boone MN (2013). High-resolution X-ray computed tomography in geosciences: A review of the current technology and applications. *Earth-Sci Rev* **123**, 1–17.
- Codd EF (1970). A relational model of data for large shared data banks. *Commun ACM* **13**, 377–387.
- Codd EF (1982). Relational database: A practical foundation for productivity. *Commun ACM* **25**, 109–117.
- Davis GR & Elliott JC (2006). Artefacts in X-ray microtomography of materials. *Mater Sci Technol* **22**, 1011–1018.
- Ditscherlein R, Furat O, de Langlard M, de Souza e Silva JM, Sygusch J, Rudolph M, Leißner T, Schmidt V & Peuker UA (2020a). Multiscale tomographic analysis for micron-sized particulate samples. *Microsc Microanal* **26**, 676–688.
- Ditscherlein R, Leißner T & Peuker UA (2020b). Preparation techniques for micron-sized particulate samples in X-ray microtomography. *Powder Technol* **360**, 989–997.
- Ditscherlein R, Leißner T & Peuker UA (2020c). Self-constructed automated syringe for preparation of micron-sized particulate samples in X-ray microtomography. *MethodsX* **7**, 100757.
- Dong KJ, Zou RP, Yang RY, Yu AB & Roach G (2009). DEM simulation of cake formation in sedimentation and filtration. *Miner Eng* **22**, 921–930.
- Erdoğan ST, Garboczi ET & Fowler DW (2007). Shape and size of microfine aggregates: X-ray microcomputed tomography vs. laser diffraction. *Powder Technol* **177**, 53–63.
- Furat O, Finegan DP, Diercks D, Usseglio-Viretta F, Smith K & Schmidt V (2021a). Mapping the architecture of single lithium ion electrode particles in 3D, using electron backscatter diffraction and machine learning segmentation. *J Power Sources* **483**, 229148.
- Furat O, Leißner T, Bachmann K, Gutzmer J, Peuker UA & Schmidt V (2019a). Stochastic modeling of multidimensional particle properties using parametric copulas. *Microsc Microanal* **25**, 720–734.
- Furat O, Leißner T, Ditscherlein R, Šedivý O, Weber M, Bachmann K, Gutzmer J, Peuker UA & Schmidt V (2018). Description of ore particles from X-ray microtomography (XMT) images, supported by scanning electron microscope (SEM)-based image analysis. *Microsc Microanal* **24**, 461–470.
- Furat O, Petrich L, Finegan D, Diercks D, Usseglio-Viretta F, Smith K & Schmidt V (2021b). Artificial generation of representative single Li-ion electrode particle architectures from microscopy data. *npj Comput Mater* **7**, 105.
- Furat O, Wang M, Neumann M, Petrich L, Weber M, Krill III CE & Schmidt V (2019b). Machine learning techniques for the segmentation of tomographic image data of functional materials. *Front Mater* **6**, 145.

- Gray J, Liu DT, Nieto-Santisteban M, Szalay A, DeWitt DJ & Heber G (2005). Scientific data management in the coming decade. *ACM SIGMOD Record* **34**, 34–41.
- Handl L, Torbahn L, Spetl A, Schmidt V & Kwade A (2017). Structural analysis and tracking of micron-sized glass particles during shear deformation: A study based on time-resolved tomographic data. *Adv Powder Technol* **28**, 1920–1929.
- He K, Gkioxari G, Dollár P & Girshick R (2017). Mask R-CNN. In *Proceedings of the IEEE International Conference on Computer Vision*, pp. 2961–2969.
- Jiang Z, Li J, Yang Y, Mu L, Wei C, Yu X, Pianetta P, Zhao K, Cloetens P, Lin F & Liu Y (2020). Machine-learning-revealed statistics of the particle-carbon/binder detachment in lithium-ion battery cathodes. *Nat Commun* **11**, 2310.
- Johnson NL, Kotz S & Balakrishnan N (1994). *Continuous Univariate Distributions*, vol. 1. J. Wiley & Sons.
- Johnson NL, Kotz S & Balakrishnan N (1995). *Continuous Univariate Distributions*, vol. 2. J. Wiley & Sons.
- Kahl WA, Dilissen N, Hidas K, Garrido CJ, López-Sánchez-Vizcaino V & Román-Alpiste MJ (2017). 3-D microstructure of olivine in complex geological materials reconstructed by correlative X-ray μ -CT and EBSD analyses. *J Microsc* **268**, 193–207.
- Kashiwaya K, Noumachi T, Hiroyoshi N, Ito M & Tsunekawa M (2012). Effect of particle shape on hydrocyclone classification. *Powder Technol* **226**, 147–156.
- Leff A & Rayfield JT (2001). Web-application development using the model/view/controller design pattern. In *Proceedings of the Fifth IEEE International Enterprise Distributed Object Computing Conference*, pp. 118–127. IEEE Computer Society.
- Leißner T, Diener A, Löwer E, Ditscherlein R, Krüger K, Kwade A & Peuker UA (2020). 3D ex-situ and in-situ X-ray CT process studies in particle technology: A perspective. *Adv Powder Technol* **31**, 78–86.
- Lin CL, Miller JD, Videla AR & Mejia JA (2010). Fine coal filtration as revealed by 3D lattice-Boltzmann simulations. *Int J Coal Prep Util* **30**, 217–238.
- Macho O, Kabát J, Gabrišová L, Peciar P, Juriga M, Fekete R, Galbavá P, Blaško J & Peciar M (2019). Dimensionless criteria as a tool for creation of a model for predicting the size of granules in high-shear granulation. *Part Sci Technol* **38**, 381–390.
- Maire E & Withers PJ (2014). Quantitative X-ray tomography. *Int Mater Rev* **59**, 1–43.
- Mullins CS (2002). *Database Administration: Practices and Procedures*. Addison-Wesley.
- Neumann M, Stenzel O, Willot F, Holzer L & Schmidt V (2020). Quantifying the influence of microstructure on effective conductivity and permeability: Virtual materials testing. *Int J Solids Struct* **184**, 211–220.
- Paredaens J, De Bra P, Gyssens M & van Gucht D (1989). *The Structure of the Relational Database Model*. Monographs in Theoretical Computer Science. An EATCS Series. Berlin, Heidelberg: Springer.
- Prifling B, Rödning M, Townsend P, Neumann M & Schmidt V (2021). Large-scale statistical learning for mass transport prediction in porous materials using 90,000 artificially generated microstructures. *Front Mater* (in print). doi:10.3389/fmats.2021.786502.
- Prifling B, Westhoff D, Schmidt D, Markötter H, Manke I, Knoblauch V & Schmidt V (2019). Parametric microstructure modeling of compressed cathode materials for Li-ion batteries. *Comput Mater Sci* **169**, 109083.
- Ronneberger O, Fischer P & Brox T (2015). U-Net: Convolutional networks for biomedical image segmentation. In *Proceedings of Medical Image Computing and Computer-Assisted Intervention*, Navab N, Hornegger J, Wells WM & Frangi AF (Eds.), pp. 234–241. Cham: Switzerland.
- Rueden CT, Schindelin J, Hiner MC, DeZonia BE, Walter AE, Arena ET & Eliceiri KW (2017). ImageJ2: ImageJ for the next generation of scientific image data. *BMC Bioinformatics* **18**, 529.
- Ruth BF, Montillon GH & Montonna RE (1933). Studies in filtration - I. Critical analysis of filtration theory. *Ind Eng Chem* **25**, 76–82.
- Schlüter S, Sheppard A, Brown K & Wildenschild D (2014). Image processing of multiphase images obtained via X-ray microtomography: A review. *Water Resour Res* **50**, 3615–3639.
- Soret M, Bacharach SL & Buvat I (2007). Partial-volume effect in PET tumor imaging. *J Nucl Med* **48**, 932–945.
- Stenzel O, Pecho O, Holzer L, Neumann M & Schmidt V (2017). Big data for microstructure-property relationships: A case study of predicting effective conductivities. *AIChE J* **63**, 4224–4232.
- Stock SR (2008). Recent advances in X-ray microtomography applied to materials. *Int Mater Rev* **53**, 129–181.
- Tongkaw S & Tongkaw A (2016). A comparison of database performance of MariaDB and MySQL with OLTP workload. In *2016 IEEE Conference on Open Systems (ICOS)*, pp. 117–119. IEEE.
- Trunk R, Marquardt J, Thäter G, Nirschl H & Krause MJ (2018). Towards the simulation of arbitrarily shaped 3D particles using a homogenised lattice Boltzmann method. *Comput Fluids* **172**, 621–631.
- Trunk R, Weckerle T, Hafen N, Thäter G, Nirschl H & Krause MJ (2021). Revisiting the homogenized lattice Boltzmann method with applications on particulate flows. *Computation* **9**, 11.
- Ueda T, Oki T & Koyanaka S (2018). Experimental analysis of mineral liberation and stereological bias based on X-ray computed tomography and artificial binary particles. *Adv Powder Technol* **29**, 462–470.
- Uhlmann M (2005). An immersed boundary method with direct forcing for the simulation of particulate flows. *J Comput Phys* **209**, 448–476.
- Westhoff D, Finegan DP, Shearing PR & Schmidt V (2017). Algorithmic structural segmentation of defective particle systems: A lithium-ion battery study. *J Microsc* **270**, 71–82.
- Wood W (2018). MariaDB solution. In *Migrating to MariaDB*, pp. 59–71. Apress.
- Yu YS, Tao YB, Ma Z & He YL (2018). Experimental study and optimization on filtration and fluid flow performance of a granular bed filter. *Powder Technol* **333**, 449–457.
- Zaslavskiy M, Kaluzhniy A, Berlenko T, Kinyaev I, Krinkin K & Turenko T (2016). Full automated continuous integration and testing infrastructure for maxscale and MariaDB. In *19th Conference of Open Innovations Association (FRUCT)*, pp. 273–278. IEEE.
- Zhong X, Burke MG, Withers PJ, Zhang X, Zhou X, Burnett TL, Liu Y, Lyon SB & Gibbon SR (2019). Multi-modal plasma focused ion beam serial section tomography of an organic paint coating. *Ultramicroscopy* **197**, 1–10.
- Zhu HP, Zhou ZY, Yang RY & Yu AB (2008). Discrete particle simulation of particulate systems: A review of major applications and findings. *Chem Eng Sci* **63**, 5728–5770.

Supplementary Material

PARROT - A Pilot Study on the Open Access Provision of Particle Discrete Tomographic Datasets

Ralf Ditscherlein^{1,*}, Orkun Furat², Erik Löwer¹, Raik Mehnert³,
Robin Trunk⁴, Thomas Leißner¹, Mathias J. Krause⁴, Volker
Schmidt², and Urs A. Peuker¹

¹Institute of Mechanical Process Engineering and Mineral Processing, Technische Universität Bergakademie Freiberg, Agricolastraße 1, D-09599 Freiberg, Germany

²Institute of Stochastics, Ulm University, D-89069 Ulm, Germany

³Mehnert IT services, Schmiedestraße 7, D-09599 Freiberg, Germany

⁴Institute of Mechanical Process Engineering and Mechanics, Karlsruher Institute for Technology (KIT), Straße am Forum 8, D-76131 Karlsruhe, Germany

*corresponding author: ralf.ditscherlein@mvtat.tu-freiberg.de, phone: +49 3731 39-2714, fax: +49 3731 39-2947

Appendix A: Three Examples of Use Cases

In this section we discuss three scientific use cases, which have been already introduced before in Section 1.3 of the main manuscript text and which are directly or indirectly dealing with particle-discrete datasets queried from the PARROT database. The use cases are embedded into three different research projects with the following titles: (i) Development of process models based on 3D information about the multiphase processes in the pore space of a filter cake (funded by DFG, project number: PE 1160/23-1), (ii) Stochastic modeling of multidimensional particle properties with parametric copulas for the investigation of microstructure effects on the fractionation of fine particle systems (funded by DFG through project Z2 of SPP 2045, project number: SCHM 997/27-2), (iii) Two-scale approach for the simulation of multidimensional fractionation of fine particles (funded by DFG through project Z4 of SPP 2045, project number: KR 4259/8-2).

A-1: Acquisition, Preprocessing and Analysis of 3D Image Data

This use case refers to results obtained in the framework of project (i) mentioned above, dealing with multiphase processes in the pore space of a filter cake which is build from particulate powders. Here, a pore is defined as interconnected void space between particles within a bulk. In contrast to the solid phase, a pore is a compact disperse property (Schubert, 1982). Often, a pore is defined as concave chamber between several particles, connected by constrictions, called pore throats. At these points, particles touch or become very close to each other. Of course, in general, the distribution of a particle characteristic depends on the kind of the shape or size characteristic considered in each case. In practice, often univariate distributions are determined of (independently measured) single particle characteristics, which, in some cases, can be combined to multivariate distributions of vectors of particle characteristics by applying suitable mathematical algorithms (Prifling et al., 2019; Furat et al., 2021b). Moreover, when used in process models like cake filtration, distributed information is often reduced to an aggregated numerical value, which is only partially able to capture the distributed nature of particle or pore space characteristics.

Cake Filtration. One possible approach to determine the 3D morphology of filter cakes non-destructively and non-intrusively (by in-situ filtration experiments) is given by the utilization of XRM, where the procedure to generate such filter cake structures is to mechanically classify particles from an initial particle system (here Al_2O_3), i.e., to divide them into different subsets such that each subset exhibits a narrow particle size distribution. These subsets are then used for filtration experiments, where the resulting filter cakes can be investigated with respect to the 3D morphology of their pore space. Based on the experimental data, it is now possible to determine a correlation function between discrete particle and pore space characteristics. However, the goal of future research is to replace this very time-consuming procedure by considering artificially generated particle subsets. For this purpose, the particulate powder (not the filter cake structure itself) will be measured tomographically and the resulting particle-discrete

data will be stored in the PARROT database. Then, by means of a filtered database query, specific subsets can be virtually extracted from this simulated particle population, i.e., the mechanical classification process is mimicked.

To achieve this medium-term goal, some preliminary work for conventionally classified particle systems must be performed first to reveal fundamental relationships between the used particle system and the resulting filter cake structure obtained in process engineering experiments. For this, we build several filter cakes from subsets of Al_2O_3 particles. Here, the structure of the pore space, described by pore radii, numbers of contact points, local tortuosity, and interconnected or isolated fluid volumes, as well as the corresponding particle size and shape characteristics are relevant for a more detailed mechanistic understanding of the micro-processes within the pore space (Löwer et al., 2020). All measurement parameters are given in Table S2, where the reconstructed image stacks of the filter cake structures can also be found.

Investigating Similarity Effects. We now investigate the question how the size distribution of Al_2O_3 particles influences the morphology of the pore space of corresponding filter cakes. For that purpose, we use aero classifying (Turbo classifier TC-15, Nisshin Engineering Inc.) to extract three particle systems with differently sized particles from the Al_2O_3 sample, see Table S1 for the particle size ranges. From these small, medium and large sized particle systems, subsamples of particles are taken for laser diffraction measurements to obtain particle size distributions for the three considered particle systems, followed by the fitting of volume-weighted log-normal distributions to the particle sizes, see Figure S1. Note that the declaration of the particle systems refers to the average particle size (small, medium, large). However, the location and shape of the corresponding size distributions differ between the three considered particle systems. The underlying distributions based on the raw data are shown in Figure S10.

More details on fitting the parameters of the log-normal distribution can be found in Section , where the fact is used that its probability density is given by a simple formula, see Formula (S3). The fitted volume-weighted probability densities $q^{(\text{small})}$, $q^{(\text{medium})}$, $q^{(\text{large})}$: $\mathbb{R} \rightarrow [0, \infty)$ for the particle sizes of the small, medium and large sized particle systems, respectively, are visualized in Figure S1. Note that for the purpose of visual inspection of self-similarity, Figure S1 shows normalized versions \tilde{q} of the considered probability densities q , which are given by

$$\tilde{q}(x) = \frac{1}{x_{50}} q(x/x_{50}) \quad \text{for all } x \in \mathbb{R}, \quad (\text{S1})$$

where x_{50} denotes the median of q . This procedure is widely described in the literature on comminution processes (Andreasen, 1957; Rumpf, 1973; Venkataraman, 1988). Location and scattering parameters of the log-normal fits are given in Table S1.

For each of the three particle systems, filtration experiments were performed and the resulting filter cakes were imaged using XRM. In order to characterize the morphology of the filter cakes' pore spaces, the three XRM tomograms have been used to determine the spherical contact distribution based on the maximum inscribed sphere

Table S1: Parameters, i.e., the median $x_{50,3}$ and a scattering parameter σ_3 , of the log-normal distributions which describe the various particle size distributions of the three particle systems under consideration, and the pore size distribution of resulting filter cakes, see Figure S1 for visualization. Note that the index 3 is indicating the quantity type - in this case volume-related quantities. The values of the self-similarity measure I are given with respect to the reference system built by medium particles in relation to the $n = 7$ support points $x_{10,3}, x_{16,3}, x_{25,3}, x_{50,3}, x_{75,3}, x_{84,3}, x_{90,3}$.

particle system (with range of particle sizes, denoted by x)	$x_{50,3}$ [μm]	$\sigma_3 = \ln(x_{84,3}/x_{50,3})$	I
medium particles; $50 \mu\text{m} < x < 200 \mu\text{m}$ (reference system)	103	0.42	—
small particles; $20 \mu\text{m} < x < 45 \mu\text{m}$	31	0.43	1.37
large particles $90 \mu\text{m} < x < 440 \mu\text{m}$	265	0.37	4.54
pore network (of corresponding filter cake)			
pore sizes, generated by medium particles (reference system)	26	0.41	—
pore sizes, generated by small particles	7	0.44	5.59
pore sizes, generated by large particles	67	0.53	15.11

approximation (Silin & Patzek, 2006). Then, volume-weighted log-normal distributions are fitted to model the pore size distributions. The fitted probability densities $q_{\text{pore}}^{(\text{small})}$, $q_{\text{pore}}^{(\text{medium})}$, $q_{\text{pore}}^{(\text{large})} : \mathbb{R} \rightarrow [0, \infty)$ for the pore sizes of filter cakes resulting from filtration experiments with the small-, medium- and large-sized particle systems, respectively, are visualized in Figure S1 and corresponding location and scattering of the fits are given in Table S1. Using the three particle systems described above, we now in-

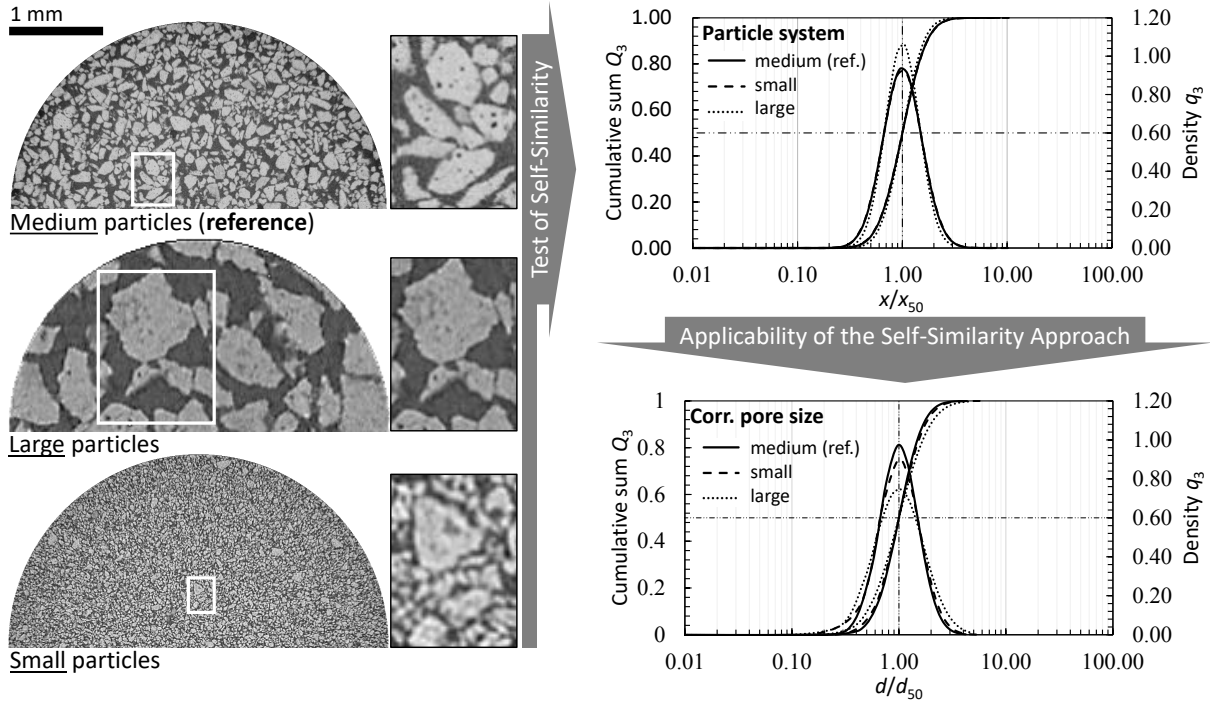


Figure S1: Planar 2D slices of medium-, small- and large-sized particle systems (left from top to bottom), with magnified details showing similar structures. Normalised cumulative distribution functions and probability densities of particle sizes for the three particle systems (right top) and their corresponding pore sizes (right bottom).

investigate the question of how the discrepancy between the particle size distribution of two different particle systems transfer to the pore size distributions of the corresponding filter cakes. As a discrepancy measure we consider a quantity based on the notion of self-similarity. More precisely, the self-similarity measure (Klichowicz et al., 2014) $I(q^{(1)}, q^{(2)})$ of two probability densities $q^{(1)}, q^{(2)} : \mathbb{R} \rightarrow [0, \infty)$ is given by

$$I(q^{(1)}, q^{(2)}) = \frac{1}{n} \sum_{k=1}^n |q^{(1)}(x_k) - q^{(2)}(x_k)|, \quad (\text{S2})$$

where $\{x_1, \dots, x_n\}$ is some set of support points $x_1, \dots, x_n \in \mathbb{R}$.

Using Formula (S2) we computed the self-similarities $I(q^{(\text{small})}, q^{(\text{medium})})$ and $I(q^{(\text{large})}, q^{(\text{medium})})$ of the particle size distributions of small and large sized particle systems with respect to the medium sized particle system as a reference, see Table S1. For this, we

used the percentiles $x_{10}, x_{16}, x_{25}, x_{50}, x_{75}, x_{84}, x_{90}$ of $q^{(\text{medium})}$ as support points in Formula (S2). Analogously, the values $I(q_{\text{pore}}^{(\text{small})}, q_{\text{pore}}^{(\text{medium})})$ and $I(q_{\text{pore}}^{(\text{large})}, q_{\text{pore}}^{(\text{medium})})$ of the self-similarity measure for the pore size distributions of the corresponding filter cakes have been computed, see Table S1.

The increase of the values of the self-similarity measure I presented in Table S1 indicate that increasing deviations of particle size distributions from the reference particle size distribution are reflected in the filter cake structures by increasing deviations of the pore size distributions from the corresponding reference distribution. As soon as experimental and tomographical data regarding the filtration experiments is available in the database, the functionality of the latter can be used for a more comprehensive analysis to better understand the influence of the nature of particle systems on the resulting morphology of the pore space within filter cakes. In particular, in addition to size characteristics of particles and pores, further characteristics which describe their shape will be considered. Then, using multivariate modeling, joint distributions of multidimensional vectors of particle/pore characteristics can be considered, see Section for further details. Moreover, using the tomographical data of the considered particle system, stochastic geometry models can be calibrated for the generation of artificial particles, so-called digital twins (Prifling et al., 2019; Furat et al., 2021c), which also can be made available in the database. This will enable the prediction of filter cake properties based on artificially generated filter cakes, where only a small number of real filtration experiments will be needed for model calibration. Thus, this would represent a significant advance in process modeling.

A-2: Statistical Analysis and Multivariate Parametric Modeling of 3D Image Data

This use case refers to results obtained in the framework of project (ii) mentioned above, dealing with microstructure effects on the fractionation of fine particle systems. An efficient way for describing complex voxelized particles in segmented image data is given by size, shape and textural characteristics (Burger & Burge, 2016; Furat et al., 2021a)—a selection of common particle characteristics can be directly accessed in the PARROT database. Moreover, entire systems of particles can then be efficiently described by fitting probability distributions to the particle characteristics extracted from image data. Especially parametric probability distributions (e.g., log-normal and beta distributions) are useful for modeling the univariate distribution of individual particle characteristics since they can be fully specified by just a few parameters (Johnson et al., 1994, 1995).

Due to the characterization of particles in segmented image data by means of possibly correlated particle characteristics, multivariate probability distributions which describe the correlation structure of these characteristics are much more informative than univariate distributions (Furat et al., 2019). Furthermore, it is possible to include characteristics which describe physical properties of individual particles computed by simulations, see Section , in order to investigate the influence of size and shape characteristics on physical particle properties. To illustrate this, we provide an example for multivariate probabilis-

tic modeling of particle characteristics by means of so-called copulas (Nelsen, 2006; Joe, 2014). More precisely, we fit a bivariate probability distribution to the two-dimensional data vectors of volume-equivalent spherical diameter and sphericity of particles observed in the aluminum oxide data set queried from the PARROT database. We start by modeling univariate probability distributions for both diameter and sphericity. Then, in a second step, a bivariate probability distribution is fitted, using a parametric copula, such that its marginal distributions coincide with the previously fitted univariate distributions. Note that in this section we consider number-weighted probability densities which we denote by f , instead of the volume-weighted versions considered in Section which were denoted by q .

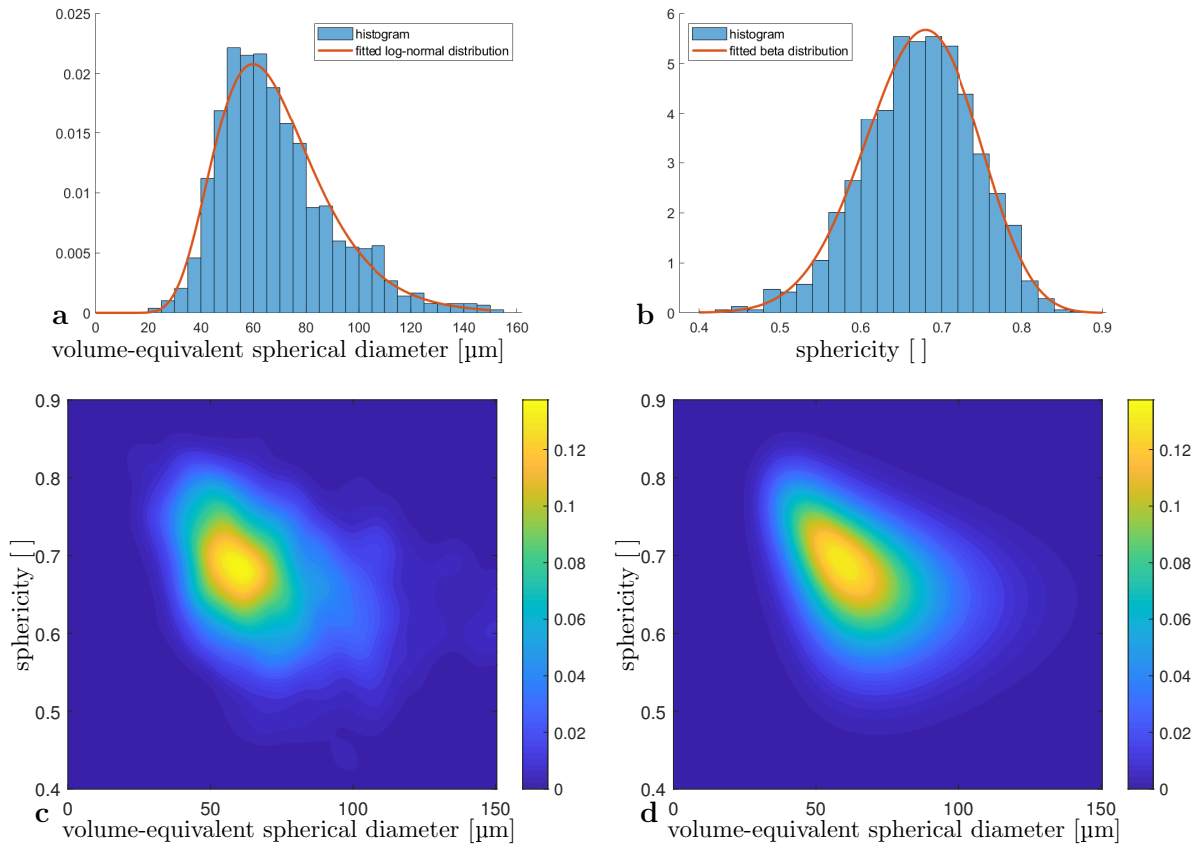


Figure S2: Histogram (blue) and fitted parametric probability density (red) of the volume-equivalent spherical diameter (a) and sphericity (b) of Al₂O₂ particles. Bivariate probability density of volume-equivalent spherical diameter and sphericity of Al₂O₂ particles computed by means of kernel density estimation (c) and the copula approach (d).

Parametric Modeling of Single Particle Characteristics. From the PARROT database we can directly access tables of particle characteristics for any specified search request. For example, for the $n = 1571$ particles segmented in the aluminum oxide

dataset, we receive vectors (d_i, s_i) of the particle's volume-equivalent spherical diameter and sphericity for each $i = 1, \dots, n$. Then, in a next step, we can fit parametric probability distributions to this data. It turns out that the log-normal distribution with probability density $f_{\mu, \sigma} : \mathbb{R} \rightarrow [0, \infty)$ given by

$$f_{\mu, \sigma}(d) = \frac{1}{d\sqrt{2\pi\sigma^2}} \exp\left(-\frac{(\ln d - \mu)^2}{2\sigma^2}\right) \quad \text{for each } d > 0 \quad (\text{S3})$$

is a good choice for modeling the volume-equivalent spherical diameters d_1, \dots, d_n , where the maximum likelihood method (Johnson et al., 1994) is used for computing optimal values of the model parameters $\mu \in \mathbb{R}$ and $\sigma > 0$. Note that for selecting an adequate parametric probability distributions among multiple ones (e.g., normal, log-normal, gamma distribution) the Akaike information criterion can be used. For more details on model selection the reader is referred to Held & Sabanés Bové (2014). The resulting probability density f_{diameter} determined in this way is visualized in Figure S2a. Analogously, a beta distribution (Johnson et al., 1995) is fitted to the sphericity data s_1, \dots, s_n —the resulting probability density $f_{\text{sphericity}}$ depicted in Figure S2b.

Parametric Modeling of Pairs of Particle Characteristics. For modeling the bivariate (joint) distribution of volume-equivalent spherical diameter and sphericity of particles, we use parametric copulas which are bivariate distributions themselves, but with special properties. More precisely, using a parametric copula density $c_\theta : [0, 1] \rightarrow [0, 1]$ with some parameter $\theta \in \mathbb{R}$ we can construct a bivariate probability density $f_\theta : \mathbb{R}^2 \rightarrow [0, \infty)$ such that

$$f_\theta(d, s) = f_{\text{diameter}}(d) f_{\text{sphericity}}(s) c_\theta(F_{\text{diameter}}(d), F_{\text{sphericity}}(s)) \quad (\text{S4})$$

for all $d > 0, s \in [0, 1]$,

where $F_{\text{diameter}}, F_{\text{sphericity}} : \mathbb{R} \rightarrow [0, 1]$ denote the cumulative distribution functions corresponding to f_{diameter} and $f_{\text{sphericity}}$, respectively (Nelsen, 2006). This construction of the bivariate probability density f_θ has the advantage that its marginal probability densities coincide with the predetermined probability densities f_{diameter} and $f_{\text{sphericity}}$. Similar to the univariate case, there are numerous families of parametric copula densities, e.g., the Gumbel, Clayton and Ali-Mikhail-Haq copulas, the parameters of which can be fitted using a maximum likelihood approach (Nelsen, 2006; Joe, 2014). In Figure S2d the bivariate probability density f_θ of volume-equivalent spherical diameter and sphericity is visualized where a Ali-Mikhail-Haq copula has been fitted to the data $(d_1, s_1), \dots, (d_n, s_n)$. This probability density is described by five parameters (the copula parameter θ and two further parameters for each of the marginal distributions). For visual comparison we also computed the bivariate probability density of volume-equivalent spherical diameter and sphericity using a non-parametric approach, namely kernel density estimation (Botev et al., 2010), see Figure S2c.

A-3: Numerical Process Modeling Based on 3D Image Data

Finally, this use case refers to results obtained in the framework of project (iii) mentioned at the beginning of Appendix A, which deals with the simulation of particle settling. Note that such a modeling approach is not limited to particles extracted from an individual tomogram. More precisely, since the PARROT database allows users to download virtual particles across different datasets according to their search query, such multivariate modeling approaches allow them to efficiently characterize their custom particle systems with relatively few parameters. Then, for example, these parameters can be correlated with results obtained by numerical simulations (see Section 1.3.3 in the main manuscript text) for investigating the influence of the geometry of particles within a particle systems on physical properties.

Surface-Resolved Simulations. In recent years, simulation methods mimicking the dynamics of objects with complex (non-spherical) shapes became increasingly popular. Prominent examples are the immersed boundary method (Uhlmann, 2005) and the homogenized lattice Boltzmann method (Trunk et al., 2021). The latter enables simulations of the settling of arbitrarily shaped particles (Trunk et al., 2018), like that depicted in Figure S3a. This allows to precisely track the settling path and velocity, an extract of the simulation result at $t = 0.235s$ is shown in Figure S3b. Both approaches have been implemented in the open source software OpenLB (Krause et al., 2021) and validated by various benchmark studies. Similar to real laboratory experiments (Horowitz & Williamson, 2010), where the settling regime of spheres and its dependence on Reynolds number and density ratio was studied, the behavior of particles with other simple shapes has been investigated too (Rahmani & Wachs, 2014; Shao et al., 2017). Regarding the particle considered in the present paper, it is apparent from Figure S3c that the object enters a state of constant rotation around its x -axis.

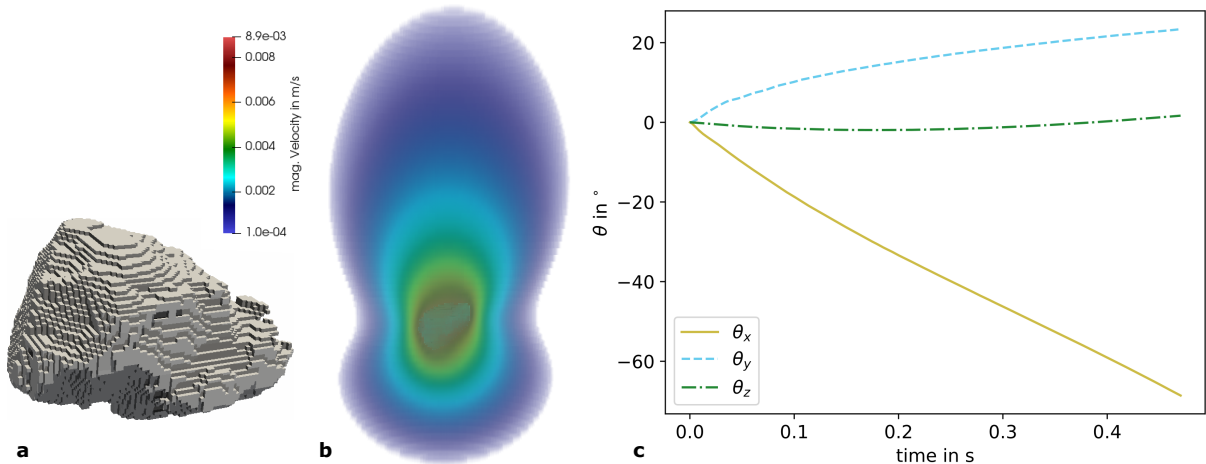


Figure S3: Surface representation of a particle retrieved from the PARROT database used for simulation (a), magnitude of velocity around a particle settling under gravity (b), angles with respect to x -, y - and z -axis over simulated time (c).

Correlation of Particle Morphology and Physical Properties. The simulation results of single settling particles can be used to quantify correlations between particle characteristics describing their 3D morphology and physical properties, respectively, i.e., to deduce structure-property relationships, which can be utilized in further large-scale simulations or to get a-priori assumptions for the processes under consideration. For more than three decades attempts have been made to extend drag relationships derived for spheres (Schiller & Naumann, 1933) to particles with more complex shapes (Ganser, 1993; Haider & Levenspiel, 1989). Due to its high complexity, this still is a topic of ongoing research, as shown by various new correlation proposals (Bagheri & Bonadonna, 2016; Hölzer & Sommerfeld, 2008). Note that the quality of structure-property relationships and their range of applicability is mainly determined by the nature and quality (e.g., voxel resolution) of datasets used to deduce them. However, most studies are based on datasets obtained in real laboratory experiments which, usually, are not comprehensive enough to validate correlations between particle characteristics describing their 3D morphology and physical properties sufficiently well and, in addition, might not be accessible to other interested parties. On the other hand, a large particle database like PARROT, not only containing various morphological particle characteristics but also their surface representation, serves as basis for reproducible results which allows the reliable quantification of structure-property relationships for a broad spectrum of particles. For example, selecting particles of a specific material or shape class enables the creation of specified correlation models. This has been performed, e.g., for volcanic pumice particles (Dioguardi & Mele, 2015; Dellino et al., 2005).

Appendix B: Exemplary Particles

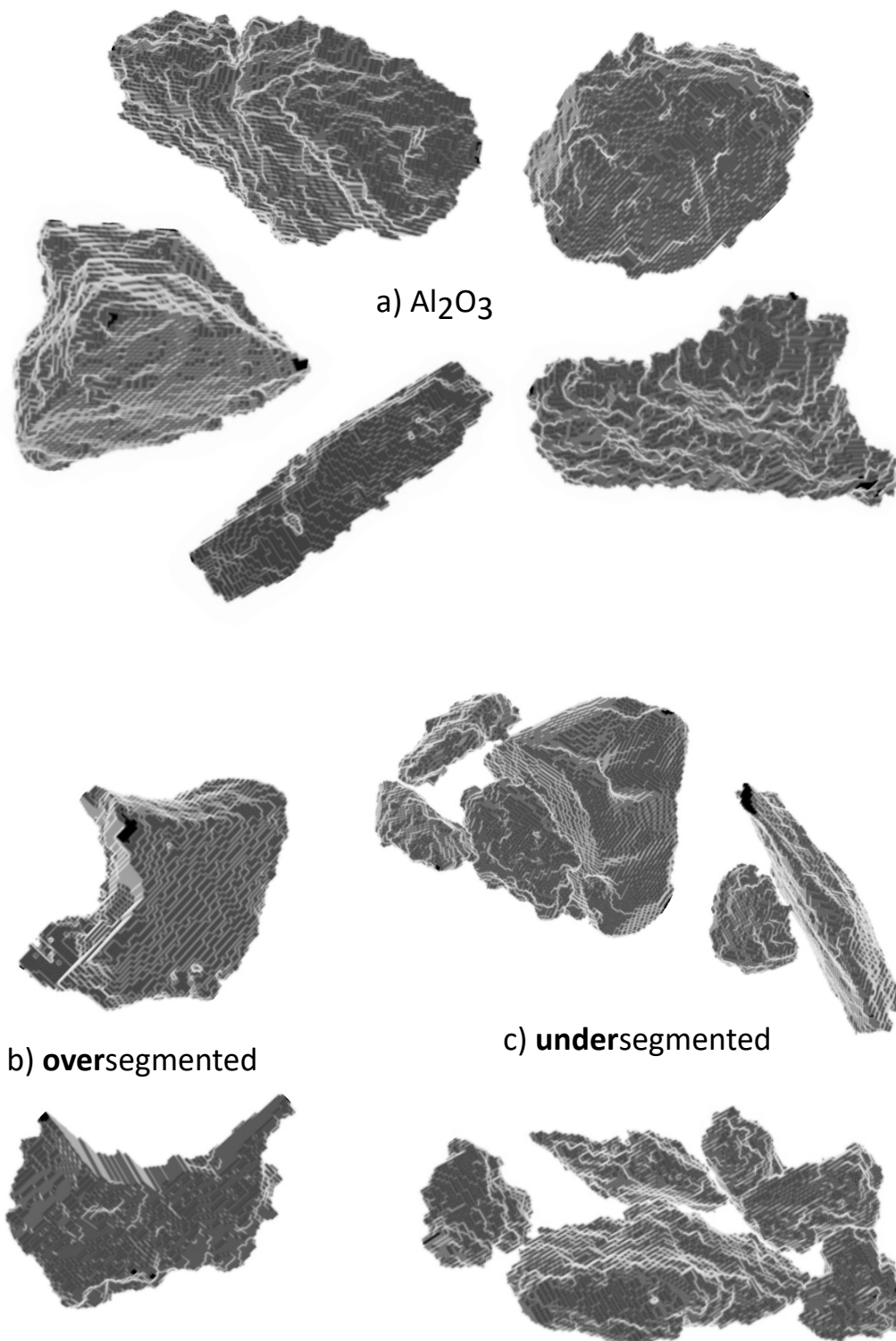


Figure S4: a) Five correctly segmented Al_2O_3 particles from the PARROT database. b) Two wrongly oversegmented Al_2O_3 particle fragments. c) Two examples of undersegmented Al_2O_3 particle clusters. Over- and undersegmented particles such as shown in b) and c) are not included in the PARROT database.

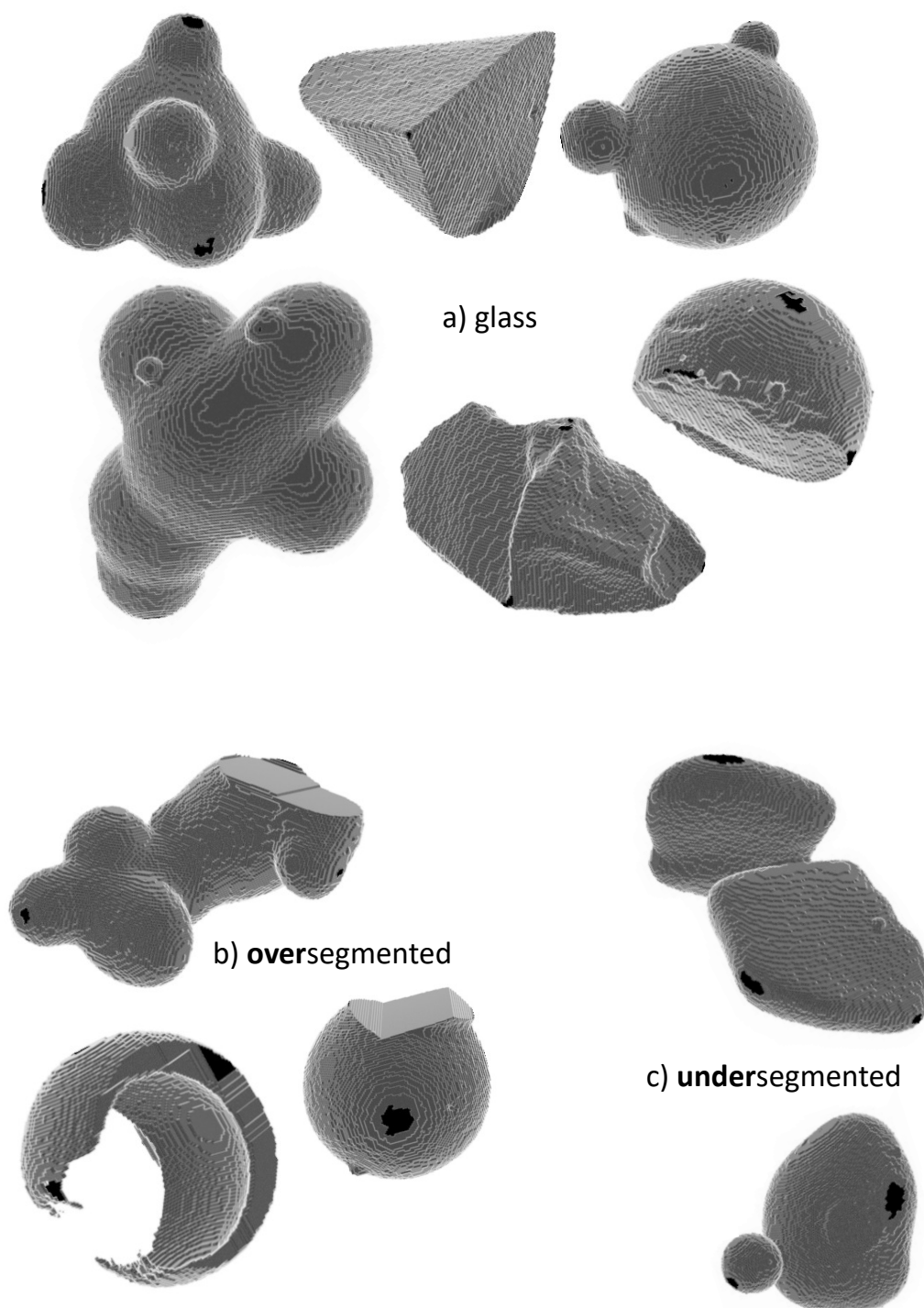


Figure S5: a) Six correctly segmented glass particles from the PARROT database. b) Three wrongly oversegmented glass particle fragments. c) Two examples of undersegmented glass particle clusters. Over- and undersegmented particles such as shown in b) and c) are not included in the PARROT database.

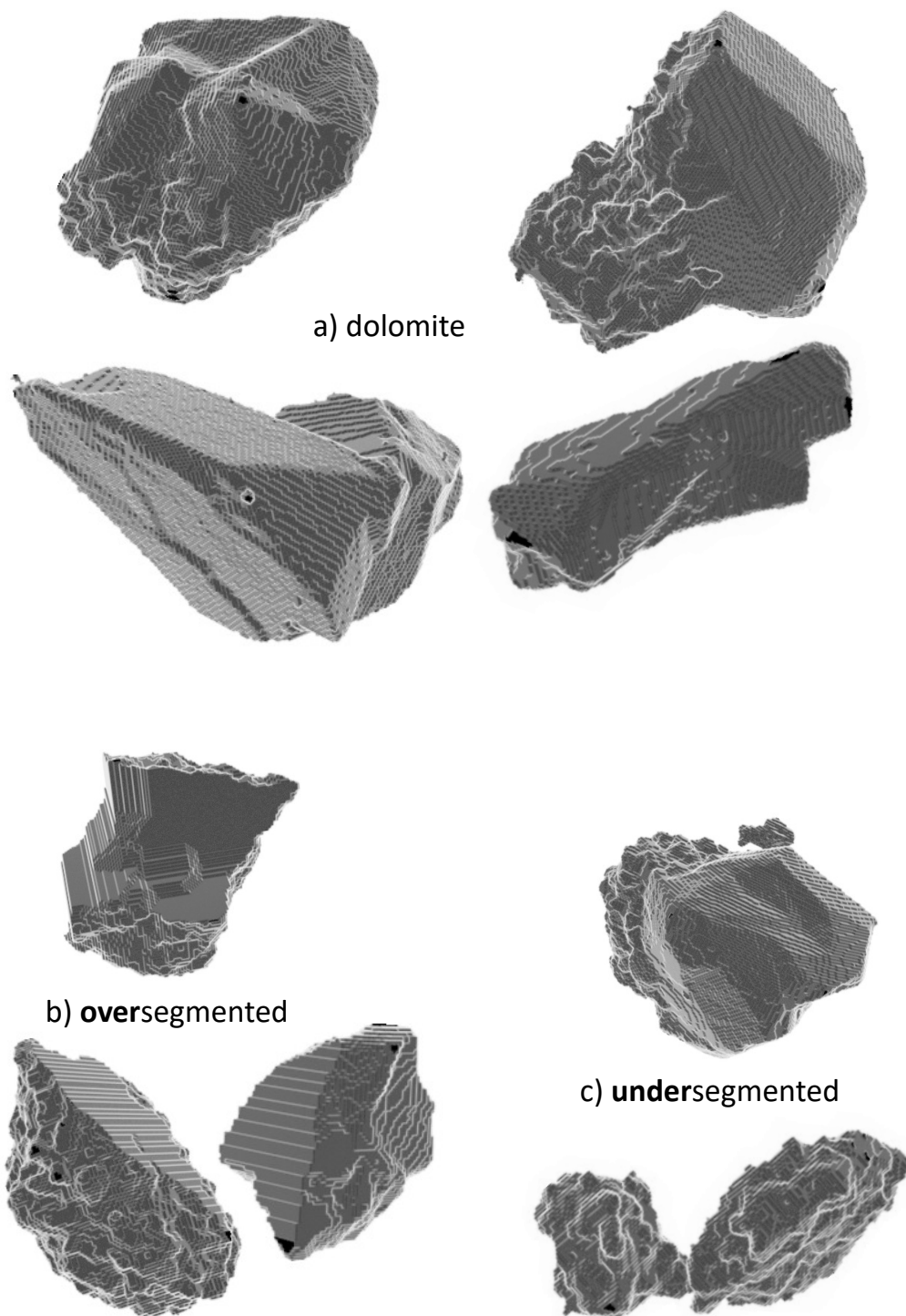


Figure S6: a) Four correctly segmented dolomite particles from the PARROT database. b) Three wrongly oversegmented dolomite particle fragments. c) Two examples of undersegmented dolomite particle clusters. Over- and undersegmented particles such as shown in b) and c) are not included in the PARROT database.

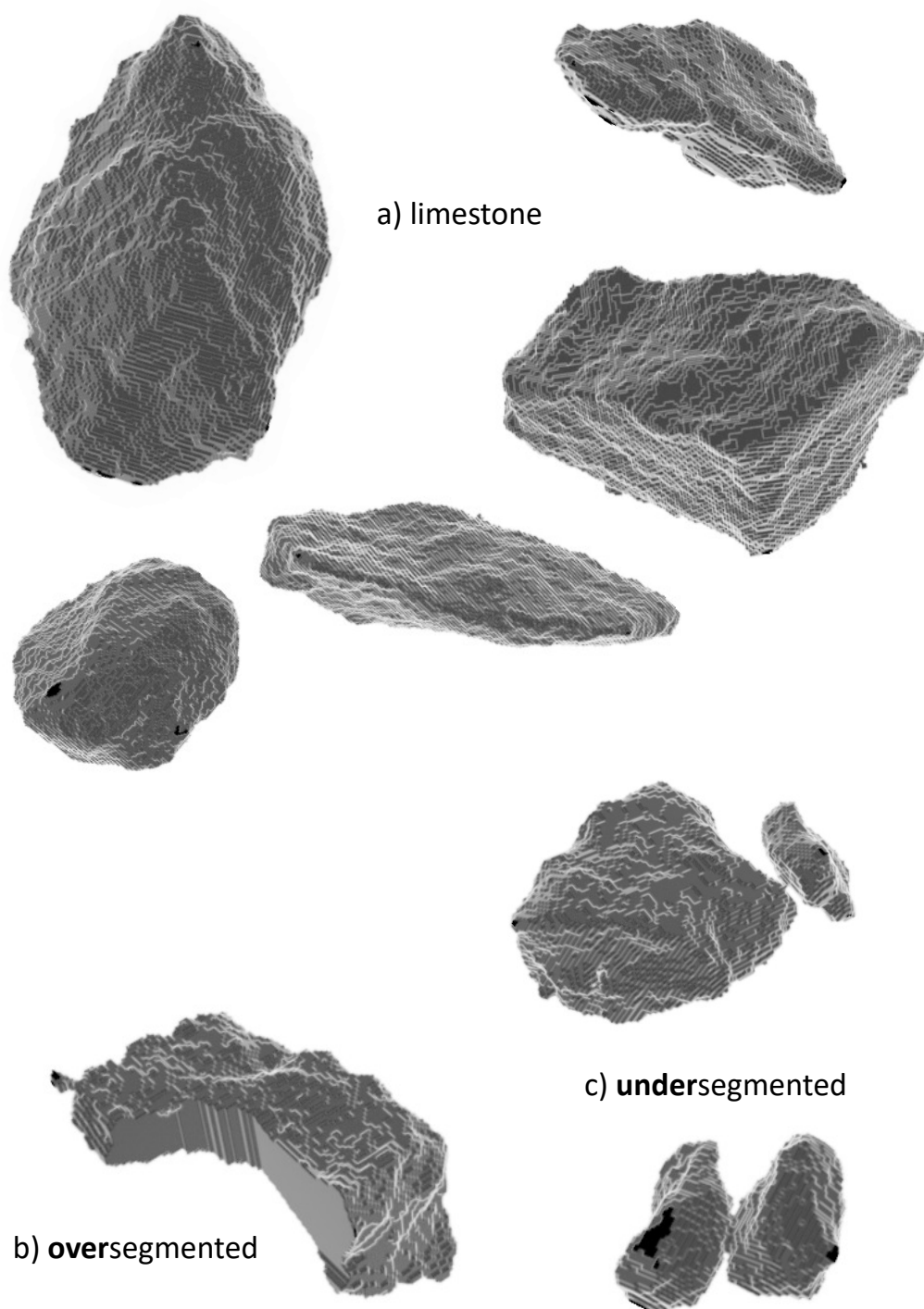


Figure S7: a) Five correctly segmented limestone particles from the PARROT database. b) One wrongly oversegmented limestone particle fragment. c) Two examples of undersegmented limestone particle clusters. Over- and undersegmented particles such as shown in b) and c) are not included in the PARROT database.

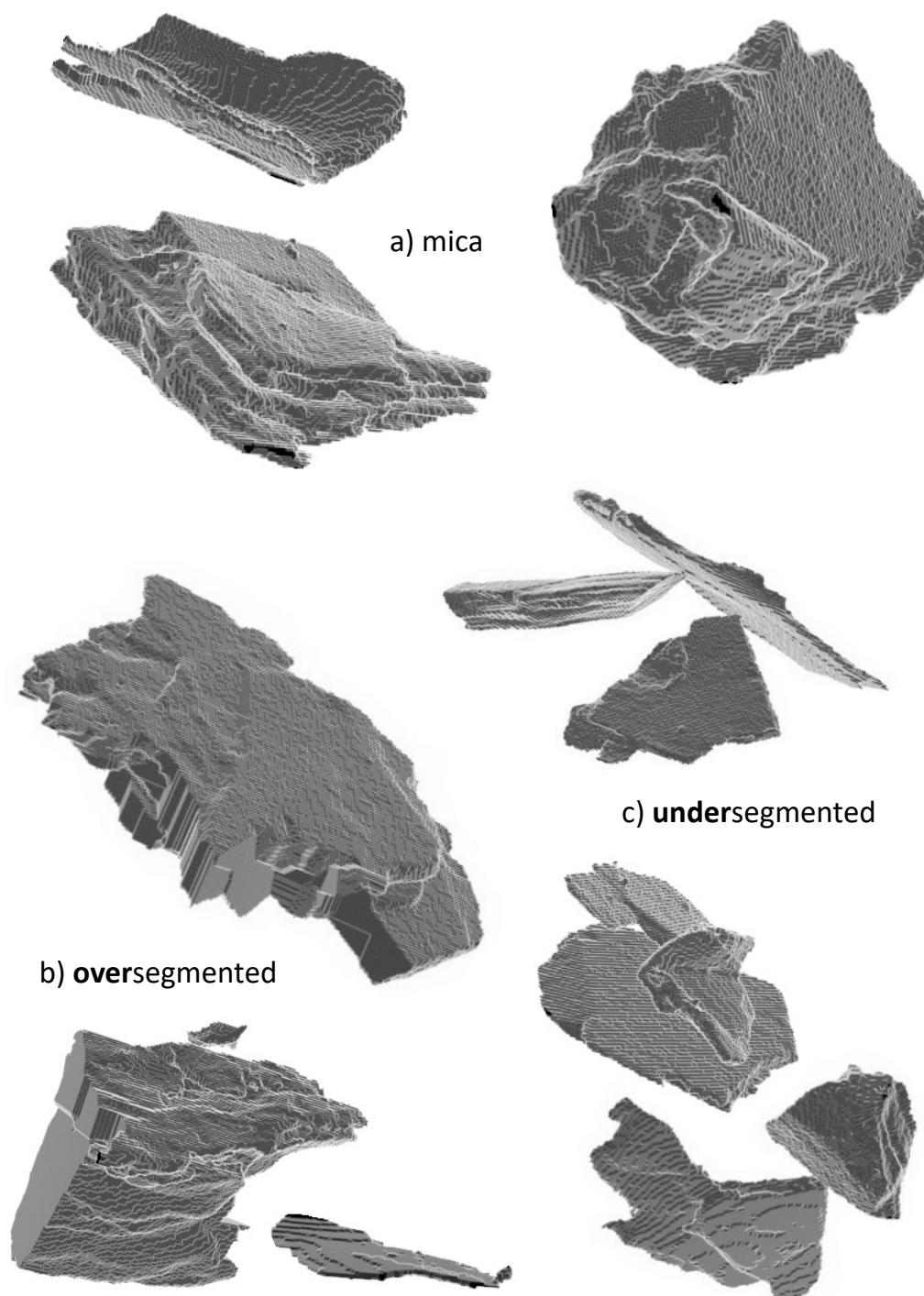


Figure S8: a) Three correctly segmented mica particles from the PARROT database. b) Three wrongly oversegmented mica particle fragments. c) Three examples of undersegmented mica particle clusters. Over- and undersegmented particles such as shown in b) and c) are not included in the PARROT database.

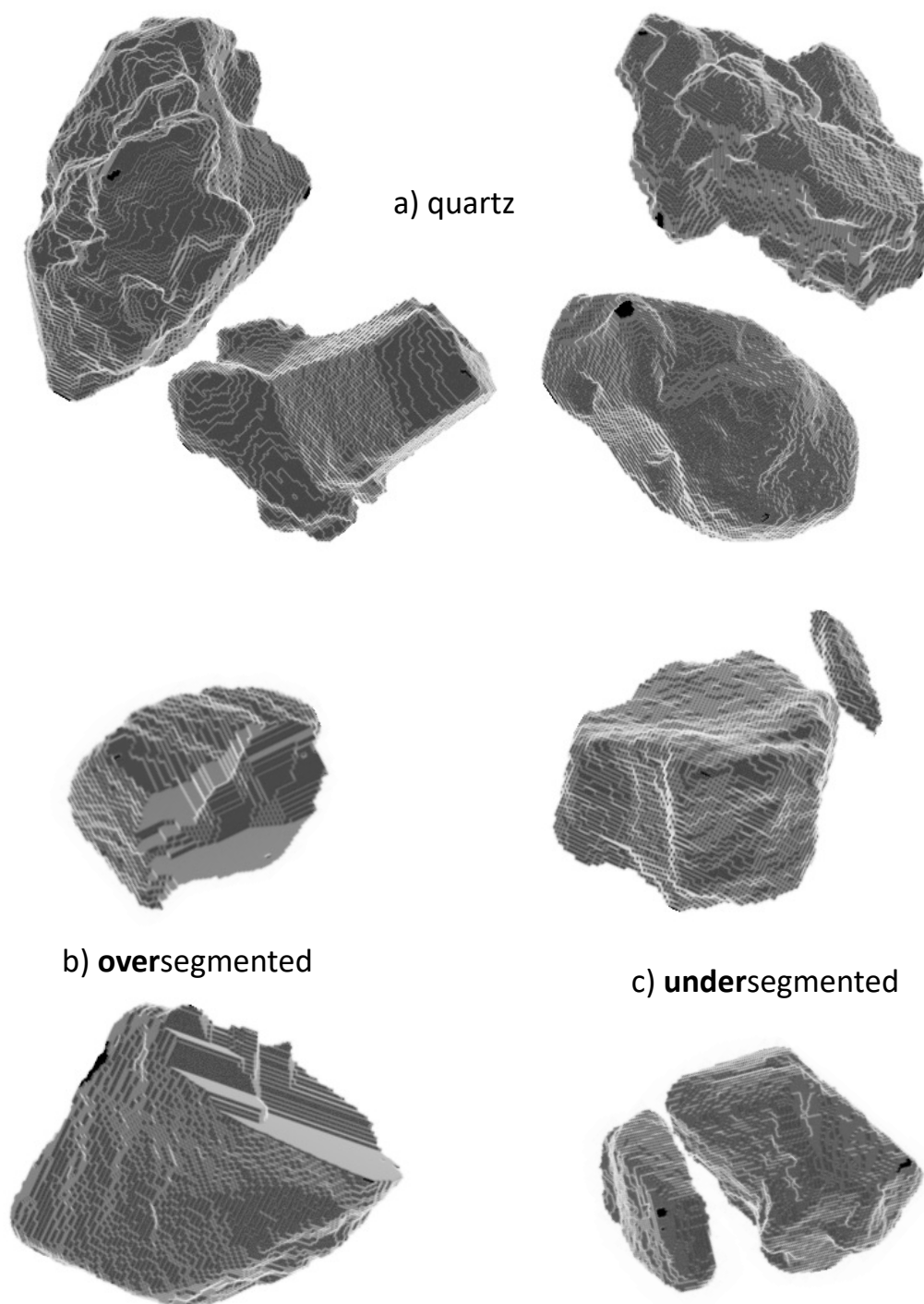


Figure S9: a) Four correctly segmented quartz particles from the PARROT database. b) Two wrongly oversegmented quartz particle fragments. c) Two examples of undersegmented quartz particle clusters. Over- and undersegmented particles such as shown in b) and c) are not included in the PARROT database.

Appendix C: ImageJ segmentation workflow

1. Histogram equalization (0.35 %)
2. Non-local means denoising (auto sigma)
3. Unsharp masking (radius 1; mask weight 0.3)
4. Despeckle
5. Unsharp masking (radius 1; mask weight 0.3)
6. Despeckle
7. Local automated threshold (Bernsen; radius 20 to 35 depending on the particle system)
8. 3D Watershed Split (radius 12); 3D object counter)

Appendix D: ImageJ macro for particle extraction

```

1 // ===== CONFIGURATION =====
2 outputFolder = getDirectory("Select_output_directory_for_extracted_
   particles!");
3 minVoxelEdgeLength = 5;
4
5 // ===== MAIN =====
6 // Iterating through all distinct gray values
7 maxGrayVal = MaxGrayValue();
8 particleID = 1;
9
10 for (grayVal = 1; grayVal < maxGrayVal; grayVal++) {
11   run("Duplicate...", "duplicate");
12   rename(particleID);
13   ExtractParticle(outputFolder, particleID, grayVal);
14   particleID++;
15 }
16
17 // ===== max gray val =====
18 function MaxGrayValue() {
19   mgv = 1;
20
21   for (i=1; i<=nSlices; i++) {
22     setSlice(i);
23     getRawStatistics(count, mean, min, max, std);
24     if (max > mgv) {
25       mgv = max;
26     }
27   }

```

```

28  print("Max_gray_value:" + d2s(mgv,0));
29  return(mgv);
30 }
31
32 // ===== EXTRACT =====
33 // Extracting each single particle from the segmented image stack.
34 // Here, each particle is determined by a distinct gray value.
35 // The method iterates through all these gray values, ignoring noise
36 // & edge-touching particles giving all particles in the volume.
37 function ExtractParticle(path, particleID, grayVal) {
38
39  // Set actual gray value to create binary image only containing
    // single particle.
40  setAutoThreshold("Default_dark_stack");
41  setThreshold(grayVal, grayVal);
42  run("Convert_to_Mask", "method=Default_background=Dark_black");
43
44  // Control if volume contains particle voxels & is NOT touching its
    // edges.
45  if (isEmpty() == 1 || isTouchingEdge() == 1) {
46    //do nothing
47  }
48  else {
49    // Cropping the full volume to the particle volume
50    run("Auto_Crop_3D");
51    rename("Cropped");
52
53    // If particles are too small compared to the voxel-resolution
    // -> excluded
54    getDimensions(width, height, channels, slices, frames);
55    if (height > minVoxelEdgeLength && width > minVoxelEdgeLength &&
        slices > minVoxelEdgeLength) {
56      run("3D_OC_Options",
57        "volume_" +
58        "surface_" +
59        "nb_of_obj._voxels_" +
60        "nb_of_surf._voxels_" +
61        "mean_distance_to_surface_" +
62        "std_dev_distance_to_surface_" +
63        "median_distance_to_surface_" +
64        "centre_of_mass_" +
65        "bounding_box_" +
66        "dots_size=5_font_size=10_
        store_results_within_a_table_named_after_the_image_(
        macro_friendly)_redirect_to=none");
67      run("3D_Objects_Counter", "threshold=1_slice=10_min.=10_max
        .=80000000000_statistics");
68
69      // Rename table to get access to the ImageJ built-in functions

```

```

70     IJ.renameResults("Statistics_for_Cropped","Results");
71     nRows = nResults;
72
73     // In case of a failure (results not containing any number)
74     if (nRows == 0) {
75         selectWindow("Cropped");
76         run("VTK_Writer_...", "save=[" + outputFolder + "Failure_" +
            particleID + ".vtk]");
77     }
78     else {
79         saveAs("Results", outputFolder + particleID + ".tsv");
80         selectWindow("Cropped");
81         run("VTK_Writer_...", "save=[" + outputFolder + particleID +
            ".vtk]");
82     }
83     close("Results");
84 }
85 close("Cropped");
86 }
87 selectWindow(particleID);
88 close();
89 }
90
91 // ===== CHECK (empty) =====
92 // Control if the thresholding gives a binarized result with NO
    particle voxels (white)
93 function isEmpty() {
94     getDimensions(width, height, channels, slices, frames);
95     allVoxelsPerSlice = height * width;
96
97     for (slice=1; slice<=nSlices; slice++) {
98         setSlice(slice);
99         getRawStatistics(n, mean, min, max, std, hist);
100        numBlackVoxels = hist[0];
101
102        if (numBlackVoxels < allVoxelsPerSlice) {
103            return(false);
104            break;
105        }
106    }
107    return(true);
108 }
109
110 // ===== CHECK (on edge) =====
111 // Checking if the particle is touching top OR bottom of the sample
    volume
112 function isTouchingEdge() {
113     getDimensions(width, height, channels, slices, frames);
114     allVoxelsPerSlice = height * width;

```

```

115
116 // Going to slice 1 (top), check how many white pixels in image (
      particle phase)
117 setSlice(1);
118 getRawStatistics(n, mean, min, max, std, hist);
119 numBlackVoxelsSlice1 = hist[0];
120
121 // ... same on the last slice (bottom)
122 setSlice(nSlices);
123 getRawStatistics(n, mean, min, max, std, hist);
124 numBlackVoxelsSliceMax = hist[0];
125
126 // Check if the particle is touching top OR bottom
127 if (numBlackVoxelsSlice1 < allVoxelsPerSlice ||
      numBlackVoxelsSliceMax < allVoxelsPerSlice) {
128     return(true);
129     break;
130 }
131 return(false);
132 }

```

Appendix E: Acquisition parameters for tomographic scan of filter structure

Table S2: Measurement parameters for three scanned filter cake structures built from the **large**-sized particle sample. Note that the uneven number of digits of the fields of view are due to an artifact minimizing tomographic measurement mode (Dynamic Ring Removal, DRR).

	Sample 1	Sample 2	Sample 3
field of view (FOV) in pixel	998 × 1001	987 × 1009	990 × 1005
sample size (cylindric, width × height) in mm	5 × 14.0	5 × 12.5	5 × 13.0
source filter (ZEISS standard)	LE 4	LE 4	LE 4
acceleration voltage/power in kV/W	50 / 4	50 / 4	50 / 4
optical magnification	4×	4×	4×
pixel size in μm	3.90	3.99	4.01
exposure time	4 s	4 s	4 s
number of projections (angular range)	2001 (360°)	2001 (360°)	2001 (360°)
camera binning	2	2	2

Appendix F: Raw data of laser diffraction measurement and class based pore size distribution

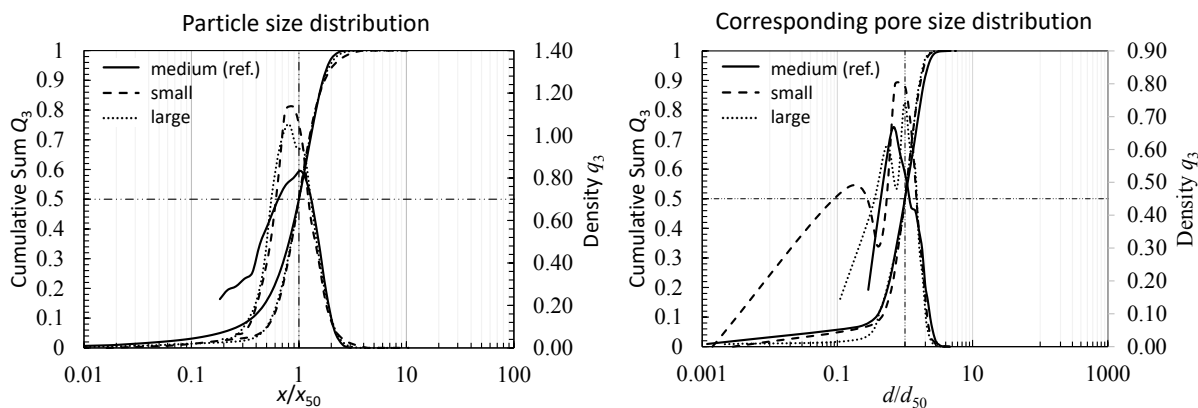


Figure S10: Particle size distribution (left) and corresponding pore size distribution (right) to all three particle systems small, medium, and large. Note the fluctuating density distribution to the left side due to class based determination by laser diffraction measurement. For better comparison, the raw data of the pore size distribution is binned within the same classes.

References

- ANDREASEN, A.H.M. (1957). The principle of similarity applied to mills and to the grinding process, *Transactions of the Institution of Chemical Engineers* **35**, 104–110.
- BAGHERI, G. & BONADONNA, C. (2016). On the drag of freely falling non-spherical particles, *Powder Technology* **301**, 526–544.
- BOTEV, Z.I., GROTHOWSKI, J.F. & KROESE, D.P. (2010). Kernel density estimation via diffusion, *The Annals of Statistics* **38**, 2916–2957.
- BURGER, W. & BURGE, M.J. (2016). *Digital Image Processing: An Algorithmic Introduction Using Java*, Springer.
- DELLINO, P., MELE, D., BONASIA, R., BRAIA, G., LA VOLPE, L. & SULPIZIO, R. (2005). The analysis of the influence of pumice shape on its terminal velocity, *Geophysical Research Letters* **32**, L21306.
- DIOGUARDI, F. & MELE, D. (2015). A new shape dependent drag correlation formula for non-spherical rough particles. experiments and results, *Powder Technology* **277**, 222–230.
- FURAT, O., FINEGAN, D.P., DIERCKS, D., USSEGLIO-VIRETTA, F., SMITH, K. & SCHMIDT, V. (2021a). Mapping the architecture of single lithium ion electrode parti-

- cles in 3D, using electron backscatter diffraction and machine learning segmentation, *Journal of Power Sources* **483**, 229148.
- FURAT, O., FRANK, U., WEBER, M., WAWRA, S., PEUKERT, W. & SCHMIDT, V. (2021b). Estimation of bivariate probability distributions of nanoparticle characteristics, based on univariate measurements, *Inverse Problems in Science and Engineering* **29**, 1343–1368.
- FURAT, O., LEISSNER, T., BACHMANN, K., GUTZMER, J., PEUKER, U.A. & SCHMIDT, V. (2019). Stochastic modeling of multidimensional particle properties using parametric copulas, *Microscopy and Microanalysis* **25**, 720–734.
- FURAT, O., PETRICH, L., FINEGAN, D., DIERCKS, D., USSEGLIO-VIRETTA, F., SMITH, K. & SCHMIDT, V. (2021c). Artificial generation of representative single Li-ion electrode particle architectures from microscopy data, *npj Computational Materials* **7**, 105.
- GANSER, G.H. (1993). A rational approach to drag prediction of spherical and non-spherical particles, *Powder Technology* **77**, 143–152.
- HAIDER, A. & LEVENSPIEL, O. (1989). Drag coefficient and terminal velocity of spherical and nonspherical particles, *Powder Technology* **58**, 63–70.
- HELD, L. & SABANÉS BOVÉ, D. (2014). *Applied Statistical Inference: Likelihood and Bayes*, Springer.
- HÖLZER, A. & SOMMERFELD, M. (2008). New simple correlation formula for the drag coefficient of non-spherical particles, *Powder Technology* **184**, 361–365.
- HOROWITZ, M. & WILLIAMSON, C.H.K. (2010). The effect of reynolds number on the dynamics and wakes of freely rising and falling spheres, *Journal of Fluid Mechanics* **651**, 251–294.
- JOE, H. (2014). *Dependence Modeling with Copulas*, CRC Press.
- JOHNSON, N.L., KOTZ, S. & BALAKRISHNAN, N. (1994). *Continuous Univariate Distributions*, vol. 1, J. Wiley & Sons.
- JOHNSON, N.L., KOTZ, S. & BALAKRISHNAN, N. (1995). *Continuous Univariate Distributions*, vol. 2, J. Wiley & Sons.
- KLICHOWICZ, M., REICHERT, M., LIEBERWIRTH, H. & MÜTZE, T. (2014). Self-similarity and energy-size relationship of coarse particles comminuted in single particle mode, *27th International Mineral Processing Congress*, Gecamin.
- KRAUSE, M.J., KUMMERLÄNDER, A., AVIS, S.J., KUSUMAATMAJA, H., DAPELO, D., KLEMENS, F., GAEDTKE, M., HAFEN, N., MINK, A., TRUNK, R., MARQUARDT, J.E., MAIER, M.L., HAUSSMANN, M. & SIMONIS, S. (2021). OpenLB—open source lattice Boltzmann code, *Computers & Mathematics with Applications* **81**, 258–288.

- LÖWER, E., PHAM, T.H., LEISSNER, T. & PEUKER, U.A. (2020). Study on the influence of solids volume fraction on filter cake structures using micro tomography, *Powder Technology* **363**, 286–299.
- NELSEN, R.B. (2006). *An Introduction to Copulas*, Springer.
- PRIFLING, B., WESTHOFF, D., SCHMIDT, D., MARKÖTTER, H., MANKE, I., KNOBLAUCH, V. & SCHMIDT, V. (2019). Parametric microstructure modeling of compressed cathode materials for li-ion batteries, *Computational Materials Science* **169**, 109083.
- RAHMANI, M. & WACHS, A. (2014). Free falling and rising of spherical and angular particles, *Physics of Fluids* **26**, 083301.
- RUMPF, H. (1973). Physical aspects of comminution and new formulation of a law of comminution, *Powder Technology* **7**, 145–159.
- SCHILLER, L. & NAUMANN, A. (1933). Über die grundlegenden Berechnungen bei der Schwerkraftaufbereitung, *Zeitschrift des Vereines Deutscher Ingenieure* **77**, 318–320.
- SCHUBERT, H. (1982). *Kapillarität in porösen Feststoffsystemen*, Springer.
- SHAO, B., LIU, G.R., LIN, T., XU, G.X. & YAN, X. (2017). Rotation and orientation of irregular particles in viscous fluids using the gradient smoothed method (GSM), *Engineering Applications of Computational Fluid Mechanics* **11**, 557–575.
- SILIN, D. & PATZEK, T. (2006). Pore space morphology analysis using maximal inscribed spheres, *Physica A: Statistical Mechanics and its Applications* **371**, 336–360.
- TRUNK, R., MARQUARDT, J., THÄTER, G., NIRSCHL, H. & KRAUSE, M.J. (2018). Towards the simulation of arbitrarily shaped 3D particles using a homogenised lattice Boltzmann method, *Computers & Fluids* **172**, 621–631.
- TRUNK, R., WECKERLE, T., HAFEN, N., THÄTER, G., NIRSCHL, H. & KRAUSE, M.J. (2021). Revisiting the homogenized lattice Boltzmann method with applications on particulate flows, *Computation* **9**, 11.
- UHLMANN, M. (2005). An immersed boundary method with direct forcing for the simulation of particulate flows, *Journal of Computational Physics* **209**, 448–476.
- VENKATARAMAN, K.S. (1988). Predicting the size distributions of fine powders during comminution, *Advanced Ceramic Materials* **3**, 498–502.

10 Appendix

10.1 Application Example 1: Fracture Analysis

Forsberg and Siviour[177] perform a strain analysis of a cylindrical bed of sugar under compressive load to determine a full **3D!** (3D!) displacement field. To correlate the same regions of the tomography scans, before and after load, the naturally occurring tin phase (approx. 15 % volume fraction) was used as high X-ray attenuating tracer. In contrast to this, Bay et al.[163] use structural sample features, in this case bone structures. Garcia et al.[42] quantify the amount of preferential grain boundary fracture compared to random fracture for different breakage conditions using XRM. Here, natural copper ore particles were used other than Xu et al.[178], who used down-cutted cubes from the same material to have a defined state for compression load tests.

Daly et al.[179] investigate the ductile fracture in a sample of pressure vessel steel over multiple scales with a combination of nano- and micro-CT supported by plasma focused ion beam (PFIB) to assist the calibration for ductile fracture models. Differences in X-ray attenuation can also arise within a nearly homogeneous matrix like cast alumina if there are inclusions above the size of three voxels. In case of fractures, the fracture surface on both opposite parts must also be at least three voxels apart, in most cases introduced by plastic deformation after the induced stress. As part of the Collaborative Research Center (CRC) 920 alumina casting samples were machined to radial symmetric samples for tensile testing (see Fig. 10.1-a). The objective is to expose the tensile sample to an oscillating alternating stress under tensile load, called ultra sonic fatigue test (USFT), until a crack develops.

The difficulty is to stop the USFT before the crack macroscopically ruptures the sample. The crack is in the process of spreading. Since the workpiece is ductile, the crack surfaces no longer close completely when the load is removed and, in the best case, the resulting distance is sufficient to make a crack surface visible via an XRM measurement. Scanning the sample before USFT delivers the initial state. Scanning after each USFT cycle shows when a crack appears. If a crack is visible, it can be correlated to the initial volume (b). The results were recently published by Wagner et al.[6].

Note that the same measurement parameters are mandatory and that the best possible alignment of the sample, e.g., by appropriate marking on the sample holder, greatly facilitates the correlation of the volumes. The same applies to comparative 2D measurements, e.g. cross-sectional images. If the preparative work is very precise during the measurement, the measurement results can be used to determine the position of potential cutting planes very precisely and thus avoid time-consuming multiple cuts and grindings.

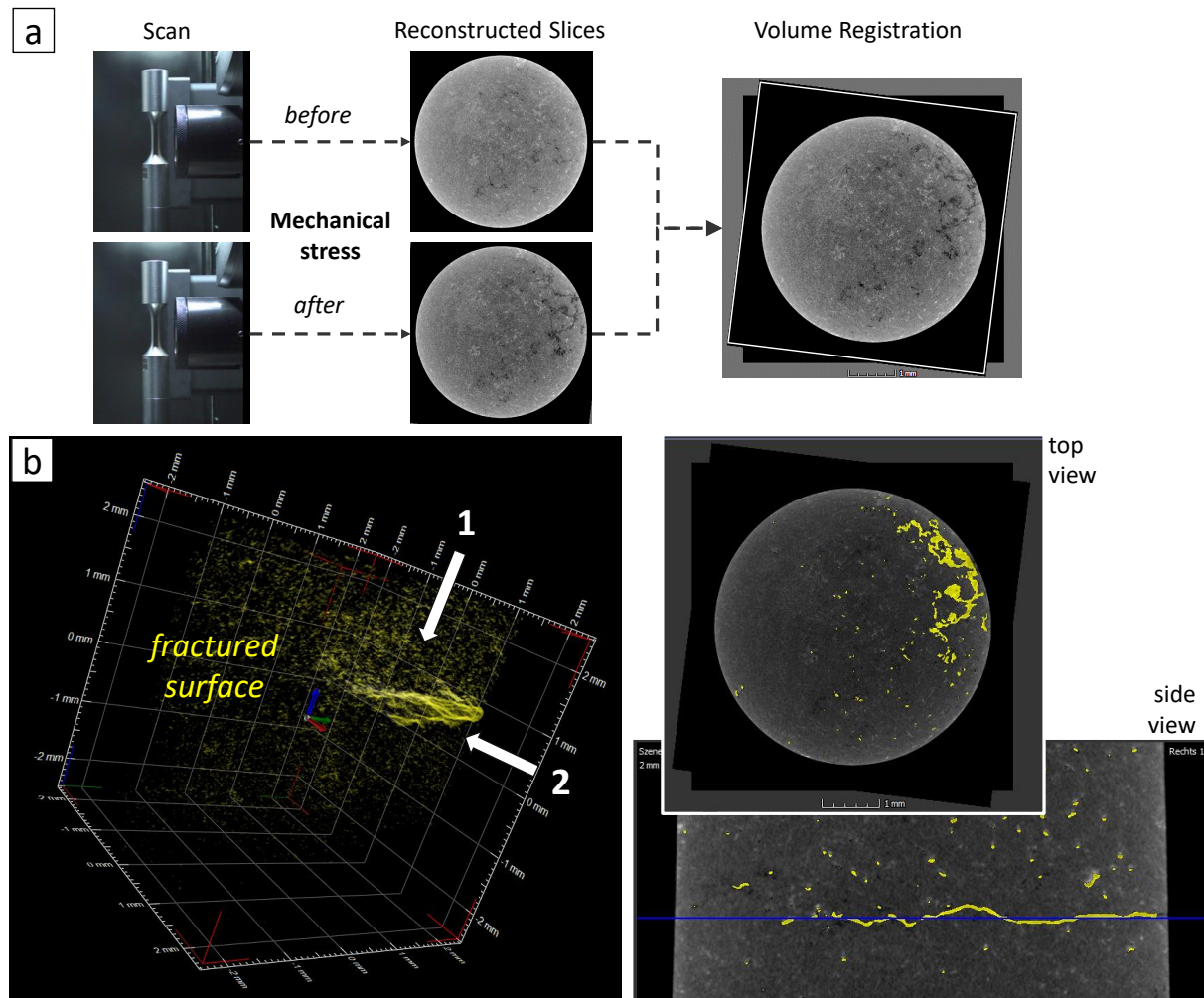


Figure 10.1: Application of XRM for fracture analysis of cast alumina sample before and after USFT (a), giving an extracted fractured surface in 3D! and in the corresponding top and side view (b).

10.2 Application Example 2: 3D Contact Angle Measurement

The contact angle between two phases is essential to describe interaction forces and develop reliable models, e.g., for the above mentioned metal melt filtration within the CRC 920. Normally, the surface is ideally smooth for such measurements. In most cases, however, real surfaces cause effects that significantly influence the contact area, in 3D the contact line. Surface unevenness, for example, leads to pinning effects that distort the contact areas and thus change the contact angle. Since these changes can be pronounced differently at certain points, it is essential to know the spatial contact angle distribution and not to limit to 2D projections, as is the case with conventional measurements.

In this particular case, with reference to the material system of the application from the CRC 920, a metal melt was chosen that can be examined at room temperature, in this case mercury. The substrate consists of aluminium oxide particles, which on the one hand represent the filter material and on the other hand serve as correlation markers. Figure 10.2 illustrates details of the measurement setup developed by my colleague Lisa Ditscherlein. (a) shows the sample mounting on top of a stainless steel pin that serves as a carrier for the particles, which were fixed with a two-component epoxy resin. After fixation, the particles were pressed tightly

with a cover glass to prevent the particles from slipping afterwards. The droplet was placed with a syringe on top of the surface.

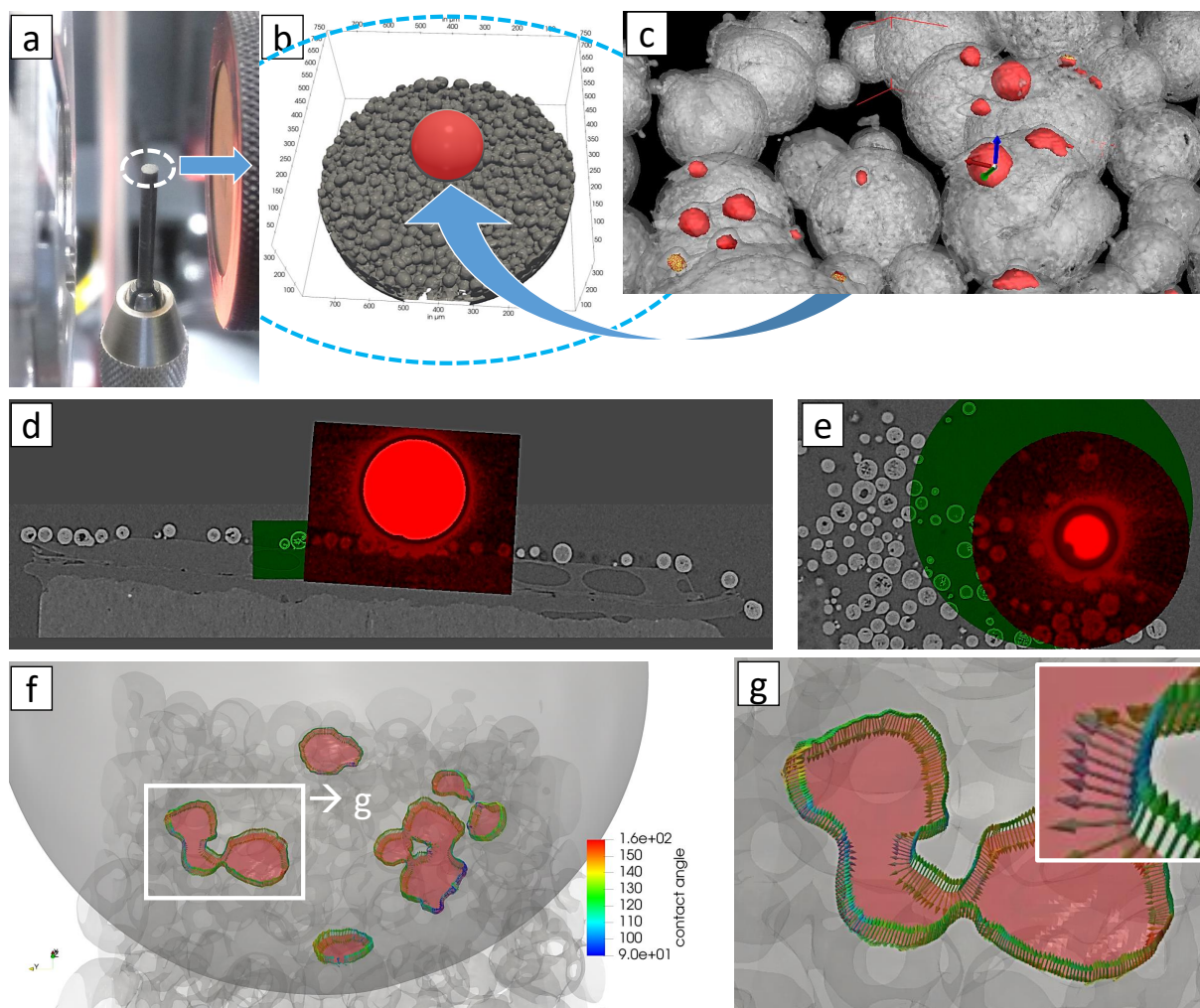


Figure 10.2: 3D contact angle measurement with a mercury droplet positioned a substrate made of alumina oxide with the mounted sample (a), the droplet on the surface (b), mercury residuals after removing the droplet (c), overlaying low-(grey) and high-resolution scans (green and red) from the side, same from the top (e), determined contact angles aligned on the contact line at the contact points (f) with the corresponding magnification (g).

If one considers the size of the droplet (approx. $300\ \mu\text{m}$), it becomes clear how difficult the correct positioning is. Surprisingly, the position of the droplet was very stable on the surface—the positions before and after repositioning were exactly the same. (b) shows the mercury droplet on top of the surface, (c) mercury residuals after removing the droplet from the surface, (d) overlaying of three different scans from the side, (1) low-resolution scan of the substrate without the droplet (gray), (2) high-resolution scan of a reduced area (green) and (3) the corresponding high-resolution scan of the droplet (red). Note that due to the extremely different X-ray attenuation coefficients of the substrate and the droplet, scans had to be performed at different energies. A low energy one for the substrate that delivers enough low energy photons to provide enough material contrast and a high energy one that manages to penetrate the extremely highly absorbing mercury droplet and allow reasonably practical scan times. This is sometimes called a dual energy approach. (e) is showing the corresponding top view. (f) and the referring magnification (g) shows the angles at the contact lines represented by vectors, all determined by self-written

algorithms by my colleague Erik Löwer.

Note, that the removing of the droplet was necessary to get two different measurement situations. One giving a situation with maximum contrast for low X-ray attenuating substrate details (low-energy scan) and one with maximum energy, where contrast within the mercury phase “doesn’t matter”, but to realize a reasonable scanning time. Mercury in this case was a border scenario that maximises the dynamic range of the system.

10.3 Influence of the Source Filter

The source filter has no influence on the grey value histogram, see Fig. 10.3-a, but on detector counts, see Fig. 10.3-b.

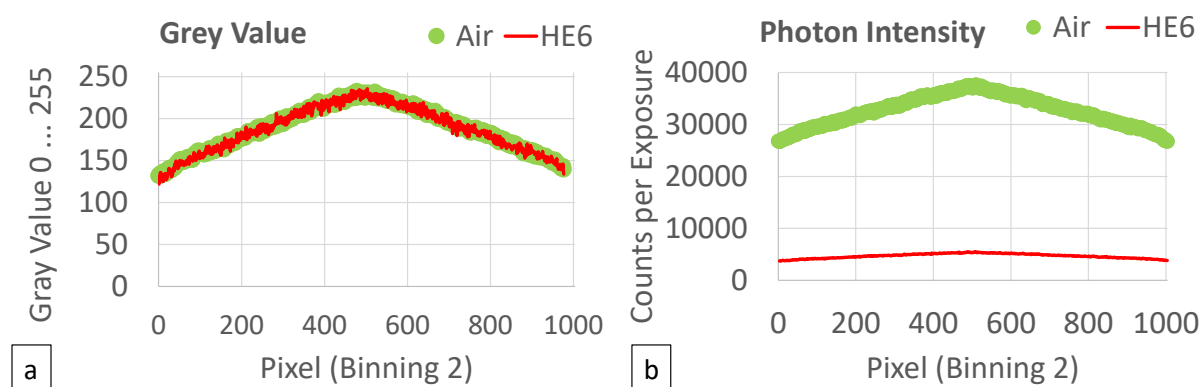


Figure 10.3: Source filter (a) showing no influence on the grey value, but (b) on the photon intensity.

Note that all referring projection images were captured with a constant exposure time of 1 s. High energy 6 (HE6), see Tab. 10.1 in Appendix 4.4.2, refers to the highest possible standard filter, which explains the extremely sharp drop in the photon intensity.

10.4 Influence of the X-rays on the Sample

Fig. 10.4 shows that the epoxy resin matrix used for particle embedding is clearly recognizable by its clear transparency. After the measurement, a significant colour change to light yellow is observed. This effect was also recognized by Parlanti et al. [98].

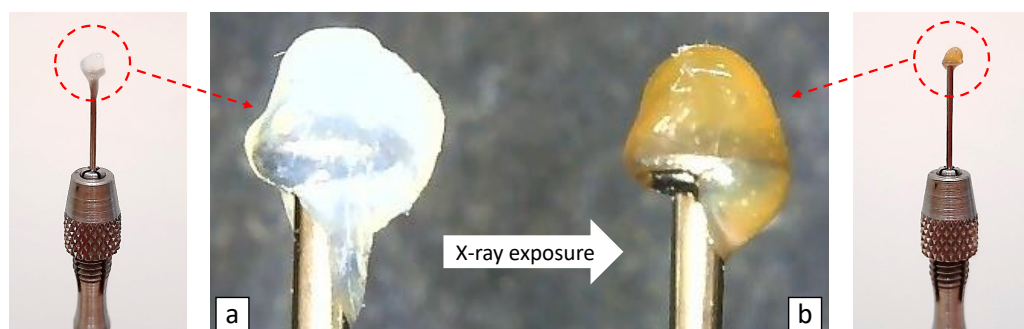


Figure 10.4: Colour change of epoxy resin matrix (a) after X-ray exposure (b) from clear transparent to light yellow – example is taken from single particle measurement. Note that (a) and (b) are different samples.

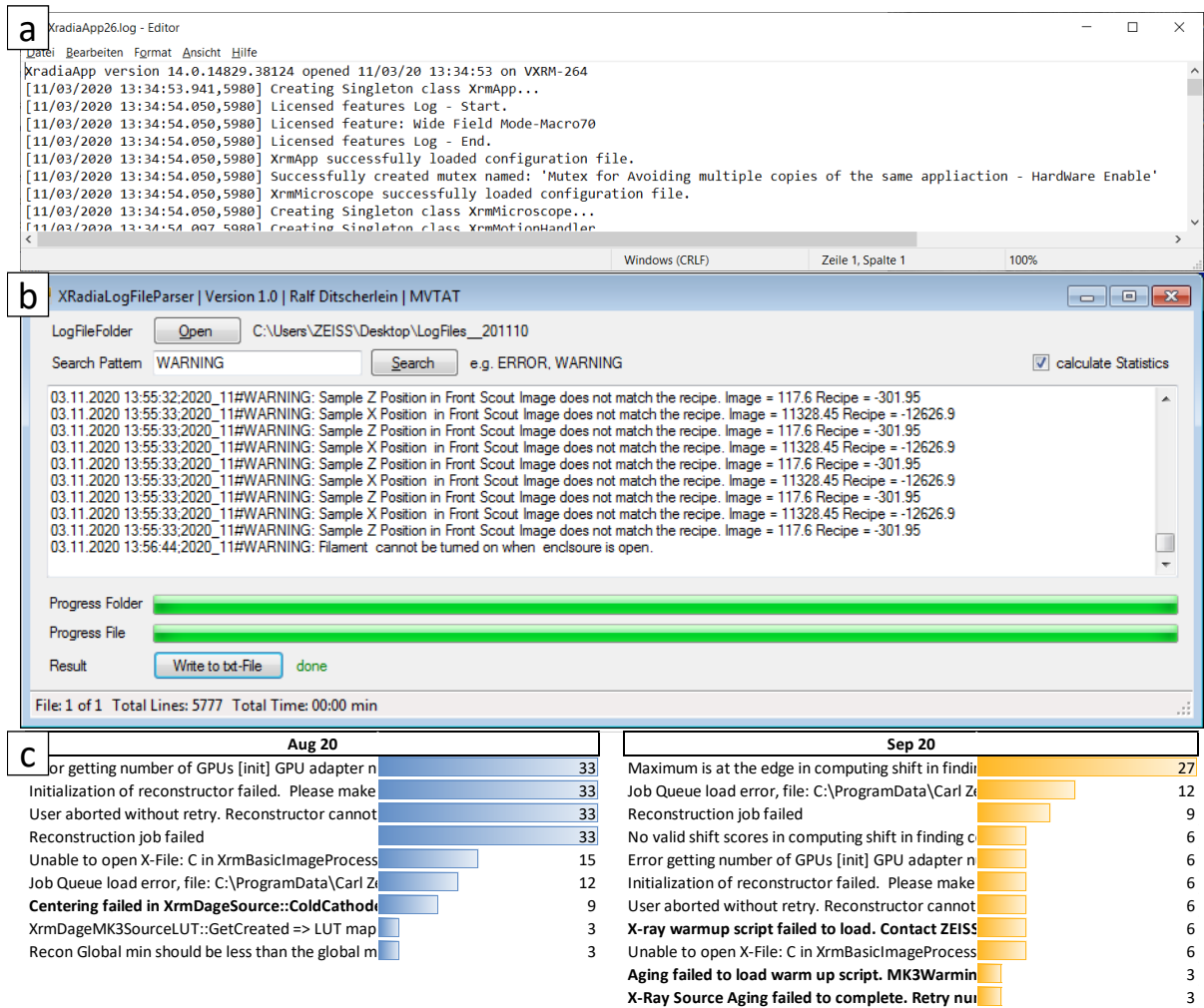


Figure 10.5: Self-coded log file parsing program. (a) shows the initial state: log files sorted by timestamp in a text file. (b) shows the graphical user interface of the parsing program and (c) a possible analysis comparing two months according to the most frequent cases of errors.

The following C# code-snippet is implemented in Visual Studio Express within the .NET framework.

```

using System;
using System.Collections.Generic;
using System.ComponentModel;
using System.Data;
using System.Drawing;
using System.Linq;
using System.Text;
using System.Threading.Tasks;
using System.Windows.Forms;
using System.IO;
using System.Text.RegularExpressions;

namespace XRadioLogFileParser
{
    public partial class Form1 : Form
    {
        string folderPath = String.Empty;
        string searchPattern = String.Empty;
        long totalLines = 0;
        DateTime startTime;

```

```
DateTime finishTime;
TimeSpan totalTime = TimeSpan.Zero;

Dictionary<string, int> dic = new Dictionary<string, int>();
string monthGroup;

public Form1()
{
    InitializeComponent();
    textBox1.Clear();
}

private void button1_Click(object sender, EventArgs e)
{
    startTime = DateTime.Now;

    string searchPattern = textBox2.Text;
    string filePath = String.Empty;
    int counter = 0;

    if (folderPath != String.Empty)
    {
        if (searchPattern != String.Empty)
        {
            //for each file
            DirectoryInfo ParentDirectory = new DirectoryInfo(folderPath);
            int fileCount = ParentDirectory.GetFiles("*.log").Length;
            progressBar2.Maximum = fileCount;
            progressBar2.Value = 0;

            foreach (FileInfo f in ParentDirectory.GetFiles("*.log"))
            {
                filePath = folderPath + "\\\" + f.Name;
                ParseFile(filePath, searchPattern);

                counter++;
                progressBar2.PerformStep();
                toolStripStatusLabel1.Text = "File: " + counter.ToString() + " of " +
                    fileCount.ToString();
                statusStrip1.Refresh();
            }

            //calculate additional statistics
            if (cbCalculateStatistics.Checked)
            {
                CalculateStatistics();
            }

            //calculate and display duration
            finishTime = DateTime.Now;
            totalTime = finishTime - startTime;
            toolStripStatusLabel3.Text = "Total Time: " + totalTime.ToString(@"mm\:ss")
                + " min";
            statusStrip1.Refresh();
        }
        else
        {
            MessageBox.Show("Please enter Search Pattern!");
        }
    }
    else
    {
        MessageBox.Show("Please select Folder with LogFiles!");
    }
}
```

```

private void button2_Click(object sender, EventArgs e)
{
    //initialize
    progressBar1.Value = 0;
    progressBar2.Value = 0;
    textBox1.Clear();
    textBox2.Clear();
    lblDone.Visible = false;

    folderBrowserDialog1.ShowDialog();
    folderPath = folderBrowserDialog1.SelectedPath.ToString();
    label5.Text = folderPath;
}

/// <summary>
/// parse the present file in the selected folder
/// </summary>
/// <param name="filePath"></param>
/// <param name="searchPattern"></param>
private void ParseFile(string filePath, string searchPattern)
{
    StreamReader file = new StreamReader(filePath);
    string line = String.Empty;
    string lineNew = String.Empty;

    int lineCount = File.ReadAllLines(filePath).Length;
    progressBar1.Maximum = lineCount;
    progressBar1.Value = 0;

    int counter = 0;

    //look for all lines in the file that contains the search pattern
    while ((line = file.ReadLine()) != null)
    {
        if (line.Contains(searchPattern))
        {
            lineNew = SplitAndRearrangeLine(line);

            //..append them to the textBox
            textBox1.AppendText(lineNew + "\r\n");
        }
        progressBar1.PerformStep();

        counter++;
    }
    file.Close();
    totalLines = totalLines + counter;
    toolStripStatusLabel2.Text = "Total Lines: " + totalLines.ToString();
}

/// <summary>
/// timestamp is bad formatted --> splitting + rearranging
/// </summary>
/// <param name="stringToSplit"></param>
/// <returns></returns>
private string SplitAndRearrangeLine(string stringToSplit)
{
    string s = stringToSplit;

    string day, month, year, hour, minute, second;
    string description;
    string lineNew;
    day = s.Substring(4, 2);
    month = s.Substring(1, 2);
    year = s.Substring(7, 4);
    hour = s.Substring(12, 2);
}

```

```

minute = s.Substring(15, 2);
second = s.Substring(18, 2);

description = s.Substring(30, s.Length - 30);
//delete leading space
description = description.Trim();
lineNew = String.Format("{0}.{1}.{2} {3}:{4}:{5};{2}_{1}#{6}", day
    , month
    , year
    , hour
    , minute
    , second
    , description);

return lineNew;
}

/// <summary>
/// calculate the statistics - how many occurrences per alert
/// </summary>
private void CalculateStatistics()
{
    //split multiline textbox into separate lines
    string[] lines = Regex.Split(textBox1.Text, "\r\n");

    //extract alert text without timestamp
    string lineAlert = String.Empty;

    foreach (var line in lines)
    {
        if (line != String.Empty)
        {
            //JOIN monthGroup (for statistics) to lineAlert
            lineAlert = line.Substring(20, line.Length - 20);

            //if the alert string is not in the dictionary
            if (!dic.ContainsKey(lineAlert))
            {
                //add key-value pair to dictionary
                dic.Add(lineAlert, 1);
            }
            else
            {
                //increment value by 1
                dic[lineAlert]++;
            }
        }
    }
}

/// <summary>
/// writing search result to txt-file
/// </summary>
/// <param name="sender"></param>
/// <param name="e"></param>
private void button3_Click(object sender, EventArgs e)
{
    try
    {
        if (textBox1.Text != String.Empty)
        {
            File.WriteAllText(folderPath + "\\PatternMatchResult.txt", textBox1.Text);
            File.WriteAllLines(folderPath + "\\PatternMatchResult_statistics.txt",
                dic.OrderByDescending(x => x.Value).Select(x => x.Key + ";" +
                    x.Value).ToArray());
            lblDone.Visible = true;
        }
    }
}

```



```
    }  
    else  
    {  
        MessageBox.Show("No search result to save!");  
    }  
}  
catch (Exception)  
{  
    MessageBox.Show("Failure while saving! " + e.ToString());  
    throw;  
}  
}  
}  
}
```

“Children bring chaos and clutter and an infinite potential for the future”
— Dan Simmons, *The Rise of Endymion* —

“Particles as well.”
— The author ☺ —